frontiers | Research Topics

Security and stability of low-carbon integrated energy systems

Edited by
Da Xie, Chenghong Gu, Dongdong Li, Nigel Schofield, Yanchi Zhang and Ignacio Hernando Gil

Published in
Frontiers in Energy Research

ISSN 1664-8714
ISBN 978-2-8325-4048-0
DOI 10.3389/978-2-8325-4048-0

About Frontiers

Frontiers is more than just an open access publisher of scholarly articles: it is a pioneering approach to the world of academia, radically improving the way scholarly research is managed. The grand vision of Frontiers is a world where all people have an equal opportunity to seek, share and generate knowledge. Frontiers provides immediate and permanent online open access to all its publications, but this alone is not enough to realize our grand goals.

Frontiers journal series

The Frontiers journal series is a multi-tier and interdisciplinary set of open-access, online journals, promising a paradigm shift from the current review, selection and dissemination processes in academic publishing. All Frontiers journals are driven by researchers for researchers; therefore, they constitute a service to the scholarly community. At the same time, the *Frontiers journal series* operates on a revolutionary invention, the tiered publishing system, initially addressing specific communities of scholars, and gradually climbing up to broader public understanding, thus serving the interests of the lay society, too.

Dedication to quality

Each Frontiers article is a landmark of the highest quality, thanks to genuinely collaborative interactions between authors and review editors, who include some of the world's best academicians. Research must be certified by peers before entering a stream of knowledge that may eventually reach the public - and shape society; therefore, Frontiers only applies the most rigorous and unbiased reviews. Frontiers revolutionizes research publishing by freely delivering the most outstanding research, evaluated with no bias from both the academic and social point of view. By applying the most advanced information technologies, Frontiers is catapulting scholarly publishing into a new generation.

What are Frontiers Research Topics?

Frontiers Research Topics are very popular trademarks of the *Frontiers journals series*: they are collections of at least ten articles, all centered on a particular subject. With their unique mix of varied contributions from Original Research to Review Articles, Frontiers Research Topics unify the most influential researchers, the latest key findings and historical advances in a hot research area.

Find out more on how to host your own Frontiers Research Topic or contribute to one as an author by contacting the Frontiers editorial office: frontiersin.org/about/contact

Security and stability of low-carbon integrated energy systems

Topic editors

Da Xie — Shanghai Jiao Tong University, China
Chenghong Gu — University of Bath, United Kingdom
Dongdong Li — Shanghai University of Electric Power, China
Nigel Schofield — University of Huddersfield, United Kingdom
Yanchi Zhang — Shanghai Dianji University, China
Ignacio Hernando Gil — Université de Bordeaux, France

Citation

Xie, D., Gu, C., Li, D., Schofield, N., Zhang, Y., Gil, I. H., eds. (2023). *Security and stability of low-carbon integrated energy systems*. Lausanne: Frontiers Media SA. doi: 10.3389/978-2-8325-4048-0

Table of contents

frontiers | Frontiers in Energy Research

TYPE Original Research
PUBLISHED 05 January 2023
DOI 10.3389/fenrg.2022.1002373

OPEN ACCESS

EDITED BY
Dongdong Li,
Shanghai University of Electric Power, China

REVIEWED BY
Nikolaos Manousakis,
University of West Attica, Greece
Neeraj Kumar Singh,
Larsen & Toubro (India), India

*CORRESPONDENCE
Zhengwei Qu,
ysu_qzw@163.com

SPECIALTY SECTION
This article was submitted to Smart Grids, a section of the journal Frontiers in Energy Research

RECEIVED 25 July 2022
ACCEPTED 14 September 2022
PUBLISHED 05 January 2023

CITATION
Qu Z, Sun W, Dong J, Zhao J and Li Y (2023), Electric power cyber-physical systems vulnerability assessment under cyber attack.
Front. Energy Res. 10:1002373.
doi: 10.3389/fenrg.2022.1002373

Electric power cyber-physical systems vulnerability assessment under cyber attack

Zhengwei Qu[1]*, Wenting Sun[1], Jie Dong[2], Jianjun Zhao[2] and Yang Li[2]

[1]School of Electrical Engineering, Yanshan University, Qinhuangdao, Hebei, China, [2]Smart Distribution Center of State Grid Jibei Electric Power Limited Company, Qinhuangdao, Hebei, China

Improving the accuracy of the vulnerability assessment of the power cyber-physical system has important practical value for protecting the vulnerable links of the system and preventing large power outages. This article studies the vulnerability assessment of power cyber-physical systems under cyber-attacks. First, from the perspective of topology, the electrical betweenness is used as the structural vulnerability index of the power system. Based on the power flow characteristics of the power network, the voltage is used as the state vulnerability index. Then, starting from the structure, the node degree and clustering coefficient are selected to analyze the structural vulnerability. Considering the service transmission characteristics of the information system, the power service importance is selected as the vulnerability assessment index of the information system. The two selected indexes are used to construct a quantitative formula, and a comprehensive index is obtained to complete the node vulnerability assessment of the power information system. Then, on the basis of the system vulnerability assessment, we screen to determine the entry and target nodes of network attacks and predict the network attack path. Finally, the effectiveness of the proposed method for vulnerability assessment and feasibility is verified by MATLAB programming simulation.

KEYWORDS

power systems, information system, attack path prediction, cyber-physical power system, vulnerability assessment

Introduction

Since modern smart grids have various deeply coupled cyber-physical components, they are vulnerable to malicious cyber-attacks. In view of the frequent power outage accidents in recent years, the vulnerability of the power system has become a research hotspot for scholars from all over the world. Scientifically identifying and evaluating the vulnerable links of power cyber-physical systems (CPSs) has very important theoretical and practical significance for studying fault propagation between the power network and information network and improving the safe and reliable operation of the power CPS.

Although there are many studies on power system vulnerability assessment and power cascading failures, the selection of vulnerability index lacks comprehensive consideration, and vulnerability is often analyzed from isolated networks. Wang et al. (2016) summarized the research status of the influencing factors of structural vulnerability and protection strategies on the basis of an overview of the modeling and vulnerability assessment methods of power information-physical interdependent networks. Zhan et al. (2014) proposed weighted complex network parameters and the comprehensive sensitivity of microgrid nodes and lines to form a microgrid vulnerability evaluation system and consider the network parameters of nodes. Lian et al. (2019) proposed an evaluation index that integrates the importance of power nodes and the topology of the information network, which provides a reference for improving the robustness of the power system. Ji et al. (2016a) summarized the modeling methods, existing models, and vulnerability assessment methods of interdependent networks, which have great reference value for future research on CPS vulnerability. Li et al. (2020) proposed a hierarchical membership function based on the vulnerability of the network on the physical side to describe the vulnerability between various levels of the evaluation index. A total of four indexes of voltage increment severity were there to analyze the entire distribution network.

Ji et al. (2016b) adopted the complex network theory and uses a multi-layer complex network model to extract the multi-layer centrality between the networks and the shortest electrical path algorithm to evaluate the robustness of the power network. Chen et al. (2007) proposed a large-scale grid structure vulnerability analysis method based on grid topology. This method emphasizes the influence of the overall architecture of the power grid on fault propagation, and helps to study the propagation mechanism of cascading faults in large power grids. Koc et al. (2016) and Fang et al. (2017). analyzed the structural vulnerability of the distributed power grids and propose a complex network method based on the maximum power flow to identify critical lines in the system. In addition, Gutiérrez et al. (2015) proposed a method based on the graph theory to analyze the vulnerability of the power grid structure. Park et al. (2012) used the N-1 method to collect all physical faults and information faults when evaluating the power system of the fusion information system, analyzed the response function of the power system under faults, and compared the reliability of the system under normal operation. The vulnerability index is used to analyze and evaluate the vulnerability of the power system. Tang et al. (2015) proposed a composite system correlation matrix that can reflect the relationship between power–communication topology. Based on the source-flow path electrical subdivision method, the communication system vulnerability index the power communication business information interaction vulnerability, and the composite system static vulnerability matrix was obtained. The vulnerability of the power–communication composite system at a certain time section can be judged. Li et al. (2018) proposed a CPS vulnerability assessment method for the distribution network in distributed cooperative control mode based on dynamic attack–defense game, which guides the design of future cooperative control systems from a risk perspective.

At present, there has been research on the vulnerability of power CPS. Although the modeling of the information side is integrated on the basis of the power network, when selecting the vulnerability index, the integrated power cyber-physical system, the analysis of multiple aspects and angles has not been fully considered in the case of combining the characteristics of each side network.

Therefore, this study proposes to establish a comprehensive vulnerability index of the power system from two aspects of topology structure and operation state based on the complex network theory and power flow characteristics of the power network. This index not only implies a relatively static and invariable network structure but also reflects the system operation state, and has the characteristics of conforming to the basic electrical laws of the power network. When considering the node vulnerability of the information system, starting from the network structure, the node degree and clustering coefficient are selected to analyze the structural vulnerability. Considering the service transmission characteristics of the information system, the importance of power business is selected as the vulnerability assessment index of the information system. A quantitative formula is constructed for the two selected indexes, and a comprehensive index is finally obtained to quantify the node vulnerability of the information system and complete the vulnerability assessment of the power information node. Then, on the basis of the system vulnerability assessment, a screen was there to determine the entry and target nodes of network attacks and predict the network attack path.

Power system vulnerability index

This section first introduces the two indexes determined from the comprehensive analysis of the structural vulnerability and state vulnerability of the power system, and combines the topological vulnerability index and the state vulnerability index in a linearly weighted manner to generate a new comprehensive evaluation index.

Power system structural vulnerability index—electrical betweenness

Betweenness is defined as the ratio of the number of paths passing through the node among the shortest paths in the network to the total number of shortest paths. Betweenness

can represent the influence of a node and can measure the importance of each node or edge in the network.

But in power systems, power does not inherently flow only along the shortest paths. Considering the node capacity, the impedance of the transmission line, and the weighted adjacency matrix, the electrical betweenness can truly reflect the occupancy of the node in the "generator-load" power transmission, and can consider the influence of the generation power and load level of different nodes, quantification of the contribution value of each node in the power flow transmission of the whole network is more in line with the actual physical meaning of the power system. Therefore, this study chooses the electrical betweenness as the structural vulnerability index of the power system.

The electrical betweenness of the node n is denoted as follows:

$$B_e(n) = \sum_{i \in G, j \in L} \sqrt{W_i W_j} B_{e,ij}(n), \tag{1}$$

where G is the generator node set and L is the load node set. (i, j) represents a "generator-load" node pair. The generator node weighting W_i is defined as the rated generating active power of the generator, and the load node weighting W_j is defined as the actual or peak load.

$B_{e,ij}(n)$ is the electrical betweenness of node n, representing the unit current injected into the node pair, and the formula is as follows:

$$B_{e,ij}(n) = \begin{cases} \frac{1}{2} \sum_m \left| I^{ij}(m,n) \right|, n \neq i, j \\ 1, n = i, j \end{cases}, \tag{2}$$

where m represents all nodes directly connected to the node; $I^{ij}(m.n)$ is the current that flows into the "generator-load" node pair (i, j) after adding a unit injection current element, which is caused on the line (m, n).

Eq. 2 reflects the occupancy rate of node pairs (i, j) in the power transmission process. According to the corresponding weights in the network, the sum of the occupancy rates of each "generator-load" node pair is $B_{e,ij}(n)$,

When calculating, it is assumed that the system has $N + 1$ nodes in total and the last one is the reference node, then its reduced-order admittance matrix is $Y(N \times N)$. Assuming that the unit injection current element added between node i and the reference node is e^i, the current calculation formula caused by it on branch (m, n) is as follows:

$$I^i(m,n) = \left(U^i(m) - U^i(n)\right) \bullet y_{mn}. \tag{3}$$

In the formula, U^i is a vector composed of voltages caused by e^i on each node, and satisfies $YU^i = e^i$; $U^i(m)$ and $U^i(n)$ are its components on nodes m and n, respectively; y_{mn} is the admittance of branch (m, n).

If the unit injection current element added between node i and node j is e^{ij}, $e^{ij} = e^i - e^j$ can be obtained. Therefore, according to the additivity of the linear circuit, the calculation formula can be obtained as follows:

$$I^{ij}(m,n) = I^i(m,n) - I^j(m,n), \tag{4}$$

where $I^{ij}(m,n)$ is the current caused by e^{ij} acting on branch (m, n), which is equal to the linear sum of the currents caused by e^i and e^j on that branch, respectively, on this branch.

In the calculation, the current caused by the unit injection current element between each node and the reference node on each branch should be calculated according to Eq. 3, and then directly subtracted according to Eq. 4 to obtain the current value which is caused by adding the current value of the unit injection current element between the "generator-load" node pairs, and then substitute it into Eq. 1 to obtain the electrical betweenness of each node, which can greatly simplify the operation.

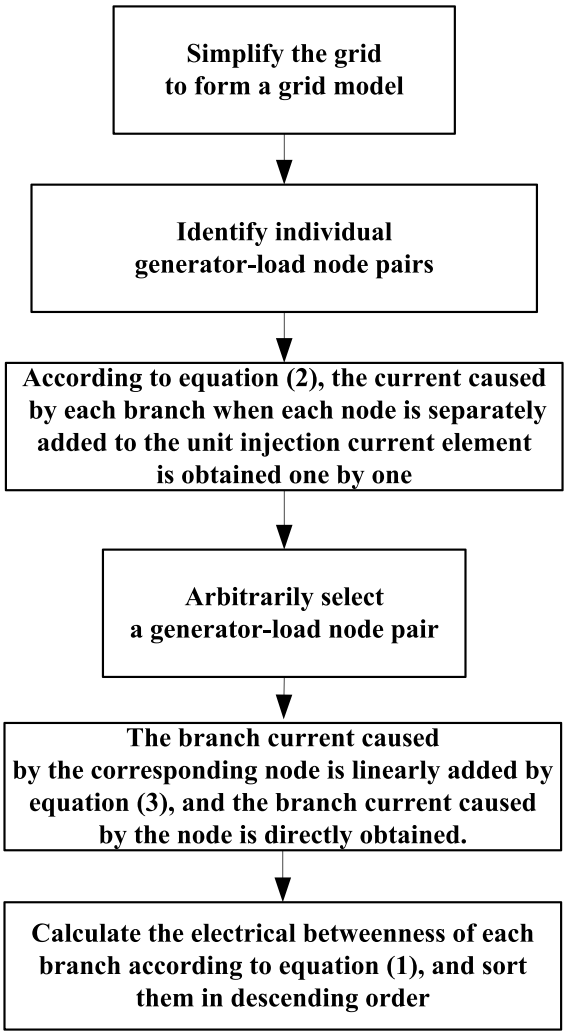

FIGURE 1
Electrical betweenness calculation flowchart.

The index is normalized, and the electrical betweenness index is defined as follows:

$$C_{be}(m,n) = \frac{B_e(m,n)}{\sum_{i\in G, j\in L}\sqrt{W_i W_j}}. \quad (5)$$

Considering that the smaller the electrical betweenness index of the node is, the more fragile the node is, so the structural vulnerability index is selected as follows:

$$C_e(m,n) = \frac{1}{C_{be}(m,n)}. \quad (6)$$

According to the calculation and analysis of the abovementioned electrical betweenness index, the steps for calculating the electrical betweenness are given as follows:

1) The topology diagram of the power grid is formed according to the abovementioned simplified method, and only the main grid part of the high-voltage transmission network is considered.
2) The nodes are divided into power generation, load, and intermediate nodes, and only the electrical betweenness of the line caused by the power generation and load node pairs is calculated. The line parameters only consider the reactance and do not consider the ground leakage capacitance. The generation node matrix, load node matrix, and line impedance matrix are formed.
3) The connectivity of the network is determined. A pair of power generation load node pairs is arbitrarily selected, and the electrical betweenness component of the line is calculated according to Eq. 1.
4) After traversing all the power generation load node pairs, the electrical betweenness of the line is calculated, arranged in descending order, and the cumulative distribution is calculated.

The flow chart of dielectric number calculation is shown in Figure 1.

Power system state vulnerability index—voltage

The power system is a complex dynamic system. There are four kinds of power system stability, among which voltage stability is an important aspect.

At present, there are many different voltage stability indexes, which are generally divided into two categories: state index and margin index. The state index is used to evaluate the stability of the system at the time according to the system operating state parameters, and the amount of calculation is relatively small. The margin index has good linearity and clear physical meaning, which can easily take into account various factors in the transition process, but the calculation process needs to solve the critical value, so the calculation process will be more complicated. The main expressions of the voltage stability index are as follows:

TABLE 1 Weight molecules corresponding to different voltage levels.

Node voltage range, δ_m	Weighting factor, ω_n
≤0.9	0.75
(0.9,0.925]	0.70
(0.925,0.95]	0.65
(0.95,0.975]	0.60
(0.975,1.0)	0.55
≥ 1.0	0.50

$$VI_n^a = |U_n(t) - U_{cr}|, \quad (7)$$

$$VI_n^b = \frac{|U_n(t) - U_{cr}|}{|U_{n0} - U_{cr}|}, \quad (8)$$

$$VI_n^c = \frac{\partial U_n}{\partial p}. \quad (9)$$

Since voltage is an important operating state parameter of the node, the voltage index is also an important index to measure the vulnerability of the node. The node state vulnerability index adopts the index of Eq. 8 as follows:

$$C_u(n) = \frac{1}{VI_n^b} = |U_{n0} - U_{cr}|/|U_n(t) - U_{cr}|. \quad (10)$$

In Eq. 10, $U_n(t)$ represents the voltage of the node n at the moment, U_{cr} is the critical voltage of the node, and U_{n0} is the voltage at the initial moment of node n ,

The calculation speed and accuracy of the node critical voltage value are directly related to the calculation of the node state vulnerability index. Therefore, seeking a relatively fast and accurate algorithm is the key to calculating the node critical voltage. At present, the main methods of the node critical voltage calculation are: continuous power flow method, load admittance method, power flow multi-solution method, and other methods.

In this study, a modified nonlinear power flow (PNFA) (Shi et al., 2010) algorithm is used to calculate the node critical voltage.

Comprehensive vulnerability index of the power system

A new comprehensive index is obtained by combining the index of structural vulnerability—electrical betweenness and the index of state vulnerability—voltage through linear weighting, which not only takes into account the impact of the damaged

TABLE 2 Types and importance of electricity businesses.

Business type/business number	Importance/order
Relay protection/I	0.99/1
Stable system/II	0.94/2
Domain measurement and scheduling automation /III	0.62/3
Substation video monitoring/IV	0.29/4
Lightning location monitoring and office automation/V	0.13/5

power system structure but also can taking into account the influence of the grid operation status on the power system.

$$C_d(n) = (1-\omega_n)C_e(n) + \omega_n C_u(n), \tag{11}$$

where $C_e(n)$ represents the topological vulnerability index of the grid node, $C_u(n)$ represents the state vulnerability index of the node, and ω_n is the different weight factor corresponding to the node at different voltage levels. $1-\omega_n\omega_n$ represents the proportion of topology information and state information in evaluating the vulnerability of power nodes.

The weight factors ω_n of node 6 under different voltage levels are shown in Table 1 (Zhang et al., 2016), where δ_m is the ratio of the actual voltage value to the reference voltage value.

Information system vulnerability index

This section introduces the selection of index from the network structure to analyze the vulnerability of the information system, considers the service transmission characteristics of the information system, and selects the power service importance as the vulnerability assessment index. Then, a quantitative formula is constructed for the two selected indexes, and a comprehensive index is finally obtained to quantify the node vulnerability of the information system and complete the vulnerability assessment of the communication network node.

Information system structural vulnerability index

Information system nodes have large scales and diverse topological structures. The commonly used indexes, when evaluating the topological importance of network nodes, are the degree centrality and betweenness centrality of nodes. Because betweenness centrality needs to grasp the global information of the entire network, it has high computational complexity for large-scale network structures such as power communication networks. Different from betweenness centrality and closeness centrality, degree centrality mainly considers the node's own information, which is simple in calculation and low in time complexity, and is suitable for large-scale networks.

In the network node, the node aggregation feature has a great influence on the influence of the node. In the transmission layer of the power information network, there are many triangular structures formed by nodes. If the betweenness used as an index and the link weight is not considered, a node with a degree of two in the triangular structure will not be included in the shortest path of the network, thereby reducing the influence and importance of this node when calculating the evaluation. At the same time, the edge nodes belonging to the access layer in the network are not easy to form in a triangular structure, and the influence represented by the clustering coefficient will reach the maximum value. It can be seen that although the clustering coefficient cannot reflect the scale of adjacent nodes, it can quantify the degree of connection between the nodes and adjacent nodes. This study analyzes the node vulnerability from the network topology structure, comprehensively considers the node degree and clustering coefficient, and proposes the network topology structure importance evaluation index T, which represents the influence of the node on the network topology structure, and defines the T value of node n as follows:

$$T(i) = \frac{k(i)}{\sqrt{\sum_{j=1}^{N}[k(j)]^2}} + \frac{c(i)}{\sqrt{\sum_{j=1}^{N}[c(j)]^2}}, \tag{12}$$

where $k(i)$ is the node degree of the node and $c(i)$ is the clustering coefficient of node n. $c(i)$ is expressed as follows:

$$c(i) = \frac{2e(i)}{[k(i)]^2 - k(i)}. \tag{13}$$

In Eq. 13, $e(i)$ represents the number of edges between all the neighbor nodes of node n.

$$f(i) = \frac{\max\limits_{j\in[1,N]}\left[\frac{c(j)}{k(j)}\right] - \frac{c(i)}{k(i)}}{\max\limits_{j\in[1,N]}\left[\frac{c(j)}{k(j)}\right] - \min\limits_{j\in[1,N]}\left[\frac{c(j)}{k(j)}\right]}, \tag{14}$$

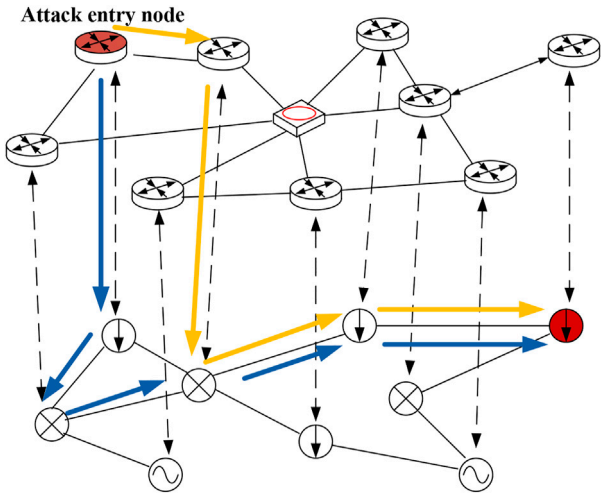

FIGURE 2
Attack-path prediction demonstration diagram.

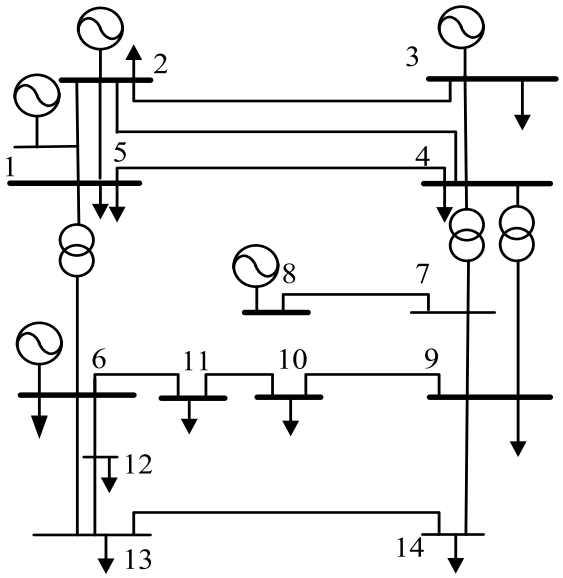

FIGURE 3
IEEE14 system wiring diagram.

where the smaller the clustering coefficient $c(i)$, the larger the node degree and the larger the value of $f(i)$.

Information system functional vulnerability index

As a special complex network structure, the information system has its own unique industrial background. The nodes are responsible for a large amount of power business data related to the power grid, mainly including relay protection, stability system, dispatch automation, wide-area measurement, and other services. The nodes undertake different types and quantities of communication services, and the service importance is used to represent the impact on the power grid when a service is interrupted or the service quality is defective. The more serious the impact on the power grid, the greater the importance of the corresponding service. The more the types and quantities of services a node undertakes, the more serious the impact of node failure on the power grid will be. Therefore, when evaluating the node vulnerability, the node business importance is used as an index to measure.

Table 2 shows the importance of various services obtained according to the security division characteristics of different services and the requirements for channels, combined with reference (Fan and Tang, 2014), which are divided into five categories, representing the average value of the importance of various services.

The number of links connected to a node and the services in each link jointly determine the importance of a node at the service layer. The more links a node is connected to, the greater the type and quantity of services carried by the links, which means that more services are transmitted through the node. Therefore, when calculating the service importance of a node, the influence of the number of links and the number and type of services on the importance of the node is considered. The calculation formula for defining the business importance of a node is as follows:

$$B(i) = \sum_{j=1}^{n} b_{kj} l_{kj}, \tag{15}$$

where $B(i)$ is the service importance of the node$i$; l is the number of links of the node$i$; b_{kj} is the importance of the k type of service undertaken by the $j$link of the node$i$; and l_{kj} is the number of the k type of service undertaken by link j.

From Eq. 15, it can be seen that the more links a node is connected to and the more business types and quantities that are more important to the operation of the power grid, the node has a greater business importance.

The information fusion is completed for the quantization results of two angles, and the method to obtain the quantized value of node vulnerability is as follows:

$$I(i) = \frac{T(i)B(i)}{1 - T(i) - B(i) + 2T(i)B(i)}. \tag{16}$$

The vulnerability quantification formula that finally defines the information node is as follows:

$$C_x(i) = \frac{I(i) - I_{\min}(i)}{I_{\max}(i) - I_{\min}(i)}. \tag{17}$$

TABLE 3 Comparison between the IEEE14 node line electrical and capacity.

Line	Electrical betweenness	Sort order	Capacity betweenness	Sort order
4–9	13,595	1	9,390	1
5–6	12,061	2	5,524	3
1–2	10,662	3	5,763	2
7–8	10,409	4	3,570	4

Network attack path prediction

This section introduces the determination of the network attack entry node according to the vulnerability value of the information system. Then, we select the key indicators for the power system nodes, sort the nodes according to the key points, and determine the network attack target nodes according to the criticality of the power nodes. Finally, we use the Dijkstra algorithm to predict the network attack path.

Determination of the attack entry node and attack target node

When attackers launch a network attack, they usually invade the network step by step and conduct the attack step by step. The most critical step in the attack process is to select the attack-entry nodes and the attack-target nodes. Based on the idea of game theory, the attacker's point of view is to minimize the implementation cost of the attacker and maximize the system loss.

Therefore, this study assumes that the attacker's vulnerability of the information system is the starting point of the attack, and the ultimate goal of the attack is to select the nodes that can make the most profit, that is, some key nodes to attack. First, we determine the attack-entry point, that is, the vulnerability point of the information system, which has been obtained from the second part of the power CPS vulnerability assessment.

The next step is to determine the attack-target node, which is also a key node.

Assuming that there are S branches between node i and node j of the physical side power grid, the impedance of each branch is $Z_1, Z_2, Z_3 \ldots\ldots Z_s$, and according to Kirchhoff's law, it can be obtained.

$$U_i - U_j = IZ_{eq.ij}. \tag{18}$$

Then, the equivalent impedance Z of the line between node i and node j pair is derived as

$$Z_{eq.ij} = \frac{\left(U_i - U_j\right)}{I}, \tag{19}$$

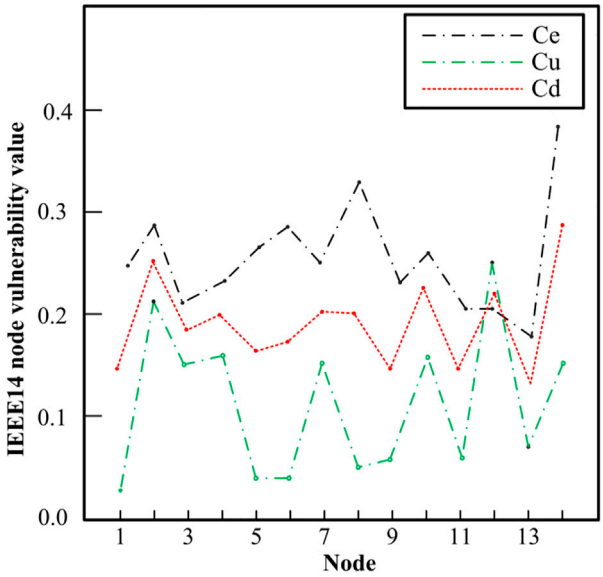

FIGURE 4
IEEE14 node vulnerability index value.

where I is the unit current injected from the port composed of the node pair; U_i and U_j are the voltages corresponding to nodes i and j, respectively.

For a physical side network with Mnodes and N branches, the sum of the equivalent impedances of all the node pairs is defined as the electrical topology quantity of the physical side system as follows:

$$Z = \sum_{i=1}^{M} \sum_{j=i+1}^{M} Z_{eq.ij}. \tag{20}$$

When a line is mistakenly cut due to a network attack in the network, the electrical topology importance factor of the line in the system is

$$C^Z = \frac{\Delta Z_k}{Z} = \frac{\Delta Z_k}{\sum_{i=1}^{M} \sum_{j=i+1}^{M} Z_{eq.ij}}, \tag{21}$$

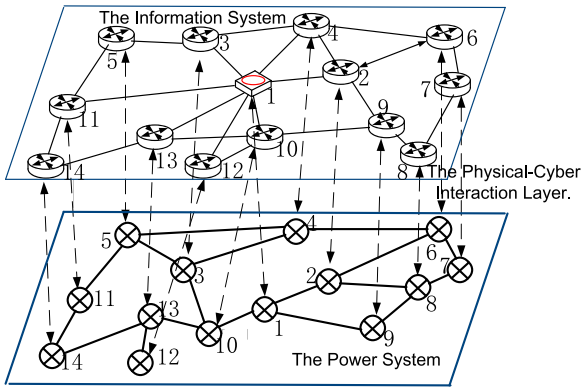

FIGURE 5
Power 14 node-information 14 node system diagram.

where Z_k is the equivalent impedance of the wrongly cut line, and the larger the value of C^Z, the greater the impact of the breaking of the branch on the system.

It is assumed that the largest connected domain in the target network contains N_0 branches before the system is attacked. When a network attack event occurs, the remaining connected areas in the network contain N_k branches. Then, the connectivity factor of the line is

$$C^G = \frac{N_0 - N_k}{N_0}. \tag{22}$$

Combining the two impact factor indicators, the impact factor of the attack-target layer is

$$C_i^e = \mu_1 C^Z + \mu_2 C^G, \tag{23}$$

where μ_1、μ_2 refers to the proportions of electrical topology importance and connectivity factor in the calculation of attack target nodes, respectively.

The attack path prediction algorithm is designed on the basis of the Dijkstra classic algorithm, referring to the effectiveness of the Dijkstra algorithm in finding the single-source shortest path in a directed graph. The algorithm needs to calculate the maximum possible path from the initially occupied node to the target node. The steps to predict the attack path are as follows:

1) First, the model of the power cyber-physical system is established
2) The introduced vulnerability index method is used to calculate the vulnerability value of the power system and information system
3) The correlation matrix of the model is input
4) The attack entry node and the attack target node is calculated

The attack path effect is shown in the figure as follows.

The blue and yellow lines in Figure 2 represent an attack path that a network attacker may take from the attack-entry node to the attack-target node. The path starts from the entry node of the information system to the attack-target node of the physical system, that is, electricity. The critical node of the system ends. By adopting the principle of finding the shortest path from a single source by using the Dijkstra algorithm, and based on the evaluation results of the vulnerability value of each node in the system, the predicted network attack path is designed, and the maximum possible attack path that the attacker may take is obtained.

Case study

In this section, the IEEE14 node is used as an example to calculate the electrical betweenness and voltage index of the system node, which proves that the selection of the power system index is more reasonable and accurate. Second, the vulnerability values of the electrical nodes and information nodes of the power cyber-physical system are calculated, which confirms that the quantitative value of the proposed comprehensive vulnerability index conforms to the actual system operation. Finally, the key indicators of the power system nodes are selected, the key points are sorted, and the network attack-target points are determined according to the key points of the power nodes. Finally, the Dijkstra algorithm is used to predict the network attack path. The effectiveness of the algorithm in path prediction is verified.

Power system vulnerability study

The IEEE14 node is used as an example, as shown in Figure 3. The electrical betweenness vulnerability index of the line is calculated based on MATLAB programming, and the electrical betweenness data of the line is obtained.

The calculated data show that the distribution of the dielectric values of the lines is extremely uneven. Most of the lines' dielectric values are near the average value, but there are still a few lines whose dielectric values are much higher than the average value. The vulnerable lines identified by the electrical betweenness index are compared with the capacity betweenness identification results proposed by He et al. (2013), as shown in Table 3.

It can be seen from Table 3 that in the identification results of the two betweenness indexes, the rankings of lines 4–9 and 5–6 are very high, and we can also consider them to be vulnerable lines. Similarly, we can see from the wiring diagram in figure 3 that these lines happen to be at important key positions, and most of the vulnerable lines obtained are long-distance connections, and their disconnection will divide the power grid into several areas, which will seriously affect the structure of the power grid.

TABLE 4 Node vulnerability value of the power cyber-physical system.

Power node	Vulnerability value	Information node	Vulnerability value
1	0.1613	1	0.7540
2	0.2702	2	0.3441
3	0.1920	3	0.3932
4	0.2108	4	0.2886
5	0.1748	5	0.3418
6	0.1867	6	0.3129
7	0.2187	7	0.3691
8	0.2157	8	0.3026
9	0.1656	9	0.3129
10	0.2338	10	0.3042
11	0.1508	11	0.3373
12	0.2300	12	0.0725
13	0.1457	13	0.2807
14	0.3046	14	0.0552

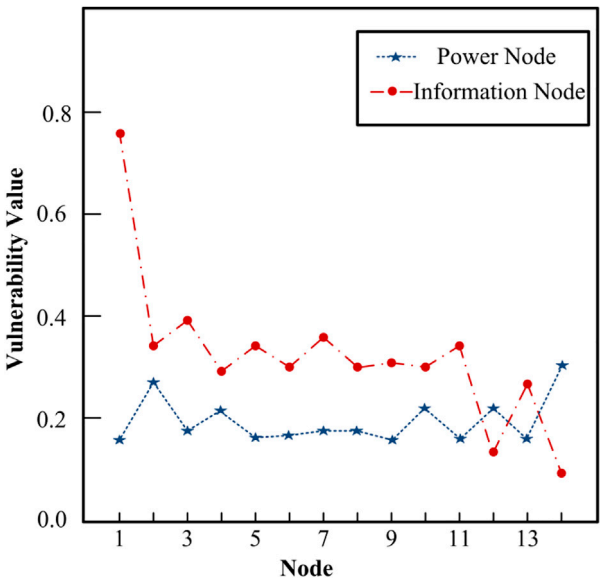

FIGURE 6
Node comprehensive vulnerability value.

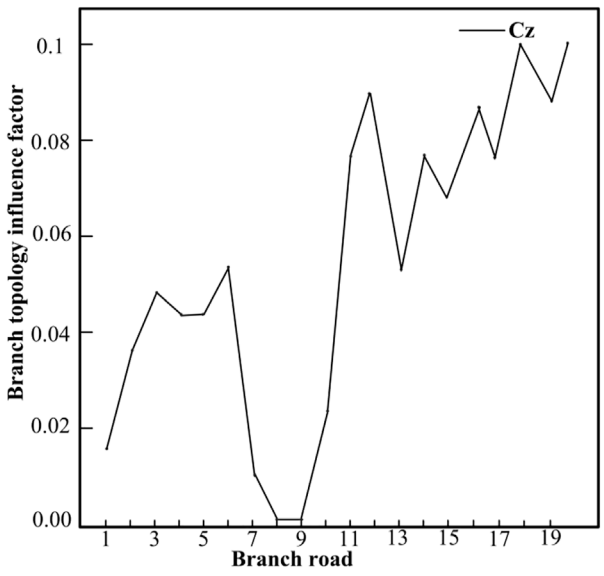

FIGURE 7
Branch topology influence factor Fig.8 Branch connectivity impact factor.

The results obtained by using the electrical betweenness as an index of the structural vulnerability of the power system are compared with the capacity betweenness model proposed in (He et al., 2013), and finally we can obtain similar results, which are more accurate and practical. Therefore, the electrical betweenness is used as The power system structural vulnerability index is more superior.

Based on MATLAB programming, the node's structural vulnerability index, electrical betweenness and state vulnerability voltage index, could be calculated. At the same time, based on the results of the structural vulnerability index and state vulnerability index, the comprehensive vulnerability index of the node is obtained, as shown in Figure 4.

From Figure 4, we can clearly know that when different indexes are selected, the vulnerability of each node is evidently different. The

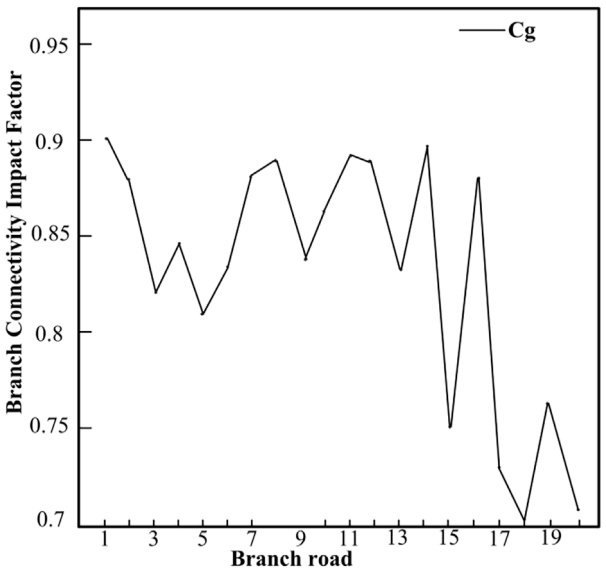

FIGURE 8
Comprehensive vulnerability index of the power cyber-physical system.

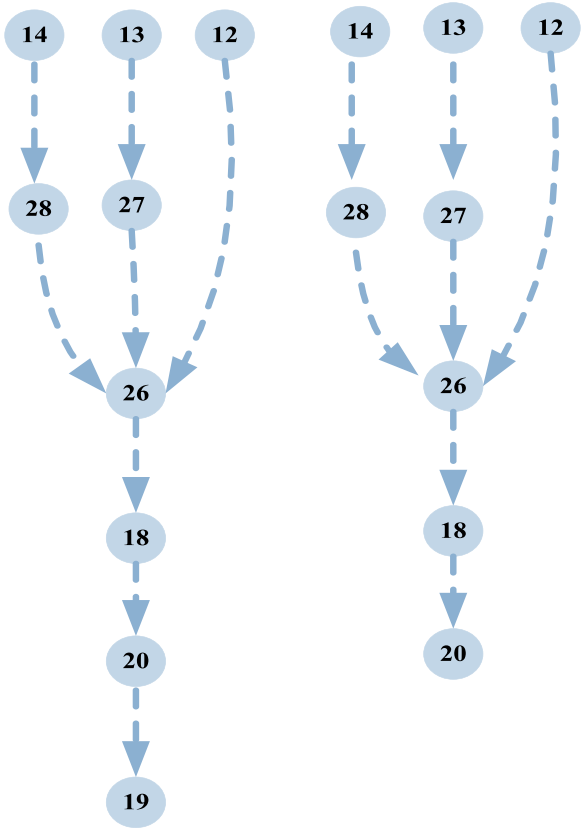

FIGURE 9
Network attack path prediction diagram.

selection of a single index will result in an inaccurate assessment of node vulnerability. Node 8 is taken, for example, from the perspective of topology, node 8 is a weak link, but the calculation results from the actual operating state show that the voltage margin is large, which indicates that the node is very fragile and operates very stably. Therefore, it is more reasonable, accurate, and practical to conduct a comprehensive vulnerability assessment of nodes at different node voltage levels based on the vulnerability analysis methods of both the state and structure. The vulnerability of power system components is not only closely related to their own inherent structural vulnerability but also closely related to the system's real-time operating parameters and network constraints.

According to the analysis of Figure 4, we can also draw a conclusion that the ranking result of the comprehensive vulnerability of each node because the state vulnerability and structural vulnerability of the node are considered, the ranking is compared with the ranking of the state, and the structural vulnerability index has changed. In short, the comprehensive vulnerability considers two aspects comprehensively, and the result can better reflect the comprehensive characteristics of the node. Compared with the unilateral vulnerability, it is more instructive for the operation of the real system.

Power cyber-physical system vulnerability study

Figure 5 is a diagram of a power cyber-physical system of power 14 nodes–information 14 nodes. In this example, the power cyber-physical composite system is divided into three layers, namely the information system, the power system, and the physical-cyber interaction layer.

Based on MATLAB programming, according to the index and calculation method that be proposed, the vulnerability index data of the power cyber-physical system is calculated based on the corresponding power and information network parameters. The results are shown in Table 4.

According to the quantification results of the vulnerability index of the power system and the calculation results of the vulnerability index of the information system, the comprehensive vulnerability index of the power cyber-physical system is obtained, as shown in Figure 6.

According to the analysis in Figure 6, we know that information node 1 has the highest business importance. In fact, as the dispatching center station, information node 1 carries the largest traffic volume and the centralized distribution of traffic, and its administrative level is the highest. Therefore, this node has the greatest impact on the network after being attacked. The key link should be focused on the protection of the node. At the same time, nodes 2, 3, and 5 are also more important in terms of topology structure and traffic

volume. Once destroyed, the consequences will be serious and the comprehensive importance obtained will be relatively high. In fact, it can be seen from the topology diagram that each of these node is a sink node, and the calculation result is consistent with the actual situation, which is also a vulnerable link in the network. According to the graph analysis, it can be seen that the power nodes 12 and 14 are located at the terminal end of the power system, and the information nodes 12 and 14 are also at the terminal edge positions in the communication network. Topological importance and business importance are both relatively low, thus nodes 12 and 14 suffer less damage after being attacked, so the quantified value of the comprehensive vulnerability index is low. All these results show that the method we mentioned is accurate and reasonable and more in line with the actual situation.

Network path prediction study

The calculation example is simulated according to the IEEE14 node system, and the attack-target node is calculated and determined according to the method proposed in the third part. The calculation results are shown in Figure 7, Figure 8.

It can also be seen from the wiring diagram of the IEEE 14 node system that if branch 5–6 is disconnected, the power grid will become the upper and lower parts, which is the branch that has the greatest impact on the system, followed by branch 20, which is in line 4–9. Therefore, it can be determined that the attack target lines 5–6, and the power system nodes 5 and 6 are the key target nodes of the attack. At this time, the attacker obtains the maximum benefit.

According to the vulnerability assessment of the information system, the nodes 12, 13, and 14 of the information system are selected as the attack entry points. Power system nodes 5 and 6 are marked as 19 and 20 in the construction model node, and the path is obtained, there are 3*2 = 6 attack paths, as shown in Figure 9.

It can be seen from the figure that nodes 16, 18, and 20 are in a key position. The attack path passes through these nodes many times, which is also a vulnerable link of the system, and its key protection should be addressed.

Conclusion

In this work, we fully consider the power flow characteristics and complex network theory of the power grid, and propose the index that can indicate the comprehensive vulnerability of the power system. These indexes fully consider the topology and operating status of the power system, not only considering the impact of the power system structure is destroyed, and the impact of the power grid operation status on the power system can be taken into account, the accuracy of the system vulnerability assessment is improved, and the assessment results are more in line with the actual operation of the power system. In the analysis of the information system, starting from the network structure, the node degree and the clustering coefficient are selected to analyze the structural vulnerability, and secondly, considering the service transmission characteristics of the information system, the importance of the power service is selected as the vulnerability assessment index of the information system. The two selected indexes are used to construct a quantitative formula, and finally a comprehensive index is obtained to quantify the node vulnerability of the information system and complete the vulnerability assessment of the nodes of the power cyber-physical system. Finally, the key nodes and weak nodes are selected to predict the network attack path. In this study, the feasibility and accuracy of the method are verified by the IEEE14 node and power cyber-physical system.

Data availability statement

The original contributions presented in the study are included in the article/Supplementary Material. Further inquiries can be directed to the corresponding author.

Author contributions

SW is the experimental designer and executor of this study, completed data analysis, and wrote the first draft of the manuscript; SX and ZX participated in the experimental design and analysis of experimental results; and QZ is the project designer and person in charge, guided the experiment design, analyzed data, wrote the thesis, and revised the manuscript. All authors read and agreed to the final text.

Conflict of interest

Authors JD, JZ and YL were employed by State Grid Jibei Electric Power Limited Company.

The remaining authors declare that the research was conducted in the absence of any commercial or financial relationships that could be construed as a potential conflict of interest.

Publisher's note

References

Chen, X., Sun, K., and Cao, Y. (2007). Structural vulnerability analysis of large power grid based on complex network theory. *Trans. China Electrotech. Soc.* 22 (10), 138. doi:10.3321/j.issn:1000-6753.2007.10.025

Fan, B., and Tang, L. (2014). Vulnerability analysis of power communication networks. *Chin. J. Electr. Eng.* 34 (7), 1191. doi:10.13334/j.0258-8013.pcsee.2014.07.022

Fang, J., Su, C., and Chen, Z. (2017). Power system structural vulnerability assessment based on an improved maximum flow approach. *IEEE Trans. Smart Grid* 2 (2), 777. doi:10.1109/TSG.2016.2565619

Gutiérrez, F., Nuño, J., and Barocio, E. (2015). Using a graph cuts approach to analyze the structural vulnerability of the power grids. *Central Am. Panama Convention*, 1. doi:10.1109/CONCAPAN.2014.7000456

He, J., Song-ling, P., Yu, B., Zhang, W., Hong-peng, L., and Yao-nian, L. (2013). Identification of vulnerable lines in power grid based on capacity betweenness index. *Power Syst. Prot. control* 41 (8), 30. doi:10.3969/j.issn.1674-3415.2011.23.019

Ji, X., Wang, B., and Chaoyang, D. (2016). Power Information-physical interdependence network vulnerability assessment and edge protection strategy. *Power Grid Technol.* 6, 1865. doi:10.13335/j.1000-3673.pst.2016.06.038

Ji, X., Wang, B., Dichen, L., and Zhao, T. (2016). A review of dependence network theory and its application in structural vulnerability analysis of power information-physical systems. *Proc. csee* 36 (17), 4521. doi:10.13334/j.0258-8013.pcsee.160492

Koc, Y., Raman, A., and Warnier, M. (2016). Structural vulnerability analysis of electric power distribution grids. *J. Power & Energy Eng.* 3 (11), 1–13. doi:10.1504/ijcis.2016.081299

Li, J., Dong, J., and Zhang, L. (2020). Comprehensive evaluation of vulnerable nodes based on membership function of grade division. *Electr. Meas. Instrum.*, 1. doi:10.19753/j.issn1001-1390.2002.08.015

Li, P., Liu, Y., Xin, H., and Qi, D. (2018). Vulnerability assessment of distribution network information physical system under distributed cooperative control mode. *Automation Electr. power Syst.* 42 (10), 22. doi:10.7500/AEPS20170705002

Lian, X., Zhang, W., Tong, Q., and Tang, W. (2019). Vulnerability assessment method of power information physical system consideringinformationnodefailure. *Glob. energy Internet* 2 (6), 523

Park, K. J., Liu, R., and Liu, X. (2012). Cyber-physical systems: Milestones and research challenges. *Comput. Commun.* 36 (1), 1–7. doi:10.1016/j.comcom.2012.09.006

Shi, Y., Han, F., Li, S., and Yang, Y. (2010). Research on improved continuous power flow algorithm based on nonlinear prediction. *Electr. Technol.* (2), 27. doi:10.3969/j.issn.1673-3800.2010.02.014

Tang, Y., Han, X., Wu, Y., Ju, Y., Xia, Z., and Ni, M. (2015). Comprehensive vulnerability assessment of power system considering the influence of communication system. *Chin. J. Electr. Eng.* 35 (23), 6066. doi:10.13334/j.0258-8013.pcsee.2015.23.013

Wang, Q., Pipattanasomporn, M., Kuzlu, M., Tang, Y., Li, Y., and Rahman, S. (2016). Framework for vulnerability assessment of communication systems for electric power grids. *IET Gener. Transm. Distrib.* 10 (2), 477–486. doi:10.1049/iet-gtd.2015.0857

Zhan, X., Xiang, T., Chen, H., Zhou, B., and Yang, Z. (2014). Vulnerability assessment and reconfiguration of microgrid through search vector artificial physics optimization algorithm. *Int. J. Electr. Power & Energy Syst.* 62 (2), 679–688. doi:10.1016/j.ijepes.2014.05.024

Zhang, C, Yu, Y., and Li, H. (2016). Comprehensive vulnerability analysis of power system nodes considering energy margin and weight factor. *Electr. Power Autom. Equip.* 36 (3), 136. doi:10.16081/j.issn.1006-6047.2016.03.021

frontiers | Frontiers in Energy Research

TYPE Methods
PUBLISHED 05 January 2023
DOI 10.3389/fenrg.2022.1014027

OPEN ACCESS

EDITED BY
Da Xie,
Shanghai Jiao Tong University, China

REVIEWED BY
Srete Nikolovski,
Josip Juraj Strossmayer University of Osijek, Croatia
Amit Kumar,
Thapar Institute of Engineering & Technology, India

*CORRESPONDENCE
Chen Jie,
xj_cj@163.com

SPECIALTY SECTION
This article was submitted to Smart Grids,
a section of the journal
Frontiers in Energy Research

RECEIVED 08 August 2022
ACCEPTED 30 August 2022
PUBLISHED 05 January 2023

CITATION
Yujing H, Jie C, Xueqin T and Yafei W (2023), Integrated photovoltaic storage joint smoothing strategy based on simultaneous perturbation stochastic approximation algorithm.
Front. Energy Res. 10:1014027.
doi: 10.3389/fenrg.2022.1014027

Integrated photovoltaic storage joint smoothing strategy based on simultaneous perturbation stochastic approximation algorithm

He Yujing[1], Chen Jie[1,2]*, Tian Xueqin[3] and Wang Yafei[1]

[1]School of Electrical Engineering, Xinjiang University, Urumqi, China, [2]School of Electrical Engineering, Shanghai Dian Ji University, Shanghai, China, [3]State Grid Economic and Technological Research Institute Co., Ltd, Beijing, China

In order to realize the real-time control of photovoltaic power generation smoothly connected to the grid under the condition that the energy storage equipment can operate safely, a control strategy combining the simultaneous perturbation stochastic approximation (SPSA) algorithm with rule control is designed. Firstly, the photovoltaic data are processed to extract the data characteristics of the power ramp, and then the grid-connected reference power is obtained through SPSA algorithm. Secondly, considering the state of charge (SOC) of energy storage equipment and the safe operating power range of hydrogen storage equipment, 24 hybrid energy storage power allocation rules are formulated by using the rule control method. Finally, according to the sampling data of every 10 s interval in typical day, the simulation is carried out on MATLAB/simulink platform. The results show that, compared with the first-order low-pass filtering algorithm and recursive fuzzy neural network (RFNN) algorithm, the SPSA algorithm has stronger smoothing ability, and the rule control can also complete the allocation according to the characteristics of the hybrid storage device while ensuring its normal operation.

KEYWORDS

photovoltaic power generation, hybrid energy storage, simultaneous perturbation stochastic approximation, rule control, energy management strategy

1 Introduction

China's government has clearly put forward the target of carbon peak in 2030 and carbon neutrality by 2060, and the proportion of non-fossil energy in primary energy consumption has increased significantly. Solar energy is a kind of renewable energy with abundant resources, wide distribution and no pollution (Nigam and Sharma, 2021). In 2020, the cumulative installed photovoltaic capacity in the world was 767.2 GW, which was significantly higher than that of 39.2 GW in 2010. Therefore, it is imperative to continue to develop ultra-large scale and ultra-high proportion of photovoltaic renewable clean energy.

However, photovoltaic power generation depends on weather parameters, such as solar irradiance, so it has strong intermittence and randomness in nature (Shaner et al., 2018). The conflict between the controllability of the non-sourced side and the high dynamics load is more prominent (Bharti et al., 2022). In order to solve this problem, experts and scholars have proposed a more flexible solution, which combines photovoltaic power generation with energy storage systems to eliminate the fluctuations of active power (Akbari et al., 2019). Energy storage systems is a widely accepted solution because most of them are geographically independent and controllable in different time frames (Castillo and Dennice 2014). The power conditioning system composed of hydrogen storage and super-capacitor is one of the ways (Bharti et al., 2022). This energy storage system belongs to the category of hybrid energy storage, which can reduce environmental costs, improve response time, energy conversion efficiency and durability. Combining a large-scale photovoltaic power generation systems with hybrid energy storage systems can significantly alleviate the uncertain random power generation challenges in power grid operation and planning (Puranen et al., 2021).

The rapid growth of photovoltaic power generation in the past few years has promoted the demand for robust energy management strategies, which take into account the specific technical features and limitations of different storage devices (Wang et al., 2021). Most of the previous off-line power management strategies assumed perfect forecast of renewable energy, demand and markets, which is difficult to achieve in practice (Li 2021). Appropriate on-line energy management strategy can balance the power of a hybrid energy system, improving system reliability and system efficiency, reducing production costs, prolonging the life of system components (Y. Wu et al., 2018). As far as technical, economic and social standards are concerned, the stochastic strategy surpasses the deterministic method, and it has high potential for real-time power management strategies (S. Yin et al., 2021). In (P. Li et al., 2020), the Lyapunov drift-plus-penalty function is applied to formulate a relaxed form of the energy management problem, more effectively taking into account the uncertainty of energy storage and power load. Tabar et al. (2019) presents the application of stochastic linear programming method in the energy management of hybrid micro-gridncertain systems considering multiple markets and rereal-timeemand response. Using this method can effectively reduce the cost, pollution and demand payment of micro-grid.

Common stochastic methods include stochastic game theory algorithm, stochastic linear programming algorithm, Lyapunov optimization algorithm, and SPSA algorithm (Ciupageanu, Barelli et al., 2020). Among them, Liapunov optimization algorithm and SPSA algorithm are gradient-based stochastic algorithm, can adapt to the time-varying environment without mandatory uncertainty modeling in the process of real-time energy management (Neely 2010). In the past, most of the articles used real-time energy management methods based on Liapunov optimization algorithm, while the smoothing strategy of photovoltaic power generation based on SPSA algorithm is not common. What's more, most of the previous articles are aimed at the single-objective or multi-objective optimization of a single online control algorithm. few articles combine the online control based on optimization algorithm with the control strategy based on rules, and apply them to the energy distribution process of hybrid energy storage, which can smooth the fluctuations and considering the characteristics of the equipment. These articles can not consider the operation characteristics of the energy storage equipment more flexibly. For example (Barelli et al., 2020), smoothes the fluctuation of wind power generation based on the stochastic approximation of simultaneous disturbance combined with a flywheel-battery storage system, but its constraint target is not suitable for the safe operation conditions of hydrogen storage. Hydrogen storage devices can realize medium and long-term storage, and the hybrid storage system composed of this devices and super-capacitors has more unique requirements on operational safety than the previous hybrid storage system composed of batteries and super-capacitors.

Therefore, a strategy of photovoltaic output fluctuation smoothing and power distribution based on SPSA algorithm and rule control is proposed. Firstly, the SPSA algorithm is applied to smooth the photovoltaic output at the system level, the result is compared with the smoothing results of the first-order low-pass filtering algorithm and the RFNN algorithm during the result verification, the smoothness drop to 0.3418 in the verification, which effectively suppresses the fluctuations. Secondly, in the energy allocation of the hybrid energy storage system, considering the SOC of the energy storage system and the power constraint of the hydrogen storage equipment, 24 rules are established for the energy allocation of the hybrid energy storage system, so that the hydrogen storage equipment can operate within the safe power constraint on the basis of giving full play to the respective advantages of energy-based and power-based equipment, so as to avoid the explosion accident caused by the excess hydrogen in oxygen.

2 Grid-connected photovoltaic hydrogen hybrid storage coupling system topology diagram

The combination of integrated photovoltaic systems and hybrid energy storage devices can reduce the active power imbalance of power grid regulation, improve the stability of power grid and increase the penetration rate of new energy. In this paper, the photovoltaic power station adopts a common AC bus topology, and the energy storage system consists of alkaline electrolyzed water (AEW), hydrogen storage tank, proton exchange membrane fuel cell (PEMFC), and super capacitor, as shown in Figure 1.

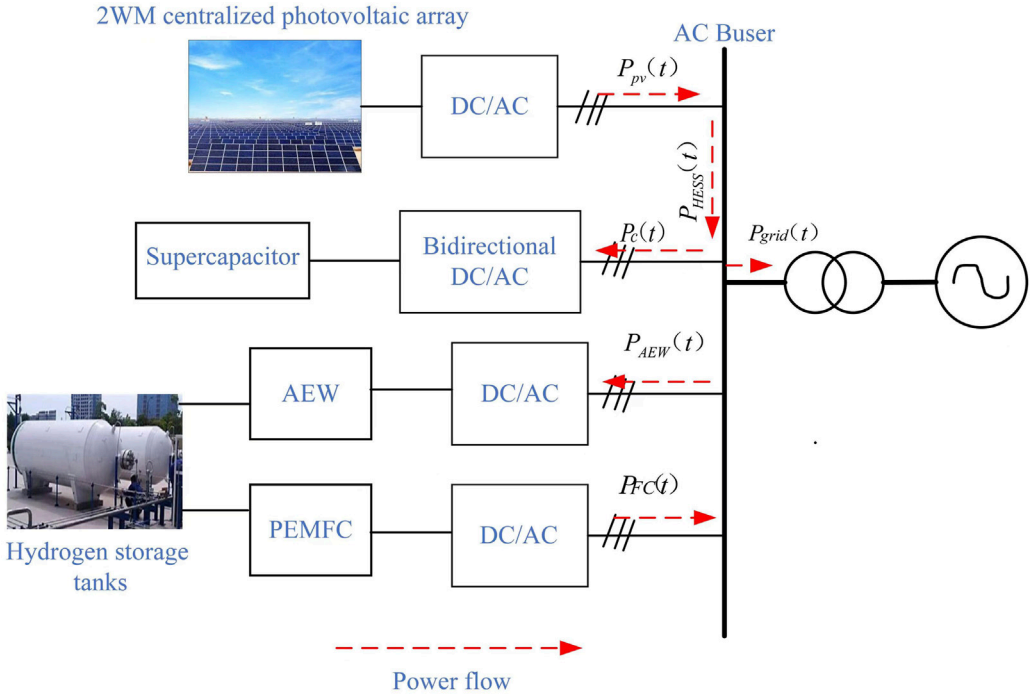

FIGURE 1
Topology of photovoltaic hydrogen hybrid energy storage system.

The energy balance equation is shown below.

$$P_{pv}(t) = P_{grid}(t) + P_{HESS} \quad (1)$$

$$P_{HESS}(t) = P_c(t) + P_H(t) \quad (2)$$

Where: $P_{pv}(t)$ is the active power emitted by the photovoltaic array at the moment t, $P_{grid}(t)$ is the power received by the grid at the moment t, $P_{HESS}(t)$ is the power allocated to the energy storage system at the moment t. $P_c(t)$ and $P_H(t)$ is the power allocated by the energy storage system to the super-capacitor and hydrogen storage system respectively, and the units of the above power are kW.

2.1 Modeling of hybrid energy storage equipment

This paper only considers the charging and discharging behavior and capacity limitation of energy storage devices, so it only discuss the relationship between charging and discharging power and SOC.

2.1.1 Operating characteristics and constraints of super-capacitor

In order to make the capacitor work in a normal state, the output power of the supercapacitor needs to be corrected with the SOC (Zhang et al., 2018). The expression is shown as follows:

$$SOC_c(i+1) = SOC_c(i) + \frac{P_c(i)*\Delta t}{E_{c\max}*\eta_D} \quad (3)$$

$$SOC_c(i+1) = SOC_c(i) + \frac{P_C(i)\eta_{cch}*\Delta t}{E_{c\max}} \quad (4)$$

$SOC(i+1)$ and $SOC(i)$ denotes the SOC at moment t and moment $t+1$ respectively; $E_{c\max}$ denotes the maximum capacity of super-capacitor; η_C is the charging efficiency, which is taken as 0.95, and η_D is the discharging efficiency, which is taken as 0.95. $P_c(t)$ is the power allocated to super-capacitor at moment t, which is taken as positive when charging and negative when discharging. Δt is the sampling time.

2.1.2 Operational characteristics and constraints of hydrogen storage system

In this paper, the pressure of the high-pressure hydrogen storage tank is used to describe the SOC of the hydrogen storage system (Wang and Lin, 2019), The expressions of hydrogen flow rate in electrolyzer and fuel cell are as follows.

$$N_C = \eta_{AEW}\frac{P_{AEW}(t)}{2FU_{AEW}(t)} \quad (5)$$

$$N_D = \frac{1}{\eta_{FC}}\frac{P_{FC}(t)}{2FU_{FC}(t)} \quad (6)$$

N_C is the hydrogen flow rate during charging, and N_D is the hydrogen flow rate during discharging. η_{AEW} is the charging

efficiency and η_{FC} is the discharging efficiency. $P_{AEW}(t)$ is the charging power of electrolytic tank and $P_{FC}(t)$ is the discharging power of fuel cell. F is the Faraday constant. $U_{AEW}(t)$ is the voltage of the electrolyzer and $U_{FC}(t)$ is the voltage of the fuel cell.

The equation for the SOC is shown as follows.

$$\Delta P_C(t) = \frac{N_C(t)^*\Delta t^*RT}{V} \tag{7}$$

$$\Delta P_D(t) = \frac{N_D(t)^*\Delta t^*RT}{V} \tag{8}$$

$$\Delta P_G(t) = P_G(t-1) + \Delta P_C(t) - \Delta P_D(t) \tag{9}$$

$$SOC_H(t) = \frac{P_G(t)}{P_{H\max}} \times 100\% \tag{10}$$

$\Delta P_C(t)$ is the increase in the pressure of the hydrogen storage tank and $\Delta P_D(t)$ is the decrease in the pressure of the hydrogen storage tank. R is the universal time constant, T is the gas temperature, and V is the volume of the hydrogen storage tank. $\Delta P_G(t)$ is the change in the total pressure of the hydrogen storage tank and $P_G(t-1)$ is the total pressure of the tank at the previous moment. $SOC_H(t)$ is the SOC of the hydrogen storage tank. $P_{H\max}$ is the maximum pressure that the hydrogen storage tank can withstand.

3 Photovoltaic power fluctuation smoothing strategy

3.1 Photovoltaic power data processing

In this paper, we take the of historical photovoltaic data of a certain place in China for example to analyze. This data includes two datasets: the first dataset is the sampling data of a centralized 2 MW photovoltaic power generation from January to July 4th at 5 min intervals. The second set of data is the sampling data every 10 s from 4:00 to 19:00 on a certain day in June.

The power slope ΔP is a measure of the photovoltaic power fluctuation, which can be expressed as the difference between the current power and the previous power. In order to use the algorithm for online control, it is necessary to use mathematical statistics and reasoning methods to find the data characteristics of the power ramp, so as to predict the value of the next second during real-time control. We averaged the daily power ramps for in the sample, and obtained the confidence intervals for the average and standard deviation for all sample points by fitting a normal distribution curve, as shown in Figure 2.

According the fitted results, the average value of power ramp is 29.7353 kW (26.6837,32.787) at 95% confidence interval, and the standard deviation is 20.6894 kW (18.7452,23.087) at 95% confidence interval. This data feature will be described in the following SPSA algorithm by the cost function.

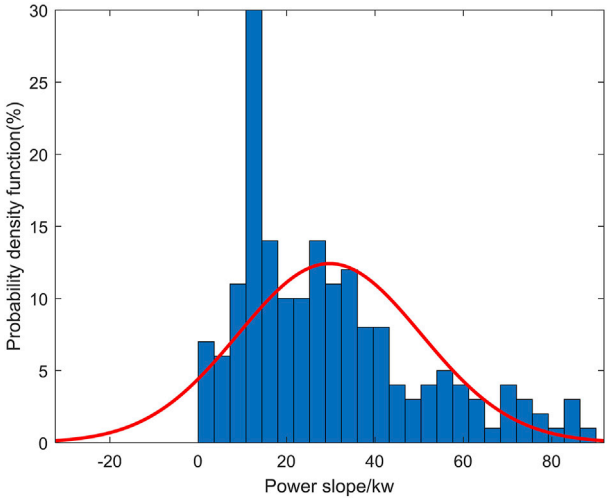

FIGURE 2
Probability density function of the power ramp.

3.2 Fluctuation smoothing strategy

In the process of smoothing the fluctuation of photovoltaic processing, this paper divides the control system into two parts: system level and equipment level, and the upper level is the lower level to output reference signals, as shown in Figure 3.

In this paper, we use the SPSA algorithm at the system level to calculate the power $P_{grid}(t)$ that satisfies the grid connection criteria after smoothing and the power $P_{HESS}(t)$ of the hybrid energy storage. The power of the hybrid energy storage device is allocated at the device level using the rule control algorithm.

3.2.1 Description of the simultaneous perturbation stochastic approximation algorithm

The input and output of the stochastic system are random signals. The stochastic approximation algorithm constructs stochastic recursive formulas based on the input and output data and uses the observed values to estimate the extreme values of the unknown function; this algorithm does not require *a priori* knowledge of the system model, i.e., it does not need to know the specific form of the cost function (Mokkadem and Pelletier, 2007).

The SPSA algorithm was put forward by Spall in 1992. In each gradient approximation, the SPSA algorithm only needs two measurements of the objective function, which is easy to implement and effictive compared to other stochastic approximation algorithms (Spall, 1997). Compared with intelligent optimization-seeking algorithms such as finite difference, simulated annealing, and genetic algorithms, the SPSA algorithm is more robust to stochastic signals in the

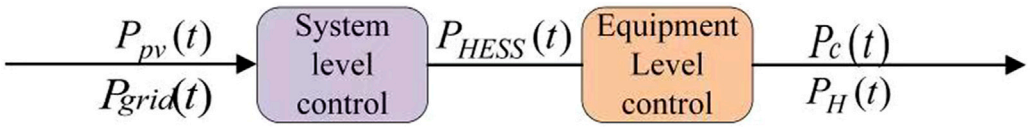

FIGURE 3
Hierarchical control structure diagram.

measurement of the cost function and has a stronger ability to find the global optimal solution.

Introduce a sequence of independent identical distributions with zero mean

$$\Delta_k = \left[\Delta_{k1}, ..., \Delta_{kp}\right]^T \tag{11}$$

Calculate the value of the cost function g (10) at $\theta_k \pm c_k\Delta_k$, as shown in the following equation.

$$y_k^{(+)} = L(\theta_k + c_k\Delta_k) + \xi_k^{(+)} \tag{12}$$

$$y_k^{(-)} = L(\theta_k - c_k\Delta_k) + \xi_k^{(-)} \tag{13}$$

$\xi_k^{(+)}, \xi_k^{(-)}$is the measurement noise term.

The gradient is estimated as

$$\hat{g}_k\ (\hat{\theta}_k) = \begin{bmatrix} \frac{y_k^{(+)} - y_k^{(-)}}{2c_k\Delta_{k1}} \\ \frac{y_k^{(+)} - y_k^{(-)}}{2c_k\Delta_{k2}} \\ \cdots \\ \frac{y_k^{(+)} - y_k^{(-)}}{2c_k\Delta_{kp}} \end{bmatrix} = \frac{y_k^{(+)} - y_k^{(-)}}{2c_k} \begin{bmatrix} \frac{1}{\Delta_{k1}} \\ \frac{1}{\Delta_{k2}} \\ \cdots \\ \frac{1}{\Delta_{kp}} \end{bmatrix} \tag{14}$$

The form of the SPSA algorithm is as follows.

$$\theta_{k+1} = \theta_k - a_k\hat{g}_k\left(\hat{\theta}_k\right) \tag{15}$$

The gain coefficient a_k, c_k, which can be obtained from the following equation.

$$a_k = \frac{a}{(k+A)^a} \tag{16}$$

$$c_k = \frac{c}{k^\gamma} \tag{17}$$

3.2.2 Application of simultaneous perturbation stochastic approximation algorithm at system level

In order to smooth the fluctuation of photovoltaic power, this paper adopts the method of minimizing the power ramp of the next second grid-connected power relative to the photovoltaic power output at the moment. The SPSA algorithm can calculate the optimal power share to the power grid at every sampling moment. The equation of the cost function is shown as follows.

$$y^k(\theta) = \left(\frac{q_{grid} \cdot \Delta P}{P_{grid}^{t-1}}\right)^2 \tag{18}$$

Each variable in the vector of unknown parameter $\boldsymbol{\theta}$ corresponds to the distribution coefficient of the power ramp ΔP allocated to the power grid, and the hybrid storage device, as shown in the following formula.

$$\theta = \left[\ q_{grid}\ \ q_{Hess}\ \right] \tag{19}$$

q_{grid} is the distribution coefficient of the grid, and q_{Hess} is the distribution coefficient of the mixed storage equipment.

Multiply the power ramp by the distribution coefficient obtained by the algorithm seeking to calculate the real-time distribution value. Then, add the power ramp allocated to the power grid with the photovoltaic power at this time to obtain the grid-connected power, as shown in the following formula.

$$P_{grid}^t = q_{grid} \times \Delta P \tag{20}$$

$$P_{HESS}^t = q_{HESS} \times \Delta P \tag{21}$$

$$P_{grid} = P_{grid}^t + P_{pv}^t \tag{22}$$

P_{grid}^t is the power allocated to the grid at time t, P_{HESS}^t is the power allocated to the hybrid storage device at time t, and P_{pv}^t is the power output of the photovoltaic at time t. The parameters ina_k and c_k are set according to the principle of the algorithm and the process of simulation as shown in Table 1.

TABLE 1 Algorithm parameters.

Parameters	
A	10
a	2.1127e-4
c	1e-2
α	0.602
γ	0.101
Number of iterations N	100

TABLE 2 Power allocation strategy when $P_{HESS}(t) > 0$.

Mode	SOC of hydrogen storage			Total power of hybrid energy storage/kW			SOC of super-capacitor			AEW power	Super-capacitor power
	<0.2	[0.2,0.8]	>0.8	$<P_{min}$	$[P_{min},P_{max}]$	$>P_{max}$	<0.05	[0.05,0.95]	>0.95	/kW	/kW
1		√		√				√		0	P_{HESS}
2		√		√					√	P_{min}	
3			√	√				√		0	P_{HESS}
4			√	√					√	0	0
5		√			√			√		P_{HESS}	0
6		√			√				√	P_{HESS}	0
7			√		√			√		0	P_{HESS}
8			√		√				√	0	0
9		√				√		√		P_{max}	$P_{HESS} - P_{max}$
10		√				√			√	P_{max}	0
11			√			√		√		0	P_{HESS}
12			√			√			√	0	0

Starting from the initial value of $\boldsymbol{\theta}$, according to the principles described in Section 2.1.1, the value of distribution coefficient is obtained iteratively.

3.2.3 Application of rule control at the device level

The concentration of hydrogen in oxygen is an important indicator to measure the safety of electrolyzers in industrial production. If it is too high, it may cause explosion. For example, Fang and Liang (2019) put forward that when the rated power of electrolyzers drops to 50%, the hydrogen concentration in oxygen will drop to about 2% within 2 hours after the power drops, reaching the upper limit of safe operation of the hydrogen production system. Secondly, when the operating power is too low, the hydrogen production and power generation efficiency will be extremely low. Therefore, the power limits of hydrogen storage equipment is set within 50% to rated power.In addition, this paper constrains the SOC of the device (within 0.2–0.8 for hydrogen storage devices and 0.05–0.95 for super-capacitors), and when the SOC does not meet the constraint, the charge/discharge power is corrected to ensure that the device is within the safe operating range.

When $SOC_x(k+1) > SOC_{x\max}$, the correction formula is as follows.

$$P_x(k) = E_{x\max} \cdot \frac{SOC_x(k) - SOC_{x\max}}{\eta_x \cdot \Delta t} \tag{23}$$

x can represent hydrogen storage tank or super-capacitor. When SOC is less than the lower limit, the calculation method of the correction power is similar and will not be repeated. According to the above constraints this paper sets up

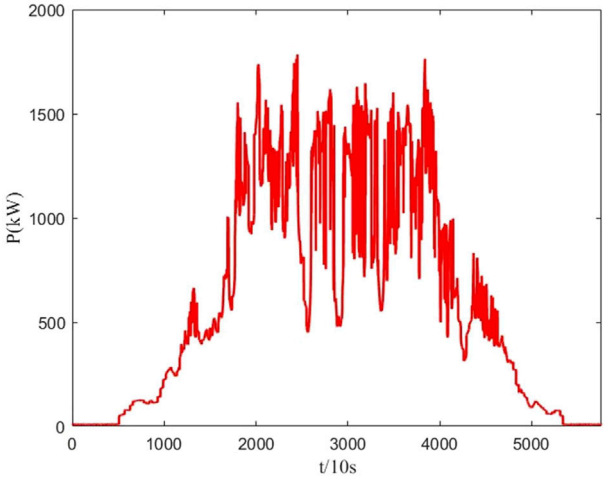

FIGURE 4
Photovoltaic power curve.

24 operation modes for the operation of hybrid energy storage system, when $P_{HESS}(t) > 0$the allocation strategy is shown in Table 2, when $P_{HESS}(t) < 0$ the principle of allocation is the same as when $P_{HESS}(t) > 0$. Several of the typical control rules are highlighted.

Mode 1 and Mode 3: When the SOC of super-capacitor is lower than the upper limit and the total power of mixed storage is less than 200kW, the power of electrolytic cell power is set to 0 and the super-capacitor power is the total power of hybrid storage.

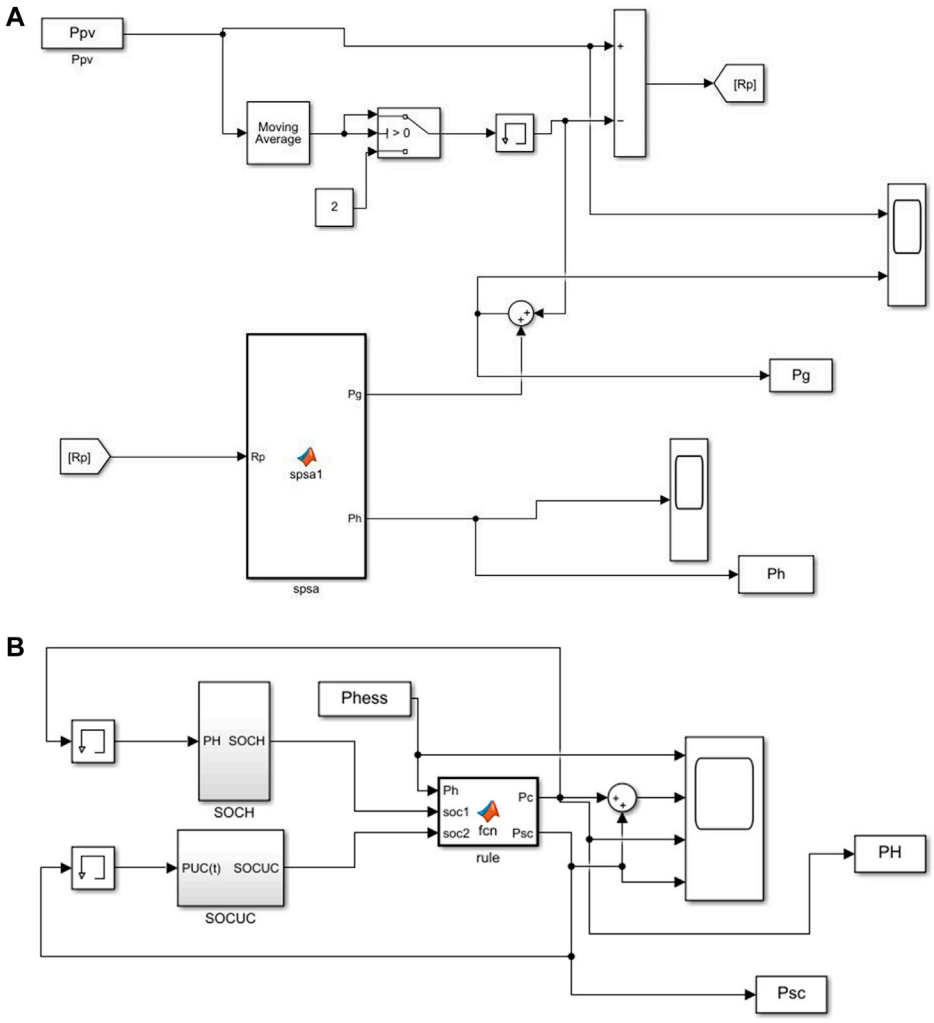

FIGURE 5
Simulation model. **(A)** Simulation model of the smoothing strategy. **(B)** Simulation model of the allocation strategy.

Mode 2: When the SOC of hydrogen storage is lower than the upper limit, the SOC of super-capacitor is higher than the upper limit and the total power of mixed storage is less than 200kW, set the power of electrolytic cell to $P_{\min}$ and the power of super-capacitor to $P_{HESS} - P_{\min}$.

Mode 5 and 6: When the SOC of hydrogen storage is below the upper limit and the total power of mixed storage is between 200 and 400kW, set the power of electrolytic cell to P_{HESS}, and the power of super capacitor to 0.

Mode 9: When the SOC of hydrogen storage and super-capacitor is lower than the upper limit, and the total power of mixed storage is more than 400kw, set the power of electrolytic cell to $P_{\max}$, and the power of super-capacitor to $P_{HESS} - P_{\max}$.

Mode 10: When only the SOC of hydrogen storage is below the upper limit and the total power of mixed storage is more than 400kw, set the power of electrolytic cell to $P_{\max}$, and the power of super-capacitor to 0.

Mode 4, 8, 12: When the SOC of both hydrogen storage and super-capacitor are over-limited, the power of both the device electrolyzer and super-capacitor is 0.

4 Example analysis

4.1 Construction of simulation model

According to the control strategy proposed in Section 2, this paper uses dataset two to build a model on MATLAB/simulink for simulation experiments. The photovoltaic power curve is shown in Figure 4. The charging and discharging efficiency of the super-capacitor is set to

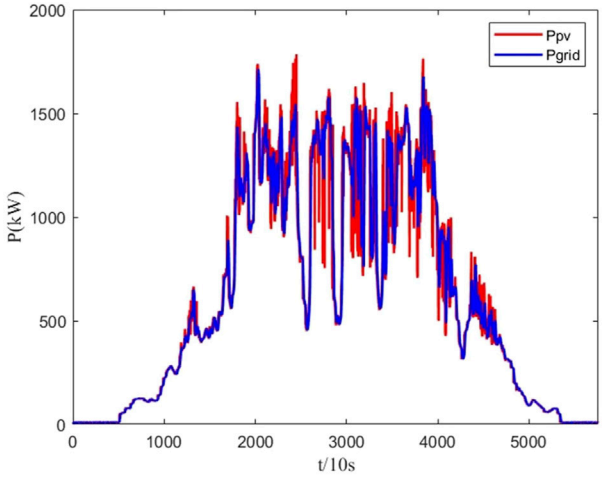

FIGURE 6
Comparison between grid-connected power calculated by SPSA and original output.

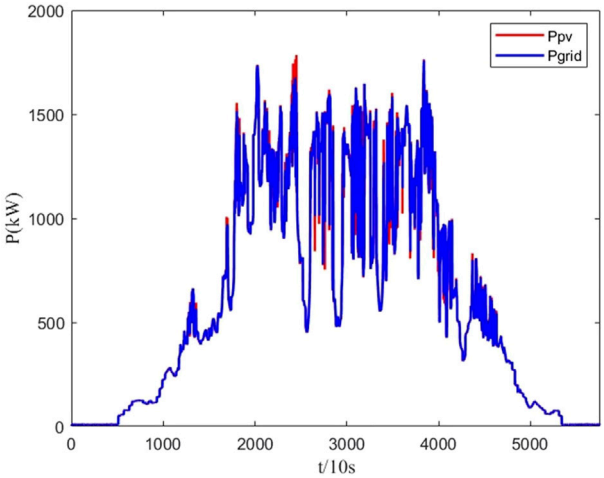

FIGURE 7
Comparison of grid-connected power calculated by low-pass filtering and original output.

95%, the charging and discharging efficiency of the electrolyzer and fuel cell is 80%, the initial SOC of the hybrid storage equipment is all 50%, and the volume of the hydrogen storage tank is 25m^2. In order to simplify the smoothing process, the photovoltaic output curve is first processed by the smoothing filtering method. The simulation model of the smoothing strategy is shown in Figure 5.

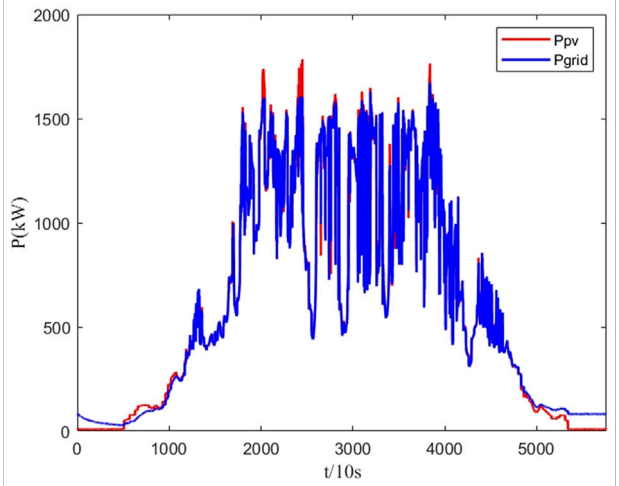

FIGURE 8
Comparison of grid-connected power calculated by RFNN and original output.

4.2 Analysis of smoothing results

4.2.1 Analysis of system-level smoothing fluctuation results using the simultaneous perturbation stochastic approximation algorithm

As shown in Figure 6, the simulation curve obtained by the SPSA algorithm with regular control is compared with the photovoltaic power generation. First-order low-pass filtering is an algorithm that can realize the function of hardware RC low-pass filtering by software programming, and it is widely used in practical projects. The principle is to adjust the ratio of the grid power at the previous time to the current time by adjusting the filter coefficient. RFNN is a recursive multilayer connected neural network that uses dynamic fuzzy rules to achieve fuzzy inference with online training and approximation capabilities (Teng and Lee, 2000). To verify the superiority of the algorithm, the smoothing result obtained by the algorithm, the low-pass filtering algorithm and RFNN algorithm are compared in three dimensions: the smoothness of the grid-connected power, the maximum power of the energy storage system and the maximum capacity of the hybrid energy storage system.

The stability of power network is used to measure the fluctuation range of power network. The lower the smoothness, the smaller the fluctuation of the grid power and the closer to the ideal power. The formula for calculating the smoothness is as follows.

$$D = \max\left\{\frac{P_g(k) - P_g(k-1)}{0.1 * P_{pv\max}}\right\} \tag{24}$$

TABLE 3 Comparison of the smoothing results of the three algorithms.

Algorithm	The smoothness	The maximum power/kW	The maximum capacity ofW the hybrid energy storage system/kW.h
SPSA	0.3418	622.5968	172.4000
First-order low-pass filtering algorithm	2.9918	688.7366	49.7541
RFNN	4.2555	327.5377	103.0683

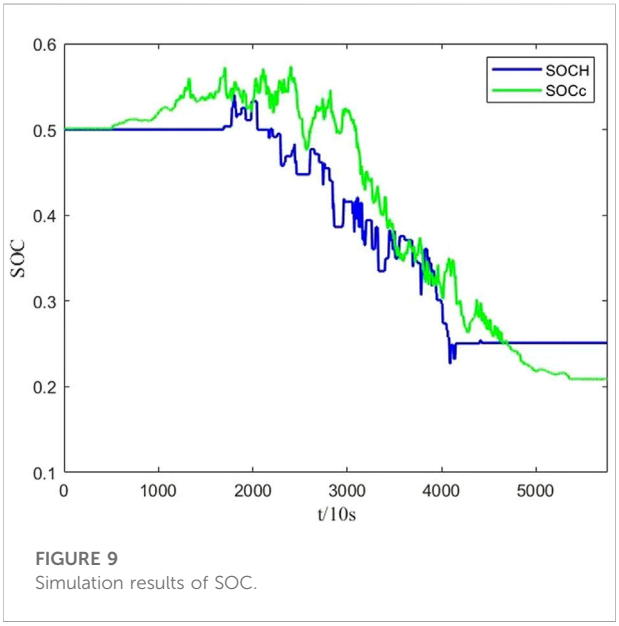

FIGURE 9
Simulation results of SOC.

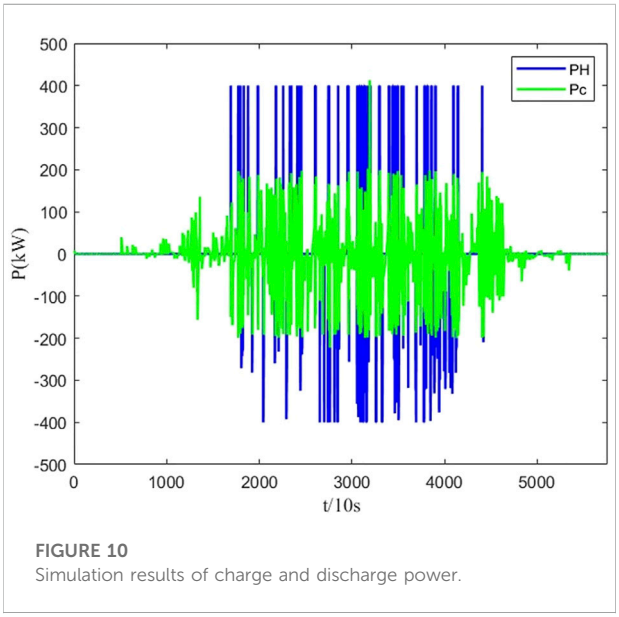

FIGURE 10
Simulation results of charge and discharge power.

where D represents the grid-connected power smoothness and $P_{pv\,\max}$ represents the maximum photovoltaic power.

The greater the maximum charging/discharging power of the energy storage system, the higher the investment cost. The maximum power of the energy storage system is calculated as follows.

$$P_{HESS\,\max} = \max(|P_{HESS}(k)|) \tag{25}$$

$P_{HESS\,\max}$ represents the maximum power of the energy storage system.

The maximum capacity of the hybrid energy storage system is calculated as follows.

$$E_{HESS}(k+1) = E_{HESS}(k) - P_{HESS}(k)\Delta t \tag{26}$$

$$E_{HESS\,\max} = \max(|E_{HESS}|) \tag{27}$$

$E_{HESS}(k)$ represents the total capacity of mixed storage at the kth sampling point, and, $E_{HESS\,\max}(k)$ represents the maximum capacity of the hybrid energy storage device.

The results of the first-order low-pass filtering method to eliminate photovoltaic output fluctuation are shown in Figure 7, in which the filter coefficient is 0.7.

The results of smoothing photovoltaic output fluctuations using the RFNN algorithm are shown in Figure 8.

A comparison of the smoothing results of the three algorithms is shown in Table 3.

It can be seen from the table that the SPSA algorithm can greatly improve the smoothness and reduce the grid-connected power fluctuation. Compared with the first-order low-pass filtering algorithm, its maximum power fluctuation is also relatively small, but its storage capacity requirement for energy storage equipment is higher and the high energy density of hydrogen is more desirable. Second, the first-order low-pass filtering algorithm has a large time-delay characteristic because it does not predict the power at the next moment (Shi et al., 2021). Compared with the RFNN algorithm, which has at least four state parameters, its initial value setting is more complicated and easy to fall into local optimum, but the initial value setting of the SPSA algorithm is limited to the distribution coefficient, which is easy to set.

4.2.2 Analysis of device level power distribution results

Set the upper limit and the lower limit of power of electrolytic cell and fuel cell to 400 and 200 kW, respectively. The maximum pressure of the hydrogen storage tank is 10 kPa and the maximum capacity of the super-capacitor is 166 kWh. The SOC simulation results of two kinds of energy storage devices are shown in Figure 8. SOC_H is the SOC of hydrogen storage, and SOC_c is the SOC of super capacitor. From the figure, it can be seen that the SOC of super-capacitor and hydrogen storage are complementary in some time periods. The simulation results of charging and discharging power are as shown in Figure 9.

It can be seen that the rule control can keep the charging and discharging power of the hydrogen storage device within the range of rated power and safe operation as much as possible, and because the rule is fixed, the hydrogen storage device can avoid frequent start and stop and rapid high-frequency fluctuations mainly caused by super capacitor.

5 Conclusion

1) The SPSA algorithm with real-time control is used to smooth the fluctuation of photovoltaic power output. Compared with the first-order low-pass filtering algorithm and RFNN algorithm, SPSA algorithm has more remarkable ability to smooth photovoltaic power, and has greater robustness.
2) The power of hybrid energy storage is distributed by the method of rule control, so that the fuel cell and electrolytic cell can work between the rated power and the minimum working power as much as possible, and the SOC of the hybrid energy storage equipment is taken into account at the same time, so that the energy storage equipment can work in a safe range.
3) The model is built and simulated using simulation software, which verifies the effectiveness of the proposed strategy and has some practical significance.

Data availability statement

The raw data supporting the conclusions of this article will be made available by the authors, without undue reservation.

Author contributions

All authors listed have made a substantial, direct, and intellectual contribution to the work and approved it for publication.

Funding

The work is supported by the central government guides local special funds for science and technology development under ZYYD2022B11.

Conflict of interest

The authors declare that the research was conducted in the absence of any commercial or financial relationships that could be construed as a potential conflict of interest.

Publisher's note

All claims expressed in this article are solely those of the authors and do not necessarily represent those of their affiliated organizations, or those of the publisher, the editors and the reviewers. Any product that may be evaluated in this article, or claim that may be made by its manufacturer, is not guaranteed or endorsed by the publisher.

References

Akbari, H., Browne, M. C., Ortega, A., Huang, M. J., Hewitt, N. J., Norton, B., et al. (2019). Efficient energy storage technologies for photovoltaic systems. *Sol. Energy* 192, 144–168. doi:10.1016/j.solener.2018.03.052

Barelli, L., Ciupageanu, D-A., Ottaviano, A., Pelosi, D., and Lazaroiu, G. (2020). Stochastic power management strategy for hybrid energy storage systems to enhance large scale wind energy integration. *J. Energy Storage* 31, 101650. doi:10.1016/j.est.2020.101650

Bharti, N., Kumar, S., and Chawla, P. (2022). *Sizing and optimization of hybrid energy storage system with renewable energy generation plant*. Singapore: Springer Nature Singapore.

Castillo, A. G., and Dennice, F. (2014). Grid-scale energy storage applications in renewable energy integration: A survey. *Energy Convers. Manag.* 84, 885–894. doi:10.1016/j.enconman.2014.07.063

Fang, R., and Liang, Y. (2019). Control strategy of electrolyzer in a wind-hydrogen system considering the constraints of switching times. *Int. J. Hydrog. Energy* 44 (46), 25104–25111. doi:10.1016/j.ijhydene.2019.03.033

Li, C. Z. a. X. (2021). "A novel real-time energy management strategy for gird-friendly microgrid: Harnessing internal fluctuation internally," in *2020 52nd north American power symposium (NAPS)* ***tempe***, 1–6.

Li, P., Duan, Q., Li, Z., Zhu, C., and Zhang, X. (2020). A Lyapunov optimization-based energy management strategy for energy hub with energy router. *IEEE Trans. Smart Grid* 11, 4860–4870. doi:10.1109/tsg.2020.2968747

Mokkadem, A., and Pelletier, M. (2007). A companion for the Kiefer–Wolfowitz–Blum stochastic approximation algorithm. *Ann. Statist.* 35 (4), 1749–1772. doi:10.1214/009053606000001451

Neely, M. J., Saber Tehrani, A., and Dimakis, A. G. (2010). "Tehrani, Arash Saber; Dimakis, Alexandros GEfficient algorithms for renewable energy allocation to delay tolerant consumers," in *2010 first IEEE international conference on Smart grid communications* (Los Angeles, CA, United: University of Southern California), 549–554. doi:10.1109/SMARTGRID.2010.5621993

Nigam, A., and Sharma, K. K. (2021). "Modeling Approach for different solar PV system: A review," *Advances in systems, control and automations*. Editors

A. K. Bhoi, P. K. Mallick, V. E. Balas, and B. S. P. Mishra (Singapore: Springer), Vol. 435. doi:10.1007/978-981-15-8685-9_70

Puranen, P. K., Antti, K., and Ahola, J. (2021). Technical feasibility evaluation of a solar PV based off-grid domestic energy system with battery and hydrogen energy storage in northern climates. *Sol. Energy* 213, 246–259. doi:10.1016/j.solener.2020.10.089

Shaner, M. R., Davis, S. J., Lewis, N. S., and Caldeira, K. (2018). Geophysical constraints on the reliability of solar and wind power in the United States. *Energy Environ. Sci.* 11, 914–925. doi:10.1039/C7EE03029K

Shi, X., Zhao, Y., Zhang, H., Wang, X., and Zhou, B. (2021). Control method of wind power fluctuation smoothing for battery energy storage system based on quasi-zero phase filter. *Automation Electr. Power Syst.* 45 (4), 45–53.

Spall, J. C. (1997). A one-measurement form of simultaneous perturbation stochastic approximation. *Automatica* 33 (1), 109–112. doi:10.1016/S0005-1098(96)00149-5

Tabar, V. S., Saeid, G., and Tohidi, S. (2019). Energy management in hybrid microgrid with considering multiple power market and real time demand response. *Energy* 174, 10–23. doi:10.1016/j.energy.2019.01.136

Teng, C-C., and Lee, C-H. (2000). Identification and control of dynamic systems using recurrent fuzzy neural networks. *IEEE Trans. Fuzzy Syst.* 8, 349–366. doi:10.1109/91.868943

Wang, M., Xiaobin, D., and Zhai, Y. (2021). Optimal configuration of the integrated charging station for PV and hydrogen storage. *Energies* 14 (21), 7087. doi:10.3390/en14217087

Wang, S., and Lin, H. (2019). Control strategy of hybrid energy storage to stabilize wind power fluctuation based on variable coefficient exponential smoothing method. *Acta Energ. Sol. Sin.* 40 (11), 3204–3212. doi:10.1016/j.rser.2017.05.283

Wu, Y., Chrenko, D., and Miraoui, A. (2018). "A real time energy management for EV charging station integrated with local generations and energy storage system," in *2018 IEEE transportation electrification conference and expo (ITEC)*, 1–6.

Yin, S., Li, J., Li, Z., and Fan, S. (2021). Energy pricing and sharing strategy based on hybrid stochastic robust game approach for a virtual energy station with energy cells. *IEEE Trans. Sustain. Energy* 12, 772–784. doi:10.1109/tste.2020.3019494

Zhang, L., Hu, X. S., Wang, Z. P., Sun, F. C., and Dorrell, D. G. (2018). A review of super-capacitor modeling, estimation, and applications: A control/management perspective. *Renew. Sustain. Energy Rev.* 81, 1868–1878. doi:10.1016/j.rser.2017.05.283

Nomenclature

Variables

P Power

N Flow rate

U Voltage

E Capacity

F Faraday constant

η *E*fficiency

D Grid-connected power smoothness

q Weighting of power ramp allocation

θ The distribution factor of the power ramp ΔP

Subscripts

pv Photovoltaic

grid Grid-connected

HESS Hybrid energy storage system

c Super-capacitor

H Hydrogen storage system

C Charge

D Discharge

AEW Alkaline electrolyzed water

FC Fuel cell

Abbreviations

RFNN recursive fuzzy neural network

SPSA simultaneous perturbation stochastic approximation

SOC State of charge

frontiers | Frontiers in Energy Research

TYPE Original Research
PUBLISHED 06 January 2023
DOI 10.3389/fenrg.2022.998492

OPEN ACCESS

EDITED BY
Ignacio Hernando Gil,
Université de Bordeaux, France

REVIEWED BY
Chenghong Gu,
University of Bath, United Kingdom
Da Xie,
Shanghai Jiao Tong University, China
Daogang Peng,
Shanghai University of Electric Power, China
Xiangyu Kong,
Tianjin University, China

*CORRESPONDENCE
Haiyun Wang,
mailto:327028229@qq.com

SPECIALTY SECTION
This article was submitted to Smart Grids, a section of the journal Frontiers in Energy Research

RECEIVED 20 July 2022
ACCEPTED 12 December 2022
PUBLISHED 06 January 2023

CITATION
Zhu S, Wang H, Wang W and Chang X (2023), A combined day-ahead and intraday optimal scheduling strategy considering a joint frequency regulation reserve scheme among wind, photovoltaic, and thermal power. *Front. Energy Res.* 10:998492. doi: 10.3389/fenrg.2022.998492

A combined day-ahead and intraday optimal scheduling strategy considering a joint frequency regulation reserve scheme among wind, photovoltaic, and thermal power

Shulin Zhu[1], Haiyun Wang[1]*, Weiqing Wang[1] and Xiqiang Chang[2]

[1]Engineering Research Center of Education Ministry for Renewable Generation and Grid Control, Xinjiang University, Urumqi, China, [2]State Grid Xinjiang Electric Power Co., Ltd., Urumqi, China

Under the premise of establishing a certain reserve power for frequency regulation, a new energy power plant (NEPP) transformed by frequency regulation control can participate in system frequency regulation. Considering the problem of cooperation between multiple NEPPs for reserve power for frequency regulation, this article presents a joint frequency regulation reserve scheme spanning wind, photovoltaic, and thermal power. A group of NEPPs composed of all NEPPs in the system works in the state of dynamic stepped output derating and participates in system frequency regulation together with thermal power units. Based on the joint frequency regulation reserve scheme and considering that the accuracy of new energy forecast directly affects the frequency regulation effect of NEPPs, we propose a combined day-ahead and intraday scheduling strategy considering the joint frequency regulation reserve scheme and derive the relevant scheduling model. The improved IEEE RTS 24-bus system is used as the test system for calculation. The results of the calculations show that the proposed strategy can optimize the participation scheme of frequency regulation of new energy, reduce the power and economic losses of new energy caused by participation in frequency regulation, and improve the ability of the power system to accommodate the output power of new energy under the premise of ensuring that the steady-state frequency deviation does not exceed the allowable frequency limits.

KEYWORDS

new energy power plants, joint frequency regulation reserve scheme, group of new energy power plants, state of dynamic stepped output derating, combined day-ahead and intraday scheduling strategy, ability of power systems to accommodate the output power of new energy, steady-state frequency deviation

1 Introduction

Improving the accommodation ability of new energy power generation is an efficient method for the traditional power system to realize the transition to low carbon. However, new energy power generation, represented by wind turbines and photovoltaics (PVs), has a fluctuating and uncertain power output that brings more power disturbance to the power

Abbreviations: AGC, automatic generation control; NEPP, new energy power plant; PV, photovoltaics; PSFR, participation state of frequency regulation; PPP, PV power plant; WPP, wind power plant.

system. This increasing power disturbance increases the demand for frequency regulation of reserve power. In the traditional power system, the frequency response capability of thermal power units is limited by their installed capacity and regulation speeds. Moreover, the new energy power generation connected to the power grid by power electronic converters operates in a state of maximum power point tracking without frequency regulation of reserve power, so that new energy power generation cannot participate in frequency regulation. With the increased scale of new energy connecting to the grid, the demand for frequency regulation reserve power may not be satisfied by the frequency response capability of the system. Thus, the power system needs more frequency response capability to meet the increasing demand for reserve power frequency regulation, and the system may not have enough ability to accommodate all the output power of new energy, which complicates the scheduling and operation of the power system with large-scale grid-connected new energy.

Owing to the development of new energy power generation control strategies, many theoretical studies about the new energy participating in frequency regulation have been conducted, showing that new energy power generation can theoretically participate in frequency. Sun and Jia (2018) used single-stage PV generation as the research target and proposed a novel system frequency support strategy based on the active power reserve. Rajan and Fernandez (2019) proposed a PV power control strategy for frequency regulation without any energy storage system. Zhang et al. (2019) analyzed how PV generation can affect the frequency stability of the power grid and introduced the current technical route of PV frequency regulation. An et al. (2020) proposed an enhanced frequency regulation strategy for wind turbines based on the conventional over-speed de-loading control. Li et al. (2021) compared different control strategies for wind turbines, such as virtual inertia control, droop control, virtual synchronizer technology, rotation speed control, pitch angle control, and additional energy storage systems; moreover, they clarified the principles, advantages, disadvantages, and application scope of each control strategy. Fan and Tang (2022) proposed a two-layer control strategy for wind farms participating in grid frequency regulation for problems caused by the direct switching of frequency power distribution and wind turbine control strategy.

Trials of new energy participation in frequency regulation have been carried out in many places in China, verifying that such regulation is feasible in the actual power system. The northwestern Chinese power grid has organized new energy sources to participate in rapid-frequency regulation research and has carried out pilot tests at the sending end of the large power grid (Chu et al., 2019; Ma et al., 2019). The southern Chinese power grid has stipulated that grid-connected new energy stations should have frequency regulation capability; therefore, the modification and detection of the frequency regulation capacity of the new energy station have been carried out simultaneously and step-by-step (Mu et al., 2021). The northeastern Chinese power grid has launched a pilot project enabling renewable power plants to actively support the power system, including by improving the primary frequency regulation capability (Liu et al., 2020).

Based on the studies mentioned previously, some researchers have presented scheduling strategies for considering new energy participation in frequency regulation. Ye et al. (2016) considered that PV power plants (PPPs) work in an output power derating state to participate in frequency regulation, and they proposed a unit commitment model according to the frequency response capability of PPPs and the dynamic frequency limit. Hao et al. (2020) considered wind turbines to participate in primary frequency regulation in deloaded operating mode, together with conventional units, and proposed an intra-day dispatch model considering the coordination optimization of the steady and transient states. Li et al. (2020) tried to incorporate the capability of wind plants in frequency regulation into daily scheduling and then proposed a frequency-constrained unit commitment model with wind plants, combining different response strategies of wind plants and incorporating them into the unit commitment model. Lu et al. (2021) proposed a frequency safety constraint construction method considering the frequency nadir and deduced a unit commitment model considering the frequency dynamic safety constraint with wind power and PV-integrated inertial control. Ge et al. (2021) deduced a distributed robust unit commitment model that considers the synchronous inertia of the synchronous generator unit and the virtual inertia and droop control of the wind power unit in the system. Ouyang et al. (2021) proposed power system frequency regulation based on dynamic variable-speed wind turbine power reserve and deduced a new grid scheduling mode based on dynamic wind power reserve. Zhang et al. (2022) proposed a frequency security-constrained scheduling approach considering wind farms and providing frequency support and reserve. A comparative table of the references mentioned in this paragraph is shown in Table 1.

The aforementioned studies can improve the frequency response capability of the power system, reduce to a certain extent the power loss of new energy caused by an insufficient frequency response capability of the system, and improve the new energy accommodation ability of the system. However, some points in the aforementioned studies still need further research. As the scale of grid-connected new energy power generation gradually increases, the number of NEPPs and new energy power units in the system will gradually rise. Moreover, new energy is gradually being regarded as a frequency regulation resource, and because there are often many types of frequency regulation resources in the system, it is necessary to consider the cooperation between these different types in the system; however, few studies have paid attention to this important subject.

To solve the problem mentioned in the previous paragraph, we propose an optimal combined day-ahead and intraday scheduling strategy that considers a joint frequency regulation reserve scheme among wind, photovoltaic, and thermal power:

1) A joint frequency regulation scheme among wind, photovoltaic, and thermal power is designed. In this scheme, the group of NEPPs works in the state of dynamic-stepped output derating.
2) An optimal combined day-ahead and intraday scheduling strategy considering the joint frequency regulation reserve scheme is proposed, and the corresponding scheduling model is derived.

According to the calculation results of the test system, the strategy proposed in this paper can reduce the reserve power provided by the new energy working in the state of output derating, reduce the new energy power loss and economic loss caused by participating in system frequency regulation, and improve the new energy accommodation capability of the system under the premise of ensuring that the steady-state frequency deviation of the system does not exceed the limit, which can provide a certain reference for the operation of the actual power system.

The rest of this paper is organized as follows. The second section describes the method by which NEPPs participate in frequency regulation. The third section introduces the joint frequency regulation scheme and deduces its objective function and

TABLE 1 Comparison of existing power system dispatching strategies, considering new energy participating frequency regulation.

Author	The method of new energy participating in frequency regulation	The number of NEPP in the test system	The time scale of the scheduling strategy	Is the cooperation of frequency regulation reserve between new energy considered?	Is the cooperation of frequency regulation reserve between new energy and thermal units considered?
Ye et al.	New energy power plants	2	Day-ahead	No	No
Hao et al.	New energy power plants	3	Day-ahead and intraday	No	No
Li et al.	New energy power plants	9	Day-ahead	No	No
Lu et al.	New energy power devices	2	Day-ahead	No	No
Ge et al.	New energy power devices	1	Day-ahead	No	No
Ouyang et al.	New energy power plant	4	Day-ahead and intraday	No	No
Zhang et al.	New energy power devices	55	Day-ahead	No	No

constraints. The fourth section gives calculation and analysis results to discuss and prove the role of the proposed scheduling strategy. The last section concludes this paper.

2 New energy participation in frequency regulation

At present, the method by which new energy generation participates in frequency regulation can be divided in two ways: the new energy power device participate in frequency regulation or the NEPP participate in frequency regulation.

Grid-connected new energy power devices in China generally do not have frequency response capabilities. To realize their participation in frequency regulation, every new energy power device that does not have frequency response capability must be transformed. In contrast, wind power plants (WPPs) and PPPs have been equipped with basic automatic generation control (AGC) systems. Under the premise of setting up reserve power, the NEPP can participate in secondary frequency regulation. Hence, the NEPP can participate in primary frequency regulation by adding a special new energy fast power control device based on AGC. In this case, the workload and economic cost are less than the transformation of each new energy device. Therefore, this is a feasible way for new energy to participate in frequency regulation.

2.1 Frequency regulation characteristics of thermal units

The thermal power unit has a droop characteristic between the active power and the frequency. When the system frequency is between the frequency regulation dead band and the maximum allowed steady-state frequency limits, the droop characteristic can be determined by Eq. 1:

$$\boldsymbol{p_g} = \boldsymbol{p_{g,0}} - \boldsymbol{p_{g,n}}\frac{\boldsymbol{f} - \boldsymbol{f_{g,db}}}{\boldsymbol{f_n}}, \tag{1}$$

where $p_{g,0}$ is the initial power of the thermal power unit; p_g is the output power of thermal power unit after primary frequency regulation; $p_{g,n}$ is the installed capacity of the thermal power unit; f is the frequency measured in the connecting point to the grid; f_n is the rated frequency of the system, with value of f_n being 50 Hz in China; and $f_{ne,db}$ is the frequency dead band of the thermal power units, which is set at 0.033 Hz.

The power–frequency droop characteristic curve of the thermal power units is shown in Figure 1, where Δp is the responded power limit for primary frequency regulation of the thermal power unit and Δf_{max} is the maximum allowed frequency deviation when the system is in steady state, with the value of Δf_{max} set at 0.2 Hz.

In this paper, the responded power limit for primary frequency regulation of the thermal power unit Δp is jointly determined by maximum allowed frequency deviation, the installed capacity, the difference coefficient, and the dead band of frequency regulation of the thermal power unit, as shown in Eq. 2:

$$\Delta \boldsymbol{p_{g,fr}} = \frac{\boldsymbol{p_{g,n,i}}}{\boldsymbol{f_n}\boldsymbol{\delta_{g,i}}\%}\left(\Delta \boldsymbol{f}_{\boldsymbol{max}} - \Delta \boldsymbol{f_{db,g,i}}\right), \tag{2}$$

where $\Delta p_{g,fr}$ is the maximum responded power for primary frequency regulation of the thermal power unit; and $p_{g,n,i}$, $\delta_{g,i}$%, and $\Delta f_{db,g,i}$ are the installed capacity, the difference coefficient, and the dead band of frequency regulation of the thermal power unit, respectively.

2.2 Characteristics of new energy power plant participation in frequency regulation

The transformed NEPP can participate in primary and secondary frequency regulation. The control structure of NEPP is shown in Figure 2.

During operation, the NEPP participating in frequency regulation operates in a state of output power derating. The whole plant is taken as the control object, which can calculate the power caused by the frequency change measured in the grid connection point and accept the power adjustment instruction sent by the system scheduling center. Based on the operation of each unit in the power plant, the power that must be adjusted is distributed to each unit through the link of active power distribution in the power plant (Mu et al., 2021).

The transformed NEPP, as shown in Figure 2, has a droop characteristic between the active power and the frequency, which is

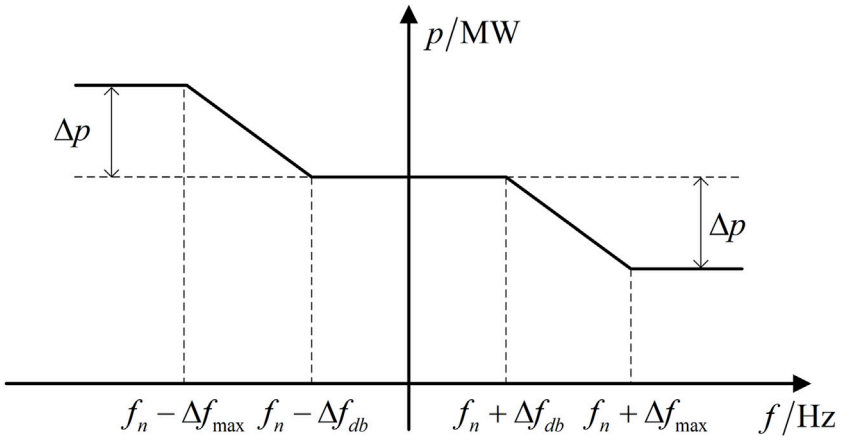

FIGURE 1
Power frequency droop characteristic curve.

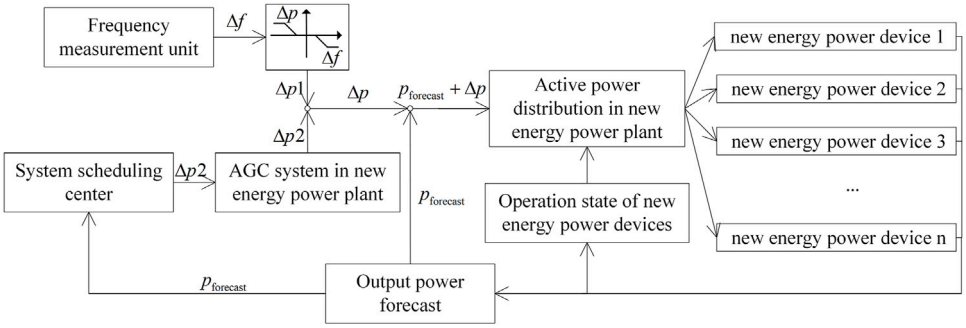

FIGURE 2
Frequency regulation control structure diagram for NEPPs.

similar to the thermal power unit. The power–frequency droop characteristic of the NEPP can also be expressed by Eq. 1. The power–frequency droop characteristic curve of the NEPP is shown in Figure 1.

As can be seen in Figure 1, the NEPP participating in frequency regulation needs to be set for upward and downward reserve power for frequency regulation. The values of upward and reserve power are both more than Δp. Therefore, $2\Delta p$ is defined as the threshold of frequency regulation of NEPP in this article. If the output power of the NEPP is more than $2\Delta p$, the NEPP is considered as being able to participate in frequency regulation, which is termed its "frequency regulation ability" in this paper.

2.3 Output model of new energy power plants

NEPPs participating in frequency regulation should set reserve power by operating in a state of output power derating, which includes reserve power for both primary and secondary frequency regulation.

To reduce the economic loss of the NEPPs caused by too much reserve power, the reserve power for the secondary frequency regulation is not set independently. Thus, the remaining reserve power after primary frequency regulation is regarded as the reserve power for secondary frequency regulation.

If the NEPP needs to participate in frequency regulation, then the reserve power for its frequency regulation must be set. Similar to the thermal power unit, the reserve power for NEPP frequency regulation $\Delta \boldsymbol{p}_{ne,fr}$ is jointly determined by the NEPP's installed capacity, the difference coefficient, and the dead band of frequency regulation. The relationship between the aforementioned quantities can also be expressed as Eq. 2.

As only NEPPs with frequency regulation ability can participate in frequency regulation, a state variable $K_{nes,fr,i,t}$ is introduced to represent the frequency response capability of the ith NEPP during time t. The value 1 means that the plant is able to participate in frequency regulation, and the value 0 means that the plant is incapable of participating in frequency regulation. The actual value of $K_{nes,fr,i,t}$ is derived from the $p_{ne,forecast,i,t}$ described in Section 2.2.

Based on the aforementioned analysis, the output model of the NEPP participating in frequency regulation can be shown in Eqs 3–6:

$$\boldsymbol{p}_{ne,i,t} + \boldsymbol{r}_{ne,up,i,t} \leq \boldsymbol{p}_{ne,forecast,i,t}, \tag{3}$$

$$p_{ne,i,t} - r_{ne,dn,i,t} \geq 0, \tag{4}$$

$$r_{ne,up,i,t} = K_{nes,fa,i,t}\Delta p_{ne,fr,i}, \tag{5}$$

$$r_{ne,dn,i,t} = K_{nes,fa,i,t}\Delta p_{ne,fr,i}, \tag{6}$$

where $p_{ne,i,t}$ and $p_{ne,forecast,i,t}$ are the planned output power and the forecast output power of the i^{th} NEPP during time t; and $r_{ne,up,i,t}$ and $r_{ne,dn,i,t}$ are the upward and downward reserve power of the i^{th} NEPP during time t.

In this mode of operation, $K_{nes,fa,i,t}$ determines whether the NEPP needs to set reserve power for frequency regulation.

3 Optimal scheduling strategy and model

This section formulates in turn the joint frequency regulation reserve scheme, the scheduling strategy, and the scheduling model.

3.1 Joint frequency regulation reserve scheme

Too little frequency regulation reserve power provided by new energy may cause an insufficient frequency response capability in the system, which will probably have difficulty satisfying the frequency regulation demand. In contrast, too much frequency regulation reserve power provided by the new energy may cause the NEPP to have large power and economic losses. Hence, it is particularly important for NEPPs to reasonably determine the time to participate in frequency regulation and the value of reserve power for frequency regulation. It is necessary to design a joint scheme to consider the cooperation of frequency regulation reserve power among wind, photovoltaic, and thermal power.

3.1.1 Cooperation between new energy and thermal power

Generally, with the increasing scale of new energy, more and more NEPPs are being connected to the system, which may make cooperation between new energy and thermal power more difficult in terms of frequency regulation. All NEPPs in the system can be regarded as a group, which can reduce the difficulty of frequency regulation cooperation. For the group of NEPPs, the output is equal to the sum of the output of all NEPPs, and the reserve power is equal to the sum of the reserve power of all NEPPs. The actual output power derating state of each NEPP depends on the output power derating state of the NEPP group.

The group of NEPPs should undertake only the auxiliary task of frequency regulation. This means that when the frequency response capability of thermal power units cannot satisfy the demand of reserve power for frequency regulation, the group of NEPPs should participate in frequency regulation. In addition, when the frequency response capability of thermal power units can satisfy the demand of reserve power for frequency regulation, the plant group should not participate in frequency regulation. Therefore, the group of NEPPs and the NEPP work in a state of dynamic output power derating, and the participation state of frequency regulation (PSFR) of NEPPs is determined by the operating state of the thermal power units and the demand of reserve power for frequency regulation.

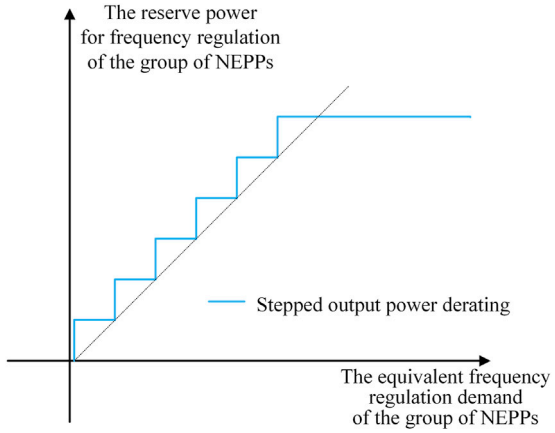

FIGURE 3
The method of stepped reserve power for frequency regulation.

Based on the aforementioned analysis, the state variable $U_{neg,fr}$ is introduced. A value of 1 means that the group of NEPPs participates in frequency regulation and that some NEPPs in the group need to participate in frequency regulation, and a value of 0 means that the group of NEPPs does not participate in frequency regulation or that any NEPP in the group need not participate in frequency regulation.

$U_{neg,fr}$ should satisfy the constraint shown in Eq. 7:

$$U_{neg,fr,t} \leq U_{g,i,t}, \quad \forall i, i = 1, 2, \ldots, N_g, \tag{7}$$

where $U_{g,i}$ is a state variable that represents the state of the i^{th} thermal power unit during time t, where 1 means that the thermal power unit operates in the startup state and 0 means that the thermal power unit operates in the shutdown state, and N_g is the number of thermal power units.

3.1.2 Cooperation between all new energy power plants

When the group of NEPPs needs to participate in frequency regulation, unnecessary reserve power may be caused if all NEPPs in the group work in the output power derating state according to a unified state. Therefore, a method called "stepped reserve power for frequency regulation" for the group of NEPPs is proposed. Only some NEPPs in the group are selected to participate in frequency regulation, according to the demand of reserve power for frequency regulation when the group of NEPPs needs to participate in frequency regulation.

The method of stepped reserve power for frequency regulation is shown in Figure 3. The frequency regulation reserve power of the NEPP group increases with an increased equivalent frequency regulation demand undertaken by the NEPP group. The number of new energy stations that need to participate in frequency regulation is determined by the equivalent frequency regulation demand undertaken by the NEPP group.

Based on the aforementioned analysis, the PSFR may be different between different NEPPs, and the cooperation of frequency regulation between each NEPP in the group should also be considered. Therefore, the state variable $U_{nes,fa,i,t}$ is introduced, representing the participating state of the i^{th} single NEPP in the group during time t. A value of 1 means

that the NEPP participates in frequency regulation, and a value of 0 means that the NEPP does not.

In this paper, only two types of NEPPs are considered: PPPs and WPPs.

Considering the differences in operational characteristics between different types of NEPPs, participation in frequency regulation will cause wear and tear to wind power units. Therefore, the PPP is of higher priority than WPP in frequency regulation (Liu et al., 2020).

For a system containing N_w WPPs and N_p PPPs, the $U_{nes,fr,i,t}$ of the i^{th} WPP in any scheduling period should satisfy the constraint shown in Eq. 8:

$$\begin{aligned} &\boldsymbol{U_{wpp,fr,i,t} \le U_{ppp,fr,j,t},} \\ &\boldsymbol{\forall i, i = 1, 2, \ldots, N_w,} \\ &\boldsymbol{\forall j, j = 1, 2, \ldots, N_p.} \end{aligned} \tag{8}$$

Among the same types of NEPPs, a NEPP with better output power state has a larger margin of output power adjustment. Thus, it takes the initiative to derate its output power as reserve power for frequency regulation, which has little impact on its economic benefits. Therefore, a NEPP with a better output power is of higher priority than a NEPP with a worse output power in frequency regulation.

The output power rate $r_{ne,output,i,t}$ is introduced to characterize the output power state of the i^{th} NEPP during the time t:

$$\boldsymbol{r_{ne,output,i,t} = \frac{p_{ne,output,i,t}}{p_{ne,n,i}}.} \tag{9}$$

A NEPP with a larger value of $r_{ne,output}$ has a better output power state. The output power states of the same type of NEPPs can be ranked from good to bad, as shown in Eq. 10:

$$\boldsymbol{r_{ne,output,i1,t}, r_{ne,output,i2,t}, \ldots, r_{ne,output,iN_{same},t},} \tag{10}$$

where N_{same} is the number of the same type of NEPP, $i1$ is the number of the NEPP with the highest output rate, $i2$ is the number of the NEPP with the second highest output rate, and $\boldsymbol{iN_{same}}$ is the number of the NEPP with the lowest output rate.

The variable $o_{ne,same,i,t}$ represents the frequency regulation sequence of the same type of NEPP. The relation between $r_{ne,output,i,t}$ and $o_{ne,same,i,t}$ can be described by Eq. 11:

$$\boldsymbol{o_{ne,same,j,t} = ij,} \tag{11}$$

where ij is the number of the NEPP with the jth highest output rate.

NEPPs of the same type should participate in frequency regulation based on $o_{ne,same,i,t}$. Therefore, the $U_{nes,fr,i,t}$ of the same type of NEPP should satisfy the constraint shown in Eq. 12:

$$\boldsymbol{U_{nes,fr,t}\left(o_{ne,same,i,t}\right) \ge U_{nes,fr,t}\left(o_{ne,same,i+1,t}\right).} \tag{12}$$

Considering the joint frequency regulation reserve scheme, the group of NEPPs should work in a state of stepped output power derating, and the NEPP should work in a state of dynamic output power derating. Whether the NEPP must set the reserve power for frequency regulation is jointly determined by $U_{neg,fr,t}$, $U_{nes,fr,i,t}$, and $K_{nes,fr,i,t}$.

3.2 The scheduling strategy

Unlike thermal power units, the output power of new energy is volatile and uncertain. On one hand, this volatility makes the output power of new energy fluctuate rapidly within an hour. Thus, the traditional scheduling strategy for the hourly time scale may not be suitable for power systems with a high proportion of new energy. On the other hand, the uncertainty gives the output power of new energy the characteristic of forecast accuracy as related to time, which means more recent forecasts will have higher accuracy (Cui et al., 2021). Moreover, the traditional day-ahead scheduling strategy cannot fully utilize this characteristic. Therefore, a combined day-ahead and intraday scheduling strategy that considers the joint frequency regulation reserve scheme is proposed in this paper. The schematic diagram of this scheduling strategy is shown in Figure 4.

As shown in Figure 4, the proposed scheduling strategy is divided into two parts according to different scheduling times: day-ahead scheduling and intraday rolling scheduling.

The day-ahead scheduling is implemented every 24 h, with a cycle of 24 h and a time resolution of 15 min. The startup and shutdown states of thermal power units can be determined in day-ahead scheduling.

The intraday rolling scheduling is implemented every 15 min, with a cycle of 4 h and a time resolution of 15 min. Intraday rolling scheduling can determine the output power state of thermal power units and the PSFR of NEPPs.

Compared with the traditional scheduling strategy, the scheduling strategy proposed in this paper is improved in two main areas. First, it adds new energy pre-processing links based on the traditional scheduling strategy. Because the joint frequency regulation reserve scheme is considered in this scheduling strategy, the frequency regulation ability and the sequence of output power derating should be determined according to the new energy forecast and the cooperation principle of frequency regulation reserve described in detail in Section 3.1 in the new energy pre-processing link. Second, it adds a NEPP output model that considers the joint frequency regulation reserve scheme and the constraint of steady frequency deviation considering new energy frequency regulation to the traditional scheduling model, which is described in detail in Section 3.3 and Section 3.4.

In this strategy, the actual PSFR for NEPPs is an optimized, calculated variable in the scheduling strategy, which is jointly determined by the demand of reserve power for frequency regulation and the operation state of thermal power units. When the demand for reserve power for frequency regulation of the system is small, the frequency response capability of thermal power units in the system can satisfy it, and no single NEPP in the group needs to participate in frequency regulation. When the demand for reserve power for frequency regulation increases further, the frequency response capability of thermal power units in the system cannot satisfy the demand, and some NEPPs in the group must therefore participate in frequency regulation. When the demand for reserve power for frequency regulation of the system increases further, even if all NEPPs in the group participate in frequency regulation, the frequency response capability of the system still cannot satisfy the demand, and some NEPPs in the group will be forced to reduce their output power to reduce the demand of reserve power for frequency regulation, so as to satisfy the demand.

This scheduling strategy can flexibly formulate the participation scheme of NEPP frequency regulation based on the demand for reserve power and the frequency response capability of conventional thermal power units. Furthermore, it fully uses the time-dependent characteristics of the forecast accuracy and improves the economy of NEPP frequency regulation.

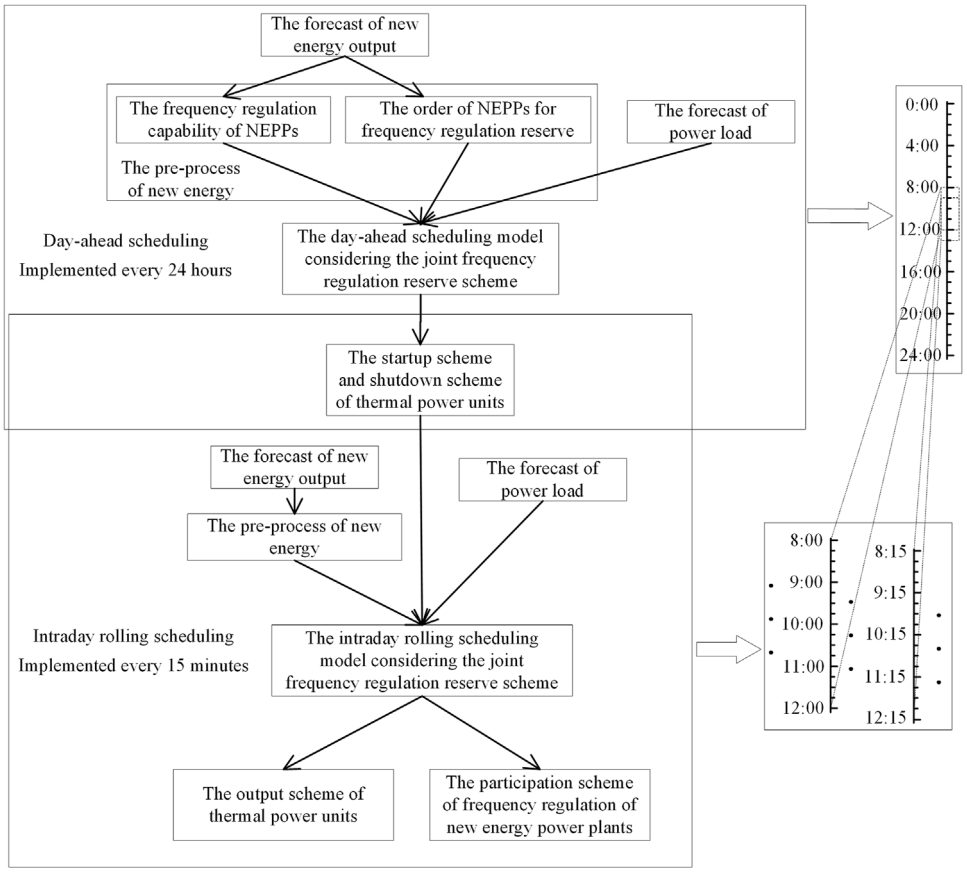

FIGURE 4
Schematic diagram of the scheduling strategy proposed in this paper.

3.3 Day-ahead scheduling model

3.3.1 Objective function

Searching for the minimum operation cost of all thermal power units is often used as the objective function of the traditional power system scheduling model. The operation cost of all thermal power units includes the coal consumption, startup, and reserve power costs. The scheduling strategy proposed in this paper accounts for the frequency regulation capability of NEPP and pursues more new energy accommodation under the premise of ensuring that the system steady-state frequency deviation does not exceed the limit. Therefore, based on the operating cost of thermal power, this paper adds the operation cost of new energy, which is composed of frequency regulation reserve cost and new energy load reduction and curtailment penalty, to form the operation cost of the system. The objective function in day-ahead scheduling can be shown as follows:

$$\min F^{da} = f_g^{da} + f_{ne,}^{da} \tag{13}$$

$$f_g^{da} = f_{g,cc}^{da} + f_{g,su}^{da} + f_{g,r}^{da}, \tag{14}$$

$$f_{ne}^{da} = f_{ne,waste}^{da} + f_{ne,r}^{da}, \tag{15}$$

$$f_{g,cc}^{da} = \sum_{t=1}^{T^{da}} \sum_{i=1}^{N_g} \left(U_{g,i,t}^{da} \left(a_{g,cc,i} \left(p_{g,i,t}^{da} \right)^2 + b_{g,cc,i} p_{g,i,t}^{da} + c_{g,cc,i} \right) \right), \tag{16}$$

$$f_{g,su}^{da} = \sum_{t=1}^{T^{da}} \sum_{i=1}^{N_g} \left(U_{g,i,t}^{da} \left(1 - U_{g,i,t-1}^{da} \right) C_{g,su,i} \right), \tag{17}$$

$$f_{g,r}^{da} = \sum_{t=1}^{T^{da}} \sum_{i=1}^{N_{agc}} \left(C_{g,r,up,i} r_{sfa,g,up,i,t}^{da} + C_{g,r,dn,i} r_{sfa,g,dn,i,t}^{da} \right), \tag{18}$$

$$f_{ne,waste}^{da} = \sum_{t=1}^{T^{da}} \sum_{i=1}^{N_{ne}} \left(C_{ne,waste,i} \left(p_{ne,forecast,i,t}^{da} - p_{ne,i,t}^{da} - r_{ne,up,i,t}^{da} \right) \right), \tag{19}$$

$$f_{ne,r}^{da} = \sum_{t=1}^{T^{da}} \sum_{i=1}^{N_{ne}} \left(C_{ne,r,i} r_{ne,up,i,t}^{da} + C_{ne,r,i} r_{ne,dn,i,t}^{da} \right), \tag{20}$$

where X^{da} represents that X is a variable in day-ahead scheduling; F^{da} is the operation cost of the system; f_g^{da} and f_{ne}^{da} are the operation costs of all thermal units and the operation cost of the NEPP group; $f_{g,cc}^{da}$, $f_{g,su}^{da}$, and $f_{g,r}^{da}$ are the costs of coal consumption for total thermal power units, the startup cost for total thermal power units, and the cost of reserve power for all thermal power units, respectively; $f_{ne,waste}^{da}$ and $f_{ne,r}^{da}$ are the punish cost of the forced output power derating of the NEPP group and the reserve power cost of the NEPP group; T^{da} is the scheduling period number; $p_{g,i,t}^{da}$ is the output power of the i^{th} thermal power unit during the time t; $a_{g,cc,i}$, $b_{g,cc,i}$, and $c_{g,cc,i}$ are cost coefficients of coal consumption of the i^{th} thermal power unit; $r_{sfa,g,up,i,t}^{da}$ and $r_{sfa,g,dn,i,t}^{da}$ are the upward and downward reserve power for secondary frequency regulation of the i^{th} AGC unit during time t; $C_{g,su,i}$ is the startup cost coefficient of the i^{th}

thermal power unit; $C_{g,r,up,i}$ and $C_{g,r,dn,i}$ are the cost coefficients of upward and downward reserve power for secondary frequency regulation of the i^{th} AGC unit; $C_{ne,waste,i}$ and $C_{ne,r,i}$ are the cost coefficients of forced derating punish and reserve power of the ith NEPP; and N_g, N_{agc}, and N_{ne} are the numbers of thermal power units, AGC units, and new energy power units, respectively.

3.3.2 Constraints

The constraints of the optimal scheduling model of the power system primarily include the output power constraint of thermal power units, the ramping constraints of thermal power units, the minimum startup and shutdown time constraints of thermal power units, and the power balance constraints. These constraints are not repeated in this paper for lack of space but are described in detail in the references. In addition to the aforementioned constraints, the constraints of NEPPs and of the steady-state frequency deviation in the context of the joint frequency regulation scheme are also considered in this paper.

Based on the analysis presented in Section 2.1, $r^{da}_{ne,up,i,t}$ and $r^{da}_{ne,dn,i,t}$ are jointly determined by $U^{da}_{neg,fr,t}$, $U^{da}_{nes,fr,i,t}$, and $K^{da}_{nes,fr,i,t}$ in the scheme of joint frequency regulation reserve. Therefore, the reserve power for frequency regulation of the NEPP can be shown as Eqs 21–22:

$$\boldsymbol{r}^{da}_{ne,up,i,t} = \boldsymbol{U}^{da}_{neg,fr,t}\boldsymbol{U}^{da}_{nes,fr,i,t}\boldsymbol{K}^{da}_{nes,fr,i,t}\Delta\boldsymbol{p}_{ne,fr,i}, \tag{21}$$

$$\boldsymbol{r}^{da}_{ne,dn,i,t} = \boldsymbol{U}^{da}_{neg,fr,t}\boldsymbol{U}^{da}_{nes,fr,i,t}\boldsymbol{K}^{da}_{nes,fr,i,t}\Delta\boldsymbol{p}_{ne,fr,i.} \tag{22}$$

Eqs 3–4, Eqs 7–12, and Eqs 21–22 constitute the constraints of NEPPs.

The constraints of steady-state frequency deviation can be transformed into the constraints of reserve power for frequency regulation, meaning that the capacity of reserve power for frequency regulation of the total system should exceed the demand of reserve power for frequency regulation of the system, as shown in Eqs. 23–24:

$$\boldsymbol{R}^{da}_{fa,cap,up,t} \geq \boldsymbol{R}^{da}_{fa,dem,t}, \tag{23}$$

$$\boldsymbol{R}^{da}_{fa,cap,dn,t} \geq \boldsymbol{R}^{da}_{fa,dem,t}, \tag{24}$$

where $R^{da}_{fa,cap,up,t}$ and $R^{da}_{fa,cap,dn,t}$ are the capacity of upward and downward reserve power for frequency regulation of the total system during time t; and $R^{da}_{fa,dem,t}$ is the demand of reserve power for frequency regulation of the total system during the time t.

Only the demand for system frequency regulation caused by the forecasted error of new energy output power and load is considered in this paper. Like the output power uncertainty of new energy and power load, the forecasted error and the demand of reserve power for frequency regulation are both uncertain, which makes the demand for reserve power for frequency regulation impossible to describe accurately and likely makes the available reserve power provided by new energy for frequency regulation lower than the scheduled reserve power provided by new energy. To address the aforementioned problem, this study regards the forecast error rate of the forecasted quantity in the system as a fuzzy variable, using a method of fuzzy chance-constrained programming based on credibility measurement to solve the model.

Thus, the demand for reserve power for frequency regulation of the system can be expressed as Eqs 25–26:

$$\boldsymbol{R}^{da}_{fa,dem,t} = \boldsymbol{\varepsilon}^{da}_{ld,t} - \boldsymbol{\varepsilon}^{da}_{neg,t} = \boldsymbol{\varepsilon}^{da}_{ld,t} - \sum_{i=1}^{N_{ne}}\boldsymbol{\varepsilon}^{da}_{nes,i,t}, \tag{25}$$

$$\boldsymbol{\varepsilon}^{da}_{X,t} = \boldsymbol{X}^{da}_{forecast,t}\tilde{\boldsymbol{e}}^{da}_{X}, \tag{26}$$

where $\varepsilon^{da}_{ld,t}$, $\varepsilon^{da}_{neg,t}$, and $\varepsilon^{da}_{nes,i,t}$ are forecast errors of the load, the output power of the group of NEPPs, and the output power of i^{th} NEPPs during time t, respectively; $X^{da}_{forecast,t}$ is the forecast value of required forecasted quantity in the system during time t; $\tilde{e}^{da}_{X}$ represents that $e^{da}_{X,t}$ is a fuzzy variable; and $e^{da}_{X,t}$ is the error rate of X during time t.

The total reserve power for frequency regulation of the system consists of the reserve power for primary frequency regulation of thermal power units, the reserve power for secondary frequency regulation of AGC units, and the reserve power for frequency regulation of the NEPP group.

The maximum upward and downward reserve power for primary frequency regulation provided by the i^{th} thermal power unit during time t can be shown in Eqs 27–29:

$$\boldsymbol{r}^{da}_{pfr,g,up,i,t} = \boldsymbol{\min}\left(\boldsymbol{U}^{da}_{g,i,t}\boldsymbol{p}_{g,max,i} - \boldsymbol{p}^{da}_{g,i,t}, \boldsymbol{R}_{g,up,i}, \Delta\boldsymbol{p}_{g,fa,i}\right), \tag{27}$$

$$\boldsymbol{r}^{da}_{pfr,g,dn,i,t} = \boldsymbol{\min}\left(\boldsymbol{p}^{da}_{g,i,t} - \boldsymbol{U}^{da}_{g,i,t}\boldsymbol{p}_{g,min,i}, \boldsymbol{R}_{g,dn,i}, \Delta\boldsymbol{p}_{g,fa,i}\right), \tag{28}$$

$$\Delta\boldsymbol{p}_{g,fa,i} = \frac{\boldsymbol{p}_{g,n,i}}{\boldsymbol{f}_n\boldsymbol{\delta}_{g,i}\%}\left(\Delta\boldsymbol{f}_{max} - \Delta\boldsymbol{f}_{g,dz,i}\right), \tag{29}$$

where $p_{g,max,i}$ and $p_{g,min,i}$ are the maximum and minimum output power of the i^{th} thermal power unit, respectively; $R_{g,up,i}$ and $R_{g,dn,i}$ are the upper and lower climbing limits of the i^{th} thermal power unit, respectively; $\Delta p_{g,fr,i}$ is the responded power limit of primary frequency regulation of the i^{th} thermal power unit; and $p_{g,n,i}$, $\delta_{g,i}$%, and $\Delta f_{g,ne,i}$ are the installed capacity, the difference coefficient, and the frequency dead band of the i^{th} thermal power unit, respectively.

The maximum upward and downward reserve power for secondary frequency regulation provided by the i^{th} AGC unit during the time t can be shown in Eqs 30–31:

$$\boldsymbol{r}^{da}_{sfr,agc,up,i,t} = \boldsymbol{min}\left(\boldsymbol{U}^{da}_{agc,i,t}\boldsymbol{p}_{agc,max,i} - \boldsymbol{p}^{da}_{agc,i,t}, \boldsymbol{R}_{agc,up,i}\right), \tag{30}$$

$$\boldsymbol{r}^{da}_{sfr,agc,dn,i,t} = \boldsymbol{min}\left(\boldsymbol{p}^{da}_{agc,i,t} - \boldsymbol{U}^{da}_{agc,i,t}\boldsymbol{p}_{agc,min,i}, \boldsymbol{R}_{agc,dn,i}\right). \tag{31}$$

Under the influence of forecast error, the upward and downward reserve power for frequency regulation provided by the group of NEPPs during time t can be shown in Eqs 32–33:

$$\boldsymbol{r}^{da}_{neg,up,t} = \sum_{i=1}^{N_{ne}}\boldsymbol{r}^{da}_{ne,up,i,t}\left(\boldsymbol{1} + \tilde{\boldsymbol{e}}^{da}_{ne}\right)), \tag{32}$$

$$\boldsymbol{r}^{da}_{neg,dn,t} = \sum_{i=1}^{N_{ne}}\boldsymbol{r}^{da}_{ne,dn,i,t}\left(\boldsymbol{1} + \tilde{\boldsymbol{e}}^{da}_{ne}\right). \tag{33}$$

To sum up, the constraints of steady-state frequency deviation can be shown in Eqs 34–35, which utilize fuzzy chance constraints:

$$\boldsymbol{Cr}\left\{\sum_{i=1}^{N_g}\boldsymbol{r}^{da}_{pfr,g,up,i,t} + \sum_{i=1}^{N_{agc}}\boldsymbol{r}^{da}_{sfr,agc,up,i,t} + \boldsymbol{r}^{da}_{neg,up,t} \geq \boldsymbol{R}^{da}_{fa,dem,t}\right\} > \boldsymbol{\alpha}^{da}, \tag{34}$$

$$\boldsymbol{Cr}\left\{\sum_{i=1}^{N_g}\boldsymbol{r}^{da}_{pfr,g,dn,i,t} + \sum_{i=1}^{N_{agc}}\boldsymbol{r}^{da}_{sfr,agc,dn,i,t} + \boldsymbol{r}^{da}_{neg,dn,t} \geq \boldsymbol{R}^{da}_{fa,dem,t}\right\} > \boldsymbol{\alpha}^{da}, \tag{35}$$

where α^{da} is the confidence level of the fuzzy chance constraint in day-ahead scheduling.

3.4 Intraday rolling scheduling model

3.4.1 Objective function

The startup and shutdown scheme of thermal power units determined in the day-ahead scheduling does not change in intraday rolling scheduling, and the startup cost of thermal power units in the intraday scheduling model is the same as $f_{g,su}^{da}$. The rest of the objective function is consistent with day-ahead scheduling:

$$\min F^{di} = f_g^{di} + f_{ne}^{di}, \tag{36}$$

$$f_g^{di} = f_{g,cc}^{da}\left(U_{g,i,t}^{da}, p_{g,i,t}^{di}\right) + f_{g,su}^{da} + f_{g,r}^{da}\left(r_{sfa,g,up,i,t}^{di}, r_{sfa,g,dn,i,t}^{di}\right), \tag{37}$$

$$f_{ne}^{da} = f_{ne,waste}^{da}\left(p_{ne,forecast,i,t}^{di}, p_{ne,i,t}^{di}, r_{ne,up,i,t}^{di}\right) + f_{ne,r}^{da}\left(r_{ne,up,i,t}^{di}, r_{ne,dn,i,t}^{di}\right), \tag{38}$$

where X^{di} represents that the variable X is a variable in intraday scheduling.

3.4.2 Constraints

Constraints for intraday rolling scheduling are similar to constraints for day-ahead scheduling.

The minimum startup and shutdown time constraints of thermal power units need not be considered in intraday scheduling because the startup and shutdown scheme of thermal power units is not changed in intraday scheduling.

The constraints of NEPPs in intraday scheduling are minimally different from the day-ahead scheduling. Since the startup and shutdown schemes of thermal power units are not changed, $r_{ne,up,i,t}^{di}$ and $r_{ne,dn,i,t}^{di}$ are jointly determined by $U_{nes,fr,i,t}^{di}$ and $K_{nes,fr,i,t}^{di}$, the reserve power for frequency regulation of the NEPP, which can be shown as Eqs 39–40:

$$r_{ne,up,i,t}^{di} = U_{nes,fr,i,t}^{di} K_{nes,fr,i,t}^{di} \Delta p_{ne,fr,i}, \tag{39}$$

$$r_{ne,dn,i,t}^{di} = U_{nes,fr,i,t}^{di} K_{nes,fr,i,t}^{di} \Delta p_{ne,fr,i}. \tag{40}$$

The remaining constraints are the same as in day-ahead scheduling, only changing X^{da} to X^{di}.

3.5 Transformation and solution of the model

Both the day-ahead and the intraday rolling scheduling models are nonlinear mixed-integer programming problems with fuzzy variables. As the model is difficult to solve directly, it must be transformed.

3.5.1 Transformation of the model

The membership function of fuzzy variables can be represented by trapezoidal membership function (Liu, B. and Peng, J., 2005), as shown in Eq. 41:

$$\mu(\tilde{e}_X) = \begin{cases} \dfrac{e_{X,4} - e_X}{e_{X,4} - e_{X,3}} & e_{X,3} \le e_X \le e_{X,4}, \\ 1 & e_{X,2} \le e_X \le e_{X,3}, \\ \dfrac{e_X - e_{X,1}}{e_{X,2} - e_{X,1}} & e_{X,1} \le e_X \le e_{X,2}, \\ 0 & other, \end{cases} \tag{41}$$

where $\mu(\tilde{e}_X)$ is the trapezoidal membership function of $\tilde{e}_X$; and $e_{X,1}$, $e_{X,2}$, $e_{X,3}$, and $e_{X,4}$ are membership function parameters of $\tilde{e}_X$.

The fuzzy chance constraint can be turned into its crisp equivalent form by the method proposed by Liu, B. and Peng, J. (2005). Thus, the corresponding crisp equivalent forms of Eqs 34–35 can be shown in Eqs 42–43:

$$\begin{aligned} &(2 - 2\alpha^{da})\left(p_{ld,forecast,t}^{da} e_{ld,3}^{da} - \sum_{i=1}^{N_{ne}}\left(\left(p_{ne,i,t}^{da} + r_{ne,up,i,t}^{da}\right) e_{ne,2}^{da}\right)\right) \\ &+ (2\alpha^{da} - 1)\left(p_{ld,forecast,t}^{da} e_{ld,4}^{da} - \sum_{i=1}^{N_{ne}}\left(\left(p_{ne,i,t}^{da} + r_{ne,up,i,t}^{da}\right) e_{ne,1}^{da}\right)\right) \\ &- \sum_{i=1}^{N_g} r_{pfr,g,up,i,t}^{da} - \sum_{i=1}^{N_{agc}} r_{sfr,agc,up,i,t}^{da} - \sum_{i=1}^{N_{ne}} r_{ne,up,i,t}^{da} \le 0, \end{aligned} \tag{42}$$

$$\begin{aligned} &(2 - 2\alpha^{da})\left(p_{ld,forecast,t}^{da} e_{ld,3}^{da} - \sum_{i=1}^{N_{ne}}\left(\left(p_{ne,i,t}^{da} + r_{ne,dn,i,t}^{da}\right) e_{ne,2}^{da}\right)\right) \\ &+ (2\alpha^{da} - 1)\left(p_{ld,forecast,t}^{da} e_{ld,4}^{da} - \sum_{i=1}^{N_{ne}}\left(\left(p_{ne,i,t}^{da} + r_{ne,dn,i,t}^{da}\right) e_{ne,1}^{da}\right)\right) \\ &- \sum_{i=1}^{N_g} r_{pfr,g,dn,i,t}^{da} - \sum_{i=1}^{N_{agc}} r_{sfr,agc,dn,i,t}^{da} - \sum_{i=1}^{N_{ne}} r_{ne,dn,i,t}^{da} \le 0, \end{aligned} \tag{43}$$

where $p_{ld,forecast,t}^{da}$ is the forecast power load during time t in day-ahead scheduling; $e_{ld,1}^{da}$, $e_{ld,2}^{da}$, $e_{ld,3}^{da}$, and $e_{ld,4}^{da}$ are membership function parameters of the fuzzy variable $\tilde{e}_{ld}^{da}$; and $e_{ne,1}^{da}$, $e_{ne,2}^{da}$, $e_{ne,3}^{da}$, and $e_{ne,4}^{da}$ are membership function parameters of the fuzzy variable $\tilde{e}_{ne}^{da}$.

3.5.2 Solution of the model

The model can be transformed into mixed-integer quadratic programming problems, which can be well solved by the commercial solver Gurobi. Therefore, the transformed model was solved using MATLAB R2018b with the Gurobi solver in this paper, and the computing environment was an Intel Core i5-8300h CPU with 8GB RAM.

4 Case study

4.1 The test system

The improved IEEE RTS 24-bus system, which can be obtained by adding a group of NEPPs to the original IEEE RTS-24 bus system (Grigg et al., 1996), was selected as the test system for this paper. The improved system has 26 thermal power units and a group of NEPPs that include three WPPs with an installed capacity of 300 MW and three PPPs with an installed capacity of 200 MW. The structure of the improved IEEE RTS 24-bus system is shown in Figure 5. The 25th and 26th thermal power units are set as the AGC unit because of high ramping rate, and all power units except for AGC units participate in primary frequency regulation. The parameters of thermal power units can be obtained from Wang et al. (1995). The frequency regulation parameters of thermal power units and NEPPs are shown in Table 2, and the membership function parameters of fuzzy variables are shown in Table 3. The confidence level of chance constraints was set to 0.8 in day-ahead scheduling and 0.9 in intraday rolling scheduling, and the cost coefficient of forced derating punish was set to 50 $\$\cdot(\mathrm{MW}\cdot 15\ \mathrm{min})^{-1}$.

The forecast curve of the required forecasted quantity in the system was obtained by adding white noise to the actual curve (Bao et al., 2016).

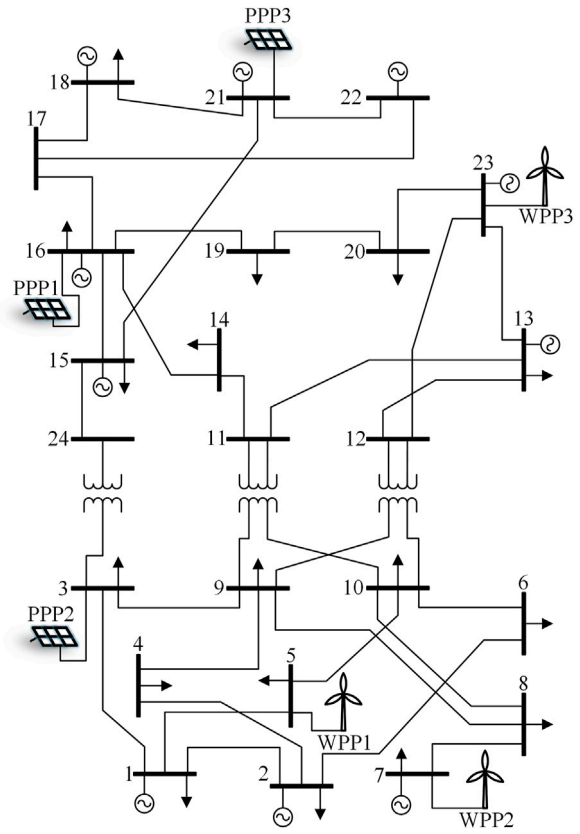

FIGURE 5
Structure of the improved IEEE RTS 24-bus system.

TABLE 3 Membership function parameters of fuzzy variables.

	e_{X1}	e_{X2}	e_{X3}	e_{X4}
e_{ne}^{da}	−0.4000	−0.1000	0.1000	0.4000
e_{load}^{da}	−0.1000	−0.0500	0.0500	0.1000
e_{ne}^{di}	−0.3000	−0.0750	0.0750	0.3000
e_{load}^{di}	−0.0750	−0.0375	0.0375	0.0750

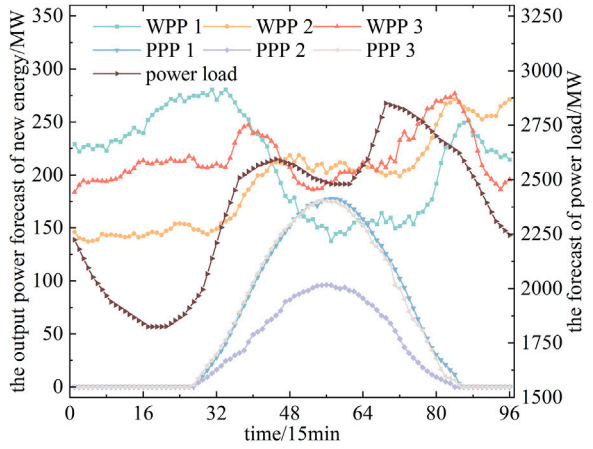

FIGURE 6
Actual curve of the quantity in a system that needs to be forecasted.

The actual curve is shown in Figure 6, and the day-ahead forecast curve and the intraday forecast curve are shown in Figure 7.

4.2 Calculation results

The system scheduled result is shown in Figure 8. The frequency response capability of thermal power units cannot satisfy the demand of reserve power for frequency regulation in the 14th, 31st, or 36th to 87th scheduling periods; some NEPPs in the group must set reserve power and participate in frequency regulation. In addition, the forced output power derating of the new energy with an extremely small value only exists in the 37th, 44th, and 66th scheduling periods.

To verify the effectiveness of the joint frequency regulation scheme, the system's PSFR from the 65th to 80th scheduling periods in day-ahead scheduling and intraday scheduling were analyzed separately, as shown in Figure 9.

As shown in Figures 9A, B, some new energy stations participate in frequency regulation from the 31st period through the 52nd period. At this time, all thermal power units are online,

TABLE 2 parameters of frequency regulation.

	δ%	Δf_{dz}/Hz	$C_{g,r,up}$/\$·(MW·15min)$^{-1}$	$C_{g,r,dn}$/\$·(MW·15min)$^{-1}$	$C_{ne,r}$/\$·(MW·15min)$^{-1}$
G1–G9	0.0500	0.0330	—	—	—
G10–G13	0.0420	0.0330	—	—	—
G14–G16	0.0380	0.0330	—	—	—
G17–G20	0.0330	0.0330	—	—	—
G21–G24	0.0300	0.0330	—	—	—
G25	0.0300	0.0330	7.7400	8.0300	—
G26	0.0300	0.0330	7.7350	8.0250	—
PPP	0.0300	0.0600	—	—	10.0000
WPP	0.0200	0.1000	—	—	10.0000

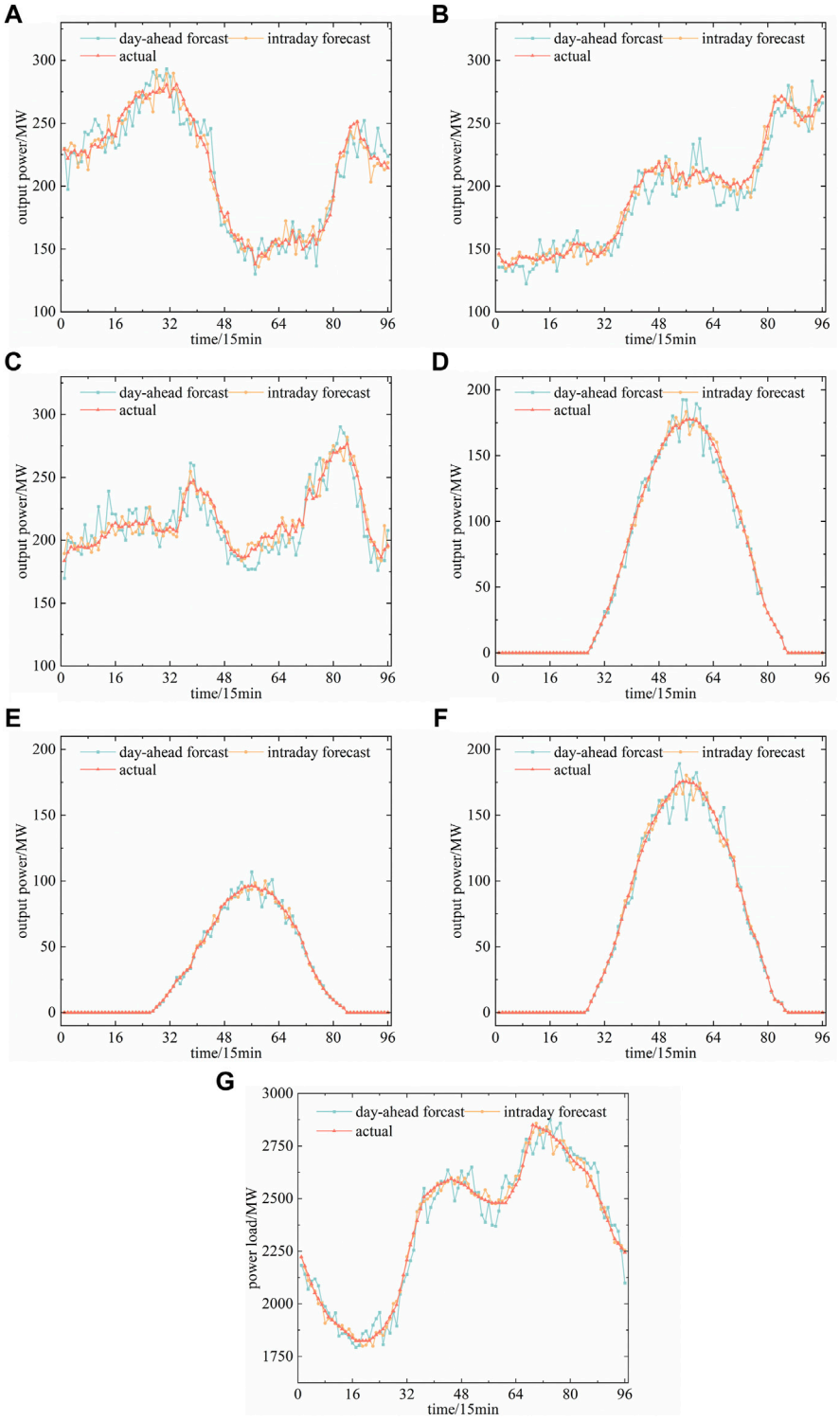

FIGURE 7
Forecast curves of the quantity in a system that needs to be forecasted: **(A)** WPP1, **(B)** WPP2, **(C)** WPP3, **(D)** PPP1, **(E)**PPP2, **(F)**PPP3, and **(G)** power load.

which conforms to the cooperation principle of frequency regulation between new energy and thermal power described in Section 3.1.1.

Figures 9B–E show that NEPPs with a higher priority level give priority to setting reserve power for frequency regulation, which conforms to the cooperation principle of frequency regulation

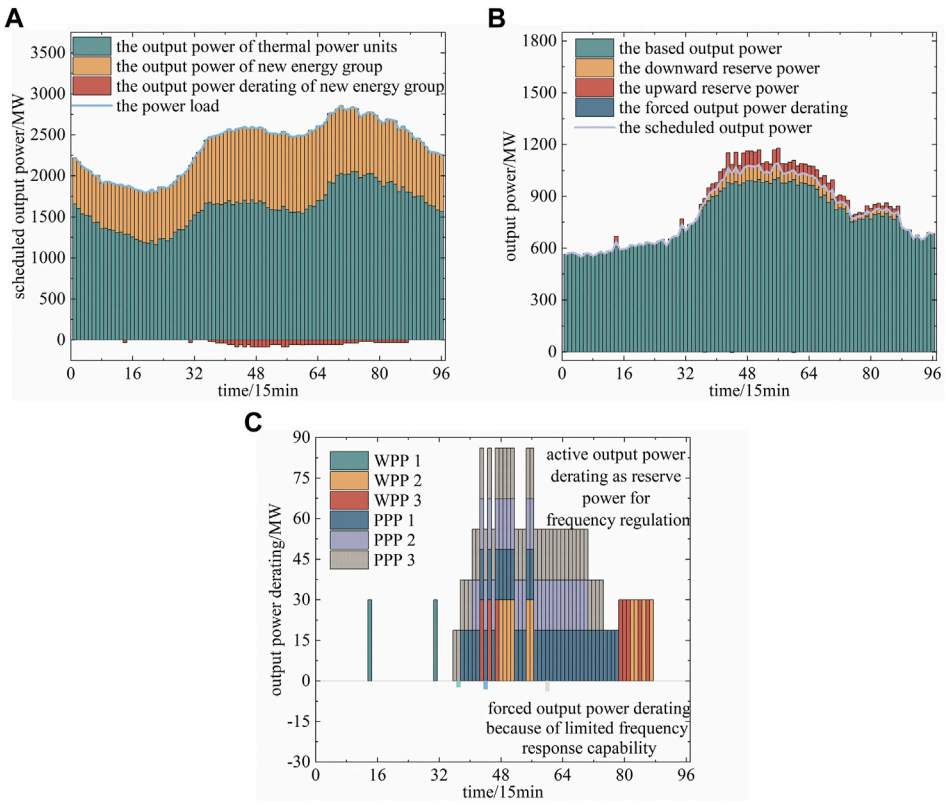

FIGURE 8
System scheduling results: **(A)** scheduled result of the system, **(B)** scheduled result of the new energy, and **(C)** output power derating of new energy.

between each NEPP in the group of NEPPs described in Section 3.1.2.

4.3 Comparison and analysis

Four comparative scheduling strategies are added to further verify the effectiveness of the scheduling strategy proposed in this paper as follows:

S1: A traditional day-ahead scheduling strategy considering the traditional system reserve power and the traditional AGC reserve power constraint (Lin et al., 2014).
S2: A scheduling strategy based on S1 that considers the constraint of reserve power for regulation, with the frequency response capability provided only by thermal power units.
S3: A scheduling strategy based on S2 that considers the frequency response capability of new energy but does not consider the joint frequency regulation reserve scheme for wind, photovoltaic, and thermal power.
S4: A scheduling strategy based on S3 that considers the joint frequency regulation reserve scheme for wind, photovoltaic, and thermal power.
S5: A combined day-ahead and intraday scheduling strategy based on S4, which is the proposed strategy in this paper.

To better control the differences between the aforementioned scheduling strategies, the time resolution was set to 15 min. Moreover, the fuzzy chance-constrained programming method based on credibility measures was used to solve the models in S2, S3, S4, and S5, and the confidence level of chance constraints was set to 0.8 in day-ahead scheduling and 0.9 in intraday rolling scheduling.

4.3.1 The analysis of frequency regulation effect

A series of analyses were conducted on the frequency regulation effect of the system, and the calculation result is shown in Figure 10.

The power disturbance of the system Δp_t was set to $\pm 30\% \sum_{i=1}^{N_{ne}} (p_{ne,forecast,i,t}^{da})$ in day-ahead scheduling and $\pm 20\% \sum_{i=1}^{N_{ne}} (p_{ne,forecast,i,t}^{da})$ in intraday scheduling during the scheduling time t, and the steady-state frequency deviation was calculated by Eq. 44,

$$\Delta \boldsymbol{f}_t = \left(\Delta \boldsymbol{p}_t - \sum_{i=1}^{N_{agc}} \boldsymbol{r}_{sfr,agc,i,t} \right) \Big/ \boldsymbol{k}_S, \tag{44}$$

where Δf_t is the steady-state frequency deviation and k_S is the unity regulation power of the total system.

The calculation result is given in Figure 10A, which shows that the steady-state frequency deviation in S1 exceeds the allowable frequency limits. This is because the constraints of steady-state frequency deviation are not considered in S1, while they are considered in S2, S3, S4, and S5 so that they can ensure that the steady-state frequency deviation is always within the allowable frequency limits in S2, S3, S4, and S5.

On the basis of the S5 proposed in this paper, the difference coefficient of the NEPP is changed and the scheduling model is calculated. The difference coefficients of the WPP/PPP were set to

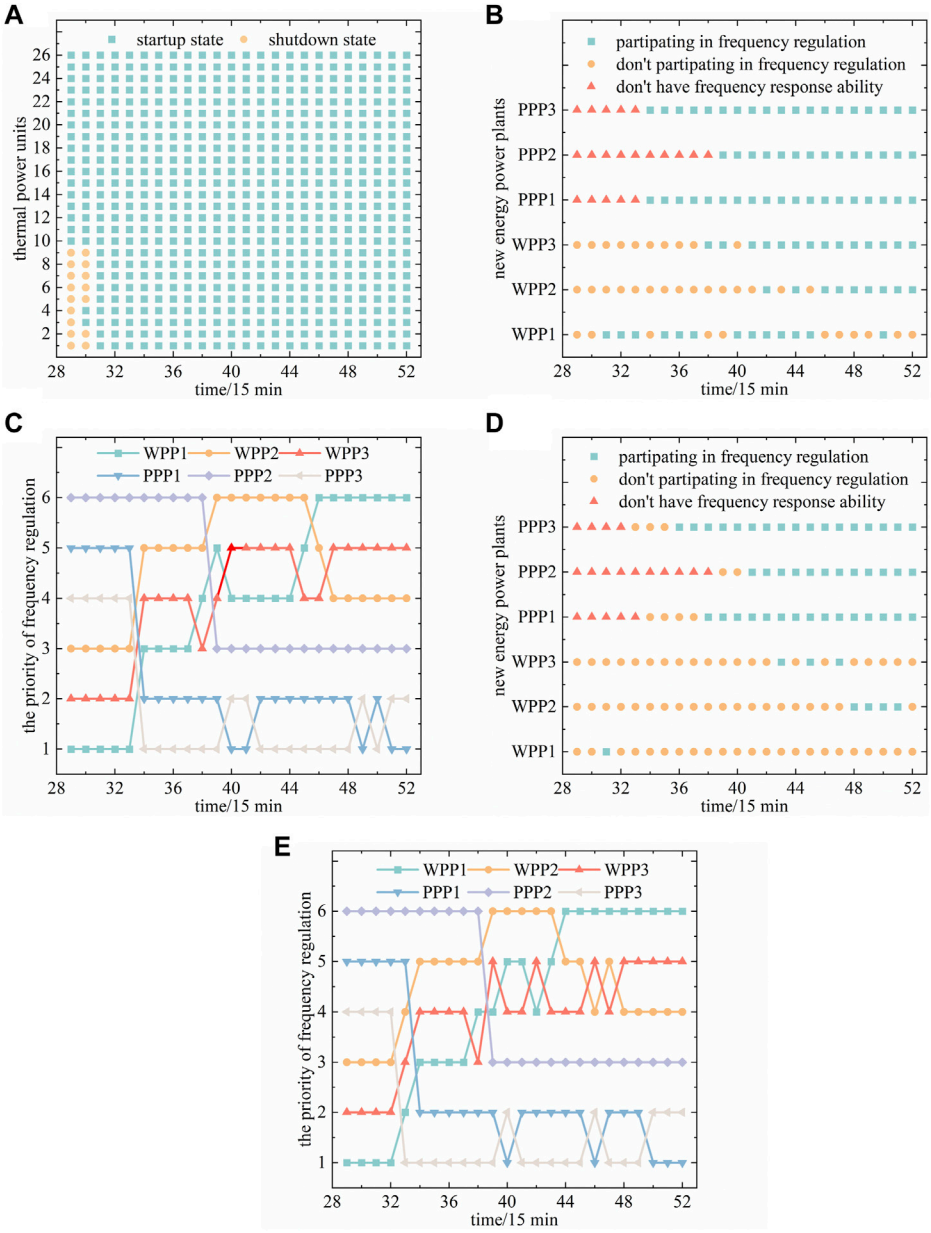

FIGURE 9
PSFR of the system in selected periods: **(A)** startup and shutdown states of thermal power units, **(B)** PSFR of NEPPs in day-ahead scheduling, **(C)** participation sequence of frequency regulation of NEPPs in day-ahead scheduling, **(D)** PSFR of NEPPs in intraday scheduling, and **(E)** participation sequence of frequency regulation of NEPPs in intraday scheduling.

0.02/0.03, 0.03/0.04, 0.04/0.05, and 0.05/0.06, with the remaining parameters of the NEPP unchanged. The calculation result is shown in Figure 10B.

According to Eq. 2, as the difference coefficient becomes bigger, the primary frequency regulation power reserve of the NEPP gradually decreases; if the output derating is still conducted according to the scheduling plan, there will have more reserve power for secondary frequency regulation, which will make the steady-state frequency deviation of the system smaller, as shown in Figure 10B.

When the new energy forecast error is large, the power disturbance faced by the system is relatively large, which affects the frequency regulation effect of the system. For S5, the new energy forecast error rates of 0.2, 0.4, and 0.6 were calculated, with the calculation results shown in Figure 10C.

As shown in Figure 10C, with the increase of new energy forecast error, the steady-state frequency deviation of the system gradually increases. When the error rate of the new energy forecast increases to a certain level (as shown in Figure 10C at 0.6), the steady-state frequency deviation of the system may exceed the allowable limit. In order to avoid this situation, the NEPPs may be forced to derate the output.

When the frequency regulation control of NEPPs is faulty, the output power of NEPPs cannot be derated according to the scheduling plan, which is equivalent to reducing the reserve power of the system

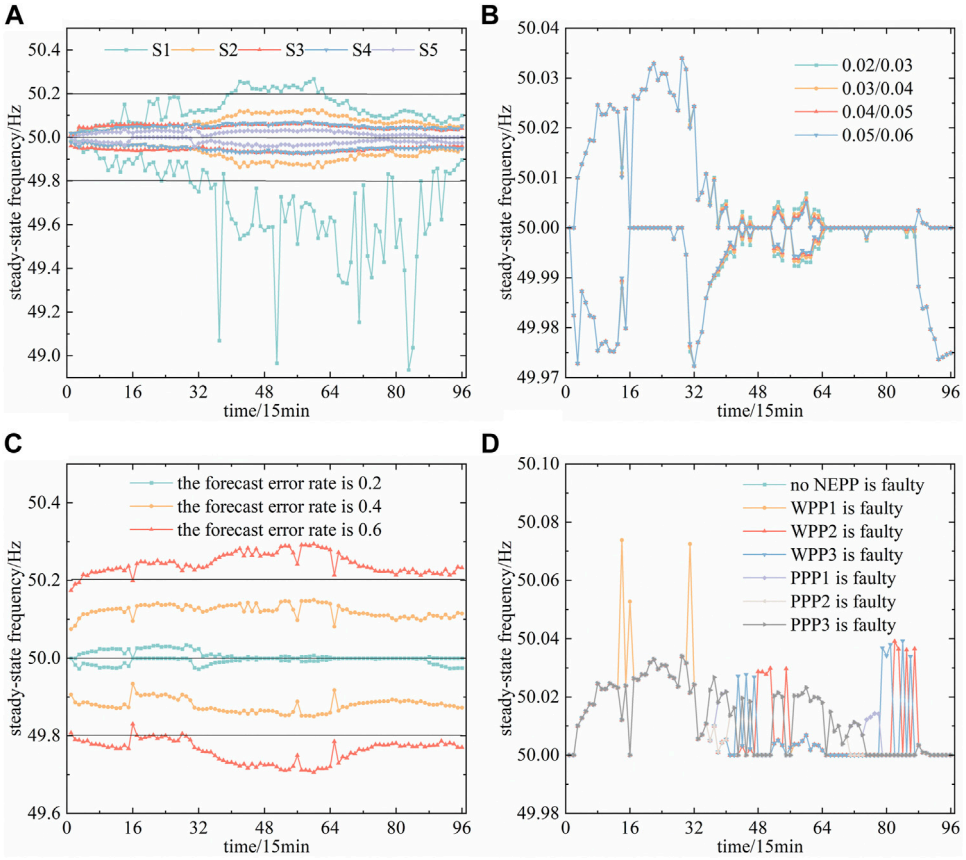

FIGURE 10
Steady-state frequency deviation of the system: **(A)** steady-state frequency deviation of the power system in the five scheduling strategies, **(B)** steady-state frequency deviation in S5 when changing difference coefficients of NEPPs, **(C)** steady-state frequency deviation in S5 when the error of new energy forecast is large, and **(D)** steady-state frequency deviation in S5 when the NEPP is faulty.

for frequency regulation while facing the positive power disturbance generated by the faulty NEPP.

When the overall forecast error of new energy is negative, the positive power disturbances generated by the faulty NEPP cancel each other out and the total power disturbance of the system becomes smaller, which does not adversely affect the frequency regulation effect of the system. Therefore, this paper focuses on the situation in which the overall forecast error of new energy is positive and the frequency regulation control for new energy is faulty.

When the overall forecast error of new energy is positive, the positive power disturbance generated by the faulty NEPP makes the total power disturbance of the system bigger, which adversely affects the frequency regulation effect of the system.

For S5, the error rate of new energy prediction was taken to be +20%, and it was assumed that WPP1, WPP2, WPP3, PPP1, and PPP2 were faulty and that PPP3 failed. The calculation results are shown in Figure 10D.

Figure 10D shows that when any NEPP in the system is faulty, although the steady-state frequency deviation of the system becomes larger, it does not exceed the allowable limit.

4.3.2 The analysis of scheduling strategy effect

Under the premise of ensuring that steady-state frequency deviation does not exceed the allowable frequency limits, the following analysis was carried out for S2, S3, S4, and S5.

TABLE 4 Costs of the four scheduling strategies.

	S2	S3	S4	S5
$f_{g,cc}$/$	609401.80	523893.7	569195.49	558334.89
$f_{g,su}$/$	980.00	1620	980.00	980.00
$f_{g,r}$/$	209960.84	173097.8	203072.29	186552.24
$f_{ne,r}$/$	0.00	219093.3	117693.33	53066.67
$f_{ne,waste}$/$	891829.08	0.00	1315.07	460.77
F/$	1712171.72	917704.8	892256.18	799394.57

The costs of S2, S3, S4, and S5 are shown in Table 4.

As shown in Table 1, S5 has the lowest total cost, compared with S2, S5 considers the frequency response capability of new energy power generation, which can improve the frequency response capability of the total system and avoid the high value of $f_{ne,waste}$ in S2. Compared with S3, S5 considers the joint frequency regulation scheme between new energy and thermal power, which can avoid the problem of NEPPs with frequency regulation capability always derating output as reserve power and reduce the high-valued $f_{ne,r}$ in S3. Compared with S4, S5 uses a more accurate forecast for rolling

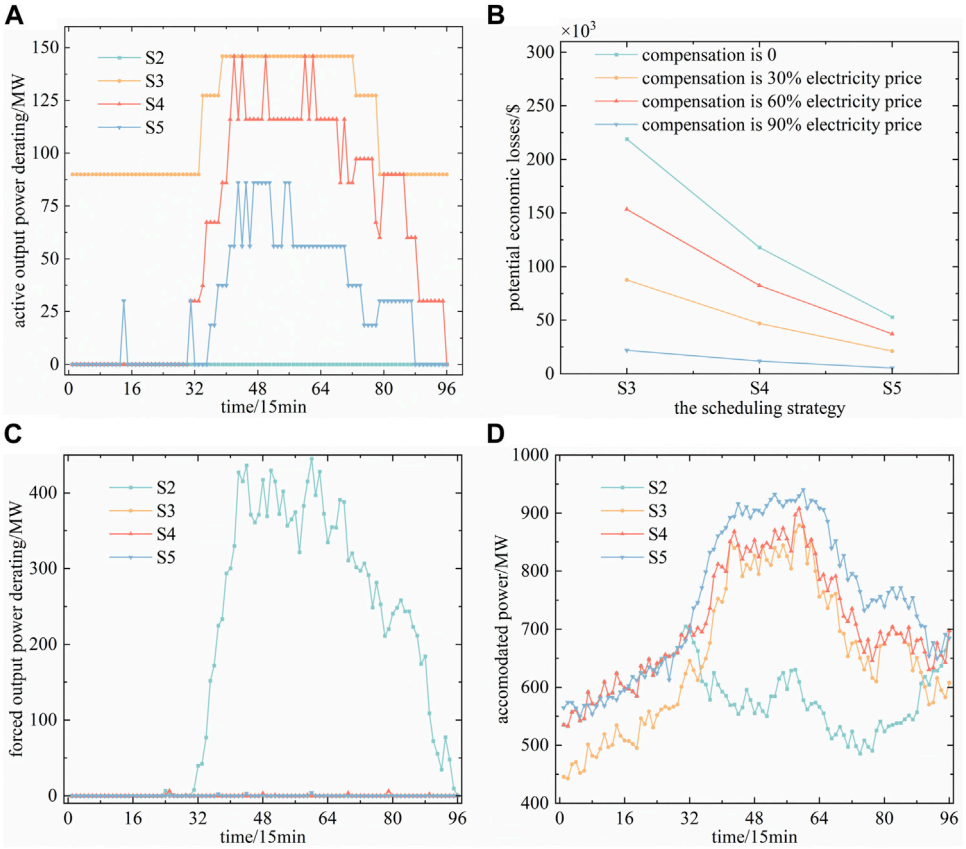

FIGURE 11
Scheduled result of new energy in the four scheduling strategies: **(A)** active output power derating, **(B)** potential economic loss, **(C)** forced output power derating, and **(D)** accommodated electricity.

calculation based on the calculation result of S4, which can further reduce $f_{ne,r}$ in S4.

Further analysis of the new energy accommodation ability of the system is shown in Figure 11.

The new energy generation participating in frequency regulation needed to derate its output power as reserve power for frequency regulation is shown in Figure 11A.

As shown in Figure 11A, the reserve power for frequency regulation of new energy does not exist in S2 because the frequency response capability of new energy is not considered in S2. Moreover, the reserve power for frequency regulation of new energy exists in S3, S4, and S5, but the values of reserve power are different in S3, S4, and S5. Since the joint frequency regulation scheme is not considered in S3, NEPPs with frequency response capability must derate their output power for reserve power of frequency regulation, and the value of reserve power provided by new energy in S3 is higher than in S4 or S5. S4 and S5 consider joint frequency regulation, with S5 as an intraday rolling scheduling based on the day-ahead scheduling S4, and S5 is implemented based on a recent forecast of new energy output power and power load. As the recent forecast has higher accuracy, the demand for reserve power of frequency regulation in S5 is lower than in S4, and the value of reserve power provided by new energy in S5 is lower than in S4.

The frequency regulation capability of new energy is considered in S3, S4, and S5. The output power of NEPPs needs to be derated as frequency regulation reserve, which causes certain power loss and economic loss to the NEPP. In S3, the output power of NEPPs with frequency regulation capabilities must always be derated as frequency regulation reserve. The cumulative power of output derating for frequency regulation in the entire scheduling cycle is 2738.667 Mwh, accounting for 14.808% of the total forecast of new energy power. In S4, the group of NEPPs works in a state of dynamic stepped output derating, and the output power of NEPPs is only derated as frequency regulation reserve during the high-frequency regulation demand period. The cumulative power of output derating for frequency regulation in the entire scheduling cycle is 1471.167 Mwh, accounting for 7.955% of the total forecast of new energy power. In S5, the demand for frequency regulation reserve is reduced because of the use of more accurate new energy intraday forecast data, and the frequency regulation provided by the group of NEPPs working in the state of dynamic stepped output derating is further reduced. The cumulative power of output derating for frequency regulation in the entire scheduling cycle is 663.333 Mwh, accounting for 3.588% of the total forecast of new energy power.

It is analyzed from the perspective of potential economic losses of new energy groups, which are shown in Figure 11B.

The fluctuation of electricity price and frequency regulation reserve compensation were not considered, and the fixed electricity price was set as 80$/MWh. The potential economic losses of the group

of NEPPs caused by output derating in S3, S4, and S5 are 219093.332, 117693.333, and 53066.667, respectively. Furthermore, considering the compensation for frequency reserve, the compensation ratio of frequency regulation was set as 30%, 60%, and 90% of the electricity price. In S3, the potential economic losses of the group of NEPPs are 87637.333, 153365.333, and 21909.333, respectively. In S4, the potential economic losses of the group of NEPPs are 47077.333, 82385.333, and 11769.333, respectively. In S5, the potential economic losses of the group of NEPPs are 21226.667, 37146.667, and 5306.667, respectively.

As Figure 11B shows, in the three types of power system strategy scheduling that consider new energy to participate in system frequency regulation, S5, the scheduling strategy proposed in this paper, has the smallest output derating and smallest potential economic losses.

The frequency response capability may not satisfy the demand of reserve power for frequency regulation in some scheduling periods, so that the new energy generation is probably forced to derate its output power, as shown in Figure 11C.

Figure 11C shows that the forced output power derating of new energy in S2 is much higher than in S3, S4, or S5 because the frequency response capability of new energy is not considered in S2. The output power of new energy in S2 is forced to derate to satisfy the system frequency regulation reserve power demand from the 31st period to the 96th period, with a high demand for frequency regulation because of the insufficient frequency response capability of thermal power units. The frequency response capability of new energy is considered in S3, S4, and S5, and the frequency response capability of the system can satisfy the demand of reserve power for frequency regulation, so the forced output power derating of new energy is almost 0.

In this paper, the accommodated power of new energy was considered to be equal to the forecast power of the new energy minus the forced power derating caused by the insufficient frequency regulation capability of the system and the active power derating of the new energy. The accommodated power of new energy is shown in Figure 11D.

Figure 11D shows that S5 has the most accommodated power of new energy in most scheduling periods. The total accommodated electricity of new energy in S2, S3, S4 and S5 is calculated as 8517.444 MWh, 10950.203 MWh, 11440.652 MWh, and 12363.027 MWh, respectively, and the total accommodation rates of new energy in S2, S3, S4, and S5 are 0.789, 0.852, 0.930, and 0.970, respectively. Thus, the accommodation ability of new energy in S5 is higher than in S2, S3, and S4.

As shown by the aforementioned comparison of the five scheduling strategies, the combined day-ahead and intraday scheduling strategy proposed in this study—which considers a joint frequency regulation reserve scheme for wind, photovoltaic, and thermal power—has the lowest cost and highest new energy accommodation ability under the premise of ensuring that the steady-state frequency deviation does not exceed the allowable frequency limits.

5 Conclusion

Based on the differences in operating characteristics between various frequency regulation resources in the system, a joint frequency regulation reserve scheme was designed between the group of NEPPs and thermal power units. A multi-time-scale scheduling strategy was proposed based on the joint frequency regulation scheme, and its model was deduced and was solved by the Gurobi solver in MATLAB. The superiority and limitations to the scheduling strategy proposed in this paper can be drawn from the aforementioned analysis as discussed as follows:

5.1 The effectiveness of the scheduling strategy

1) The frequency regulation capability of new energy and the constraint of steady-state frequency deviation are both considered in this strategy, which can improve the frequency regulation capability of the system and ensure that the steady-state frequency is within the allowable range.
2) A joint frequency regulation reserve scheme including wind, photovoltaic, and thermal power was designed in this paper. In the scheme, the group of NEPPs works in a state of dynamic stepped output power derating, and the frequency regulation cooperation is considered. The comparison and analysis show that this scheme has the smallest new energy frequency regulation reserve power, which can effectively reduce the power and economic losses caused by the new energy participating in system frequency regulation.
3) This article proposes a combined day-ahead and intraday power system scheduling strategy considering the joint frequency regulation reserve scheme. On one hand, when the intraday rolling scheduling is carried out, the high-precision new energy forecast may reduce the frequency regulation demand of the system, in turn reducing the frequency regulation reserve power provided by the new energy. On the other hand, considering the frequency regulation capability of the new energy, the frequency regulation ability of the system is improved, which can avoid the large quantity of forced output derating of new energy caused by insufficient frequency regulation capability of the system.
4) In general, in the combined day-ahead and intraday power system scheduling strategy considering the joint frequency regulation reserve scheme across wind, photovoltaic, and thermal power proposed in this paper, although the output power derating of NEPPs must be carried out, it improves the frequency regulation capability of the system so as to avoid a large amount of forced output derating of new energy. The new energy accommodation and new energy accommodation rate of the system are both improved.

5.2 The limitations to the scheduling strategy

1) The frequency regulation capability of the NEPPs is affected by the prediction error value of the new energy output power. If the prediction error is large, the available reserve capacity for frequency regulation of new energy power plants in actual operation will be quite different than in the scheduling plan, which is described in detail in Section 4.3.1.
2) The dynamic frequency response model of the system has not been researched in this paper. When the system has a large active power disturbance for a short time, it may have a very high instantaneous frequency drop rate due to insufficient system inertia.
3) The strategy proposed in this article is rather simple in terms of frequency regulation cooperation between NEPPs. Photovoltaic power plants always have a higher priority for participating in

frequency regulation than wind power plants, and they must always set the frequency regulation reserve, which may affect the enthusiasm of frequency regulation for photovoltaic power plants. Between different wind power plants, those with higher output rates are prioritized for power derating, and the operating status of wind turbines inside the wind power plants is not considered, which may lead to an increased mechanical loss of the internal wind turbine during some periods.

Data availability statement

The original contributions presented in the study are included in the article/Supplementary Material; further inquiries can be directed to the corresponding author.

Author contributions

SZ: idea, methodology, and writing—original draft preparation. HW: writing—review and editing. WW: academic regulation supervision. XC: engineering—practical guidance.

Funding

This work was supported by the National Key R&D Program of China (2021YFB1507005) and the Key Research and Development Program of Xinjiang Uygur Autonomous Region (2022B01020-3).

Conflict of interest

XC was employed by the company State Grid Xinjiang Electric Power Co., Ltd.

The remaining authors declare that the research was conducted in the absence of any commercial or financial relationships that could be construed as a potential conflict of interest.

Publisher's note

References

An, Y., Li, Y., Zhang, J., Wang, T., and Liu, C. (2020). "Enhanced frequency regulation strategy for wind turbines based on over-speed de-loading control," in 2020 5th Asia Conference on Power and Electrical Engineering (ACPEE), Chengdu, China, 04-07 June 2020, 442–446. doi:10.1109/ACPEE48638.2020.9136254

Bao, Y., Wang, B., Li, Y., and Yang, S. (2016). Rolling dispatch model considering wind penetration and multi-scale demand response resources. *Proc. CSEE* 31 (17), 4589–4600. doi:10.13334/j.0258-8013.pcsee.151343

Chu, Y., Xu, H., Cheng, S., Liu, X., Guo, X., Li, Z., et al. (2019). "Actual measurement and analysis of fast response capability of photovoltaic plants participating in the frequency regulation of northwest power grid," in 2019 IEEE 8th International Conference on Advanced Power System Automation and Protection (APAP), Xi'an, China, 21-24 October 2019, 825–829. doi:10.1109/APAP47170.2019.9224642

Cui, Y., Zhang, J., Zhong, W., Wang, Z., and Zhao, Y. (2021). Scheduling strategy of wind penetration multi-source system considering multi-time scale source-load coordination. *Power Syst. Technol.* 45 (05), 1828–1837. doi:10.13335/j.1000-3673.pst.2019.2577

Fan, H., and Tang, M. (2022). A two-layer control strategy of the wind farm participating in grid frequency regulation. *Alex. Eng. J.* 61 (8), 6371–6381. doi:10.1016/j.aej.2021.11.064

Ge, X., Liu, Y., Fu, Y., and Jia, F. (2021). Distributed robust unit commitment considering the whole process of inertia support and frequency regulations. *Proc. CSEE* 41 (12), 4043–4058. doi:10.13334/j.0258-8013.pcsee.200974

Grigg, C., Wong, P., Albrecht, P., Allan, R., Bhavaraju, M., Billinton, R., et al. (1996). The IEEE reliability test system-1996. A report prepared by the reliability test system task force of the application of probability methods subcommittee. *IEEE Trans. Power Syst.* 14 (3), 1010–1020. doi:10.1109/59.780914

Hao, L., Ji, J., Jiang, R., Chen, H., Fang, B., and Li, Y. (2020). "Intra-day rolling dispatch considering large-scale wind power participation in primary frequency regulation and unit fast start-up capability," in 2020 IEEE 4th Conference on Energy Internet and Energy System Integration (EI2), Wuhan, China, 30 October 2020 - 01 November 2020, 1923–1928. doi:10.1109/EI250167.2020.9347042

Li, H., Lu, Z., Qiao, Y., and Zhang, B. (2020). "Frequency dynamics constrained unit commitment with wind plants," in 2020 IEEE Power & Energy Society General Meeting (PESGM), QC, Canada, 02-06 August 2020, Montreal, 1–5. doi:10.1109/PESGM41954.2020.9281617

Liu, B., and Peng, J. (2005). *A course in uncertainty theory*. Beijing: Tsinghua University Press.

Li, W., Zhu, X., Zhou, H., Yao, W., and Wen, J. (2021). "Overview of frequency regulation technology of power system with high wind power penetration," in 2021 International Conference on Power System Technology (POWERCON), Haikou, China, 08-09 December 2021, 1176–1182. doi:10.1109/POWERCON53785.2021.9697583

Lin, T., Ye, J., Chen, R., Xu, X., and Qin, X. (2014). Study on unit commitment with steady-state frequency constraints of power system including large-scale wind turbine. *J. Electr. Power Sci. Technol.* 29 (04), 18–24.

Liu, Y., Shao, G., Zang, H., and Wang, C. (2020). Analysis of renewable energy participation in primary frequency regulation and parameter setting scheme of power grid. *Power Syst. Technol.* 44 (02), 683–689. doi:10.13335/j.1000-3673.pst.2019.0822

Lu, J., Mao, Y., Liu, L., Cheng, H., Zhang, J., and Zhang, X. (2021). "Unit commitment of power system with wind power and photovoltaic considering frequency safety constraint," in 2021 IEEE Sustainable Power and Energy Conference (iSPEC), Nanjing, China, 23-25 December 2021, 1486–1493. doi:10.1109/iSPEC53008.2021.9735461

Ma, X., Sun, X., Cheng, L., Guo, X., Liu, X., and Wang, Z. (2019). "Parameter setting of new energy sources generator rapid frequency response in northwest power grid based on multi-frequency regulation resources coordinated controlling," in 2019 IEEE 8th International Conference on Advanced Power System Automation and Protection (APAP), Xi'an, China, 21-24 October 2019, 218–222. doi:10.1109/APAP47170.2019.9224749

Mu, R., Wu, S., Chen, J., and He, T. (2021). Study on the detection technology of frequency regulation capability of grid connected new energy station. *Yunnan Electr. Power* 49 (06), 80–86.

Ouyang, J., Yuan, Y., Li, M., Pang, M., Jiang, H., and Zhong, L. (2021). Optimal dispatching method of high-proportion wind power systems considering wind power reserve for frequency adjustment. *Power Syst. Technol.* 45 (06), 2192–2201. doi:10.13335/j.1000-3673.pst.2020.1049

Rajan, R., and Fernandez, F. M. (2019). Power control strategy of photovoltaic plants for frequency regulation in a hybrid power system. *Int. J. Elect. Power Energy Syst.* 110, 171–183. doi:10.1016/j.ijepes.2019.03.009

Sun, M., and Jia, Q. (2018). "A novel frequency regulation strategy for single-stage grid-connected PV generation," in 2018 2nd IEEE Conference on Energy Internet and Energy System Integration (EI2), Beijing, China, 20-22 October 2018, 1–6. doi:10.1109/EI2.2018.8582246

Wang, S. J., Shahidehpour, S. M., Kirschen, D. S., Mokhtari, S., and Irisarri, G. D. (1995). Short-term generation scheduling with transmission and environmental constraints using an augmented Lagrangian relaxation. *IEEE Trans. Power Syst.* 10 (3), 1294–1301. doi:10.1109/59.466524

Ye, J., Lin, T., Bi, R., Chen, R., and Xu, X. (2016). "Unit commitment in isolated grid considering dynamic frequency constraint," in 2016 IEEE Power and Energy Society General Meeting (PESGM), Boston, MA, 17-21 July 2016, 1–5. doi:10.1109/PESGM.2016.7741654

Zhang, J., Wang, N., Huang, R., Ma, M., and He, S. (2019). Survey on frequency regulation technology of power grid by high-penetration PV. *Power Syst. Prot. Control* 47 (15), 179–186. doi:10.19783/j.cnki.pspc.181042

Zhang, Z., Zhou, M., Wu, Z., Liu, S., Guo, Z., and Li, G. (2022). A frequency security constrained scheduling approach considering wind farm providing frequency support and reserve. *IEEE Trans. Sust. Energy* 13 (2), 1086–1100. doi:10.1109/TSTE.2022.3150965

frontiers | Frontiers in Energy Research

TYPE Original Research
PUBLISHED 10 January 2023
DOI 10.3389/fenrg.2022.1036984

OPEN ACCESS

EDITED BY
Da Xie,
Shanghai Jiao Tong University, China

REVIEWED BY
Arturo Garcia Perez,
University of Guanajuato, Mexico
Tao Rui,
Anhui University, China

*CORRESPONDENCE
Qiong Li,
powerdsp339@163.com

SPECIALTY SECTION
This article was submitted to Smart Grids, a section of the journal Frontiers in Energy Research

RECEIVED 05 September 2022
ACCEPTED 22 November 2022
PUBLISHED 10 January 2023

CITATION
Wu Y, Li Q, Long G, Chen L, Cai M and Wu W (2023), Research on arc grounding identification method of distribution network based on waveform subsequence segmentation-clustering.
Front. Energy Res. 10:1036984.
doi: 10.3389/fenrg.2022.1036984

Research on arc grounding identification method of distribution network based on waveform subsequence segmentation-clustering

Yihui Wu[1], Qiong Li[1]*, Guohua Long[2], Liangliang Chen[1], Muliang Cai[2] and Wenbao Wu[3]

[1]Nanchang Hangkong University, Nanchang, China, [2]National Network Jiangxi Electric Power Co. Ltd., Nanchang, China, [3]China Power Construction Group Jiangxi Electric Power Construction Co. Ltd., Nanchang, China

The traditional method of detecting fault current based on threshold judgment method is limited by the current size and is easily disturbed by noise, and it is difficult to adapt to the arc ground fault detection of the distribution network. Aiming at this problem, this paper proposes a single-phase arc-optic ground fault identification method based on waveform subsequence splitting fault segmentation, combined with three-phase voltage-zero sequence voltage waveform feature extraction clustering. First of all, the waveform fault segment is segmented and located, secondly, the characteristic indexes of the time domain and frequency domain of the combined three-phase voltage-zero sequence voltage waveform are established, and the multidimensional feature distribution is reduced by the principal component analysis method, and finally, the characteristic distribution after the dimensionality reduction is identified by the K-means clustering algorithm based on the waveform subsequence. Experimental results show that the arc light grounding fault identification method proposed in this paper achieves 97.12% accurate identification of the test sample.

KEYWORDS

arc grounding, waveform subsequences, K-means clustering, fault identification, sequence segmentation

1 Introduction

According to the survey, more than 80% of the power outage losses are caused by distribution network failures, so the fault diagnosis of distribution networks has always been the research object of power supply units. Among them, arc light grounding fault is not easy to find and the harm is huge, and the mechanism is complex, which is a category of grounding faults that are difficult to detect. Therefore, it is of great significance to propose a reliable and efficient arc-ray grounding identification algorithm for the operation of the distribution network.

The traditional arc-optic grounding fault identification method of the distribution network is based on the steady-state or transient electrical parameters and the set threshold (Chen et al., 2021), and in the fault identification method based on the transient electrical parameters, the characteristic parameters of the typical fault type are first extracted, including wavelet transform (WT) (Qin et al., 2018; Lin et al., 2019; Wei et al., 2020a), empirical mode decomposition (EMD) (Guo et al., 2019; Cai and Wai, 2022), and S transformation (ST) (Peng et al., 2019); Then, the arc ground fault is classified and identified by the pattern recognition method, mainly including the neural network method (Siegel et al., 2018; Du et al., 2019a), the Support Vector Machine (SVM) (Xia et al., 2019; Dang et al., 2022), the fuzzy control method (Zeng et al., 2016), the clustering (Wang et al., 2015), etc., in addition, the high-precision current transformer can be used to improve the fault identification ability (Paul, 2015), but the detection cost is also significantly increased.

Reference (Mishra et al., 2016) classifies arc ground faults through fault data, extracts five fault features, and inputs them into a fuzzy inference system for identification. Although the identification effect is remarkable, the establishment of fuzzy control rules relies on historical experience, and the ability to learn independently is poor. Reference (Gadanayak and Mallick, 2019; Wang et al., 2021) combined Variational Mode Decomposition (VMD) and support vector machine to identify arc ground faults. Different eigenmode functions were obtained by decomposing the collected ground fault signals by VMD, and the faults were extracted. The typical characteristics of the signal are found, the displacement entropy with the greatest contribution is found, and the arc ground fault is identified by the support vector machine. However, support vector machines need a large number of samples for training, and mode aliasing effects are prone to occur during empirical mode decomposition, and the parameters of variational mode decomposition need to be selected manually. Reference (Guo M. F. et al., 2018) proposed a ground fault detection method based on wavelet transform and Convolutional Neural Network (CNN). The time-frequency components were obtained through wavelet transform, and then each component was normalized. Identify fault features. However, the selection of wavelet transform basis functions has limitations, and the neural network needs to be trained on a large number of samples. Reference (Wei et al., 2020b) proposed a generalized S-transform with variable factors to detect ground faults. This method has stronger adaptability and higher detection accuracy, but local over-fitting is prone to occur in the S-transform calculation process. Reference (Zhang et al., 2019) proposed a fault identification method based on waveform feature extraction and matrix analysis and clustering. This method can identify different grounding resistances, but the efficiency and accuracy of the algorithm need to be improved.

For this reason, this paper proposes a time series characteristic analysis method combining three-phase voltage and zero-sequence voltage waveforms to solve the problems that the threshold value setting cannot be automated and requires a large number of samples training in the traditional detection of electrical parameters and threshold values. At the same time, in view of the problems of traditional waveform analysis feature dimension redundancy and large amount of calculation, a method of arc grounding fault identification for distribution network based on segmentation-clustering is proposed.

The main contributions of this paper are:

(1) Considering that there are developing faults in the field data, the direct use of the wave recorder data will cause the eigenvalues of the arc ground fault to be confused with other types of fault data. Therefore, a waveform subsequence segmentation method based on the sliding *t*-test is proposed to achieve the same Segmentation of different types of fault data in recorded wave data.
(2) A fault identification model combining the time series feature extraction of three-phase voltage and zero-sequence voltage waveforms is established. Through the analysis of experimental data, the boundary conditions of arc ground fault and other faults are obtained, which effectively improves the traditional feature extraction based on current analysis. The problem.

The first part of this paper analyzes the waveform characteristics based on waveform subsequence segmentation, the second part proposes an arc-flash grounding fault identification algorithm based on segmentation-clustering, the third part carries out numerical example simulation and analysis, and finally gives the conclusion.

2 Waveform feature analysis based on fault waveform subsequence segmentation

2.1 Waveform subsequence segmentation

The data source of the on-site arc ground fault is mainly the recorded data of the fault recorder. When a fault occurs, the fault recorder can automatically and accurately record the changes of various electrical quantities in the process before and after the fault occurs. Due to the development of ground faults, it is possible to evolve from one type of fault to another. As shown in Figure 1, no fault occurred in the time period of 1.0 s–1.08 s; arc ignition occurred many times in the time period of 1.08 s–2.7 s; resonance fault occurred in the time period of 2.7 s–3.1 s; 3.1 s–3.5 return to normal within s time period.

If the data analysis of the fault segment of the wave recorder is used directly, the analysis of fault

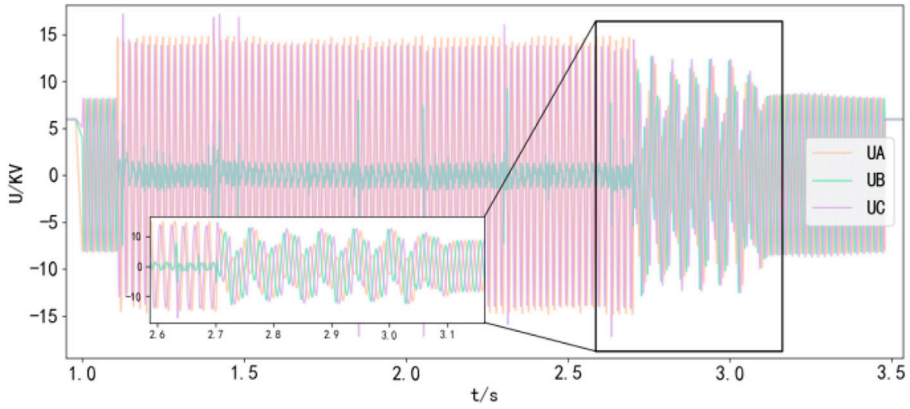

FIGURE 1
Three-phase voltage waveform diagram of developing fault.

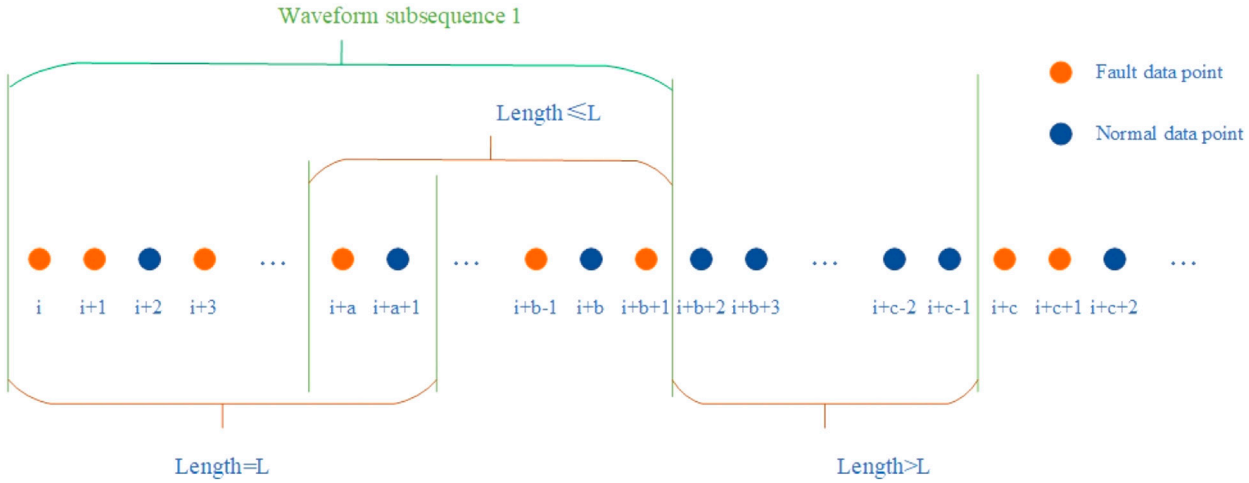

FIGURE 2
Schematic diagram of waveform subsequence segmentation.

characteristics may be confused, so each fault needs to be segmented. To this end, this paper proposes a fault subsequence segmentation method based on sliding *t*-test. Compared with other sequence segmentation algorithms, this method is simple in algorithm and less computationally expensive. Due to the strong periodicity of the fault voltage waveform, the parameter selection problem of the sliding *t*-test becomes simple, and the selected parameters are applicable to all the recorder data.

Sliding *t*-test tests for mutation by calculating whether the difference between the mean of two groups of samples is significant, t follows a distribution with $df = n_1 + n_2 - 2$ degrees of freedom, Given a significant level of $\alpha = 0.05$, the critical value $t_{0.05}$ is obtained by looking up the t distribution table, if $|t_i| > t_\alpha$,a fault is considered to have occurred at that point. For time series $X(t)$ of length n, set time $i(n_1 \le i \le n - n_2)$ as the reference point, The two subsequences x_1 and x_2 before and after the reference point define the statistic t_i at time i:

$$t_i = \frac{1}{\sqrt{\frac{(n_1 s_1^2 + n_2 s_2^2)}{(n_1 - n_2 - 2)^*}} \sqrt{\frac{1}{n_1} + \frac{1}{n_2}}} \left(\overline{x_1} - \overline{x_2}\right) \quad (1)$$

In the formula (Du et al., 2019b): n_1 and n_2 are the sample sizes of the two subsequences, $\overline{x_1}$ and $\overline{x_2}$ are the average of the two subsequences, s_1^2 and s_2^2 are the variances of the two subsequences.

TABLE 1 Time-domain waveform characteristics table.

Type	Mean				Variance			
	U_A/kV	U_B/kV	U_C/kV	U_0/kV	U_A	U_B	U_C	U_0
Arc grounding	−0.449	0.039	−0.409	−0.819	113.749	6.261	82.247	238.297
Ferromagnetic resonance	−0.223	0.212	0.268	0.256	39.791	40.559	46.308	62.438
Normal	0.287	−0.061	−0.234	−0.008	36.239	35.824	36.580	7.351
Type	**Kurtosis**				**Peak to peak**			
	U_A	U_B	U_C	U_0	U_A/kV	U_B/kV	U_C/kV	U_0/kV
Arc grounding	−1.647	0.089	−1.169	−1.851	29.359	12.632	29.067	44.765
Ferromagnetic resonance	−1.026	−1.023	−1.153	−0.472	23.541	24.665	25.018	35.469
Normal	−1.385	−1.450	−1.453	1.855	16.096	16.057	16.267	2.795

TABLE 2 Frequency domain waveform characteristics table.

Type	Odd harmonic content of zero sequence voltage			Center frequency		Frequency standard deviation		Root mean square frequency	
	3 times (%)	5 times (%)	7 times (%)	Fault phase voltage	Zero sequence voltage	Fault phase voltage	Zero sequence voltage	Fault phase voltage	Zero sequence voltage
Arc grounding	6.937	2.503	2.266	213.947	143.786	234.466	204.445	317.408	476.532
Ferromagnetic resonance	2.547	0.765	0.194	183.792	93.655	357.686	260.193	402.143	208.420
Normal	24.514	1.244	1.217	—	312.341	—	384.744	—	495.566

As shown in Figure 2, when the sliding *t*-test is performed on the fault recorder data in this paper, there is at least a segment of non-fault sample points before the fault sample point i and the length is at least L, the length of the sequence (i, i+a+1) is L, the length of the sequence (i+a, i+b+1) is less than or equal to L, the length of the sequence (i+b+1, i+c-1) is greater than L and all are normal sample points, the sequence (i, i+b+1) is a waveform subsequence. In this paper, the following considerations are made for subsequence segmentation:

(1) Sequence (i, i+a+1), that is, a sequence of length L at the beginning of the fault is temporarily stored as the initial waveform subsequence.
(2) If there are fault points in the sequence (i+a, i+b+1), that is, taking the last fault point of the waveform subsequence as the starting point and there are fault points in the supplementary sequence of length L, all the fault points before the last fault point of the supplementary sequence are merged with the initial waveform subsequence, and the initial waveform subsequence is replaced. If there is no fault point within the supplementary sequence, the initial waveform subsequence is split into the final waveform subsequence and labeled.
(3) Repeat step (2) until all waveform subsequences are segmented.

2.2 Waveform feature analysis

2.2.1 Time domain waveform characteristics

Time Domain Analysis enables intuitive and accurate analysis of systems in the time domain. For the arc grounding system, time domain indicators such as mean value, variance, peak-to-peak value and kurtosis coefficient are selected for analysis. The mean shows the average level of the data, the variance measures the degree of dispersion of the data, the peak-to-peak value shows the difference between the highest value and the lowest value of the signal in a period, and the kurtosis coefficient reflects the distribution characteristics of the vibration signal. The calculation of the kurtosis coefficient when the fourth power is used, the influence of noise can be reduced and the signal-to-noise ratio can be improved.

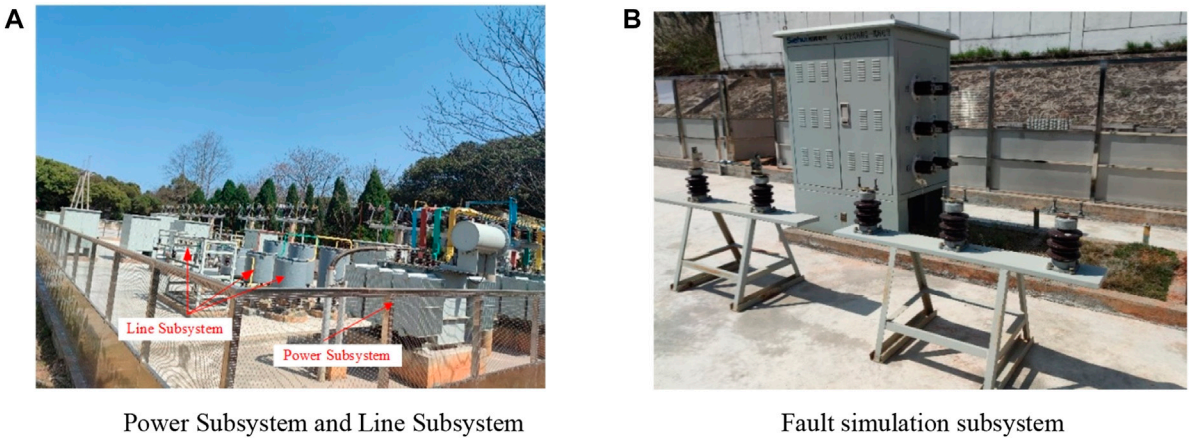

FIGURE 3
Physical experiment platform. **(A)** Power Subsystem and Line Subsystem. **(B)** Fault simulation subsystem.

Through the time domain feature extraction of arc ground fault, ferromagnetic resonance fault and normal conditions, the time domain eigenvalues of the three types of data shown in Table 1 are obtained. In the table, the zero-sequence voltage variance of arc ground fault is obviously larger than that of ferromagnetic resonance fault and normal condition. And the mean value of the normal situation is closer to zero, the zero-sequence voltage kurtosis value of the normal situation is the largest, and it is distinguished from the other two faults. The peak-to-peak value of the normal case is close to zero, and the peak-to-peak value of the three-phase voltage of the arc ground fault is larger than the other two cases except for the faulty phase.

The variances and peak-to-peak values of zero sequence voltages and three-phase voltages of the four characteristics can distinguish arc grounding faults, ferromagnetic resonance faults and normal conditions.

2.2.2 Frequency domain waveform characteristics

Frequency domain analysis is a method of evaluating system performance using graphical analysis in the frequency domain. It can not only reflect the steady-state performance of the system, but also can be used to study the stability and transient performance of the system. For the arc grounding system, frequency domain time scales such as odd harmonic content, spectral gravity center frequency, spectral frequency standard deviation, and spectral root mean square frequency are selected for analysis. The harmonic content is the amount obtained by subtracting the fundamental wave component from the alternating current. The voltage in the power grid is mainly 50 Hz. In some cases, a higher frequency signal will appear. When the frequency of the harmonic signal is the fundamental wave signal when the frequency is an odd multiple, the harmonic is called an odd harmonic. The center of gravity frequency can describe the frequency of the signal component with larger components in the frequency spectrum of the signal, and reflects the situation of the signal power spectrum. The frequency standard deviation describes the spread of the power spectrum energy distribution. The root mean square frequency is the arithmetic square root of the mean square frequency, which can be regarded as the radius of inertia.

The frequency domain eigenvalues of the three types of data shown in Table 2 are obtained by extracting the frequency domain features for arc ground fault, ferromagnetic resonance fault and normal conditions. The third harmonic content of the normal condition in the table is significantly higher than the other two fault conditions. Under normal conditions, the centroid frequency of zero-sequence voltage, the standard deviation of spectral frequency and the frequency of spectral root mean square are the largest. The frequency of the spectral center of gravity of the arc ground fault is slightly larger than that of the ferromagnetic resonance fault.

The spectral centroid frequency, spectral frequency standard deviation, and spectral root mean square frequency of the frequency domain waveform feature can clearly distinguish the three cases. The arc ground fault, ferromagnetic resonance fault and the normal zero-sequence voltage odd harmonic content can also distinguish the three cases.

In Algorithm 1, input the recorder data CFG file, and the sliding step. After initialization, the t index is calculated. When the t index exceeds the significant interval, it is saved in A, and then the fault points in A are merged and subsequences are divided. Finally, the time domain and frequency domain eigenvalues of each subsequence are extracted, and the subsequence and the eigenvalue matrix are output.

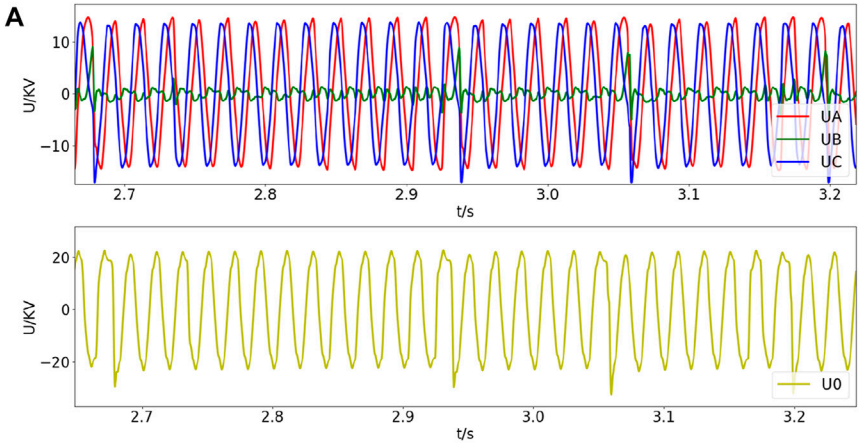

Three-phase voltage and zero-sequence voltage waveform of arc ground fault

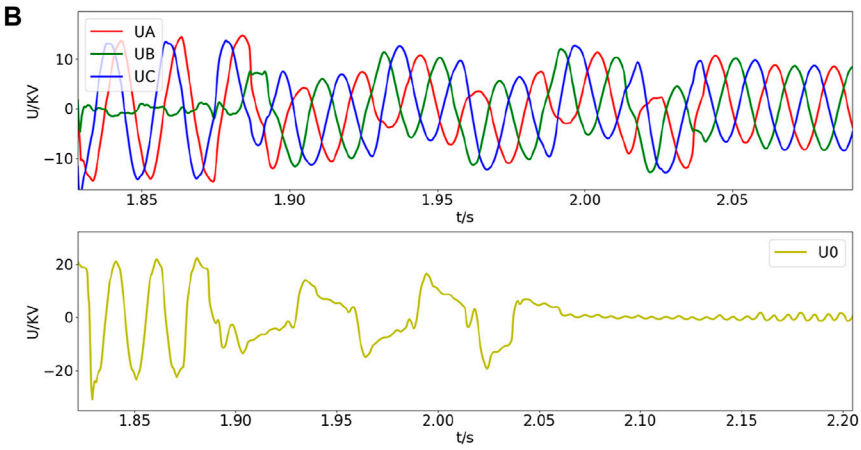

Three-phase voltage and zero-sequence voltage waveform of ferromagnetic resonance fault

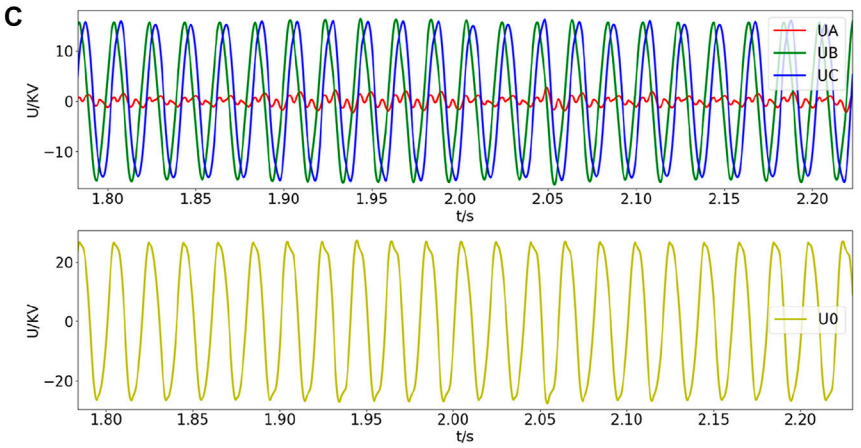

Three-phase voltage and zero-sequence voltage waveform of general ground fault

FIGURE 4
Typical failure diagram of the test sample. **(A)** Three-phase voltage and zero-sequence voltage waveform of arc ground fault. **(B)** Three-phase voltage and zero-sequence voltage waveform of ferromagnetic resonance fault. **(C)** Three-phase voltage and zero-sequence voltage waveform of general ground fault.

TABLE 3 Variance explanation rate table.

Element	Variance explained rate		
	Characteristic root	Percent variance	Accumulation %
1	13446.99	92.34	92.34
2	1051.66	7.22	99.56
3	40.07	0.28	99.84
4	14.30	0.10	99.93
5	8.22	0.06	99.99
6	1.23	0.01	100.00
7	0.07	0.00	100.00
8	0.00	0.00	100.00
9	0.00	0.00	100.00
10	0.00	0.00	100.00

Input: CFG file D, L .
Output: subsequence z , feature matrix x.

```
input D;
initialize L, N=length(D), A;
for i=1,2,…,N-L do
    Calculate t_i by formula (1);
    if |t_i| > t_α then
        add i to A;
    end if
end for
combine z in A;
split subsequence;
extract x;
return z, x;
```

Algorithm 1. Subsequence segmentation and feature extraction.

3 Arc ground fault identification algorithm based on segmentation-clustering

3.1 Feature dimensionality reduction based on principal component analysis

The extraction of key feature indicators is an effective method for dimensionality reduction of high-dimensional feature vectors, that is, through data correlation analysis, the original data is converted into effective parameters that are independent of each other and contain the main information. The principal component analysis method uses the knowledge of linear algebra to reduce the dimensionality of the data, and converts multiple variables into a few irrelevant comprehensive variables to more comprehensively reflect the entire data set. The comprehensive variables are called principal components, and the principal components are not correlated with each other, that is, the information they represent does not overlap. This method can effectively reduce the parameter redundancy and improve the efficiency of fault diagnosis (Wang et al., 2015). The steps of principal component analysis are as follows:

1) Input m pieces of n-dimensional data, and form the original data into a matrix $X = \{x_1, x_2, x_3, \ldots, x_n\}$ of n rows and m columns, where x_i is an m-dimensional vector.
2) Zero-means each row of matrix X, that is, subtracts the mean of that row.
3) Calculate the covariance matrix C.

$$C = \begin{pmatrix} Cov(x_1, x_1) & \cdots & Cov(x_1, x_n) \\ \vdots & \ddots & \vdots \\ Cov(x_n, x_1) & \cdots & Cov(x_n, x_n) \end{pmatrix} \tag{2}$$

In the formula: $Cov(x_i, y_j)$ represents the covariance of x_i and y_j.

4) Calculate the eigenvalues and eigenvectors of the covariance matrix, sort the eigenvalues from large to small, select the largest N, and then use the corresponding N eigenvectors as row vectors to form the eigenvector matrix P.
5) Transform the data into a new space constructed by N feature vectors, that is, $Y = PX$.

3.2 Cluster analysis model based on K-means

The K-means algorithm is a typical distance-based clustering algorithm, and the distance is used as an evaluation index for similarity, that is, the closer the distance between two samples, the greater the similarity.

First determine the value of k, which means the number of aggregated classes.

Second, randomly select k initial cluster centers. Randomly select k centroid vectors $\{\mu_1, \mu_2, \ldots, \mu_k\}$ from the data set $D = \{x_1, x_2, \ldots x_m\}$, and the coordinates of the centroid vectors are selected by the formula:

$$\begin{cases} C_{[x]} = \left(min_x + range_x * rand(\,)\right) \\ C_{[y]} = \left(min_y + range_y * rand(\,)\right) \\ C_{[z]} = \left(min_z + range_y * rand(\,)\right) \end{cases} \tag{3}$$

In the formula: min_x represents the smallest value in the X coordinate, $range_x$ represents the difference between the maximum value and the minimum value of the X coordinate, and $rand(\,)$ represents a random number between (0,1). Y and Z are the same.

Then assign sample points. Calculate the distance between the sample $x_i\,(i = 1, 2, \ldots m)$ and each centroid vector d_{ij}:

$$d_{ij} = \left\| x_i - \mu_j \right\|_2^2 \tag{4}$$

In the formula: μ_j is the mean vector of the cluster. Assuming that the cluster is divided into $(C_1, C_2, \ldots C_k)$, the x_i is credited to the class C_j with the smallest distance. At this point, the centroid of μ_j is recalculated and updated, and the expression is:

$$\mu_j = \frac{1}{|C_j|} \sum_{x \in C_j} x \tag{5}$$

Repeat the steps of allocating sample points and updating the cluster center until all the sample points are allocated, the category of all the sample points does not change or the number of iterations reaches the specified maximum value, the clustering is stopped. Output the clusters where clustering is done.

In Algorithm 2, the eigenmatrix is input first, then the mean value is removed, and the covariance matrix, eigenvalues, and eigenvectors are calculated. Then reduce the dimension of the original feature matrix. Then initialize the centroid, and when there are still cluster assignment results that change, calculate the distance between the centroid and the sample point, assign the sample point, and update the centroid. Finally, output the dimension reduction matrix, each cluster data and the cluster center.

Input: feature matrix x, k.
Output: dimensionality reduction matrix Y, category y, cluster center μ.

```
input x;
remove the average;
covariance matrix by formula (2);
calculate eigenvalue, eigenvectors;
eigenvector matrix P;
Y=P*x;
initialize k centroids, y;
repeat
for i=1 to n then
    calculate distance by formula (4);
    assign data points;
    for j=1 to k do
        calculate μ by formula (5);
    end for
end for
until y no longer changes
return Y, y, μ;
```

Algorithm 2. Feature dimensionality reduction and clustering.

3.3 A fault identification algorithm based on segmentation and clustering of waveform subsequences

Combined with the above analysis, this paper proposes an arc-ground fault identification algorithm for distribution network based on waveform subsequence segmentation-clustering. The fault identification process is as follows:

1) Step 1: Valid segment data extraction.

After the data is input, the data needs to be preprocessed to extract the data at the moment of failure, that is, the valid segment data.

2) Step 2: Segment and extract the waveform subsequence sequence.

Using the method proposed in Section 1.1, the waveform subsequences are segmented.

3) Step 3: Feature value and feature vector extraction.

The sub-waveform sequence is analyzed in time domain and frequency domain, and the characteristic index proposed in Section 1.2 is calculated and combined into a characteristic vector.

4) Step 4: Feature dimensionality reduction.

For the eigenvalues and eigenvectors extracted in the third step, the dimension is high, and most of the information is redundant, so the principal component analysis method proposed in Section 2.1 is used to reduce the dimension of the data, and the original ten-dimensional data is reduced to three-dimensional.

5) Step 5: K-means clustering.

The clustering algorithm proposed in Section 2.2 is used to perform cluster analysis on the dimensionally reduced 3D data. In this paper, the value of k is selected as 3, that is, the data is clustered into three categories.

6) Step 6: Cluster data output.
7) Step 7: Identify the fault category.

3.4 Arc ground fault safe boundary model

The arc ground fault safety boundary refers to the arc ground fault data: If the fault data falls within the safety boundary, the

TABLE 4 Feature vector table.

Index	Factor load factor		
	Principal component 1 (92.34%)	Principal component 2 (7.22%)	Principal component 3 (0.28%)
Variance	0.93	0.35	−0.06
Kurtosis	−0.01	0.01	0.09
Peak-to-Peak	0.11	0.09	0.20
Mean	−4.55E-4	0.01	0.04
Center frequency	−0.15	0.45	−0.76
Frequency standard deviation	−0.21	0.49	0.60
Rms frequency	−0.26	−0.65	−0.07
5th harmonic	−2.64E-5	−6.71E-5	1.22E-4
5th harmonic	−1.94E-5	−4.72E-5	6.83E-5
7th harmonic	−1.67E-5	−3.88E-5	5.43E-5

fault data can be accurately identified as the fault category; if the fault data falls on the safety boundary or outside the safety boundary, there are the fault data may be identified as other types of faults. And the arc ground fault safety boundary can be effectively distinguished from other types of faults.

The center of the arc ground fault safety boundary is the cluster center of the arc ground fault type data after clustering, and the equatorial radius and polar radius of the safety boundary are shown in Eq. 6.

$$\begin{cases} a = \frac{\sqrt{2}}{2} * (max(x) - min(x)) \\ b = \frac{\sqrt{2}}{2} * (max(y) - min(y)) \\ c = \frac{\sqrt{2}}{2} * (max(z) - min(z)) \end{cases} \tag{6}$$

In the formula, a, b, and c are the radius of one equator and the radius of two poles, respectively, $max(x/y/z)$ is the maximum value of the clustered arc ground fault type data along the x/y/z direction, $min(x/y/z)$ is the minimum value along the x/y/z direction.

In Algorithm 3, the safety boundary model is established by formula Eq. 6 and the arc ground fault clustering center μ through the arc ground fault data.

Input: Arc Ground Fault Data Y, μ.
Output: Security Boundary

1: **input** Y, μ;
2: calculate the polar radius and equatorial radius by formula (6);
3: the center of the circle is μ;
4: **return** Security Boundary;

Algorithm 3. Security Boundary Model.

4 Case study

4.1 Experimental conditions

The experimental data comes from the arc grounding physics experiment platform, which includes power supply subsystem, circuit subsystem, fault simulation subsystem and measurement subsystem. Figure 3A shows the power supply subsystem and the circuit subsystem.

In the training samples selected in the experiment: 540 data of arc ground fault (including high resistance ground fault) and 18 data of ferromagnetic resonance fault; in the test sample: 75 data of arc ground fault (including high resistance ground fault), ferromagnetic resonance two fault data. As shown in Figures 4A–C are several typical arc ground faults, ferromagnetic resonance faults and general ground faults of the test samples, respectively.

4.2 Analysis of waveform feature parameter distribution results

Combined with the waveform feature analysis proposed in Section 1.2, the time domain features and frequency domain features are accumulated to obtain ten eigenvalues, and a large number of features have redundancy, so feature dimension reduction is performed. The variance explanation rate of each feature index obtained by the principal component analysis method is shown in Table 3.

According to the cumulative variance contribution rate shown in Table 1, the cumulative explanation rate of the first three principal components is 99.84%, so the first three principal components can be considered to represent the original variables.

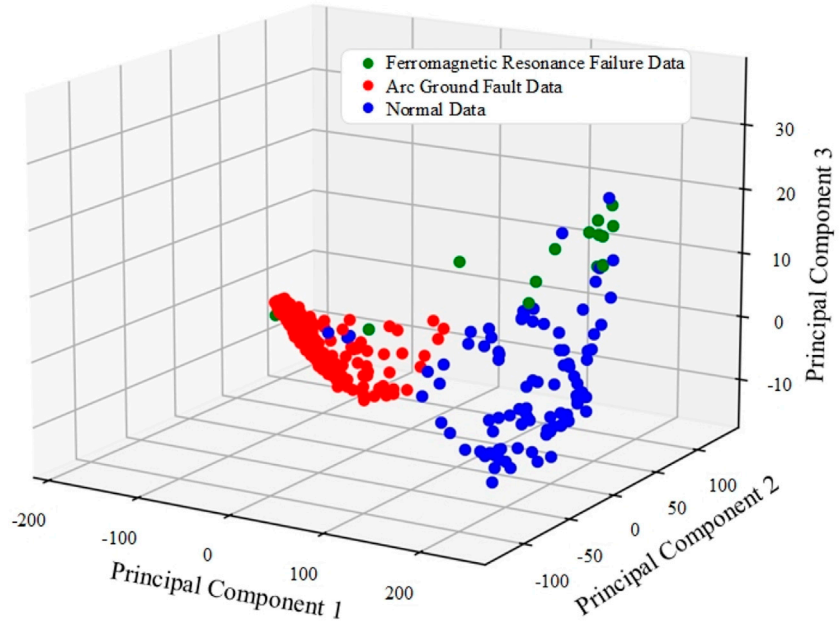

FIGURE 5
Distribution map of arc grounding, ferromagnetic resonance, and normal conditions.

TABLE 5 Distance table between training samples and cluster centers.

Training data	Distance from class 1	Distance from class 2	Distance from class 3	Judgment
1	10.22	112.46	243.55	Class 1
2	9.83	113.51	242.40	Class 1
3	13.02	114.86	242.28	Class 1
4	14.85	116.37	241.49	Class 1
5	130.36	59.65	349.47	Class 2
6	212.92	321.10	35.78	Class 3
7	276.04	386.51	35.85	Class 3
8	202.56	312.47	38.31	Class 3
9	219.14	330.72	29.11	Class 3
10	195.82	308.16	59.08	Class 3

Table 4 is the eigenvector table. The indicators in the table are the standardized variance, kurtosis, peak-to-peak value, mean value, barycentric frequency, frequency standard deviation, root mean square frequency, third harmonic, fifth harmonic, and seventh harmonic. It can be seen from the table that the principal component 1 has a large positive correlation with the variance; the principal component 2 has a large negative correlation with the root mean square frequency, and has a large positive correlation with the frequency standard deviation and the center of gravity frequency; There is a negative correlation with the frequency standard deviation and a large positive correlation with the frequency standard deviation.

The waveform characteristic parameter distribution of the training samples is shown in Figure 5. In the figure, the arc ground fault data is concentrated in the vicinity of (−50, 15, 0), while the ferromagnetic resonance fault data and normal data are scattered in (125, 50, 0), respectively. 15) and (200,-75,-10). Therefore, the data after dimensionality reduction can better describe the arc ground fault, and can effectively distinguish the arc ground fault from the other two faults.

TABLE 6 Distance table between test sample and cluster center

Test data	Distance from class 1	Distance from class 2	Distance from class 3	Judgment
1	42.81	226.33	238.69	Class 1
2	254.80	14.58	79.18	Class 2
3	282.92	26.26	62.33	Class 2
4	275.28	18.04	62.24	Class 2
5	264.57	14.12	78.47	Class 2
6	268.78	12.14	72.73	Class 2
7	283.49	27.20	61.63	Class 2
8	180.39	79.03	95.43	Class 2
9	201.62	67.54	64.52	Class 3
10	243.36	88.53	31.89	Class 3

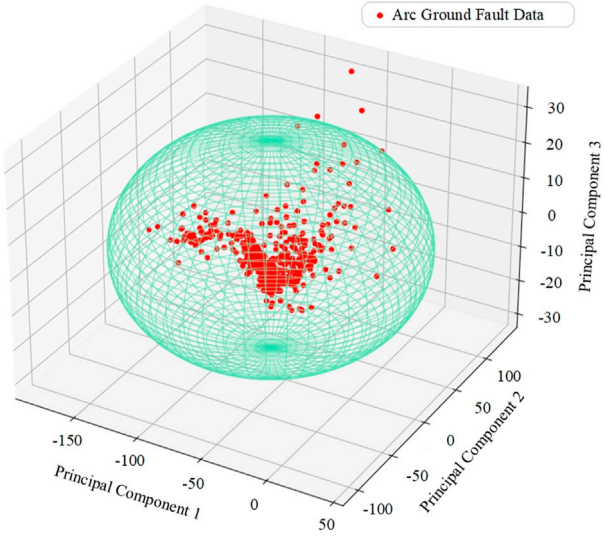

FIGURE 6
Arc grounding safety boundary.

4.3 Model identification verification

1) After the model is trained with training samples, the distance from each sample to each cluster center is shown in Table 5, and the last column is the fault type discrimination. Type 1 is arc ground fault, type 2 is ferromagnetic resonance fault, and type 3 is normal condition. Calculate the distance between the training data and each cluster center, and divide the data into the closest classes.
2) After the test sample data is identified by the model, the distance and attribution type of each test sample from each cluster center are shown in Table 6. It can be concluded from the table that the sample points are always closer to one of the cluster centers, and farther away from the other two types of sample centers. Type 1 is arc ground fault, type 2 is normal, and type 3 is ferromagnetic resonance fault.
3) Combined with the safety boundary proposed by Eq. 6, the equatorial radius and polar radius of the safety boundary are calculated. After calculation, the equatorial radius of the safety boundary is 111.0 and 119.5, and the polar radius is 29.7. The cyan spherical area in Figure 6 is the safety boundary of arc ground fault, and the red sample points are the data classified as arc ground fault after clustering. It can be seen from the figure that most of the arc ground fault data falls within the safety boundary, that is, the safety boundary can more accurately distinguish arc ground faults from other faults.
4) For the arc grounding system of the distribution network, the identification of high resistance grounding faults is a difficult point (Kavaskar and Mohanty, 2019). The arc high-resistance fault has obvious intermittent, the phase voltage is basically unchanged, the zero-off time is long, and it lasts for several cycles intermittently. At the same time, the zero-sequence voltage has nonlinear distortion (Zhang et al., 2021). The identification of single-phase ground fault is mainly realized by detecting the zero-sequence voltage. When the zero-sequence voltage suddenly increases, it is judged that a ground fault occurs.

For arc high-resistance grounding faults, the method proposed in this paper is used to segment the fault waveform sub-sequence, extract features, and reduce the dimension to obtain the principal component components of four types of samples after dimension reduction as shown in Table 7. Among them, the high-resistance grounding samples And the low resistance ground samples are within the safety boundary, while the normal case and ferromagnetic resonance fault samples are outside the safety boundary. Combining with Figure 7, it is obvious that the method proposed in this paper can also accurately identify the arc high-resistance ground fault.

TABLE 7 Principal component components after dimension reduction for four types of samples.

Type	Principal component 1	Principal component 2	Principal component 3	Relative position
Low resistance ground fault	−45.08	101.58	−17.82	Inside
High resistance ground fault	20.62	−9.30	−1.81	Inside
Ferromagnetic resonance	−60.90	59.21	73.66	Outside
Normal	−249.37	9.80	−40.94	Outside

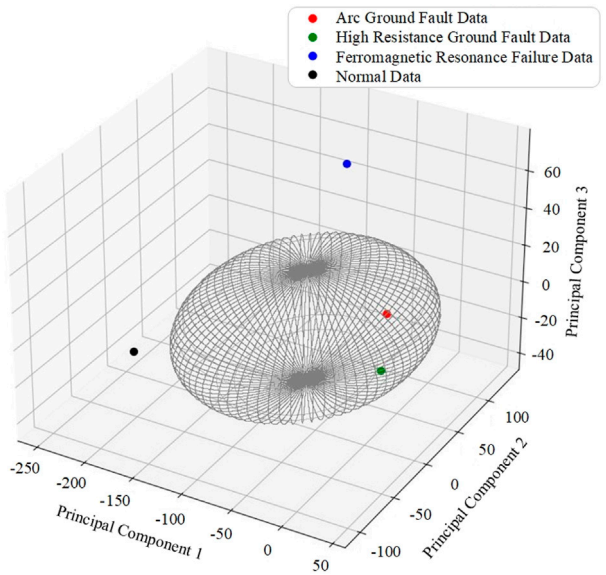

FIGURE 7
The relative positions of the four types of sample data and the security boundary.

4.4 Algorithm comparison

4.4.1 Segmentation accuracy comparison

Through the above analysis, the algorithm proposed in this paper is compared with the wavelet transform algorithm and the variational mode decomposition algorithm. The waveform subsequence segmentation algorithm proposed in this paper only needs to determine the sliding step size L and the 95% significant interval range when selecting parameters. Since the fault recorder data has strong periodicity, and the period is 80, L = 80 is selected. For the selection of L, the detection effects corresponding to different L values are shown in Figure 8. The figure shows the detection effect of the sliding *t*-test when L = 40, 80, and 120, respectively. When L = 40 and L = 120, the entire recorded wave data is judged as fault, when L = 80, the fault data can be detected accurately.

Wavelet transform can decompose the signal into a series of signal sub-sequences, which has the characteristics of multi-resolution analysis. In practical applications, discrete wavelet transform with less computational complexity and higher accuracy is often used. The Symlet wavelet function is an approximately symmetrical wavelet function after the improvement of the db function. The support range of the symN wavelet is 2N-1, the vanishing moment is N, and it also has good regularity. Compared with the dbN wavelet, the wavelet is consistent with the dbN wavelet in terms of continuity, support length, filter length, etc., but the symN wavelet has better symmetry, that is, it can reduce the time to analyze and reconstruct the signal to a certain extent. Phase distortion. For the fault recorder data, this paper selects the wavelet function sym8 as the fundamental wave function, and the number of decomposition layers is 9. The decomposition results are shown in Figure 9. The figure is the approximate coefficient CA9 and the detail coefficient CD9-CD1 after wavelet transformation. The threshold detection is performed on the five detail coefficients CD1 and CD2 with obvious fault characteristics. As the threshold increases, the arc ground fault detection is more obvious, but only the start time of the fault can be found. When the waveform subsequence is divided, the end time of the fault needs to be set as the start time of the next fault. In CD7, the fault detection is more accurate, but the arc ground fault and ferromagnetic resonance fault between the sampling points (60, 80) cannot be accurately divided, and it needs to be handled manually. If the threshold is increased, some arc ground faults cannot be accurate detection.

The variational modal decomposition method is an adaptive, completely non-recursive modal variation and signal processing method, which is suitable for non-stationary sequences, and decomposes to obtain relatively stable subsequences containing multiple different frequency scales. The VMD algorithm decomposes the original non-stationary signal f into k relatively stationary sub-signals with different center frequencies w_k and priority bandwidths. Each sub-signal, as a modal component of the original signal, can reflect the original signal at different time scales Structure. As shown in Figure 10, IMF2 and IMF3 are more accurate in detecting faults. Although IMF3 can detect the fault segment, it is greatly affected by the threshold value. If the threshold value increases, although the arc ground fault can be distinguished from the ferromagnetic resonance fault, But the fault end-point detection of Ferromagnetic resonance faults becomes inaccurate. No matter whether the threshold of IMF4 is increased or decreased, the fault point cannot be accurately detected. For

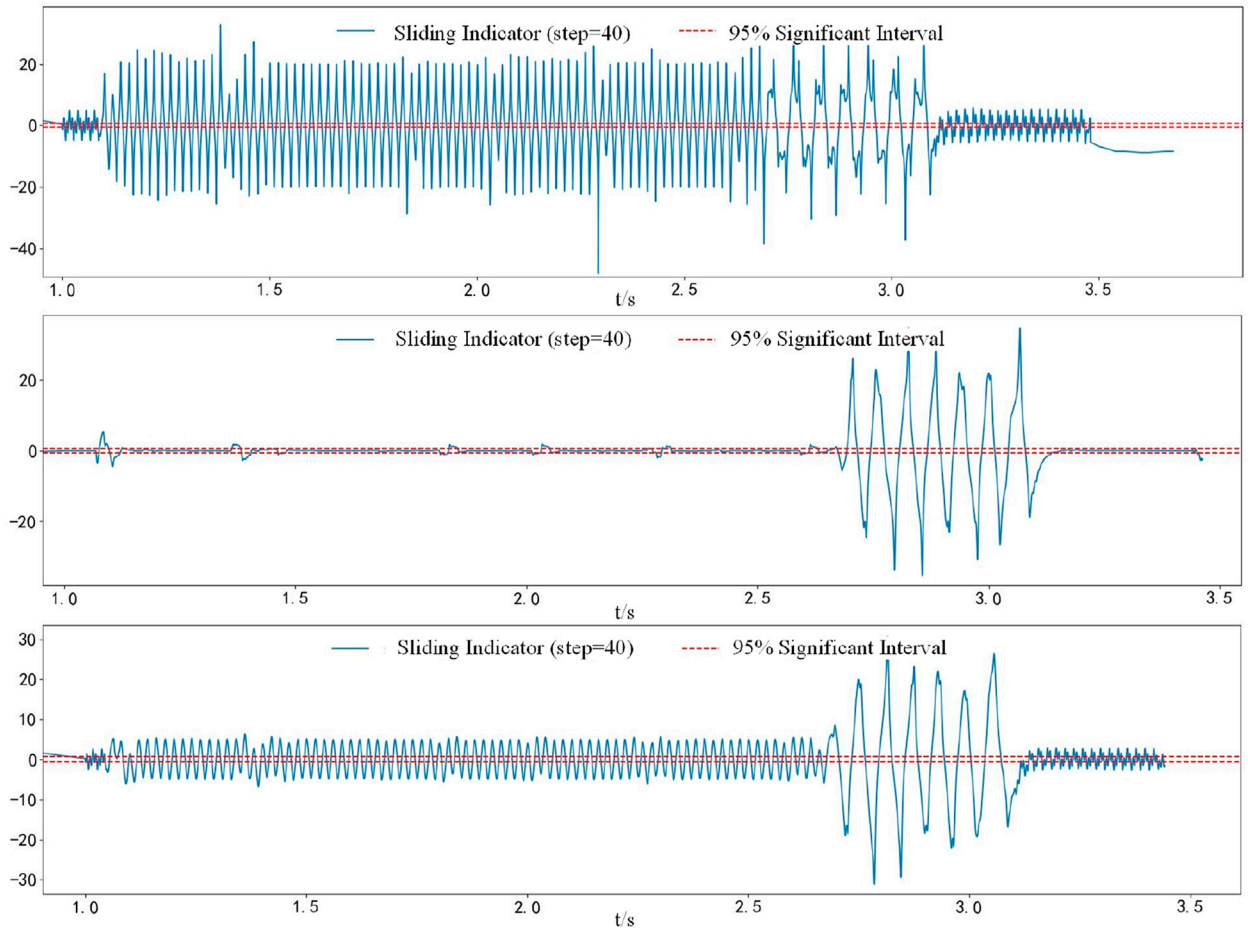

FIGURE 8
Detection results of different sliding steps.

the fault detection of IMF5-IMF7, although the fault location can be detected, the fault detection cannot be completed, and the detection of arc ground fault is invalid.

Table 8 compares the detection and segmentation of faults by the method proposed in this paper, wavelet transform and variational modal decomposition for different experimental samples. Variational modal decomposition can only detect ferromagnetic resonance faults, and wavelet transform cannot accurately detect general ground faults. The main reason is that the end point of arc ground fault cannot be accurately detected during wavelet transform detection. Arc ground faults start as an end point, resulting in general ground faults being divided into arc ground faults.

4.4.2 Comparison of recognition accuracy

After the fault data is segmented and eigenvalue extracted, the fault type needs to be identified. Comparing the algorithm proposed in this paper with WT-CNN and VMD-SVM, the CNN model structure consists of input layer, convolution layer, pooling layer, activation function layer, fully connected layer and output layer group layer. For the processed data, the output layer is the final result, and the convolution layer, pooling layer and activation function layer together form a hidden layer of CNN. The structure and parameters of the CNN models introduced in this paper for comparison are shown in Table 9.

SVM is a shared supervised learning method suitable for small sample, nonlinear and high-dimensional data. For a given collinear classifiable training dataset, a kernel function is used to map the data from the original feature space to a high-dimensional feature space, so that the linear inner product is nonlinear, and then the classification interval is maximized in the high-dimensional feature space. Optimal hyperplane. Penalty factor C and RBF kernel function parameters are two important parameters in SVM. Penalty factor $C > 0$, the larger C is, the greater the penalty for misclassification, but overfitting is easy; the smaller C is, the less the penalty for misclassification is, the complexity of

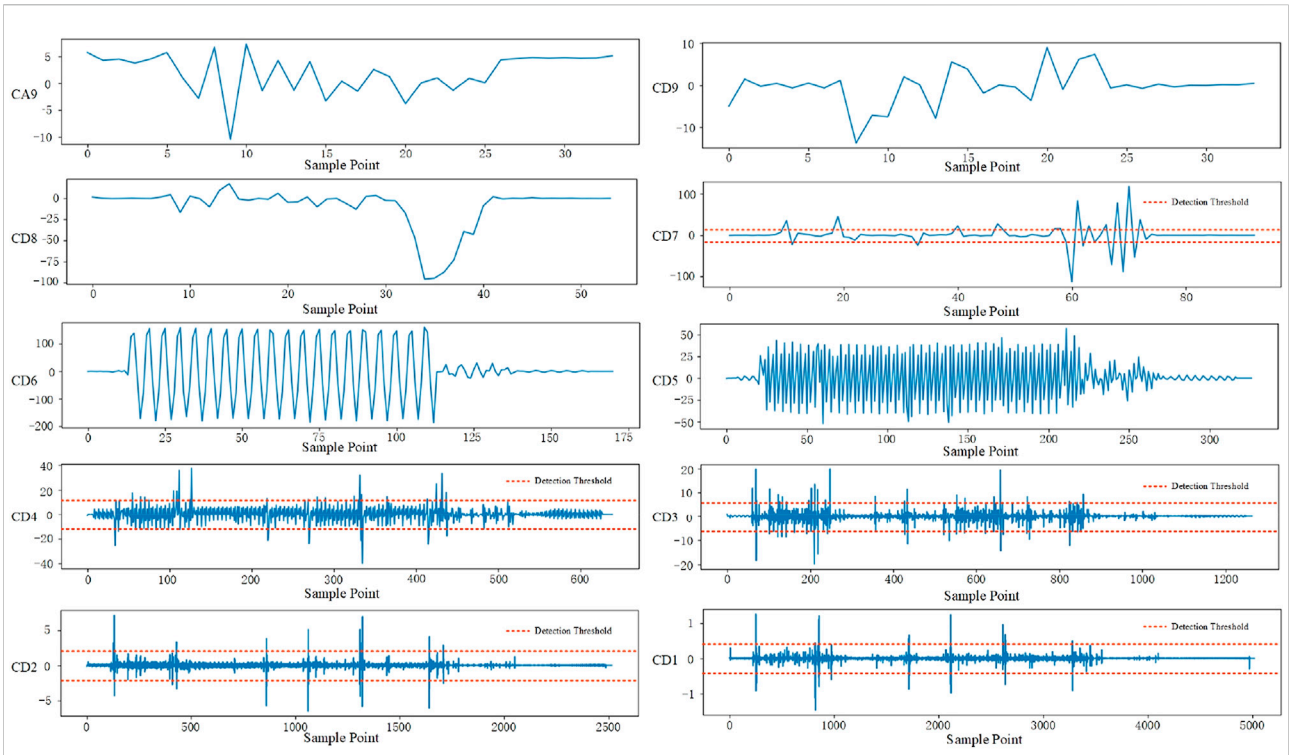

FIGURE 9
Wavelet analysis components of each layer.

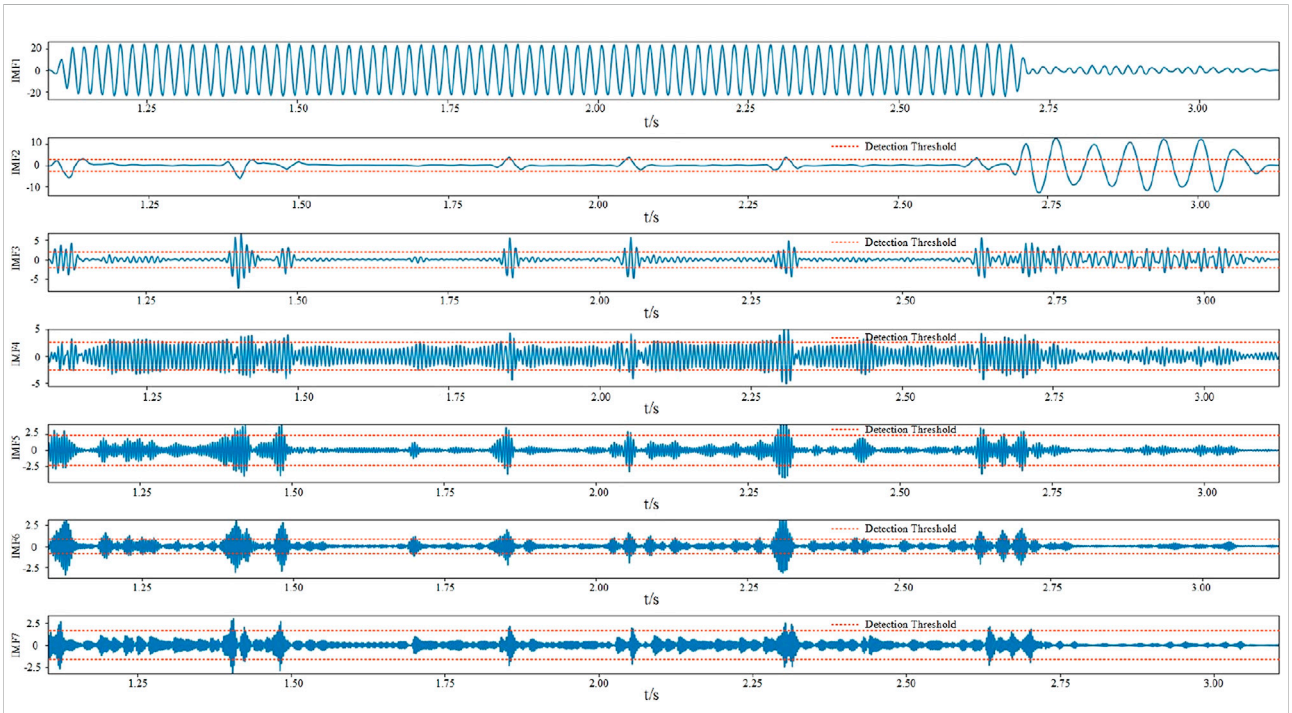

FIGURE 10
Variational modal decomposition of components at each layer.

TABLE 8 Comparison of fault segmentation accuracy of different methods.

Sample number	Actual number of failures (ferromagnetic resonance/arc light/general ground)	Ours	WT	VMD
Sample 1	1/6/5	1/6/5	0/6/1	0/6/5
Sample 2	1/4/3	1/4/3	1/3/2	0/4/3
Sample 3	0/2/1	0/2/1	0/2/1	0/2/1
Sample 4	0/4/3	0/4/3	0/4/1	0/4/3
Sample 5	0/1/1	0/1/1	0/1/1	0/1/1
Segmentation accuracy	—	100%	71.875%	93.75%

TABLE 9 CNN model structure and parameters.

Layers	Structural layer	Parameter
1	Input layer	—
2	Convolutional layer 1	3 × 3,8
3	Pooling layer 1	2 × 2
4	Convolutional layer 2	3 × 3,16
5	Pooling layer 2	2 × 2
6	Fully connected layer	3 nodes
7	Output layer	3 classes

TABLE 10 Identification performance of different algorithm models.

Algorithm model	Recognition accuracy (%)
WT-CNN	93.81
VMD-SVM	94.74
Ours	97.12

the model is reduced, and underfitting is prone to occur. γ determines the distribution of the data mapped to the new feature space. The smaller γ, the more support vectors, the greater the smoothing effect of the model, and the easier it is to underfit; easy to overfit.

For the problem that the arc ground fault sub-sequence cannot be accurately segmented in the methods WT-CNN and VMD-SVM, the fault merging method proposed in this paper is used to determine the fault end point. For ferromagnetic resonance faults, the waveform sub-sequence is manually segmented segmentation. It can be seen from Table 10 that the identification accuracy rates of several algorithms listed in the table are all greater than 90%. The recognition accuracy of the algorithm model proposed in this paper is 97.12%, and the recognition accuracy ratio is 3.31% and 2.38% higher than that of WT-CNN and VMD-SVM, respectively.

5 Conclusion

Aiming at the problems of inaccurate fault detection and redundant feature extraction in traditional detection based on electrical parameters and thresholds, this paper proposes a segmentation-clustering-based arc-ground fault identification method for distribution networks. First, a sliding t-test was used to segment the waveform subsequences, considering the presence of developing faults in the recorder data. Secondly, extract eigenvalues in time domain and frequency domain for the segmented waveform subsequences, and reduce the dimension of the eigenmatrix by using principal component analysis method. Then, cluster analysis is carried out on the characteristic parameter distribution after dimension reduction, and the identification accuracy of the algorithm is verified by using the safety boundary model. Finally, compared with the traditional arc ground fault identification method, the following conclusions are drawn:

(1) Compared with the traditional arc ground fault identification method, the segmentation-clustering algorithm proposed in this paper can more accurately segment the fault. The influence of different types of fault data on waveform characteristic values is reduced.
(2) The combined three-phase voltage and zero-sequence voltage waveform eigenvalue extraction and principal component analysis dimensionality reduction established in this paper reduce the problem of insufficient feature extraction based on traditional electrical parameter analysis, and reduce the redundancy of feature data.
(3) Compared with WT-CNN and VMD-SVM, the identification accuracy of the identification method proposed in this paper is improved by 3.31% and 2.38%, respectively.

Data availability statement

The raw data supporting the conclusion of this article will be made available by the authors, without undue reservation.

Author contributions

GL, MC, and WW provide data and technical support, QL and LC provide research methods and experimental guidance, and YW conduct experimental research.

Funding

This work was supported by China Power Construction Group Jiangxi Electric Power Construction Co., Ltd., Jiangxi Provincial Department of Science and Technology Project "Development of Wind Farm Dynamic Operation and Maintenance System Based on AR Smart Glasses", and national Natural Science Foundation project "Research on Multi-classification and Efficiency Loss Prediction of Photovoltaic Module Defects for Unbalanced Distribution." The funder was not involved in the study design, collection, analysis, interpretation of data, the writing of this article, or the decision to submit it for publication.

Conflict of interest

Authors GL and MC were employed by National Network Jiangxi Electric Power Co. Ltd. Author WW was employed by 3China Power Construction Group Jiangxi Electric Power Construction Co. Ltd.

The remaining authors declare that the research was conducted in the absence of any commercial or financial relationships that could be construed as a potential conflict of interest.

Publisher's note

References

Cai, X., and Wai, R. J. (2022). Intelligent DC arc-fault detection of solar PV power generation system via optimized VMD-based signal processing and PSO–SVM classifier. *IEEE J. Photovolt.* 12 (4), 1058–1077. doi:10.1109/JPHOTOV.2022.3166919

Chen, J., Li, H., Deng, C., and Wang, G. (2021). Detection of single-phase to ground faults in low-resistance grounded MV systems. *IEEE Trans. Power Deliv.* 36 (3), 1499–1508. doi:10.1109/TPWRD.2020.3010165

Dang, H. L., Kwak, S., and Choi, S. (2022). Parallel DC arc failure detecting methods based on artificial intelligent techniques. *IEEE Access* 10, 26058–26067. doi:10.1109/ACCESS.2022.3157298

Du, R., Shang, F., and Ma, N. (2019). Automatic mutation feature identification from well logging curves based on sliding t test algorithm. *Clust. Comput.* 22, 14193–14200. doi:10.1007/s10586-018-2267-z

Du, Y., Liu, Y., Shao, Q., Luo, L., Dai, J., Sheng, G., et al. (2019). Single line-to-ground faulted line detection of distribution systems with resonant grounding based on feature fusion framework. *IEEE Trans. Power Deliv.* 34 (4), 1766–1775. doi:10.1109/tpwrd.2019.2922480

Gadanayak, D., and Mallick, R. (2019). Interharmonics based high impedance fault detection in distribution systems using maximum overlap wavelet packet transform and a modified empirical mode decomposition. *Int. J. Electr. Power & Energy Syst.* 112, 282–293. doi:10.1016/j.ijepes.2019.04.050

Guo, M. F., Yang, N. C., and Chen, W. F. (2019). Deep-Learning-based fault classification using hilbert-huang transform and convolutional neural network in power distribution systems. *IEEE Sens. J.* 19, 6905–6913. doi:10.1109/jsen.2019.2913006

Guo, M. F., Zeng, X. D., Chen, D. Y., and Yang, N. C. (2018). Deep -Learning-Based earth fault detection using continuous wavelet transform and convolutional neural network in resonant grounding distribution systems. *IEEE Sens. J.* 18, 1291–1300. doi:10.1109/jsen.2017.2776238

Kavaskar, S., and Mohanty, N. K. (2019). Detection of high impedance fault in distribution networks. *Ain Shams Eng. J.* 101, 5–13. doi:10.1016/j.asej.2018.04.006

Lin, C., Gao, W., and Guo, M. F. (2019). Discrete wavelet transform-based triggering method for single-phase earth fault in power distribution systems. *IEEE Trans. Power Deliv.* 34 (5), 2058–2068, Oct. doi:10.1109/TPWRD.2019.2913728

Mishra, M, Routray, P., and Rout, P. K. (2016). A universal high impedance fault detection technique for distribution system using S-transform and pattern recognition. *Technol. Econ. Smart Grids Sustain. Energy* 1, 9. doi:10.1007/s40866-016-0011-4

Paul, D. (2015). High -resistance grounded power system. *IEEE Trans. Ind. Appl.* 51, 5261–5269. doi:10.1109/tia.2015.2422825

Peng, N., Ye, K., Liang, R., Hou, T., Wang, G., Chen, X., et al. (2019). Single-Phase-to-Earth faulty feeder detection in power distribution network based on amplitude ratio of zero-mode transients. *IEEE Access* 7, 117678–117691. doi:10.1109/ACCESS.2019.2936420

Qin, X., Wang, P., Liu, Y., Guo, L., Sheng, G., and Jiang, X. (2018). Research on distribution network fault recognition method based on time-frequency characteristics of fault waveforms. *IEEE Access* 6, 7291–7300. doi:10.1109/ACCESS.2017.2728015

Siegel, J. E., Pratt, S., Sun, Y., and Sarma, S. E. (2018). Real-time deep neural networks for internet-enabled arc-fault detection. *Eng. Appl. Artif. Intell.* 74, 35–42. doi:10.1016/j.engappai.2018.05.009

Wang, L., Qiu, H., and Yang, P. (2021). Arc Fault detection algorithm based on variational mode decomposition and improved multi-scale fuzzy entropy. *Energies* 14, 4137. doi:10.3390/en14144137

Wang, Y., Zhou, J., Li, Z., Dong, Z., and Xu, Y. (2015). Discriminant-analysis-based single-phase earth fault protection using improved PCA in distribution systems. *IEEE Trans. Power Deliv.* 30 (4), 1974–1982. doi:10.1109/TPWRD.2015.2408814

Wei, M., Shi, F., Zhang, H., Jin, Z., Bao, H., Zhou, J., et al. (2020). High impedance arc fault detection based on the harmonic randomness and waveform distortion in

the distribution system. *IEEE Trans. Power Deliv.* 35 (2), 837–850. doi:10.1109/TPWRD.2019.2929329

Wei, Z., Mao, Y., Yin, Z., Sun, G., and Zang, H. (2020). fault detection based on the generalized S-transform with a variable factor for resonant grounding distribution networks. *IEEE Access* 8, 91351–91367. doi:10.1109/ACCESS.2020.2994139

Xia, K., He, S., Tan, Y., Jiang, Q., Xu, J., and Yu, W. (2019). Wavelet packet and support vector machine analysis of series DC ARC fault detection in photovoltaic system. *IEEJ Trans. Elec. Electron. Eng.* 14, 192–200. doi:10.1002/tee.22797

Zeng, X., Yu, K., Wang, Y., and Xu, Y. (2016). A novel single phase grounding fault protection scheme without threshold setting for neutral ineffectively earthed power systems. *CSEE J. Power Energy Syst.* 2 (3), 73–81. doi:10.17775/CSEEJPES.2016.00038

Zhang, H., Wang, J., Liu, Z., Han, J., Liu, J., and Zhu, H. "Comparative analysis of ferroresonance and arc high impedance grounding fault in high voltage transmission line," in Proceedings of the 2021 International Conference on Power System Technology (POWERCON), Haikou, China, December 2021, 2331–2335. doi:10.1109/POWERCON53785.2021.9697581

Zhang, L., Wang, Y., Yan, H., and Shi, F. "Single-phase-to-ground fault diagnosis based on waveform feature extraction and matrix analysis," in Proceedings of the 2019 9th International Conference on Power and Energy Systems (ICPES), Perth, Australia, December 2019, 1–6. doi:10.1109/ICPES47639.2019.9105483

frontiers | Frontiers in Energy Research

TYPE Original Research
PUBLISHED 10 January 2023
DOI 10.3389/fenrg.2022.1045809

OPEN ACCESS

EDITED BY
Weiye Zheng,
South China University of Technology, China

REVIEWED BY
Xinran Zhang,
Central Conservatory of Music, China
Zhiyuan Tang,
Sichuan University, China
Xue Lyu,
University of Wisconsin-Madison, United States

*CORRESPONDENCE
Da Xie,
xieda@sjtu.edu.cn

SPECIALTY SECTION
This article was submitted to Smart Grids, a section of the journal Frontiers in Energy Research

RECEIVED 16 September 2022
ACCEPTED 21 October 2022
PUBLISHED 10 January 2023

CITATION
Sun S, Tang C, Hailati G and Xie D (2023), Voltage monitoring based on ANN-aided nonlinear stability analysis for DC microgrids.
Front. Energy Res. 10:1045809.
doi: 10.3389/fenrg.2022.1045809

Voltage monitoring based on ANN-aided nonlinear stability analysis for DC microgrids

Shengxin Sun[1], Chenyu Tang[1], Gulizhati Hailati[2] and Da Xie[1]*

[1]The Key Laboratory of Control of Power Transmission and Conversion, Ministry of Education, The Department of Electrical Engineering, Shanghai Jiao Tong University, Shanghai, China, [2]The Department of Automation, The School of Intelligent Manufacturing and Control Engineering, Shanghai Polytechnic University, Shanghai, China

Due to the low inertia of the DC microgrid, the DC bus voltage is prone to drop or oscillate under disturbance. It is also challenging to supervise the stability of a DC microgrid since it is a highly nonlinear dynamic system with high dimensionality and randomness. To tackle this problem, this paper proposes a new method using ANN-aided nonlinear dynamic stability analysis for monitoring the DC bus voltage, which is combined with two steps. The first step is to establish six corresponding nonlinear accurate discrete iterative models of six switching modes of the PV-battery-load-based DC microgrid system, based on the Poincaré map theory, in order to judge the stability quantitatively with a promoted stability margin index. The second step is to use artificial neural networks (ANNs) to forecast the operating mode of the system when random changes occur in environmental circumstances and load power; this will aid the first step in being efficient and adaptable while determining stability cases. And the employed ANNs are trained with the datasets, including the circuit data, ambient temperature, irradiance, and load power, which are generated by MATLAB/Simulink simulation. Theoretical and simulation analyses are carried out under different operating conditions to validate the proposed method's efficacy in judging the DC microgrid's destabilizing oscillation and stable running.

KEYWORDS

voltage monitoring, nonlinear stability analysis, artificial neural network, poincaré map, DC microgrid

1 Introduction

The DC microgrid emerged due to the integration of DC distributed energy resources (DERs), installation of battery storage systems (BSSs) and growing use of DC loads (Ahmed et al., 2020). In addition, there has been a recent increase in research interest in it, mostly because of its high transmission efficiency and good quality, requiring few power conversion stages and no reactive power (Zolfaghari et al., 2022). However, the DC microgrid utilizes numerous power electronic devices to interface energy sources and consumers, resulting in low inertia, particularly when operated independently of the primary power grid (Holari et al., 2021). This is manifested in variations in the behavior of the microgrid's interface inputs or outputs, such as random intermittent fluctuations in the DERs and rapid changes in power loads, which can result in the DC bus voltage

sagging or oscillating (Lu et al., 2015; Xia et al., 2019). Furthermore, as the scale of the modern DC microgrids continues to expand, the characteristics of high-dimensionality, nonlinearity, and strong coupling have become increasingly apparent (Zia et al., 2019), posing substantial operational security changes. Therefore, it is clear that a practical stability monitor approach that enables real-time monitoring of the microgrid's status and provides the basis for online tuning controller parameters to achieve adequate adaptive control could be valuable (Khodamoradi et al., 2019).

Stability monitoring methods for DC microgrids include linear and nonlinear analysis methods. The linear analysis method (Eberlein and Rudion, 2021) uses the averaged model of linear approximation in the neighbourhood of the equilibrium point to analyze small-signal stability. Nonetheless, the effective range of the linearization region is frequently unclear, and the DC microgrid contains distinct and complex nonlinear features that are largely ignored, causing the stability calculations to be grossly distorted. Thus, nonlinear stability analysis is more appropriate for DC microgrids.

Nonlinear stability analysis is primarily based on nonlinear models, including quadratic or cubic nonlinear models, piecewise linear models, and discrete iterative models. According to the Taylor expansion, quadratic or cubic nonlinear models (Wang et al., 2018) retain partial nonlinear high-order terms at the equilibrium point. Piecewise linear models (Marx et al., 2012) are formed of a finite number of local linear models to approximate the original nonlinear model. Discrete iterative models (Aroudi et al., 2007) are characterized by a finite number of dynamical models corresponding to a set of toggling switching conditions. This is based on the Poincaré map theory of nonlinear dynamics, which is suitable for discontinuous systems in control engineering, such as power electronic circuits. As for a single converter system, the models above can accurately reflect the nonlinear characteristics to varying degrees. Researchers have developed various stability analysis methods such as the numerical simulation method (Seth and Banerjee, 2020), Lyapunov direct method (Toro et al., 2021), Takagi-Sugeno method (Mehran et al., 2009), saltation matrix (Wu et al., 2020), trajectory sensitivities (Geng and Hiskens, 2019), and Jacobian matrix eigenvalue analysis (Wang et al., 2020). However, as the DC microgrids expand, the number of electronic power conversion devices and the systems' scale will increase. Consequently, these approaches may encounter numerous issues, such as extensive computation, slow calculation rates, low conservative analysis results, complex subspace division, difficulty solving the saltation matrix, and difficulty deriving the Jacobian matrix.

Therefore, in light of DC microgrids with complex structures, improved stability analysis methods are proposed according to the Lyapunov theory in (Zhang et al., 2022) and (Xie et al., 2021) for various DC microgrids. However, the offered solutions are limited to specific equivalent models, challenging generalization to other systems. Moreover, References (Ahmadi and Kazemi, 2020) and (Xia et al., 2020) present a nonlinear analysis framework applicable to other DC microgrids. Nevertheless, the modeling process is cumbersome and requires manual screening of features to reduce order, which makes it difficult to achieve flexible and accurate system monitoring. To address this issue, data-driven methods utilizing artificial intelligence technology are being developed, which primarily aim to classify prediction models or fit stable regions in various scenarios. Decision trees (Vanfretti and Narasimham Arava, 2020), support vector (Gomez et al., 2011), deep learning (Tian et al., 2022), and artificial neural network (ANN) (Tan et al., 2019) are relevant techniques. In references (Gomez et al., 2011; Tan et al., 2019; Vanfretti and Narasimham Arava, 2020; Tian et al., 2022), classical stability analysis methods are combined with intelligent technologies to achieve intelligent stability monitoring *via* offline training and online testing using massive datasets. Existing research focuses mostly on the traditional power system, and the intelligent stability monitoring approaches to DC microgrids are relatively rare.

To monitor the performance of DC microgrids, an intelligent nonlinear stability monitoring tool is urgently required. Poincaré map is a conventional and effective stability analysis theory in nonlinear dynamics (Tse and Di Bernardo, 2002; Moreno-Font et al., 2009). However, as the number of power electronic switches in the system increases, the iterative mapping order becomes difficult to determine, which makes it challenging to construct discrete iterative models and estimate stability calculations. Consequently, driven by the intelligent background, this paper proposes a voltage monitoring method using the Poincaré map combined with an artificial neural network for the PV-battery-load-based DC microgrid. The neural network predicts the operation mode, which facilitates discrete iterative modeling and Jacobian matrix calculation under varying input and output conditions. Thus, a stability margin is provided to quantify the operational performance. A typical case study is utilized to validate conclusions.

The remainder of this paper is structured as follows: Section 2 describes the structure and discrete iterative model of the DC microgrid; Section 3 presents the ANN-aided nonlinear voltage stability monitor method; Section 4 validates the proposed approach in numerical simulations of real scenes; Section 5 reports the conclusions of this paper.

2 Structure and modeling of the DC microgrid

2.1 Structure of the DC microgrid

Figure 1 depicts the structure of the conventional PV-battery-load-based DC microgrid understudied, which comprises a PV distributed generator (PVDG), a battery storage system (BSS),

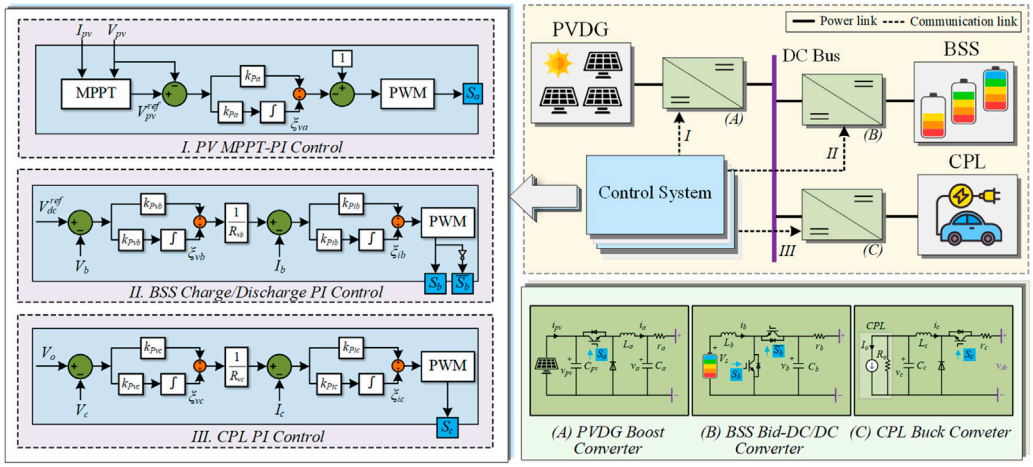

FIGURE 1
Structure of the PV-battery-load-based DC microgrid system.

and a constant power load (CPL). The PVDG is linked to the DC bus with its boost converter. And the BSS is also connected to the same DC bus through a bidirectional dc/dc converter. As to the CPL, its equivalent model (Rahimi and Emadi, 2009) is linked to the DC bus with a buck converter. The model represents a real system to some extent. A control system contains the corresponding cascaded-PI reference voltage-current control for each device, which controls corresponding switches to ensure the uninterrupted power flow. And we refer to the cascaded-PI reference voltage-current control as the PI control for short. Particularly, the PVDG side has a maximum power point tracking (MPPT) controller and a PI controller, which can ensure the PV arrays operate at the maximum power point in any weather condition. The PI controller of BSS adjusts the operational status of the bidirectional DC/DC converter to keep the BSS charge/discharge working in a predefined state of the charge band and simultaneously maintain the DC bus voltage stable. This article assumes that the battery state can always meet the working conditions. The PI controller of CPL ensures that loads of different powers can work in the corresponding rated state.

2.2 Modeling of the DC microgrid

2.2.1 State equations

In nonlinear dynamics, the DC microgrid is considered a discontinuous piecewise affine system whose structure is altered when certain conditions change. The state space of the system model is divided into a finite number of non-smooth continuous subspaces, where the system model differs according to the subspace. In the power electronic switch control system, the partition of the subspace corresponds to the control law of the state change of the switch. In the following discussion, it is assumed that PVDG, BSS, and CPL remain in operation. To simplify the calculation and algorithm, the corresponding boost, buck, and bidirectional DC/DC converters of PVDG, BSS, and CPL devices are set to have the same switching frequency, and the start and end of a switching cycle are the same. Figure 2 depicts the switching timing diagrams of the three converters. Specifically, S_m =1 (m = a, b, c) presidents that the power switch is turned ON, and S_m = 0 presidents that it is turned OFF, where the subscript "m" is utilized to represent the variable associated with corresponding devices of the DC microgrid system, i.e. for the PVDC device (a), the BSS device (c), the CPL device (c). Therefore, the stable operation modes are classified into six types, including *M1*, *M2*, *M3*, *M4*, *M5*, *M6*, based on the six different switching sequences of the three switches. In Figure 2, t_0, t_1, t_2, t_3, and t_4 are the switching instants when the switch is flipped. Moreover, the system structure and its corresponding state equation change 4 times when the four switch conditions toggle in turn during one period for each operation mode.

According to the four switch conditions toggling, the piecewise state equations for each operation mode in one period are as follows:

$$\dot{\boldsymbol{x}} = \begin{cases} \boldsymbol{A}_1\boldsymbol{x} + \boldsymbol{B}_1, t_0 \le t < t_1 \\ \boldsymbol{A}_2\boldsymbol{x} + \boldsymbol{B}_2, t_1 \le t < t_2 \\ \boldsymbol{A}_3\boldsymbol{x} + \boldsymbol{B}_3, t_2 \le t < t_3 \\ \boldsymbol{A}_4\boldsymbol{x} + \boldsymbol{B}_4, t_3 \le t < t_4 \end{cases} \tag{1}$$

where, $\boldsymbol{x} = [\boldsymbol{x}_{pv}, \boldsymbol{x}_{bss}, \boldsymbol{x}_{cpl}]^T$ is the state variable vector for the PV-battery-load-based DC microgrid system, which consists of the PVDG state vector $\boldsymbol{x}_{pv} = [v_{pv}, i_a, v_a, \xi_{va}]^T$, the BSS state vector $\boldsymbol{x}_{bss} = [i_b, v_b, \xi_{vb}, \xi_{ib}]^T$, and the CPL state vector $\boldsymbol{x}_{cpl} = [i_c, v_c, \xi_{vc}, \xi_{ic}]^T$. Concretely, v_{pv} is the output voltage of the PV arrays, i_m and v_m (m = a, b, c) are the current of the inductance L_m and the voltage of the capacitance C_m in the corresponding converter, and ξ_{vm} and ξ_{im} are the integrated outputs of the PI voltage and current loops, respectively, as shown in Figure 1. $\boldsymbol{A}_1$, $\boldsymbol{B}_1$, $\boldsymbol{A}_2$, $\boldsymbol{B}_2$, $\boldsymbol{A}_3$, $\boldsymbol{B}_3$, $\boldsymbol{A}_4$, and

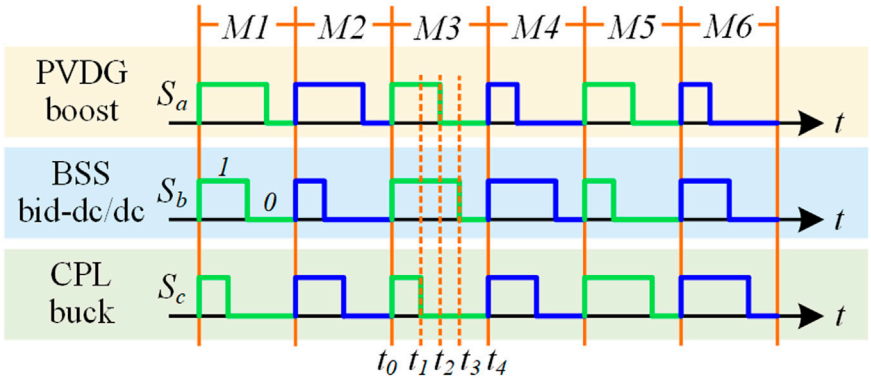

FIGURE 2
Switching sequence diagrams and six stable operation modes.

TABLE 1 State matrices of six operation modes.

	M1	*M2*	*M3*	*M4*	*M5*	*M6*
$\boldsymbol{A}_1$	$\boldsymbol{A}_{a1} \oplus \boldsymbol{A}_{b1} \oplus \boldsymbol{A}_{c1}$					
$\boldsymbol{B}_1$	$\boldsymbol{B}_{a1} \oplus \boldsymbol{B}_{b1} \oplus \boldsymbol{B}_{c1}$					
$\boldsymbol{A}_2$	$\boldsymbol{A}_{a1} \oplus \boldsymbol{A}_{b1} \oplus \boldsymbol{A}_{c2}$	$\boldsymbol{A}_{a1} \oplus \boldsymbol{A}_{b2} \oplus \boldsymbol{A}_{c1}$	$\boldsymbol{A}_{a1} \oplus \boldsymbol{A}_{b1} \oplus \boldsymbol{A}_{c2}$	$\boldsymbol{A}_{a2} \oplus \boldsymbol{A}_{b1} \oplus \boldsymbol{A}_{c1}$	$\boldsymbol{A}_{a1} \oplus \boldsymbol{A}_{b2} \oplus \boldsymbol{A}_{c1}$	$\boldsymbol{A}_{a2} \oplus \boldsymbol{A}_{b1} \oplus \boldsymbol{A}_{c1}$
$\boldsymbol{B}_2$	$\boldsymbol{B}_{a1} \oplus \boldsymbol{B}_{b1} \oplus \boldsymbol{B}_{c2}$	$\boldsymbol{B}_{a1} \oplus \boldsymbol{B}_{b2} \oplus \boldsymbol{B}_{c1}$	$\boldsymbol{B}_{a1} \oplus \boldsymbol{B}_{b1} \oplus \boldsymbol{B}_{c2}$	$\boldsymbol{B}_{a2} \oplus \boldsymbol{B}_{b1} \oplus \boldsymbol{B}_{c1}$	$\boldsymbol{B}_{a1} \oplus \boldsymbol{B}_{b2} \oplus \boldsymbol{B}_{c1}$	$\boldsymbol{B}_{a2} \oplus \boldsymbol{B}_{b1} \oplus \boldsymbol{B}_{c1}$
$\boldsymbol{A}_3$	$\boldsymbol{A}_{a1} \oplus \boldsymbol{A}_{b2} \oplus \boldsymbol{A}_{c2}$	$\boldsymbol{A}_{a1} \oplus \boldsymbol{A}_{b2} \oplus \boldsymbol{A}_{c2}$	$\boldsymbol{A}_{a2} \oplus \boldsymbol{A}_{b1} \oplus \boldsymbol{A}_{c2}$	$\boldsymbol{A}_{a2} \oplus \boldsymbol{A}_{b1} \oplus \boldsymbol{A}_{c2}$	$\boldsymbol{A}_{a2} \oplus \boldsymbol{A}_{b2} \oplus \boldsymbol{A}_{c1}$	$\boldsymbol{A}_{a2} \oplus \boldsymbol{A}_{b2} \oplus \boldsymbol{A}_{c1}$
$\boldsymbol{B}_3$	$\boldsymbol{B}_{a1} \oplus \boldsymbol{B}_{b2} \oplus \boldsymbol{B}_{c2}$	$\boldsymbol{B}_{a1} \oplus \boldsymbol{B}_{b2} \oplus \boldsymbol{B}_{c2}$	$\boldsymbol{B}_{a2} \oplus \boldsymbol{B}_{b1} \oplus \boldsymbol{B}_{c2}$	$\boldsymbol{B}_{a2} \oplus \boldsymbol{B}_{b1} \oplus \boldsymbol{B}_{c2}$	$\boldsymbol{B}_{a2} \oplus \boldsymbol{B}_{b2} \oplus \boldsymbol{B}_{c1}$	$\boldsymbol{B}_{a2} \oplus \boldsymbol{B}_{b2} \oplus \boldsymbol{B}_{c1}$
$\boldsymbol{A}_4$	$\boldsymbol{A}_{a2} \oplus \boldsymbol{A}_{b2} \oplus \boldsymbol{A}_{c2}$					
$\boldsymbol{B}_4$	$\boldsymbol{B}_{a2} \oplus \boldsymbol{B}_{b2} \oplus \boldsymbol{B}_{c2}$					

$\boldsymbol{B}_4$ are state matrices, changing with the operation mode varying, and their detailed descriptions of six operation modes are given in Table 1.

In Table 1, $\boldsymbol{A}_{m1}$, $\boldsymbol{B}_{m1}$, $\boldsymbol{A}_{m2}$, and $\boldsymbol{B}_{m2}$ ($m = a, b, c$) are the state matrices for PVDG, BSS, and CPL devices. Concretely, $\boldsymbol{A}_{m1}$ and $\boldsymbol{B}_{m1}$ correspond to the power switch on with S_m =1, and $\boldsymbol{A}_{m2}$ and $\boldsymbol{B}_{m2}$ correspond to the power switch off with $S_m = 0$. And they are expressed as follows:

$$\boldsymbol{A}_{a1} = \begin{bmatrix} 0 & -1/C_{pv} & 0 & 0 \\ 1/L_a & 0 & -1/L_a & 0 \\ 0 & 1/C_a & -1/C_a r_a & 0 \\ -k_{1va} & 0 & 0 & 0 \end{bmatrix} \quad \boldsymbol{A}_{a2} = \begin{bmatrix} 0 & 0 & 0 & 0 \\ 0 & 0 & -1/L_a & 0 \\ 0 & 1/C_a & -1/C_a r_a & 0 \\ -k_{1va} & 0 & 0 & 0 \end{bmatrix} \quad \boldsymbol{B}_{a1} = \boldsymbol{B}_{a2} = \left[\frac{i_{pv}}{C_{pv}}, 0, \frac{v_{dc}}{C_a r_a}, k_{1va} v_{pv}^{ref}\right]^T$$

$$\boldsymbol{A}_{b1} = \begin{bmatrix} 0 & 0 & 0 & 0 \\ 0 & -1/C_b r_b & 0 & 0 \\ 0 & -k_{1vb} & 0 & 0 \\ -k_{1ib} & \frac{-k_{pvb} k_{1ib}}{R_{vb}} & \frac{-k_{1ib}}{R_{vb}} & 0 \end{bmatrix} \quad \boldsymbol{A}_{b2} = \begin{bmatrix} 0 & -1/L_b & 0 & 0 \\ 1/C_b & -1/C_b r_b & 0 & 0 \\ 0 & -k_{1vb} & 0 & 0 \\ -k_{1ib} & \frac{-k_{pvb} k_{1ib}}{R_{vb}} & \frac{-k_{1ib}}{R_{vb}} & 0 \end{bmatrix} \quad \boldsymbol{B}_{b1} = \boldsymbol{B}_{b2} = \left[\frac{V_s}{L_b}, \frac{v_{dc}}{C_b}, k_{1vb} v_{dc}^{ref}, \frac{k_{pvb} k_{1vb} v_{dc}^{ref}}{R_{vb}}\right]^T$$

$$\boldsymbol{A}_{c1} = \begin{bmatrix} -r_c/L_c & -1/L_c & 0 & 0 \\ 1/C_c & P_c/C_b V_o^2 & 0 & 0 \\ 0 & -k_{1vc} & 0 & 0 \\ -k_{1ic} & \frac{-k_{pvc} k_{1ic}}{R_{vc}} & \frac{-k_{1ic}}{R_{vc}} & 0 \end{bmatrix} \quad \boldsymbol{A}_{c2} = \begin{bmatrix} 0 & -1/L_c & 0 & 0 \\ 1/C_c & P_c/C_b V_o^2 & 0 & 0 \\ 0 & -k_{1vc} & 0 & 0 \\ -k_{1ic} & \frac{-k_{pvc} k_{1ic}}{R_{vc}} & \frac{-k_{1ic}}{R_{vc}} & 0 \end{bmatrix} \quad \boldsymbol{B}_{c1} = \left[\frac{v_{dc}}{L}, -\frac{2P_c}{V_o C_o}, k_{1vc} V_o, \frac{k_{pvc} k_{1vc} V_o}{R_{vc}}\right]^T$$

$$\boldsymbol{B}_{c2} = \left[0, -\frac{2P_c}{V_o C_o}, k_{1vc} V_o, \frac{k_{pvc} k_{1vc} V_o}{R_{vc}}\right]^T$$

Where, k_{Pvm}, k_{Ivm}, k_{Pim}, k_{Iim}, R_{vm} ($m = a, b, c$) are proportional, integral, damping coefficients of corresponding PI controllers, r_m is the line resistance between the equipment and the DC bus, V_s is the output voltage of the batteries, P_c and V_o are the output voltage and power at the operating point of the CPL, and V *ref dc* is the reference voltage of the DC bus, as shown in Figure 1.

It should be mentioned that while the matrices $\boldsymbol{A}_1$, $\boldsymbol{B}_1$, $\boldsymbol{A}_2$, $\boldsymbol{B}_2$, $\boldsymbol{A}_3$, $\boldsymbol{B}_3$, $\boldsymbol{A}_4$ and $\boldsymbol{B}_4$ are direct sums of $\boldsymbol{A}_{m1}$, $\boldsymbol{B}_{m1}$, $\boldsymbol{A}_{m2}$, and $\boldsymbol{B}_{m2}$, there remains still some coupling between the state equations of the individual devices linked together with the DC bus.

2.2.2 Discrete iterative model

In the nth switching cycle, let the initial conditions of state variables at the beginnings of the nth and (n+1)th switching cycle be marked as $\boldsymbol{x}_n$ and $\boldsymbol{x}_{n+1}$. Based on the Poincaré map (Aroudi et al., 2007), during one period, local maps $\mathbf{P}_k$ (k = 1, 2, 3, 4) can be defined as the following forms:

$$\begin{aligned} &\mathbf{P}_1: \boldsymbol{x}_n \rightarrow \boldsymbol{x}_{n+\tau_1}: = \boldsymbol{\varphi}_1(\tau_1, \boldsymbol{x}_n) \\ &\mathbf{P}_2: \boldsymbol{x}_{n+\tau_1} \rightarrow \boldsymbol{x}_{n+\tau_1+\tau_2}: = \boldsymbol{\varphi}_2(\tau_2, \boldsymbol{x}_{n+\tau_1}) \\ &\mathbf{P}_3: \boldsymbol{x}_{n+\tau_1+\tau_2} \rightarrow \boldsymbol{x}_{n+\tau_1+\tau_2+\tau_3}: = \boldsymbol{\varphi}_3(\tau_3, \boldsymbol{x}_{n+\tau_1+\tau_2}) \\ &\mathbf{P}_4: \boldsymbol{x}_{n+\tau_1+\tau_2+\tau_3} \rightarrow \boldsymbol{x}_{n+1}: = \boldsymbol{\varphi}_4(\tau_4, \boldsymbol{x}_{n+\tau_1+\tau_2+\tau_3}) \end{aligned} \tag{2}$$

where $\boldsymbol{x}_{n+\tau_1}$, $\boldsymbol{x}_{n+\tau_1+\tau_2}$, and $\boldsymbol{x}_{n+\tau_1+\tau_2+\tau_3}$ represent the ending state of the corresponding switch condition, or the initial state of the next condition, $\tau_k = t_k - t_{k-1}$ (k = 1, 2, 3, 4)is the duration of one corresponding switch condition, and $\boldsymbol{\varphi}_k$ is the state transition vector function given as:

$$\begin{aligned}
\boldsymbol{\varphi}_1(\tau_1, \boldsymbol{x}_n) &= \boldsymbol{\phi}_1(\tau_1)\boldsymbol{x}_n + \boldsymbol{\psi}_1(\tau_1) \\
\boldsymbol{\varphi}_2(\tau_2, \boldsymbol{x}_{n+\tau_1}) &= \boldsymbol{\phi}_2(\tau_2)\boldsymbol{x}_{n+\tau_1} + \boldsymbol{\psi}_2(\tau_2) \\
\boldsymbol{\varphi}_3(\tau_3, \boldsymbol{x}_{n+\tau_1+\tau_2}) &= \boldsymbol{\phi}_3(\tau_3)\boldsymbol{x}_{n+\tau_1+\tau_2} + \boldsymbol{\psi}_3(\tau_3) \\
\boldsymbol{\varphi}_4(\tau_4, \boldsymbol{x}_{n+\tau_1+\tau_2+\tau_3}) &= \boldsymbol{\phi}_4(\tau_4)\boldsymbol{x}_{n+\tau_1+\tau_2+\tau_3} + \boldsymbol{\psi}_4(\tau_4)
\end{aligned} \tag{3}$$

where $\boldsymbol{\phi}_k(\tau_k) = e^{\boldsymbol{A}_k\tau_k}$ and $\boldsymbol{\psi}_k(\tau_k) = \int_0^t e^{\boldsymbol{A}_k\tau_k} d\tau_k \boldsymbol{B}_k$. It should be noted that if matrix $\boldsymbol{A}_k$ is invertible, the matrix function $\boldsymbol{\psi}_k(\tau_k) = \boldsymbol{A}_k^{-1}(e^{\boldsymbol{A}_k\tau_k} - \boldsymbol{I})\boldsymbol{B}_k$, where $\boldsymbol{I}$ denote the identity matrix. In the case of a singular $\boldsymbol{A}_k$, $\boldsymbol{\psi}_k(\tau_k)$ is expressed as follows:

$$\boldsymbol{\psi}_k(\tau_k) = \left(\boldsymbol{I}\tau_k + \frac{\boldsymbol{A}_k\tau_k^2}{2} + \frac{\boldsymbol{A}_k^2\tau_k^3}{6} + \cdots\right)\boldsymbol{B}_k$$

The global Poincaré map $\mathbf{P}$ from the nth to (n+1)th switching cycle, can be defined as a composition of four different local maps $\mathbf{P}_k$:

$$\mathbf{P} = \mathbf{P}_4 \circ \mathbf{P}_3 \circ \mathbf{P}_2 \circ \mathbf{P}_1 \tag{4}$$

where the mathematical symbol "$\circ$" represents a composite map of two maps, its order is immutable, i.e., $\mathbf{P}_2 \circ \mathbf{P}_1 = \mathbf{P}_2(\mathbf{P}_1)$ is different from $\mathbf{P}_1 \circ \mathbf{P}_2 = \mathbf{P}_1(\mathbf{P}_2)$.

Therefore, the discrete iterative map from $\boldsymbol{x}_n$ to $\boldsymbol{x}_{n+1}$ during one period is described as follows:

$$\begin{aligned}
\boldsymbol{x}_{n+1} &= \boldsymbol{\varphi}_4(\tau_4, \boldsymbol{\varphi}_3(\tau_3, \boldsymbol{\varphi}_2(\tau_2, \boldsymbol{\varphi}_1(\tau_1, \boldsymbol{x}_n)))) \\
&= \boldsymbol{\Phi}(\tau)\boldsymbol{x}_n + \boldsymbol{\Psi}(\tau)
\end{aligned} \tag{5}$$

where

$$\begin{aligned}
\boldsymbol{\Phi}(\tau) &= \boldsymbol{\phi}_4(\tau_4)\boldsymbol{\phi}_3(\tau_3)\boldsymbol{\phi}_2(\tau_2)\boldsymbol{\phi}_1(\tau_1) \\
\boldsymbol{\Psi}(\tau) &= \boldsymbol{\phi}_4(\tau_4)\boldsymbol{\phi}_3(\tau_3)\boldsymbol{\phi}_2(\tau_2)\boldsymbol{\psi}_1(\tau_1) + \boldsymbol{\phi}_4(\tau_4)\boldsymbol{\phi}_3(\tau_3)\boldsymbol{\psi}_2(\tau_2) \\
&\quad + \boldsymbol{\phi}_4(\tau_4)\boldsymbol{\psi}_3(\tau_3) + \boldsymbol{\psi}_4(\tau_4)
\end{aligned}$$

3 ANN-aided nonlinear voltage stability monitor method

3.1 Principle of nonlinear analysis

Based on the Poincaré map theory, observing the position of the eigenvalues of Jacobian matrix $\boldsymbol{J}_P$ at fixed point $\boldsymbol{x}^*$ in relation to the unit circle can be used to determine the nonlinear dynamic behaviour of the DC microgrid system. In addition, the eigenvalues can be determined from the eigenequation at the fixed-point $\boldsymbol{x}^*$, which consists of the following:

$$\det(\boldsymbol{J}_P - \lambda\boldsymbol{I})|_{\boldsymbol{x}=\boldsymbol{x}^*} = 0 \tag{6}$$

where λ is the eigenvalue of $\boldsymbol{J}_P$, and if all eigenvalues have a modulus length less than 1, the system is stable; otherwise, the system is unstable.

The Jacobian matrix $\boldsymbol{J}_P$ is expressed as (Wang et al., 2020):

$$\boldsymbol{J}_P = \boldsymbol{\Phi}(\tau) - \frac{\partial\mathbf{P}}{\partial t}\left(\frac{\partial\boldsymbol{\sigma}}{\partial t}\right)^{-1}\left(\frac{\partial\boldsymbol{\sigma}}{\partial\boldsymbol{x}_n}\right) \tag{7}$$

where

$$\boldsymbol{\sigma}(\tau, \boldsymbol{x}_n) = \begin{bmatrix}
\boldsymbol{K}_1\left(\boldsymbol{x}_{ref} - \mathbf{P}_1(\boldsymbol{x}^*, t_1^*)\right) - h(t) \\
\boldsymbol{K}_2\left(\boldsymbol{x}_{ref} - \mathbf{P}_2 \circ \mathbf{P}_1(\boldsymbol{x}^*, t_1^*, t_2^*)\right) - h(t) \\
\boldsymbol{K}_3\left(\boldsymbol{x}_{ref} - \mathbf{P}_3 \circ \mathbf{P}_2 \circ \mathbf{P}_1(\boldsymbol{x}^*, t_1^*, t_2^*, t_3^*)\right) - h(t)
\end{bmatrix} \tag{8}$$

where $\boldsymbol{x}_{ref} = [V_{pv}^{ref}, 0, 0, 1, 0, V_{dc}^{ref}, 0, 0, 0, V_o]^T$ is the reference vector, where V_{pv}^{ref} is the output of MPPT controller, also the reference input voltage of subsequent PI controller, and V_{dv}^{ref} is the reference voltage of the DC bus, as shown in Figure 1 $h(t) = S_L + (S_U - S_L)$ (t mod T)/T is T-period sawtooth signal of time that are used to generate PWM switching trigger signals, S_U and S_L are the high and low levels of the sawtooth signal respectively, and T is the switching period. $\boldsymbol{K}_1$, $\boldsymbol{K}_2$, and $\boldsymbol{K}_3$ are the control parameter column vectors that are the direct sum of one of $\boldsymbol{K}_a = [-k_{pva}, 0, 0, 1]$, $\boldsymbol{K}_b = [k_{Pib}, k_{Pib}k_{Pvb}/R_{vb}, -k_{Pib}/R_{vb}, -1]$, or $\boldsymbol{K}_c = [k_{Pic}, k_{Pib}k_{Pvc}/R_{vc}, -k_{Pic}/R_{vc}, -1]$ with two zero vector $\boldsymbol{0}_{1\times4}$, depending on which mode the system is operating in, i.e.,

M1: $\boldsymbol{K}_1 = \boldsymbol{0}_{1\times4} \oplus \boldsymbol{0}_{1\times4} \oplus \boldsymbol{K}_c$, $\boldsymbol{K}_2 = \boldsymbol{0}_{1\times4} \oplus \boldsymbol{K}_b \oplus \boldsymbol{0}_{1\times4}$, $\boldsymbol{K}_3 = \boldsymbol{K}_a \oplus \boldsymbol{0}_{1\times4} \oplus \boldsymbol{0}_{1\times4}$;

M2: $\boldsymbol{K}_1 = \boldsymbol{0}_{1\times4} \oplus \boldsymbol{K}_b \oplus \boldsymbol{0}_{1\times4}$, $\boldsymbol{K}_2 = \boldsymbol{0}_{1\times4} \oplus \boldsymbol{0}_{1\times4} \oplus \boldsymbol{K}_c$, $\boldsymbol{K}_3 = \boldsymbol{K}_a \oplus \boldsymbol{0}_{1\times4} \oplus \boldsymbol{0}_{1\times4}$;

M3: $\boldsymbol{K}_1 = \boldsymbol{0}_{1\times4} \oplus \boldsymbol{0}_{1\times4} \oplus \boldsymbol{K}_c$, $\boldsymbol{K}_2 = \boldsymbol{K}_a \oplus \boldsymbol{0}_{1\times4} \oplus \boldsymbol{0}_{1\times4}$, $\boldsymbol{K}_3 = \boldsymbol{0}_{1\times4} \oplus \boldsymbol{K}_b \oplus \boldsymbol{0}_{1\times4}$;

M4: $\boldsymbol{K}_1 = \boldsymbol{K}_a \oplus \boldsymbol{0}_{1\times4} \oplus \boldsymbol{0}_{1\times4}$, $\boldsymbol{K}_2 = \boldsymbol{0}_{1\times4} \oplus \boldsymbol{0}_{1\times4} \oplus \boldsymbol{K}_c$, $\boldsymbol{K}_3 = \boldsymbol{0}_{1\times4} \oplus \boldsymbol{K}_b \oplus \boldsymbol{0}_{1\times4}$;

M5: $\boldsymbol{K}_1 = \boldsymbol{0}_{1\times4} \oplus \boldsymbol{K}_b \oplus \boldsymbol{0}_{1\times4}$, $\boldsymbol{K}_2 = \boldsymbol{K}_a \oplus \boldsymbol{0}_{1\times4} \oplus \boldsymbol{0}_{1\times4}$, $\boldsymbol{K}_3 = \boldsymbol{0}_{1\times4} \oplus \boldsymbol{0}_{1\times4} \oplus \boldsymbol{K}_c$;

M6: $\boldsymbol{K}_1 = \boldsymbol{K}_a \oplus \boldsymbol{0}_{1\times4} \oplus \boldsymbol{0}_{1\times4}$, $\boldsymbol{K}_2 = \boldsymbol{0}_{1\times4} \oplus \boldsymbol{K}_b \oplus \boldsymbol{0}_{1\times4}$, $\boldsymbol{K}_3 = \boldsymbol{0}_{1\times4} \oplus \boldsymbol{0}_{1\times4} \oplus \boldsymbol{K}_c$.

In combination with 5 and 7, there are:

$$\frac{\partial\boldsymbol{\sigma}}{\partial\boldsymbol{x}_n} = \begin{bmatrix}
-\boldsymbol{K}_1\boldsymbol{\phi}_1(\tau_1) \\
-\boldsymbol{K}_2\boldsymbol{\phi}_2(\tau_2)\boldsymbol{\phi}_1(\tau_1) \\
-\boldsymbol{K}_3\boldsymbol{\phi}_3(\tau_3)\boldsymbol{\phi}_2(\tau_2)\boldsymbol{\phi}_1(\tau_1)
\end{bmatrix} \tag{9}$$

$$\frac{\partial\boldsymbol{\sigma}}{\partial t} = \begin{bmatrix}
-\boldsymbol{K}_1\dot{\boldsymbol{x}}_1^- - \dot{h}_1(t_1) & 0 & 0 \\
-\boldsymbol{K}_2\boldsymbol{\phi}_2(\tau_2)\Delta\dot{\boldsymbol{x}}_1 & -\boldsymbol{K}_2\dot{\boldsymbol{x}}_2^- - \dot{h}_2(t_2) & 0 \\
-\boldsymbol{K}_3\boldsymbol{\phi}_3(\tau_3)\boldsymbol{\phi}_2(\tau_2)\Delta\dot{\boldsymbol{x}}_1 & -\boldsymbol{K}_3\boldsymbol{\phi}_3(\tau_3)\Delta\dot{\boldsymbol{x}}_2 & -\boldsymbol{K}_3\dot{\boldsymbol{x}}_3^- - \dot{h}_3(t_3)
\end{bmatrix} \tag{10}$$

$$\frac{\partial\mathbf{P}}{\partial t} = \begin{bmatrix} \boldsymbol{\phi}_3(\tau_3)\boldsymbol{\phi}_2(\tau_2)\Delta\dot{\boldsymbol{x}}_1 & \boldsymbol{\phi}_3(\tau_3)\Delta\dot{\boldsymbol{x}}_2 & \dot{\boldsymbol{x}}_3^- \end{bmatrix} \tag{11}$$

where

$$\begin{cases} \Delta\dot{\boldsymbol{x}}_1 = \dot{\boldsymbol{x}}_1^- - \dot{\boldsymbol{x}}_1^+ \\ \dot{\boldsymbol{x}}_1^- = \boldsymbol{A}_1\mathbf{P}_1(\boldsymbol{x}^*) + \boldsymbol{B}_1 \\ \dot{\boldsymbol{x}}_1^+ = \boldsymbol{A}_2\mathbf{P}_2(\boldsymbol{x}^*) + \boldsymbol{B}_2 \end{cases}, \begin{cases} \Delta\dot{\boldsymbol{x}}_2 = \dot{\boldsymbol{x}}_2^- - \dot{\boldsymbol{x}}_2^+ \\ \dot{\boldsymbol{x}}_2^- = \boldsymbol{A}_2\mathbf{P}_2 \circ \mathbf{P}_1(\boldsymbol{x}^*) + \boldsymbol{B}_2 \\ \dot{\boldsymbol{x}}_2^+ = \boldsymbol{A}_3\mathbf{P}_2 \circ \mathbf{P}_1(\boldsymbol{x}^*) + \boldsymbol{B}_3 \end{cases},$$

$$\dot{\boldsymbol{x}}_3^- = \boldsymbol{A}_3\mathbf{P}_3 \circ \mathbf{P}_2 \circ \mathbf{P}_1(\boldsymbol{x}^*) + \boldsymbol{B}_3, \ \dot{\boldsymbol{x}}_3^+ = \boldsymbol{A}_1\mathbf{P}_3 \circ \mathbf{P}_2 \circ \mathbf{P}_1(\boldsymbol{x}^*) + \boldsymbol{B}_1$$

Furthermore, the eigenvalue modulo length obtained from Eqn 6 can be used to reflect the system's operating conditions and

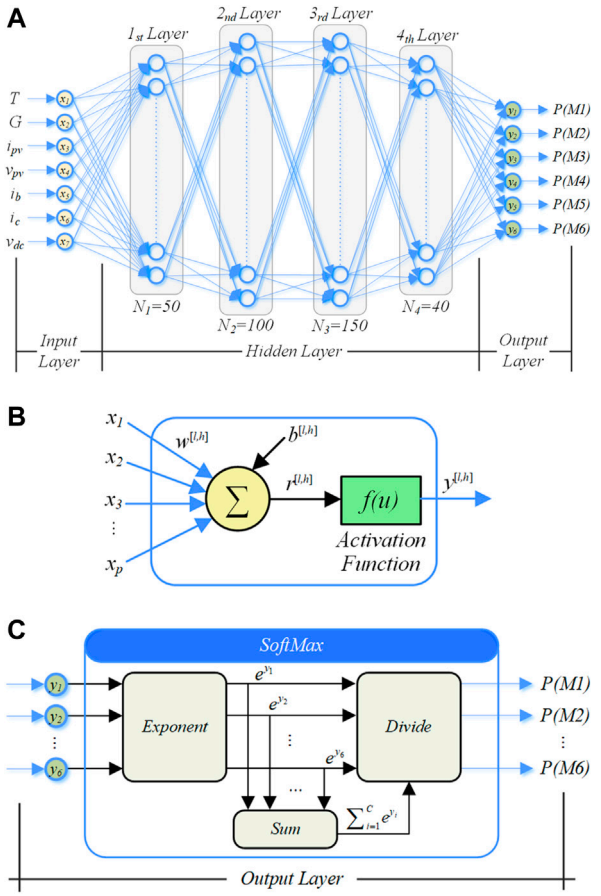

FIGURE 3
The structure of the designed ANNs. **(A)** The detailed structural information of the neural network. **(B)** The neural node structure. **(C)** The structure of *SoftMax* in the output layer.

stability margins. Here, the proposed stability margin ε is defined as:

$$\varepsilon = 1 - |\lambda_{Max}| \tag{12}$$

where ε represents the degree of system stability, and λ_{Max} represents the eigenvalue with the longest modulus. Define a critical value $\varepsilon_r > 0$, which is the minimum value of the system stability margin. A warning will be issued if the system stability margin drops below the critical level. And if the system is stable, $1 > \varepsilon > \varepsilon_r$, otherwise $\varepsilon < 0$.

3.2 Implementation of ANN

The above content illustrates the theoretical principle of nonlinear analysis, which is dependent upon the system state. In this section, ANNs is applied to complete the procedure of multivariate classification to achieve the operating prediction mode. Figure 3A shows our neural network structure, which is fully connected and includes a 7-dimensional input layer, a 6-dimensional output layer, and four hidden layers. Specifically, the input vector [T, G, i_{pv}, v_{pv}, i_b, i_c, v_{dc}] including ambient temperature (T), solar irradiance (G), the output current and voltage of PV arrays (i_{pv} and v_{pv}), the output current of battery (i_b), the running current of CPL (i_c), and the DC bus voltage (v_{dc}), are the measured variables of the DC microgrid system, and the output is the probability of the operating modes $P(Mi)$ (i = 1, 2, ...,6). Moreover, the neural node structure is illustrated in Figure 3B, which contains a linear and a nonlinear portion. The hyperparameters of the linear portion include connection weighs vector $w^{[l,h]}$ and a bias factor $b^{[l,h]}$ (l presents the serial number of the hidden layers, and h presents the serial number of neurons in one hidden layer). The nonlinear portion adopts Rectified Linea Unit (ReLU) function as an activation function $f(u)$. The generic structure of the neural node can be stated as follows:

$$r^{[l,h]} = \sum_{k=1}^{p} w_k^{[l,h]} x_k + b^{[l,h]} \tag{13}$$

$$y^{[l,h]} = f\left(r^{[l,h]}\right) = f\left(\sum_{k=1}^{p} w_k^{[l,h]} x_k + b^{[l,h]}\right) \tag{14}$$

where $r^{[l,h]}$ is the input of the activation function f, $y^{[l,h]}$ is the output of the hth neural node in the lth hidden layer, and p presents the number of neurons in the previous layer.

Furthermore, the output of the full-connected ANNs is converted into the form that fulfils Formula (15) by the *SoftMax* algorithm, and its structure is shown in Figure 3C.

$$P(Mi) = \frac{e^{y_i}}{\sum_{i=1}^{C} e^{y_i}} \text{for } i = 1, 2, ..., C \tag{15}$$

where Mi represents the operation mode, and $P(Mi)$ is the probability of each operating state, y_i is the input of the output layer, as well as the output of the full connected layers, and C = 6 represents total six operation modes, namely six outputs of the ANNs. The *SoftMax* algorithm is to normalize the values of the output layer lie in the range (0, 1) and the sum of the values equal 1, as expressed in Formula (16), so that these output values can be interpreted as probabilities, where the highest probability is most like the best candidate label (Maxwell et al., 2017).

$$\begin{cases} P(Mi) \in [0, 1] \\ \sum_{i} P(Mi) = 1 \end{cases} \tag{16}$$

Moreover, together with *the Cross-Entropy Loss*, *SoftMax Cross-Entropy Loss* is arguably one of the most commonly used in classification tasks using neural network (Liu et al., 2016). So, it is used as the loss function of the system, as follows:

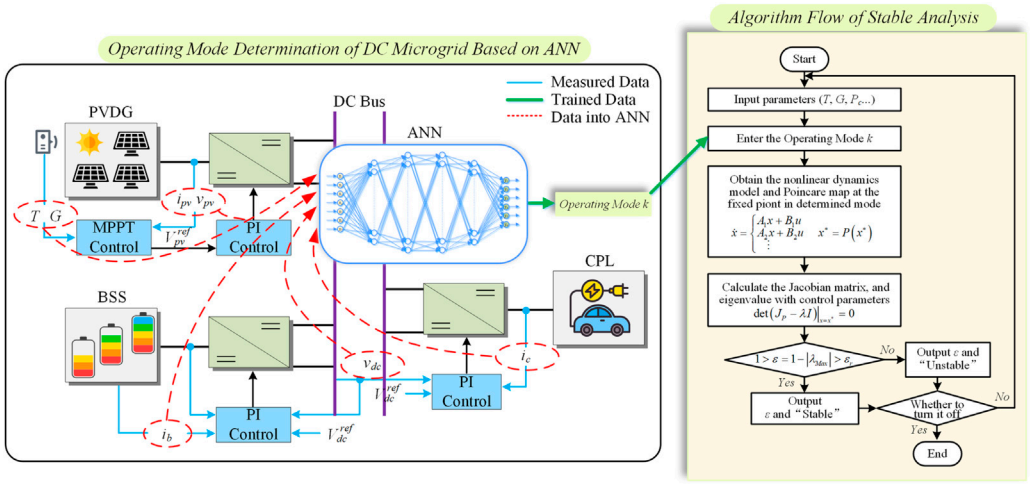

FIGURE 4
The framework of the proposed ANN-aided nonlinear voltage stability monitor method.

$$Loss = \frac{1}{N}\sum_{j} L_j = -\frac{1}{N}\sum_{j}\sum_{i=1}^{C} s_{ji}\log\left(P\left(Mi\right)\right) \tag{17}$$

where *Loss* is the loss function, N is the number of samples, i and j present each sample, and s_{ji} is a symbol function that can take either 0 or 1. Specifically, when the jith output value is the best candidate label, s_{ji} is 1, and others is 0.

Above all, the framework of the proposed ANN-aided nonlinear voltage stability monitor method is illustrated in Figure 4. The proposed method consists of two parts. The first step is the nonlinear stability analysis algorithm. It is based on the Poincaré map theory in nonlinear dynamics, according to the model demonstrated in Section 2.2 and the formula of calculating the stability margin ε derived in Section 3.1, to write the algorithm to evaluate the system's stability quantitatively. In the second step, the ANNs are used to predict the operating mode of the DC microgrid. To aid the first step in efficient computation, when environmental conditions and CPL change randomly, the results predicted by the ANNs are passed on to it. To be more specific, the data set [T, G, i_{pv}, v_{pv}, i_b, i_c, v_{dc}] generated by MATLAB/Simulink simulation is divided into training and test sets. Then the ANNs are trained and tested, and the predicted operating mode results are fed to stable calculations. We should point out that this paper calculates stability for a specific system state and does not consider the changing process between the two states.

4 Simulation results

To evaluate the effectiveness of the proposed voltage stability monitor method, throughout this section, we produce a comprehensive introduction to neural network hyper-parameters tuning, and then combine the nonlinear stability analysis with the proposed stability margin to quantitatively analysis and predict the system's operating state. The specific control and circuit parameters of the PV-battery-load-based DC microgrid system are shown in Table 2.

To begin with, the inputs and outputs of the ANNs are gathered to be trained by measured variables, including ambient temperature (T), solar irradiance (G), the output current and voltage of PV arrays (i_{pv} and v_{pv}), the output current of battery (i_b), the running current of CPL (i_c), the DC bus voltage (v_{dc}), and the manually labelled corresponding operation modes (Mi, i =1,2, . . . ,6). To simulate the random and intermittent disturbances of the DC microgrid, the variations of the inputs and outputs of the system, including ambient temperature, solar irradiance (Sidi et al., 2015) and various

TABLE 2 Parameters of PV-battery-load-based DC microgrid system.

PV-Distributed Generation (PVDG)	
Rated Maximum Power - P_N	6.9 kW
Filters - L_a, C_a, C_{pv}	300μH, 220μF, 220 μF
Line Resistance - r_a	200 mΩ
PI Controller - k_{Pa}, k_{Ia}	1.5, 0.1
Battery Storage System (BSS)	
Nominal Voltage - V_b	192 V
Filters - L_b, C_b	200μH, 220 μF
Line Resistance - r_b	100 mΩ
PI Controller- k_{Pvb}, k_{Ivb}, k_{Pib}, k_{Iib}, R_{vb}	0.001, 1, 0.01, 1, 1
Constant Power Load (CPL)	
Nominal Voltage - V_o	220 V
Filters - L_c, C_c	200μH, 300 μF
Line Resistance - r_c	100 mΩ
PI Controller - k_{Pvc}, k_{Ivc}, k_{Pic}, k_{Iic}, R_{vc}	1, 0.02, 0.1, 0.2, 1

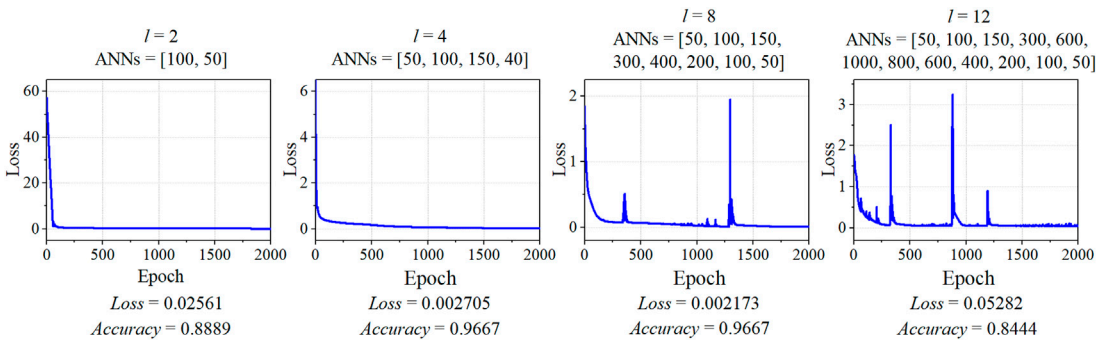

FIGURE 5
Loss of training process, and *Accuracy* of test datasets, for the number of hidden layers $l \in \{2, 4, 8, 12\}$ with different ANNs, for learning rate η = 0.001.

TABLE 3 (*Loss*, *Accuracy*) for varying number of hidden neurons ($u = [u_1, u_2, u_3, u_4]$) and learning rate (η).

η / $[u_1, u_2, u_3, u_4]$	0.1	0.01	0.001	0.0001
[20, 50, 80, 20]	(1.2037, 0.03333)	(0.6649, 0.5222)	(0.01342, 0.8778)	(0.06319, 0.8000)
[50, 100, 150, 40]	(1.2037, 0.03333)	(0.06039, 0.7889)	(0.002705, 0.9667)	(0.01745, 0.9333)
[100, 500, 250, 50]	(1.2037, 0.03333)	(0.03869, 0.9222)	(0.0006942, 0.9778)	(0.001710, 0.9778)
[200, 800, 600, 100]	(1.2037, 0.03333)	(0.0001658, 0.9778)	(0.0002747, 0.9778)	(0.009430, 0.9778)

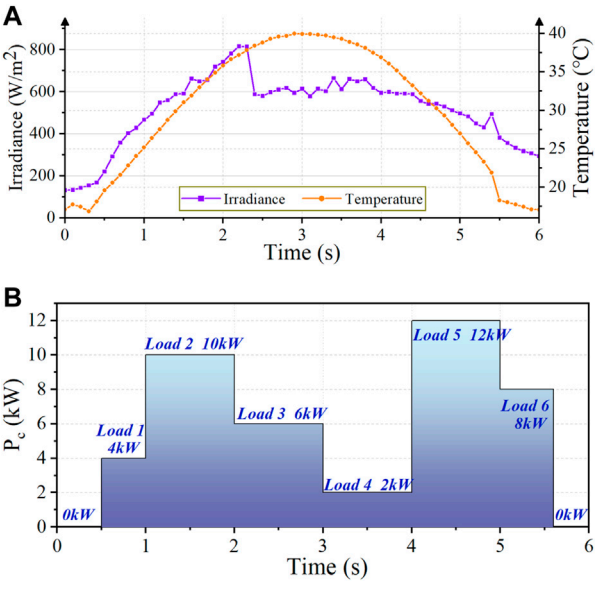

FIGURE 6
Variation of input and output conditions of the studied DC microgrid system. **(A)** Variation of solar irradiance and ambient temperature. **(B)** Variation of CPLs.

consumed power loads, are set to generate 600 groups of environmental states. For each state, ten groups are collected and marked to ensure the accuracy of the data collection. As the nonlinear dynamic stability analysis method in this paper is a steady-state analysis, a simulation duration of 5 s is chosen, ten sets of data are initially sampled at intervals of 0.2 s between 3 and 5 s, and one set of the sampled datasets is selected as the final original datasets to guarantee that all the data sets are in the stable or unstable states. Moreover, stratified sampling (Qian et al., 2009) is employed to keep the distribution of data consistent as much as possible to ensure that each category within a dataset is adequately represented in the sample, and the datasets are divided into 85% training sets and 15% test sets.

Because we are dealing with relatively small datasets with six classes, the choice of hyper-parameters is harder and more important. For training the networks, the stochastic gradient descent (SGD) optimizer is utilized, and we set weight decay of 2×10^{-5} of SGD, which is equivalent to L2 regularization, to improve the model's generalization capacity (Loshchilov and Hutter, 2017). There are several hyper-parameters that need to be fine-tuned, i.e., number of hidden layers, number of neurons, and learning rate. So, three-fold cross-validation is used to set them. We consider the number of hidden layers (l),

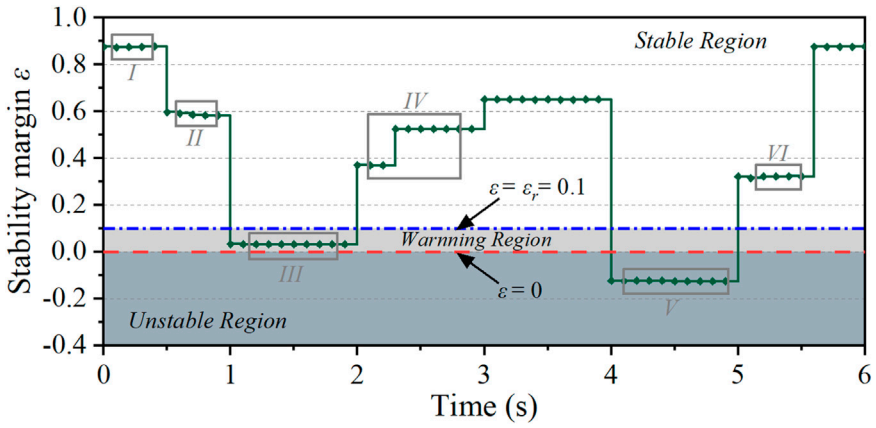

FIGURE 7
The dynamic variation of stability margin during conditions changing.

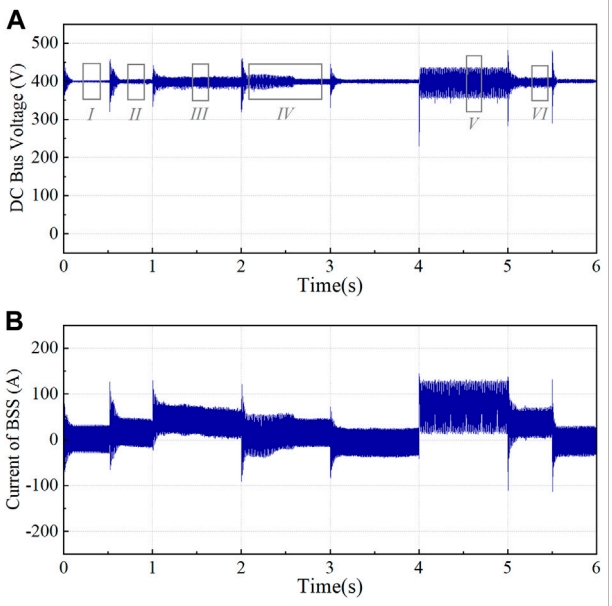

FIGURE 8
System Dynamics during conditions changing. **(A)** Dynamic of DC bus voltage. **(B)** Dynamic of BSS current.

the number of neurons (u), the learning rate (η), with momentum of 0.8, 2000 epochs, and other default parameters throughout.

We introduce the multi-label *Accuracy* measure, as defined in (Read et al., 2011), (Read and Perez-Cruz, 2014), to report the performance of ANNs with different hyper-parameters as follows:

$$Accuracy = \frac{1}{N}\sum_{i=1}^{N}\frac{\left|\mathbf{y}_i \wedge \hat{\mathbf{y}}_i\right|}{\left|\mathbf{y}_i \vee \hat{\mathbf{y}}_i\right|} \tag{18}$$

where $\mathbf{y}_i$ is the true set of labels, and $\hat{\mathbf{y}}_i$ is the predicted set of labels. $\wedge$ and $\vee$ are the bitwise AND and OR functions, respectively, i.e. $|\{0, 1, 0\} \vee \{0, 0, 1\}| = 2$, and $|\{0, 1, 0\} \wedge \{0, 0, 1\}| = 0$. N is the number of test examples. $Accuracy \in [0, 1]$ denotes that the better correctness of the prediction, the closer *Accuracy* is to 1.

The results in Figure 5 show the *Loss* and *Accuracy* to evaluate the performance of a varying number of hidden layers $l \in \{2, 4, 8, 12\}$, and, i.e. ANNs = {100, 50} denotes the first hidden layer has 100 hidden units and the second has 50 hidden units. Having two hidden layers results in an accuracy of 0.8889, adding two more gives 0.9667, and neural networks with eight hidden layers also produce 0.9967. Appending more hidden layers up to 12 totally has no effect on *Accuracy* and even reduces it. The changing trend of *Loss* is opposite to *Accuracy*, which means the lower *Loss*, the higher *Accuracy*. It can be found that a deeper neural network may not be best. Thus, we choose an optimal number of hidden layers $l = 4$.

There are other hyper-parameters available to be tuned: the number of neurons in hidden layers ($u = [u_1, u_2, u_3, u_4]$) and learning rate (η), where $u_1 \sim u_4$ denote the number of neurons in the corresponding layer. The results of (*Loss*, *Accuracy*) for varying number of hidden neurons and learning rate $\eta \in \{0.1, 0.01, 0.001, 0.0001\}$ are listed in Table 3. Using a learning rate of 0.1 leads to an accuracy of 0.03333 in all the four hidden neuron conditions, reducing it to 0.01 produces a higher accuracy, and $\eta = 0.001$ reaches an accuracy of 0.9778. Further, dropping the learning rate to 0.0001 has no benefit on accuracy and could actually make it worse. So, 0.01 is selected as the appropriate learning rate. More hidden neurons may improve accuracy;

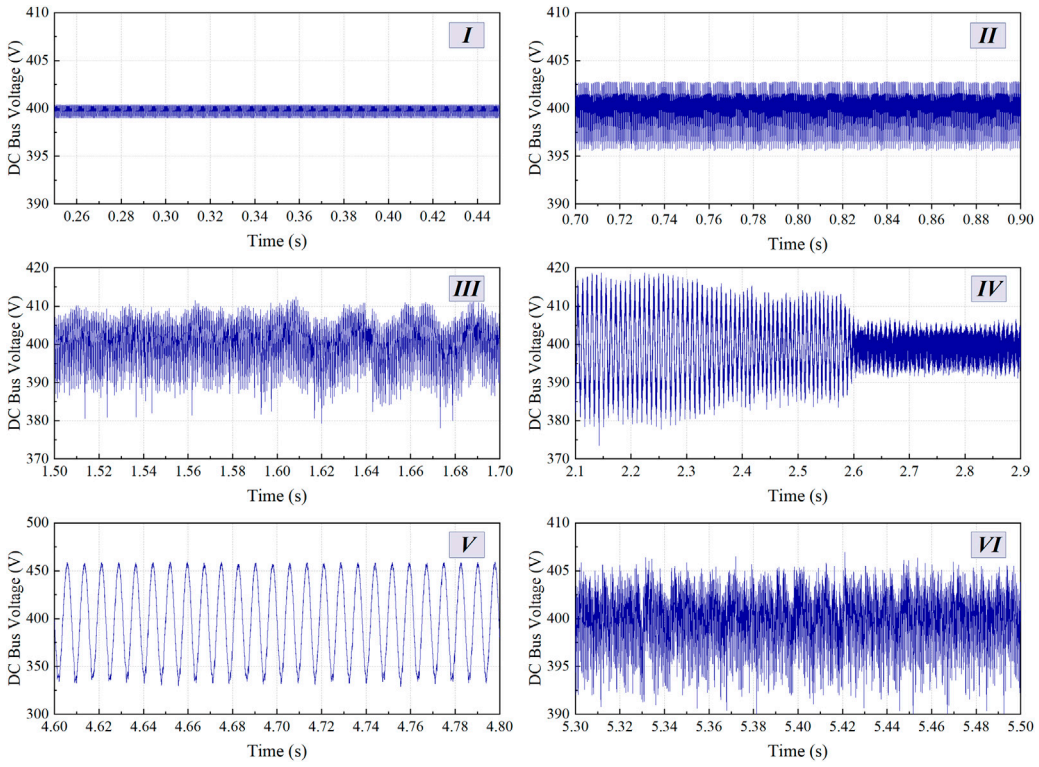

FIGURE 9
Zoomed dynamic of DC bus voltage during conditions changing.

however, to avoid the over-fitting of complex networks, accuracy of 0.9667 could be sufficient for our need, which is verified in the following simulation. Therefore, the search procedure shows that the ANNs with 100, 500, 250, and 50 neurons in corresponding hidden layers are the better choice.

The trained ANNs are then used to assist in calculating the nonlinear stability margin to monitor the DC bus voltage when both input and output conditions of the system change simultaneously. This paper simulates a real DC microgrid system by integrating fluctuations in solar radiation and ambient temperature of the photovoltaic panel and variations in the power consumption of the CPLs. Figures 6A,B depicts the variation of input and output conditions, and the variation of solar irradiance and ambient temperature in Figure 6A corresponds to the reference (Sidi et al., 2015). To study the effect of the irradiance and temperature variations throughout the day on the operation of the DC microgrid system, we compressed the data in the time range of a day into 6 s to facilitate simulation.

The dynamic of the calculated stability margin ε under varying input and output conditions is depicted in Figure 7. This figure shows that overall when the solar radiation and ambient temperature gradually vary, the calculated stability margin ε varies slightly. In contrast, a quick shift in CPL will have a major impact on the stability margin ε. In practice, the linked load's power consumption frequently fluctuates abruptly, indicating that the change in CPL's power consumption significantly impacts on system stability. At 0–0.5s and 5.5~6s, the CPL is 0kW, which implies that the system output is zero, and the stability margin is about 0.87, which is relatively the largest, indicating that the system is most stable at this time. When the loads of 4kW and 10 kW are connected respectively at 0.5s and 1s, the stability margins decrease to around 0.59 and 0.032, respectively. In the period of 1–2 s, the stability margin falls to about 0.032, and the DC bus voltage waveform fluctuates by 2.5% in amplitude. In addition, we calculate that under the same climatic conditions for 1–2 s when the constant power load was 9.6kW, the DC bus voltage fluctuated by about 2.5%, and the stability margin was 0.091. To ensure that the bus voltage fluctuates by less than 2.5%, we have set the critical value stability margin at 0.1. The access load is then reduced to 6kW, and the stability margin increases at 2 s. Additionally, when solar radiation drops sharply, the stability margin will increase sharply, such as at 2.3 s, as the stability margin jumps from 0.37 to 0.52. After that, the access load grows abruptly to 12 kW at 4 s, leading the stability margin to decrease to approximately -0.13 and the system to lose stability. Finally, the system resumes steady operation at 5s and 5.5s

when the load is gradually lowered to 6 kW and 0kW, and ε is correspondingly increased to around 0.32 and 0.87. From the preceding analysis, it can be concluded that the DC microgrid's stability declines with rising CPL, and there is a critical CPL value.

The corresponding time domain simulation is conducted to further verify the correctness of the proposed voltage stability monitoring method, and Figures 8A,B depicts the dynamic waveforms of the DC bus voltage and the BSS charging and discharging current. In this figure, the time-domain waveforms of the DC bus voltage and BSS current vary in response to the weather conditions input to the system and the power consumed by the CPL, which appears to be operating steadily throughout the process. However, these dynamic waveforms appear to not match the stability margin calculation. Therefore, the typical states I ~ VI, in which the system is in different degrees of stability, are selected and marked in Figure 7 and Figure 8. Figure 9 shows the zoomed waveforms corresponding to the DC bus voltage during the appropriate state.

In Figure 9, the amplified waveforms of states I and II are both stable, and the DC bus voltage fluctuation amplitude in state II is larger than that in state I, which corresponds to the variation of the stability margin in Figure 7. In state III, the fluctuation range of the DC bus voltage is greater, and it contains some harmonics. The stability margin is below critical stability margin of ε_r = 0.1 and close to 0, indicating that the system is in a critical stability state. In addition, it shows that the critical stability margin is set at a reasonable value, and an early warning should be given to alert of potential instability. The DC bus voltage continues to fluctuate in state IV under the disturbance of CPL. However, the waveform fluctuates less due to the sudden drop in solar irradiance, which is consistent with the calculation result of the stability margin. As a result of the sudden increase in CPL, the DC bus voltage of state V exhibits constant-amplitude oscillations, at which time the stability margin is less than 0, and the system is unstable. Lastly, when the CPL is reduced, the DC bus voltage waveform of state VI ceases to oscillate. However, this may be due to the previous oscillation as the bus voltage has some glitches at this time, but it is overall stable. In conclusion, the time domain waveform results demonstrate the precision of the proposed voltage stability monitoring method.

5 Conclusion

This paper proposes a voltage monitoring method using ANN-aided nonlinear dynamic stability analysis for the DC microgrid. In the proposed method framework, the trained neural network generates the predicted operating mode of the DC microgrid, which is then input into the nonlinear analysis algorithm based on the Poincaré map theory to calculate the stability margin. Moreover, this method makes the theoretical analysis of Poincaré mapping flexible and convenient, thereby solving the problem that the iterative mapping order is difficult to determine as the number of power electrons rises. A thorough introduction to neural network hyper-parameters tuning is provided. The theoretical and simulation analyses further verify the accuracy of the proposed analysis method. In the case study, it is found that when the solar irradiance and ambient temperature of the PVDG or the CPL change greatly, the stability margin varies from close to 1 to a negative value, which indicates that changes in the behaviour of the input and output interfaces could cause the DC microgrid to be unstable, such as oscillations in the bus voltage. Also, this nonlinear intelligent approach can be extended to other relatively small-scale power electronics-dominated power systems to monitor their stability. As for the larger system, the approximate modeling or more complex neural networks may be considered to utilized in the future study.

Data availability statement

The original contributions presented in the study are included in the article/supplementary material, further inquiries can be directed to the corresponding author.

Author contributions

SS: inspiration and implement of algorithm, simulation validation, manuscript writing and reviewing; CT: simulation validation, and manuscript reviewing; GH: supervision, and manuscript reviewing; DX: inspiration of algorithm, supervision, and manuscript reviewing.

Funding

This work was supported in part by National Natural Science Foundation of China under Grant 52077137, 51677114.

Conflict of interest

The authors declare that the research was conducted in the absence of any commercial or financial relationships that could be construed as a potential conflict of interest.

Publisher's note

All claims expressed in this article are solely those of the authors and do not necessarily represent those of their affiliated

organizations, or those of the publisher, the editors and the reviewers. Any product that may be evaluated in this article, or claim that may be made by its manufacturer, is not guaranteed or endorsed by the publisher.

References

Ahmadi, H., and Kazemi, A. (2020). The Lyapunov-based stability analysis of reduced order micro-grid via uncertain LMI condition. *Int. J. Electr. Power & Energy Syst.* 117, 105585. doi:10.1016/j.ijepes.2019.105585

Ahmed, M., Meegahapola, L., Vahidnia, A., and Datta, M. (2020). Stability and control aspects of microgrid architectures–A comprehensive review. *IEEE Access* 8, 144730–144766. doi:10.1109/access.2020.3014977

Aroudi, A. E., Debbat, M., and Martinez-Salamero, L. (2007). Poincaré maps modeling and local orbital stability analysis of discontinuous piecewise affine periodically driven systems. *Nonlinear Dyn.* 50, 431–445. doi:10.1007/s11071-006-9190-1

Eberlein, S., and Rudion, K. (2021). Small-signal stability modelling, sensitivity analysis and optimization of droop controlled inverters in LV microgrids. *Int. J. Electr. Power & Energy Syst.* 125, 106404. doi:10.1016/j.ijepes.2020.106404

Geng, S., and Hiskens, I. A. (2019). Second-order trajectory sensitivity analysis of hybrid systems. *IEEE Trans. Circuits Syst. I.* 66 (5), 1922–1934. doi:10.1109/tcsi.2019.2903196

Gomez, F., Rajapakse, A., Annakkage, U., and Fernando, I. (2011). "Support vector machine-based algorithm for post-fault transient stability status prediction using synchronized measurements," in 2011 IEEE Power and Energy Society General Meeting, Detroit, MI, USA, July 24-28.

Holari, Y. T., Taher, S. A., and Mehrasa, M. (2021). Power management using robust control strategy in hybrid microgrid for both grid-connected and islanding modes. *J. Energy Storage* 39, 102600. doi:10.1016/j.est.2021.102600

Khodamoradi, A., Liu, G., Mattavelli, P., Caldognetto, T., and Magnone, P. (2019). Analysis of an online stability monitoring approach for DC microgrid power converters. *IEEE Trans. Power Electron.* 34 (5), 4794–4806. doi:10.1109/tpel.2018.2858572

Liu, W., Wen, Y., Yu, Z., and Yang, M. (2016). Large-margin softmax loss for convolutional neural networks. arXiv preprint arXiv:1612.02295.

Loshchilov, I., and Hutter, F. (2017). Decoupled weight decay regularization. arXiv preprint arXiv:1711.05101.

Lu, X., Sun, K., Guerrero, J. M., Vasquez, J. C., Huang, L., and Wang, J. (2015). Stability enhancement based on virtual impedance for DC microgrids with constant power loads. *IEEE Trans. Smart Grid* 6 (6), 2770–2783. doi:10.1109/tsg.2015.2455017

Marx, D., Magne, P., Nahid-Mobarakeh, B., Pierfederici, S., and Davat, B. (2012). Large signal stability analysis tools in DC power systems with constant power loads and variable power loads—a review. *IEEE Trans. Power Electron.* 27 (4), 1773–1787. doi:10.1109/tpel.2011.2170202

Maxwell, A., Li, R., Yang, B., Weng, H., Ou, A., Hong, H., et al. (2017). Deep learning architectures for multi-label classification of intelligent health risk prediction. *BMC Bioinforma.* 18 (14), 523–131. doi:10.1186/s12859-017-1898-z

Mehran, K., Giaouris, D., and Zahawi, B. (2009). Modeling and stability analysis of closed loop current-mode controlled cuk converter using takagi-sugeno fuzzy approach. *IFAC Proc. Vol.* 42 (7), 223–228. doi:10.3182/20090622-3-uk-3004.00043

Moreno-Font, V., El Aroudi, A., Calvente, J., Giral, R., and Benadero, L. (2009). Dynamics and stability issues of a single-inductor dual-switching DC–DC converter. *IEEE Trans. Circuits Syst. I.* 57 (2), 415–426. doi:10.1109/tcsi.2009.2023769

Qian, L., Zhou, G., Kong, F., and Zhu, Q. (2009). "Semi-supervised learning for semantic relation classification using stratified sampling strategy," in Proceedings of the 2009 conference on empirical methods in natural language processing, Singapore, Aug 6-7, 1437–1445.

Rahimi, A. M., and Emadi, A. (2009). An analytical investigation of DC/DC power electronic converters with constant power loads in vehicular power systems. *IEEE Trans. Veh. Technol.* 58 (6), 2689–2702. doi:10.1109/tvt.2008.2010516

Read, J., and Perez-Cruz, F. (2014). Deep learning for multi-label classification. arXiv preprint arXiv:1502.05988.

Read, J., Pfahringer, B., Holmes, G., and Frank, E. (2011). Classifier chains for multi-label classification. *Mach. Learn.* 85 (3), 333–359. doi:10.1007/s10994-011-5256-5

Seth, S., and Banerjee, S. (2020). Electronic circuit equivalent of a mechanical impacting system. *Nonlinear Dyn.* 99, 3113–3121. doi:10.1007/s11071-019-05457-w

Sidi, C. El B. E., Ndiaye, M. L., Ndiaye, A., and Ndiaye, P. A. (2015). Outdoor performance analysis of a monocrystalline photovoltaic module: Irradiance and temperature effect on exergetic efficiency. *Int. J. Phys. Sci.* 10 (11), 351–358. doi:10.5897/ijps2015.4356

Tan, B., Yang, J., Tang, Y., Jiang, S., Xie, P., and Yuan, W. (2019). A deep imbalanced learning framework for transient stability assessment of power system. *IEEE Access* 7, 81759–81769. doi:10.1109/access.2019.2923799

Tian, Z., Shao, Y., Sun, M., Zhang, Q., Ye, P., and Zhang, H. (2022). Dynamic stability analysis of power grid in high proportion new energy access scenario based on deep learning. *Energy Rep.* 8 (6), 172–182. doi:10.1016/j.egyr.2022.03.055

Toro, V., Mojica-Nava, E., and Rakoto-Ravalontsalama, N. (2021). Stability analysis of DC microgrids with switched events. *IFAC-PapersOnLine* 54 (14), 221–226. doi:10.1016/j.ifacol.2021.10.356

Tse, C. K., and Di Bernardo, M. (2002). Complex behavior in switching power converters. *Proc. IEEE* 90 (5), 768–781. doi:10.1109/jproc.2002.1015006

Vanfretti, L., and Narasimham Arava, V. S. (2020). Decision tree-based classification of multiple operating conditions for power system voltage stability assessment. *Int. J. Electr. Power & Energy Syst.* 123, 106251. doi:10.1016/j.ijepes.2020.106251

Wang, B., Sun, K., and Kang, W. (2018). Nonlinear modal decoupling of multi-oscillator systems with applications to power systems. *IEEE Access* 6, 9201–9217. doi:10.1109/access.2017.2787053

Wang, Y., Xu, L., Chen, L., and Zhou, J. (2020). Discrete iterative map model-based stability analysis of capacitor current ripple-controlled SIDO CCM buck converter. *IEEE J. Emerg. Sel. Top. Power Electron.* 8 (4), 3272–3280. doi:10.1109/jestpe.2020.2972651

Wu, H., Pickert, V., Ma, M., Ji, B., and Zhang, C. (2020). Stability study and nonlinear analysis of DC–DC power converters with constant power loads at the fast timescale. *IEEE J. Emerg. Sel. Top. Power Electron.* 8 (4), 3225–3236. doi:10.1109/jestpe.2020.2966375

Xia, Y., Wei, W., Yu, M., and Wang, P. (2019). Stability analysis of PV generators with consideration of P&O-based power control. *IEEE Trans. Ind. Electron.* 66 (8), 6483–6492. doi:10.1109/tie.2018.2864695

Xia, Y., Wei, W., Long, T., Blaabjerg, F., and Wang, P. (2020). New analysis framework for transient stability evaluation of DC microgrids. *IEEE Trans. Smart Grid* 11 (4), 2794–2804. doi:10.1109/tsg.2020.2964583

Xie, W., Han, M., Cao, W., Guerrero, J. M., and Vasquez, J. C. (2021). System-level large-signal stability analysis of droop-controlled DC microgrids. *IEEE Trans. Power Electron.* 36 (4), 4224–4236. doi:10.1109/tpel.2020.3019311

Zhang, Z., Yang, X., Zhao, S., Wu, D., Cao, J., Gao, M., et al. (2022). Large-signal stability analysis of islanded DC microgrids with multiple types of loads. *Int. J. Electr. Power & Energy Syst.* 143, 108450. doi:10.1016/j.ijepes.2022.108450

Zia, M. F., Elbouchikhi, E., and Benbouzid, M. (2019). Optimal operational planning of scalable DC microgrid with demand response, islanding, and battery degradation cost considerations. *Appl. Energy* 237, 695–707. doi:10.1016/j.apenergy.2019.01.040

Zolfaghari, M., Gharehpetian, G. B., Shafie-khah, M., and Catalão, J. P. S. (2022). Comprehensive review on the strategies for controlling the interconnection of AC and DC microgrids. *Int. J. Electr. Power & Energy Syst.* 136, 107742. doi:10.1016/j.ijepes.2021.107742

frontiers | Frontiers in Energy Research

TYPE Original Research
PUBLISHED 10 January 2023
DOI 10.3389/fenrg.2022.1020894

OPEN ACCESS

EDITED BY
Yanchi Zhang,
Shanghai Dianji University, China

REVIEWED BY
Rui Wang,
Northeastern University, China
Baling Fang,
Hunan University of Technology, China

*CORRESPONDENCE
Xitian Wang,
x.t.wang@sjtu.edu.cn

SPECIALTY SECTION
This article was submitted to Smart Grids, a section of the journal Frontiers in Energy Research

RECEIVED 16 August 2022
ACCEPTED 29 September 2022
PUBLISHED 10 January 2023

CITATION
Zhao C, Wang X, Liu Z and Liu S (2023), The observability and controllability metrics of power system oscillations and the applications.
Front. Energy Res. 10:1020894.
doi: 10.3389/fenrg.2022.1020894

The observability and controllability metrics of power system oscillations and the applications

Chenghan Zhao, Xitian Wang*, Ziyu Liu and Shiyu Liu

Ministry of Education Key Laboratory of Power Transmission and Power Conversion Control, Department of Electrical Engineering, Shanghai Jiao Tong University, Shanghai, China

Power system oscillation has caused many serious accidents in renewable energy grid connection system. The concept of observability and controllability in control theory has been widely applied to power system oscillation study. In this paper, observability metric (OM) and controllability metric (CM) are defined from the perspective of oscillation modes, acting as a novel quantification method to quantify the observability and controllability of power system with distinct or repeated eigenvalues. Furthermore, in order to compare the reflection degree and control effect of signals in different oscillation modes, the mode comprehensive observability metric (MCOM) and comprehensive controllability metric (MCCM) are proposed. The proposed method shows clearer relationship between controllability/observability and oscillation modes by combining the information of conjugate eigenvalues together. The advantages of metrics are illustrated by comparing with theoretical derivations and calculation results of three traditional methods: participation factor, residue method and geometric measures. Finally, the metrics are applied to a subsynchronous damping controller (SSDC) design for better performance in oscillation monitoring and suppression. With the small-signal model and corresponding time-domain simulation, the effectiveness of the proposed method is verified.

KEYWORDS

oscillation mode, observability metric, controllability metric, oscillation suppression, subsynchronous oscillation

1 Introduction

The concept of observability and controllability from modern control theory can assess systems, whether their internal states can be reflected by outputs and whether they can be affected by inputs (Angulo et al., 2020). However, a continuous indicator is needed to evaluate the observation and control performance under different measurement settings, system structures and parameter configurations. To provide quantitative information about the observability and controllability degree of a system, residue methods and geometric measures have been proposed (Heniche and Kamwa, 2002; Wang et al., 2017).

In recent years, the rapid development of renewable energy has brought more oscillation stability problems for power systems (Song and Blaabjerg, 2017; Xie et al., 2017; Li et al., 2020). The grid-connection of the renewable energy needs many electronic devices like converters, and these electronic devices together with their control system may form an equivalent "LC resonance circuit" with other parts of the power grid and generate oscillations. When the part of grid-connecting electronic system show "negative damping" at the oscillation frequency, the oscillation will diverge, and there will be oscillation stability problems.

Oscillation is a type of dynamic stability problem, and the modal analysis is one of the important methods. Since modal variables cannot be directly measured, accordingly, if the actual measured value can reflect the modal variable, the mode is assumed to be observable; if the control input can control the change of the modal variable, the mode is assumed to be controllable. So, the observability, controllability and relative methods are widely applied to power system oscillation study.

The residue method is often applied in input signals selection and controller parameters design in studying power system oscillation. Gallardo et al. (2017) and Oscullo and Gallardo (2020) used the residue method to find the best position of power system stabilizers to suppress electromechanical oscillations. The damping degradation degree and components that lead to the stability degradation can be estimated by calculating the residue under the open-loop state, providing the basis for controller design (DuFu and Wang, 2018). To achieve better adaptation in various operation conditions, the residue approach was applied to design the power oscillation damping controllers (Ping et al., 2014). By analyzing residue results under various working conditions, it is possible to determine the optimal position to insert the subsynchronous notch filter into the controller (Liu et al., 2017). The main drawback of the residue method is that only one oscillation eigenvalue is considered. The residue is a common quantitation indicator, but it is not suitable for comparing signals with different units.

The geometric measure first proposed aiming at the selection of the control loops permitting a good observability and controllability of system's poles is defined based on the cosine of the angle between the left/right eigenvector and the input/output matrix of the system state space equation (Hamdan and Hamdan, 1987). It can be used with the advantage of normalization, but it cannot solve systems with repeated eigenvalues (Domínguez-García et al., 2014).

The method of participation factor in the power system can also reflect part of system observability and controllability degree (He et al., 2019; Huang et al., 2019; Lei et al., 2019; Zhou et al., 2019). To monitor oscillation, Lei et al. (2019) and Huang et al. (2019) respectively determined the type and locations of components causing oscillation by calculating the participation factor. To suppress oscillations, strong correlation variables were determined by the participation factor method, and then, a damping controller was designed (Zhou et al., 2019). Besides, the optimal parameter design of controllers can be determined by analyzing the participation factors of dominant modes (He et al., 2019). However, participation factor methods can only reflect the observability from state variables but not actual measurable values.

This paper proposes the novel observability metric and controllability metric from the perspective of modal analysis. We can use the concept of metric to quantify the observability and controllability to monitor and control oscillations. Modal observability metric (OM) represents the degree of reflection of monitoring point measurement on a power system mode. Controllability metric (CM) characterizes the performance of actuating point control input on a power system mode.

The main contributions are as follows: 1) the concepts of observability and controllability metrics for system with distinct and repeated eigenvalues are proposed from the viewpoint of oscillation modes, and it is proved mathematically that their effects can degenerate into residue and participation factors under certain conditions; 2) in order to compare control effect of different input signals and reflection degree of different output signals to different oscillation modes, the concepts of dominant mode observability ratio, dominant mode controllability ratio, oscillation mode comprehensive observability metric (MCOM) and mode comprehensive controllability metric (MCCM) are proposed. Compared with the residue method, geometric measures and participation factor, MCOM and MCCM can solve the global modal analysis (not only one eigenvalue at a time), applicable to systems with not only distinct but also repeated eigenvalues.

The rest of this paper is organized as follows: In Section 2, the concepts of observability metric and controllability metric are defined respectively, and from the perspective of controller design, Section 3 defines MCOM and MCCM. In Section 4, their meaning and advantages are analyzed. In Section 5, the theory is verified by the small-signal model and time-domain simulation. Finally, in Section 6 the conclusion is given.

2 Observability metric and controllability metric

In this section, the definition of observable ratio and controllable ratio are proposed to normalize units. And to comprehensively consider the relative observation and control effect of all the oscillation modes concerned, comprehensive observability metric and comprehensive controllability metric are defined. Before all these definitions, the controller characteristic requirements need to be analyzed.

2.1 System model and modal transformation

A general N_s-order system can be expressed in the form of state space in Eq. 1. Where $\boldsymbol{X}$ is the state variables matrix (N_s-order); $\boldsymbol{u}$ is the system input; $\boldsymbol{Y}$ is the system output; $\boldsymbol{A}$, $\boldsymbol{B}$ and $\boldsymbol{C}$ matrixes are the system state, input and output coefficient matrixes, respectively.

$$\begin{cases} \dot{\boldsymbol{X}} = \boldsymbol{AX} + \boldsymbol{Bu} \\ \boldsymbol{Y} = \boldsymbol{CX} \end{cases} \tag{1}$$

It is assumed that N complex eigenvalues are obtained through analyzing the system coefficient matrix $\boldsymbol{A}$ ($N \leq N_S$ for the existing of real eigenvalues). And N_1 is set as the number of complex eigenvalues in various values.

When eigenvalues are all distinct ($N_1 = N$), the system can be completely decoupled by a linear transformation. It can be proved that the right eigenvector $\boldsymbol{E}$ exists to convert the state space expression of the system into Eq. 2.

$$\begin{cases} \dot{\boldsymbol{Z}} = \boldsymbol{\Lambda Z} + \boldsymbol{F}^T\boldsymbol{Bu} \\ \boldsymbol{Y} = \boldsymbol{CEZ} \end{cases} \tag{2}$$

where $\boldsymbol{Z}$ is the transferred decoupled state variables matrix (or modal variables matrix); $\boldsymbol{\Lambda}$ is the eigenvalue diagonal matrix in Eq. 3, $\boldsymbol{F}$ is the left eigenvector matrix, satisfying $\boldsymbol{E}^{-1} = \boldsymbol{F}^{\mathrm{T}}$. Where, i is the number of complex eigenvalues in various values, $i = 1 \sim N_1$.

$$\boldsymbol{\Lambda} = diag\left[\lambda_1 \ \cdots \ \lambda_i \ \cdots \ \lambda_{N_1}\right] \tag{3}$$

For a more general case, i.e., if there are repeated eigenvalues ($N > N_1$), the coefficient matrix cannot be completely decoupled by a linear transformation. In the theory of linear systems (Pratzel-Wolters, 1982), Jordan canonical form is defined as the minimum coupling form that can be achieved. The transformation matrix $\boldsymbol{Q}$ exists to convert the state space expression of the system into Eq. 4, acting as an approximately right eigenvector.

$$\begin{cases} \dot{\boldsymbol{Z}} = \boldsymbol{JZ} + \boldsymbol{L}^T\boldsymbol{Bu} \\ \boldsymbol{Y} = \boldsymbol{CQZ} \end{cases} \tag{4}$$

where $\boldsymbol{J}$ is the Jordan canonical form matrix; $\boldsymbol{L}$ acts as an approximate left eigenvector matrix, satisfying $\boldsymbol{Q}^{-1} = \boldsymbol{L}^{\mathrm{T}}$. Let the ith different eigenvalue includes s_i repeated eigenvalues. Each eigenvalue λ_i corresponds to a set of modal variables $\boldsymbol{Z}_{i(si\times 1)}$, approximate right eigenvector $\boldsymbol{q}_{i(N\times si)}$ and approximate left eigenvector $\boldsymbol{l}_{i(N\times si)}$. Therefore, the coefficient matrix can be transformed into the form of Eq. 5.

$$\boldsymbol{J} = diag\left[\boldsymbol{J}_1 \ \cdots \ \boldsymbol{J}_i \ \cdots \ \boldsymbol{J}_{N_1}\right] \tag{5}$$

Similarly, the Jordan block corresponding to the ith distinct characteristic eigenvalue is $\boldsymbol{J}_i$, and its dimension is s_i. The concrete form is related to the algebraic multiplicity and geometric multiplicity of Jordan block. In particular, when the algebraic multiplicity is equal to geometric multiplicity, the form of Jordan block is Eq. 6. When the two multiplicities are different, they may be related to strong resonance (Dobson et al., 2001). In this paper, we only study the cases satisfying Eq. 6, which may be caused by multiple machines.

$$\boldsymbol{J}_i = \begin{bmatrix} \lambda_i & 1 & & \\ & \lambda_i & \ddots & \\ & & \ddots & 1 \\ & & & \lambda_i \end{bmatrix} \tag{6}$$

To more accurately characterize oscillation mode $b \in (1,2\ldots N_1/2)$, a pair of conjugate eigenvalues in the $\boldsymbol{\Lambda}$ or s_b pairs of conjugate eigenvalues in $\boldsymbol{J}$ are considered together. Each pair of conjugate eigenvalues describes the characteristics of the same mode, and s_b pairs of conjugate repeated eigenvalues describe the characteristics of s_b coupled modes with the same frequency. Consider the coupled modes together, we get oscillation modal variable matrix $\tilde{\boldsymbol{Z}}_{b(2sb\times 1)}$.

The relevant information corresponding to mode b in the system with distinct or repeated eigenvalues is shown in Table 1, where, $\boldsymbol{\Lambda_{b(2\times 2)}}$, $\tilde{\boldsymbol{J}}_{b(2sb\times 2sb)}$ and $\tilde{\boldsymbol{Z}}_{b(2sb\times 1)}$ are defined as Eqs. 7–9.

$$\boldsymbol{\Lambda}_b = diag\left[\lambda_b \ \ \bar{\lambda}_b\right] \tag{7}$$

$$\tilde{\boldsymbol{J}}_b = diag\left[\boldsymbol{J}_b \ \ \bar{\boldsymbol{J}}_b\right] \tag{8}$$

$$\tilde{\boldsymbol{Z}}_b = \left[\boldsymbol{Z}_b \ \ \bar{\boldsymbol{Z}}_b\right]^{\mathrm{T}} \tag{9}$$

2.2 Definition of observability metric

The degree of modal observability measures the ability of the output $\boldsymbol{Y}$ to reflect the mode of the system.

When eigenvalues are distinct, to reflect the observable degree of the oscillation mode, the system output $\boldsymbol{Y}$ is expressed as the sum of the modal components in Eq. 10.

$$\boldsymbol{Y} = \sum_{b=1}^{M} \boldsymbol{C}\left[\boldsymbol{e}_b \ \ \bar{\boldsymbol{e}}_b\right]\tilde{\boldsymbol{Z}}_b \tag{10}$$

In Eq. 10, only M oscillation mode component terms are shown, corresponding to N_1 eigenvalues ($N_1 = 2M$). Eq. 10 indicates that the observable degree of the oscillation mode in the measured output $\boldsymbol{Y}$ can be represented by matrix $\boldsymbol{C}\left[\boldsymbol{e}_b \ \ \bar{\boldsymbol{e}}_b\right]$. Therefore, the definition of the observability metric of oscillation mode b is proposed in Eq. 11.

$$m_{ob} = \left\|\boldsymbol{C}\left[\boldsymbol{e}_b \ \ \bar{\boldsymbol{e}}_b\right]\right\|_F \tag{11}$$

where $\|\cdot\|_F$ is the Frobinus norm of the matrix. The observability metric m_{ob} can quantitatively reflect the observability degree of a system mode. Specifically, the larger m_{ob} is, the stronger the observability degree of the oscillation mode $\tilde{\boldsymbol{Z}}_b$ is in the output

TABLE 1 Information corresponding to mode *b*.

Mode *b*	Eigenvalues	Modal variable	Coefficient matrix	Right eigenvectors	Left eigenvectors
Distinct	λ_b; $\bar{\lambda}_b$	$\tilde{\boldsymbol{Z}}_{b(2\times1)}$	$\boldsymbol{\Lambda}_{\boldsymbol{b}(2\times2)}$	$\boldsymbol{e}_{b(N\times1)}$	$\boldsymbol{f}_{b(N\times1)}$
				$\bar{\boldsymbol{e}}_{b(N\times1)}$	$\bar{\boldsymbol{f}}_{b(N\times1)}$
repeated	λ_b; $\bar{\lambda}_b$	$\tilde{\boldsymbol{Z}}_{b(2sb\times1)}$	$\tilde{\boldsymbol{J}}_{b(2sb\times2sb)}$	$\boldsymbol{q}_{b(N\times sb)}$	$\boldsymbol{l}_{b(N\times sb)}$
				$\bar{\boldsymbol{q}}_{b(N\times sb)}$	$\bar{\boldsymbol{l}}_{b(N\times sb)}$

signal $\boldsymbol{Y}$. This means the component of the oscillation mode can be better reflected in the output signal.

When the eigenvalues are repeated, $\boldsymbol{Y}$ is expressed in Eq. 12.

$$\boldsymbol{Y} = \sum_{b=1}^{M} \boldsymbol{C}[\ \boldsymbol{q}_b\ \ \bar{\boldsymbol{q}}_b\ ]\tilde{\boldsymbol{Z}}_b \tag{12}$$

In this case, the definition of OM is proposed in Eq. 13.

$$m_{ob} = \left\| \boldsymbol{C}[\ \boldsymbol{q}_b\ \ \bar{\boldsymbol{q}}_b\ ] \right\|_F \tag{13}$$

2.3 Definition of controllability metric

The controllability degree of the system measures the control ability of input $\boldsymbol{u}$ to the system modal variable $\boldsymbol{Z}$.

When the eigenvalues are distinct, to reflect the controllability of oscillation modes, the variables in state equation are separated in Eq. 14, considering the input in Eq. 2.

$$\dot{\boldsymbol{Z}}_i = \boldsymbol{\Lambda}_i \boldsymbol{Z}_i + \boldsymbol{f}_i^T \boldsymbol{B}\boldsymbol{u} \tag{14}$$

To more clearly express the properties of oscillation mode, Eq. 14 can be expressed as Eq. 15.

$$\dot{\tilde{\boldsymbol{Z}}}_b = \boldsymbol{\Lambda}_b \tilde{\boldsymbol{Z}}_b + [\ \boldsymbol{f}_b\ \ \bar{\boldsymbol{f}}_b\ ]^T \boldsymbol{B}\boldsymbol{u} \tag{15}$$

Matrix $[\ \boldsymbol{f}_b\ \ \bar{\boldsymbol{f}}_b\ ]^T \boldsymbol{B}$ can characterize the controllability of input $\boldsymbol{u}$ to oscillation modal variable$\tilde{\boldsymbol{Z}}_b$, so the definition of controllability metric of oscillation mode b is proposed in Eq. 16.

$$m_{cb} = \left\| [\ \boldsymbol{f}_b\ \ \bar{\boldsymbol{f}}_b\ ]^T \boldsymbol{B} \right\|_F \tag{16}$$

The controllability metric m_{cb} can quantitatively reflect the controllability degree of system modes. Specifically, the larger the controllability metric is, the stronger the control effect of the input $\boldsymbol{u}$ on the oscillation modal variable $\tilde{\boldsymbol{Z}}_b$ is, which means the oscillation mode b is more easily affected by inputs.

When eigenvalues are repeated, variables in the state equation can be expressed as Eq. 17.

$$\dot{\tilde{\boldsymbol{Z}}}_b = \tilde{\boldsymbol{J}}_b \tilde{\boldsymbol{Z}}_b + [\ \boldsymbol{l}_b\ \ \bar{\boldsymbol{l}}_b\ ]^T \boldsymbol{B}\boldsymbol{u} \tag{17}$$

In this case CM is proposed in Eq. 18.

$$m_{cb} = \left\| [\ \boldsymbol{l}_b\ \ \bar{\boldsymbol{l}}_b\ ]^T \boldsymbol{B} \right\|_F \tag{18}$$

3 Comprehensive observability metric and comprehensive controllability metric

In this section, the definition of observable ratio and controllable ratio are proposed to normalize units. And to comprehensively consider the relative observation and control effect of all the oscillation modes concerned, comprehensive observability metric and comprehensive controllability metric are defined. Before all these definitions, the controller characteristic requirements need to be analyzed.

3.1 Damping control performance analysis

Power system oscillation suppression methods mainly include optimization of converter control parameters and installation of control device (Tang et al., 2016; Wu et al., 2015; Wu et al., 2018; Wang et al., 2014). The design of the control device includes the issue of measurement and control. In terms of measurement, the output signal needs to contain oscillation information. That is to say, the dominant mode of oscillation should be observable. Besides, to reduce the influence of other oscillation modes, the observability of the dominant oscillation mode should be greater than that of other oscillation modes. In terms of control, generally speaking, the controller will affect many modes, and the mode close to the oscillation frequency will be more affected. Therefore, it is necessary to select the optimal input signal actuating point, to better control the dominant mode of oscillation with less effect on other modes.

Based on the needs of comprehensively considering the reflection result and control effect on different oscillation modes, this section puts forward the concepts of

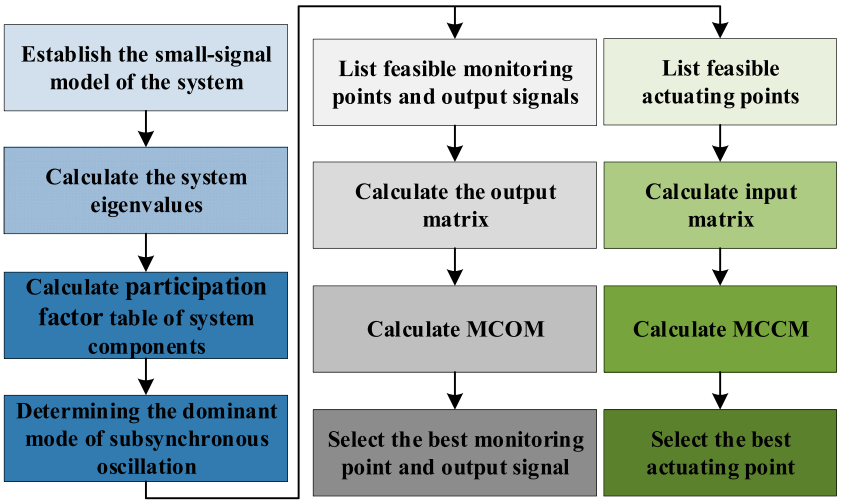

FIGURE 1
Application flow of MCOM and MCCM.

comprehensive observability metric and comprehensive controllability metric.

Before deriving the definition of MCOM and MCCM, it is necessary to first introduce the method of determining the dominant mode. 1) The unstable mode is determined by eigenvalue analysis. 2) Calculate system component participation factor. The system component participation coefficient of system eigenvalue is calculated as Eq. 19.

$$\rho_{eb} = \sum_{X_k \in X_e} p_{kb} \tag{19}$$

where p_{kb} is the participation factor corresponding to the kth state variable and mode b. X_e is the set of all state variables of the component e. The larger the ρ_{eb}, the stronger the connection between the oscillation mode b and the corresponding actual system component e. If the analysis shows that the oscillation mode is strongly related to the components interacting with the subsynchronous control, such as series capacitor or grid side converter controller, the mode can be considered as the dominant mode of subsynchronous oscillation (SSO). For low-frequency oscillation, it may be related to generator, etc.

3.2 Definition of comprehensive observability metric

Suppose that the s is one of the dominant oscillation modes among the M oscillation frequencies. As the dominant mode of the oscillation, its observability metric is m_{os}. To measure the influence of other oscillation modes on the observability of the dominant oscillation mode, the definition of the observable ratio of the dominant mode of the oscillation is proposed as Eq. 20.

Where $M'$is the number of oscillation modes within the frequency range of the oscillation types studied among M oscillation modes. For SSO, it ranges from 1 to 100 Hz.

$$R_{os} = m_{os} \Big/ \sum_{b=1}^{M'} m_{ob} \tag{20}$$

The meaning of the observable ratio is: the closer R_{os} to 1, the larger the relative proportion of the dominant mode of the oscillation in the output $\boldsymbol{Y}$, the easier the output to observe the dominant mode component of the oscillation.

Based on R_{os}, the definition of the MCOM of the dominant mode of oscillation is proposed in Eq. 21.

$$m_{sos} = m_{os} R_{os} \tag{21}$$

m_{sos} reflects the observability of the dominant mode in the measured output $\boldsymbol{Y}$ and the relationship between the observability dominant mode and that of other oscillation modes. The larger the m_{sos} for a certain output, the better the output can reflect the dominant component of oscillation, and the oscillation component accounts for a larger proportion in the signal, which means the output is a more suitable signal.

3.3 Definition of comprehensive controllability metric

Similarly, let the controllability metric of the dominant mode of the oscillation be m_{cs}. To measure the relative controllability of the input to the dominant mode and other modes of the oscillation, the definition of the controllable ratio of the dominant mode of the oscillation is proposed in Eq. 22.

$$R_{cs} = m_{cs} \Big/ \sum_{b=1}^{M'} m_{cb} \tag{22}$$

where M' is the same as the previous definition. The meaning of the controllability ratio of the dominant mode of oscillation is: If R_{cs} is close to 1, the control ability of input $\boldsymbol{u}$ to the dominant mode of oscillation is much greater than that of other modes.

Considering the above factors, the definition of MCCM of dominant modes m_{scs} is proposed in Eq. 23.

$$m_{scs} = m_{cs} R_{cs} \tag{23}$$

m_{scs} reflects the control effect of input $\boldsymbol{u}$ to dominant modes, and the relationship between the control effect of the dominant mode and that of other oscillation modes. The larger the m_{scs} for an input point, the stronger the control ability to the dominant mode, and the influence of the input point on other oscillation modes is relatively small, so it is more suitable to be used as the actuating point.

3.4 Application algorithm of metrics

For all the theory we proposed, the application flowchart is shown in Figure 1. Firstly, the eigenvalue analysis of the system is carried out to determine the unstable oscillation mode. Then, system component participation coefficients of system eigenvalues are calculated. For the confirmed dominant mode of oscillation, the best output signal, monitoring point and actuating point are selected.

4 Characteristics analysis of the metrics

To analyze the functions and advantages of OM and CM, their physical meanings are illustrated by deducing time-domain expression of state equations. It is mathematically proved that the effect of metrics can degenerate into residue and related factor under certain conditions. The advantages of applying MCOM and MCCM are also illustrated through comparison with geometric measures.

4.1 Analysis based on time domain solutions

In order to analyze the significance of controllability metric, the time-domain solution of the oscillation mode state equation is analyzed. When eigenvalues are distinct, the time-domain solution corresponding to Eq. 15 can be written in Eq. 24.

$$\tilde{\boldsymbol{Z}}_b(t) = \begin{bmatrix} z_{b0} e^{\lambda_b t} \\ \bar{z}_{b0} e^{\bar{\lambda}_b t} \end{bmatrix} + \begin{bmatrix} \int_0^t e^{\lambda_b (t-\tau)} \boldsymbol{f}_b^T \boldsymbol{B}\boldsymbol{u}(\tau) d\tau \\ \int_0^t e^{\bar{\lambda}_b (t-\tau)} \bar{\boldsymbol{f}}_b^T \boldsymbol{B}\boldsymbol{u}(\tau) d\tau \end{bmatrix} = e^{\boldsymbol{\Lambda}_b t} \tilde{\boldsymbol{z}}_{b0} + \int_0^t e^{\boldsymbol{\Lambda}_b (t-\tau)} \begin{bmatrix} \boldsymbol{f}_b & \bar{\boldsymbol{f}}_b \end{bmatrix}^T \boldsymbol{B}\boldsymbol{u}(\tau) d\tau \tag{24}$$

where $\tilde{\boldsymbol{z}}_{b0}$ is the initial oscillation values of corresponding mode component b. It has two elements, z_{b0} and $\bar{z}_{b0}$, corresponding to eigenvalues λ_b and $\bar{\lambda}_b$ respectively.

For repeated eigenvalues, the time-domain solution corresponding to Eq. 17 are shown in Eq. 25, deducting from the coupling relationship of Jordan canonical state variables.

$$\tilde{\boldsymbol{Z}}_b(t) = e^{\boldsymbol{J}_b t} \tilde{\boldsymbol{z}}_{b0} + \int_0^t e^{\boldsymbol{J}_b (t-\tau)} \begin{bmatrix} \boldsymbol{l}_b & \bar{\boldsymbol{l}}_b \end{bmatrix}^T \boldsymbol{B}\boldsymbol{u}(\tau) d\tau \tag{25}$$

Eqs. 24, 25 can be rewritten as Eq. 26.

$$\tilde{\boldsymbol{Z}}_b(t) = \tilde{\boldsymbol{Z}}_{b0}(t) + \tilde{\boldsymbol{Z}}_{b1}(t) \tag{26}$$

It can be seen that the first term is the zero-input response of the system. It represents the solution of the oscillation mode$\tilde{\boldsymbol{Z}}_b$ without input signal, reflecting the characteristics of the system mode itself. The second term is the zero-state response of the system, which reflects the control effect of input $\boldsymbol{u}$ on the mode. When the value of CM is large, the control effect of input $\boldsymbol{u}$ on the mode is greater, which is consistent with the definition of controllability metric.

The time-domain solution of system output $\boldsymbol{Y}$ can be expressed as the sum of the time domain solutions of each modal component, shown as Eq. 27.

$$\begin{aligned} \boldsymbol{Y}(t) &= \tilde{\boldsymbol{Y}}_1(t) + \cdots + \tilde{\boldsymbol{Y}}_b(t) + \cdots + \tilde{\boldsymbol{Y}}_M(t) \\ &= \begin{cases} \sum_{b=1}^{M} \boldsymbol{C}\begin{bmatrix} \boldsymbol{e}_b & \bar{\boldsymbol{e}}_b \end{bmatrix} \tilde{\boldsymbol{Z}}_b(t) & \text{distinct} - \text{eigenvalues} \\ \sum_{b=1}^{M} \boldsymbol{C}\begin{bmatrix} \boldsymbol{q}_b & \bar{\boldsymbol{q}}_b \end{bmatrix} \tilde{\boldsymbol{Z}}_b(t) & \text{repeated} - \text{eigenvalues} \end{cases} \end{aligned} \tag{27}$$

where $\tilde{\boldsymbol{Y}}_b$is the component corresponding to the oscillation mode $\tilde{\boldsymbol{Z}}_b$ in output $\boldsymbol{Y}$, and the time domain expression of $\tilde{\boldsymbol{Y}}_b$ can be obtained from Eq. 26, shown as Eq. 28.

$$\tilde{\boldsymbol{Y}}_b(t) = \begin{cases} \boldsymbol{C}\begin{bmatrix} \boldsymbol{e}_b & \bar{\boldsymbol{e}}_b \end{bmatrix} \tilde{\boldsymbol{Z}}_{b0}(t) + \boldsymbol{C}\begin{bmatrix} \boldsymbol{e}_b & \bar{\boldsymbol{e}}_b \end{bmatrix} \tilde{\boldsymbol{Z}}_{b1}(t) & \text{distinct} - \text{eigenvalues} \\ \boldsymbol{C}\begin{bmatrix} \boldsymbol{q}_b & \bar{\boldsymbol{q}}_b \end{bmatrix} \tilde{\boldsymbol{Z}}_{b0}(t) + \boldsymbol{C}\begin{bmatrix} \boldsymbol{q}_b & \bar{\boldsymbol{q}}_b \end{bmatrix} \tilde{\boldsymbol{Z}}_{b1}(t) & \text{repeated} - \text{eigenvalues} \end{cases} \tag{28}$$

Eq. 25 can be regarded as a modal variable, and the modal observability metric can reflect the observability degree of the oscillation mode variable in the output $\boldsymbol{Y}$. It can be seen from Eq. 28 that if the oscillation mode variable b changes by 1 unit, the value of the mode component in the system output $\boldsymbol{Y}_b$ will change by the corresponding value of OM, which is consistent with the definition of observability metric.

Current research shows that residue, participation factor and geometric measures can reflect the observability and

controllability of a system to a certain extent. In the following section, the differences and relations among metrics, participation factor, residue and geometric measures are analyzed to further explain the advantages of metrics.

4.2 Comparative analysis with participation factor

The participation factor is the physical quantity that defines the correlation between the kth state variable X_k and the ith eigenvalueλ_i.The participation factor p_{ki} is defined as Eq. 29.

$$p_{ki} = f_{ki}e_{ki} \Big/ \boldsymbol{f}_i^T \boldsymbol{e}_i \tag{29}$$

where f_{ki}, e_{ki} represent the kth row and ith column elements of the left eigenvector matrix $\boldsymbol{F}$ and the right eigenvector matrix $\boldsymbol{E}$.

The absolute value of the participation factor p_{ki} reflects the correlation of the kth state variable X_k and λ_i. The participation factor in Eq. 29 is extended to express the correlation between all state variables and eigenvalues as Eq. 30.

$$\boldsymbol{p}_i = \boldsymbol{e}_i \boldsymbol{f}_i^T \Big/ \boldsymbol{f}_i^T \boldsymbol{e}_i \tag{30}$$

The kth diagonal element of the participation factor matrix can represent the correlation between the state variable X_k and the eigenvalue λ_i, i.e., the participation factor p_{ki}. From participation factors, the time solution of $\boldsymbol{Y}_i$ will be Eq. 31. The equations hold for $\boldsymbol{E}^{-1} = \boldsymbol{F}^{\mathrm{T}}$.

$$\begin{aligned} \boldsymbol{Y}_i(t) &= \boldsymbol{e}_i \boldsymbol{z}_{i0}(t) + \int_0^t e^{\lambda_i (t-\tau)} \boldsymbol{p}_i \boldsymbol{u}(\tau) d\tau \\ &= \boldsymbol{e}_i \boldsymbol{z}_{i0}(t) + \int_0^t e^{\lambda_i (t-\tau)} \boldsymbol{e}_i \boldsymbol{f}_i^T \boldsymbol{u}(\tau) d\tau \end{aligned} \tag{31}$$

From Eq. 31, the large value of input $|p_{ki}|$ reflects the strong controllability and observability of X_k to λ_i. The large value of $\|\boldsymbol{p}_i\|_F$ can reflect the strong controllability and observability of the system to mode i.

To compare the difference between metrics and participation factors, consider Eqs. 24, 28 with distinct eigenvalues. We can rewrite the time solution of the output signal component $\tilde{\boldsymbol{Y}}_b$ as Eq. 32.

$$\begin{aligned} \tilde{\boldsymbol{Y}}_b(t) = \boldsymbol{C}\left[\, \boldsymbol{e}_b \;\; \bar{\boldsymbol{e}}_b \,\right] \tilde{\boldsymbol{Z}}_{b0}(t) + \Bigg(& \int_0^t e^{\lambda_b (t-\tau)} \boldsymbol{C} \boldsymbol{e}_b \boldsymbol{f}_b^T \boldsymbol{B} \boldsymbol{u}(\tau) d\tau \\ & + \int_0^t e^{\bar{\lambda}_b (t-\tau)} \boldsymbol{C} \bar{\boldsymbol{e}}_b \bar{\boldsymbol{f}}_b^T \boldsymbol{B} \boldsymbol{u}(\tau) d\tau \Bigg) \end{aligned} \tag{32}$$

When the input matrix $\boldsymbol{B}$ and output matrix $\boldsymbol{C}$ are N-order unit matrices, Eq. 32 can degenerate into the form of Eq. 31, except that conjugate components are considered simultaneously. In this way, the state variable $\boldsymbol{X}$ is considered as the output of the system.

It can be seen that the differences between the participation factor method and our metrics method proposed are that: 1) the participation factor can only reflect the controllability and observability of state variable $\boldsymbol{X}$, while the method in this paper reflects the controllability and observability of any actual control input and measurement output signal. 2) for the system with repeated values, because of the uncoupling relationship among different modes, the participation factor cannot reflect the observability and controllability of same oscillation mode with clear physical meaning.

4.3 Comparative analysis with residue method

The residue is defined according to the transfer function from input$\boldsymbol{u}$ to output $\boldsymbol{Y}$ in the system, which is expressed in the form of residue and eigenvalues, shown as Eqs. 33, 34. Compare to the method of participation factor, it is not limited in the case that $\boldsymbol{C}$ and $\boldsymbol{B}$ are unit matrices.

$$G_{jl}(s) = \sum_{i=1}^{N_1} \frac{R_{ijl}}{s - \lambda_i} \tag{33}$$

$$R_{ijl} = \boldsymbol{c}_j \boldsymbol{e}_i \boldsymbol{f}_i^T \boldsymbol{b}_l \tag{34}$$

Eq. 33 shows the transfer function between the lth input and the jth output of the original open-loop system. Where R_{ijl} is the residue related to the ith mode, jth output and lth input in the open-loop system. $\boldsymbol{c}_j$ stands for the jth row of output matrix $\boldsymbol{C}$. $\boldsymbol{b}_l$ stands for the lth column of input matrix $\boldsymbol{B}$.

Residue matrix $\boldsymbol{R}_i = \boldsymbol{C}\boldsymbol{e}_i \boldsymbol{f}_i^T \boldsymbol{B}$ reflects the transfer characteristic of the ith mode λ_i from input $\boldsymbol{u}$ to output $\boldsymbol{Y}$.

In Eq. 32, the second term corresponds to the time domain solution of the zero-state response of system output, reflecting the impact of the input on the mode component in the output $\boldsymbol{Y}$. This includes the expression of residue, which further explains that residue reflects the characteristics of input to output.

When the initial oscillation value of the system, i.e. the first term of Eq. 32 is approximately zero, there is only zero state response term in the output of the mode component in the system. Thus, the residue can reflect the controllability and observability of the modal component. However, when the system is greatly disturbed, the initial value of oscillation is large, then the residue cannot reflect the characteristics of the mode, i.e., the zero-input response of the system output. In this case, the residue can still reflect the controllability of the modal component, but it cannot directly reflect the observable degree of the modal component. Metrics can measure controllability and observability independently, which is more advantageous when

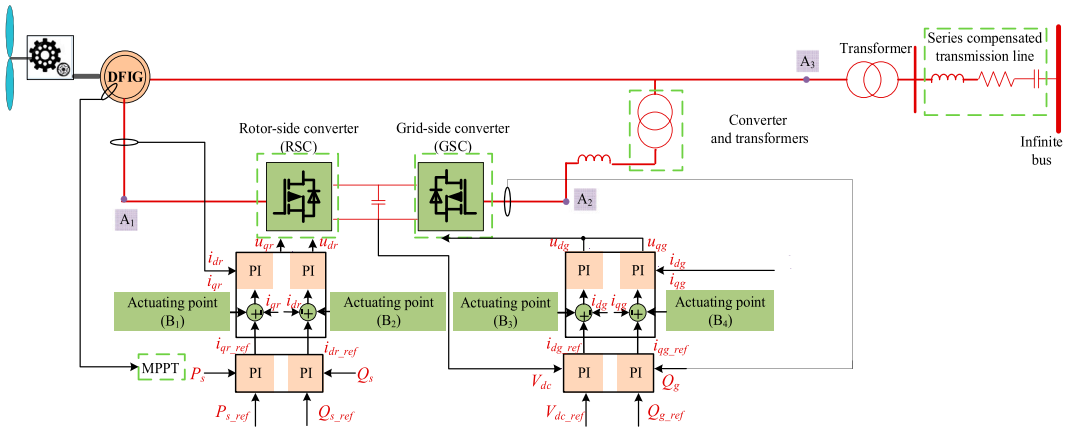

FIGURE 2
DFIG system and the feasible positions of monitoring points and actuating points.

TABLE 2 System component participation coefficients.

Frequency (Hz)	SC	RL	PC	T	M	Conv	G
8.3	0.56	0	0.48	0	0	0	0

(SC-series capacitor in compensated transmission line, RL-resistance and reactance in compensated transmission line, PC-parallel capacitor, T-transformer, M-multimass, Conv-convertor, G-generator).

TABLE 3 The MCOM of oscillation mode.

MCOM	U_d	U_q	I_d	I_q	P
A1	0.00001	0	0	0	0
A2	0.00001	0.00002	0	0	0
A3	0.00001	0.00002	1.2789	1.59611	0.55458

TABLE 4 The MCCM of oscillation mode.

Actuating point		MCCM
RSC	APC inner loop	86.38
	RPC inner loop	122.35
GSC	APC inner loop	0.009561
	RPC inner loop	0.008129

only the measurement effect needs to be judged. Besides, the observability and controllability index calculated by residue method is dimensional and can only be used for the comparison of the same type of signals.

4.4 Comparative analysis with geometric measures

The controllability and observability geometric measures are defined as the cosine of the eigenvector and the column or row of input or output matrix, shown as Eqs. 35, 36.

$$m_{cl} = \cos\left(\theta\left(\boldsymbol{f}_i, \boldsymbol{b}_l\right)\right) = \left|\boldsymbol{b}_l^T \boldsymbol{f}_i\right| / \left\|\boldsymbol{f}_i\right\| \left\|\boldsymbol{b}_l\right\| \tag{35}$$

$$m_{oj} = \cos\left(\theta\left(\boldsymbol{e}_i, \boldsymbol{c}_j\right)\right) = \left|\boldsymbol{c}_j \boldsymbol{e}_i\right| / \left\|\boldsymbol{e}_i\right\| \left\|\boldsymbol{c}_j\right\| \tag{36}$$

Where the meaning of $\boldsymbol{b}_l$ and $\boldsymbol{c}_j$ are consistent with Eq. 34. The larger the value of m_{cl}, the more aligned the lth input u_l with the ith eigenvalue. When the value of m_{cl} is close to 0, it means that these two vectors are nearly orthogonal, the control effect of u_l to mode component λ_i is weak. Similarly, the larger the value of m_{oj}, the more observable the mode component λ_i from the jth output y_j. Geometric measures normalize different units, and can measure the observability and controllability degree of the system independently. But the drawbacks compared to MCOM and MCCM are still obvious: 1) only one eigenvalue is studied at a time. It cannot show the relative monitoring and control effect with other modes, which is also important for the control device design. 2) the relevant information belonging to the same oscillation mode b (one pair of conjugate eigenvalues for distinct eigenvalues system and s_b pairs of conjugate eigenvalues for repeated eigenvalues system) are not considered together. Therefore, the physical meaning is not clear enough.

5 Application case study

To verify the effectiveness of MCOM and MCCM, this section applies them to the design of SSDC in a subsynchronous oscillation as shown in Figure 2. The

TABLE 5 Eigenvalues of system with SSDC inserted at different points.

Frequency (Hz)	Without SSDC	RPC	APC
8.3	**0.2485 + 51.8143i**	**−0.3158 + 51.9971i**	**−5.015 + 52.0435i**
8.2	−0.7194 + 51.7826i	−0.3652 + 50.0325i	1.521 + 51.254i
4.3	**−1.6329 + 27.0344i**	**−1.6335 + 27.0366i**	**−1.6345 + 27.0337i**
20.3	−2.3936 + 127.686i	−.4966 + 128.1397i	−3.2084 + 127.9487i
91.7	−0.0035 + 576.3534i	−0.0752 + 576.2622i	0.0875 + 576.2818i

APC, SSDC installed on the inner loop of active power control (APC); RPC, SSDC installed on the inner loop of reactive power control (RPC).

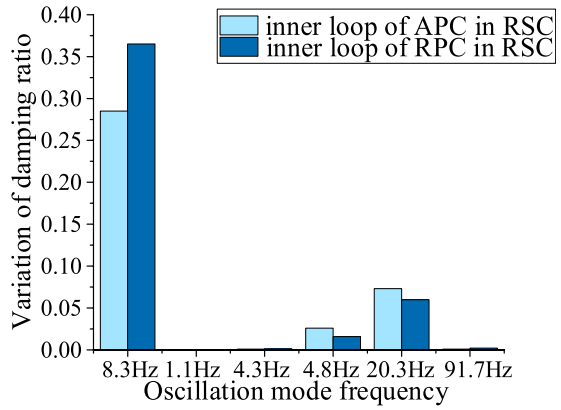

FIGURE 3
Damping ratios of various modes with SSDC at different points.

TABLE 6 The residue of oscillation mode.

Residue		U_d	U_q	I_d	I_q	P
RSC	APC inner loop	0.1337	0.1827	104.2577	104.3418	36.5295
	RPC inner loop	0.1633	0.2231	127.2726	127.3754	44.5934
GSC	APC inner loop	0.0002	0.0003	0.1587	0.1588	0.0556
	RPC inner loop	0.0002	0.0002	0.1336	0.1337	0.0468

TABLE 7 The m_{oj} of oscillation mode.

Output	U_d	U_q	I_d	I_q	P
m_{oj}	0.0005	0.0006	0.3663	0.3666	0.3484

system is a wind farm system in North China where subsynchronous oscillation has occurred. It contains 1.25 MW, 690 V doubly-fed wind turbines and series compensation of less than 8% equivalent compensation degree.

TABLE 8 The m_{cl} of oscillation mode.

Actuating point		m_{cl}
RSC	APC inner loop	0.4215
	RPC inner loop	0.5271
GSC	APC inner loop	0.0007
	RPC inner loop	0.0005

5.1 Mode comprehensive observability metric and mode comprehensive controllability metric calculation

Small-signal model is built in MATLAB/SIMULINK. In the test system, A_1, A_2, A_3 are taken as output signal monitoring points, corresponding to rotor side, grid side and wind farm outlet side respectively. Voltage, current and active power signals are measured as output signals. B_1, B_2, B_3, B_4 are taken as feasible actuating points for input signals, corresponding to the inner loop of active power control (APC) and reactive power control (RPC) of rotor side converter (RSC) and the inner loop of APC and RPC of grid side converter (GSC).

Perform eigenvalue analysis. All eigenvalues are distinct; therefore, we can apply the theory in the first case. The eigenvalues of unstable oscillation are 0.2485 ± 51.8143i, and the corresponding frequency is 8.3 Hz. The oscillation modes corresponding to other eigenvalues are stable. Furthermore, the participation factor analysis is carried out, and the participation coefficients of system components are calculated. It shows in Table 2 that the unstable oscillation mode is strongly related to the components interacting with the subsynchronous control (series capacitor in compensated transmission line). Therefore, the mode can be considered as the dominant mode of subsynchronous oscillation.

5.1.1 Mode comprehensive observability metric calculation and output signal/monitoring point selection

The MCOM of the dominant mode is calculated. It can be seen from Table 3 that the MCOM of dominant mode with

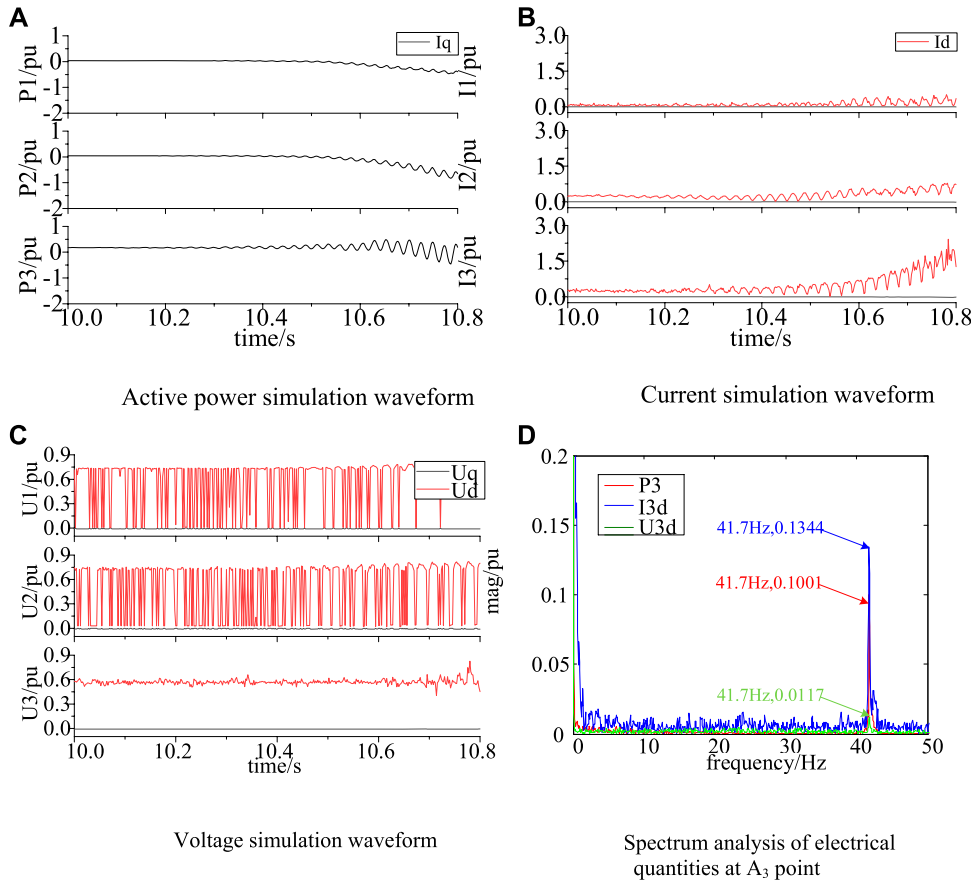

FIGURE 4
Simulations of each monitoring point and spectrum analysis of A_3. **(A)** Active power simulation waveform **(B)** Current simulation waveform **(C)** Voltage simulation waveform **(D)** Spectrum analysis of electrical quantities at A3 point.

current and active power signals in monitoring point A_3 are far greater than that of A_1 and A_2. Therefore, A_3 can better reflect the dominant mode components of subsynchronous oscillation. Moreover, for A3, the MCOM of the current is larger than that of the active power (m_{sos} (I_q) = 1.596, m_{sos} (I_d) = 1.279). So, the current of monitoring point A_3 is the most suitable output signal for the system.

5.1.2 Mode comprehensive controllability metric calculation and subsynchronous damping controller actuating point selection

In order to select the best actuating point for the SSDC, the inner loop of APC and RPC channels of the RSC and GSC is taken as the input signal points, and the MCCM of the dominant mode is calculated. The results are shown in Table 4.

It can be seen from Table 4 that the MCCM of the RSC is greater than that of the GSC, which shows that for the dominant mode, the relative control effect of the SSDC on the RSC is stronger than that of the GSC, i.e., the influence on other oscillation modes is small. Furthermore, actuating point in the inner loop of the RPC has the largest MCCM, so we choose to install SSDC in the inner loop of RPC in RSC.

5.1.3 Modal analysis comparison with and without subsynchronous damping controller

In order to analyze the effectiveness of the result above, the current signal at the outlet of the DFIG is selected as the output signal, and SSDC is installed on the inner loop of the APC and the inner loop of the RPC of the RSC respectively. The system eigenvalues after installing the SSDC are shown in Table 5.

It can be seen from Table 5 that compared with the dominant mode damping of subsynchronous oscillation without SSDC, two kinds of SSDC can effectively improve the damping of subsynchronous oscillation. However, when the APC loop is selected as the actuating point, the controller will have a greater

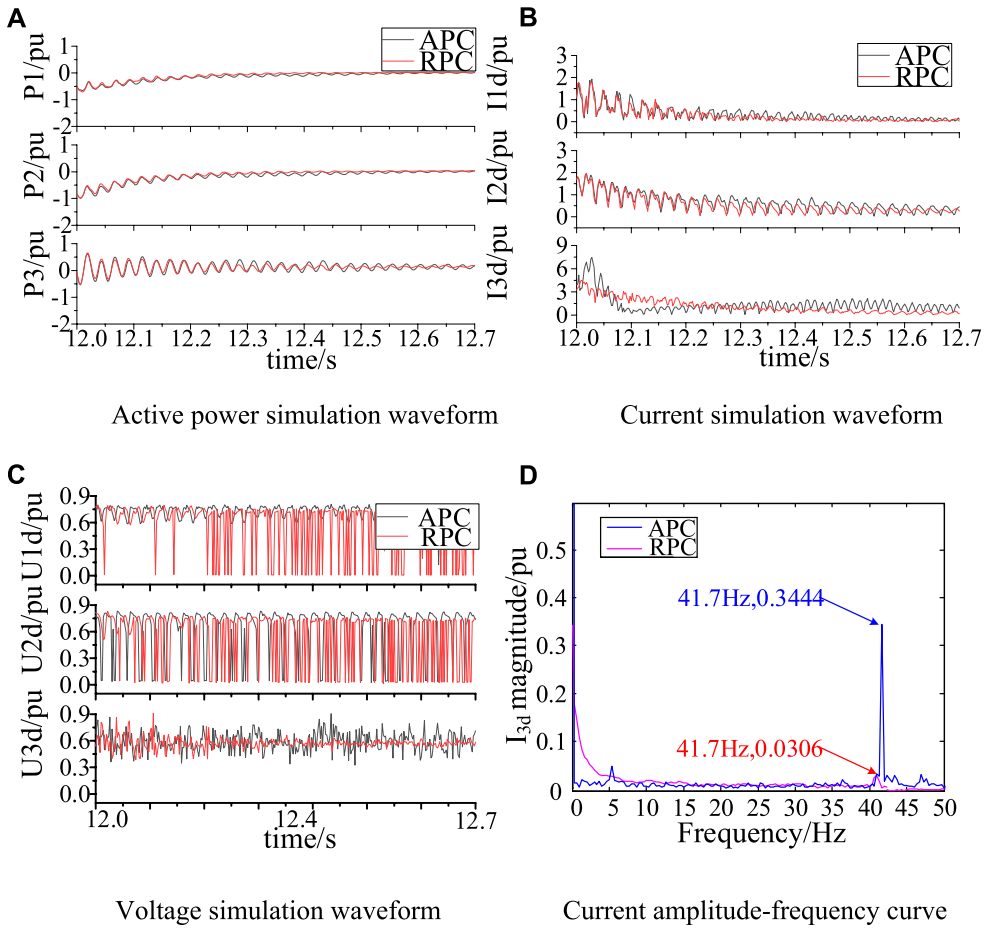

FIGURE 5
Simulations at different monitor points with control in APC and RPC. **(A)** Active power simulation waveform **(B)** Current simulation waveform **(C)** Voltage simulation waveform **(D)** Current amplitude-frequency curve.

control effect on the damping of another oscillation mode (4.8 Hz), and even lead to the negative damping of the mode. The reason is that the frequency of the oscillation mode is 8.2Hz, which is very close to that of the dominant mode. i.e., the control signal in APC loop has a strong influence on the oscillation modes except the dominant mode, which is consistent with the analysis of the MCCM.

In order to better explain the influence of installing additional controllers at different positions on different modes of the system, the variation of damping ratio of different oscillation modes before and after the installation of SSDC is compared, and the results are shown in Figure 3.

In the Figure 3, the light color and the dark color respectively show the influence on the system eigenvalues with SSDC installed on the inner loop of the APC and RPC of RSC. It can be seen that compared with the SSDC installed in the APC, the one installed in the RPC has a greater impact on dominant mode, and has less impact on other oscillation modes.

5.1.4 Calculation results of other methods

5.1.4.1 Results of participation factor

The components related to the oscillation mode are determined by the calculation of the participation factor, as shown in Table 2. However, since the state variables are not necessarily measurable, the reflection of the measured variables on the mode cannot be reflected by the participation factor.

5.1.4.2 Results of residue method

Calculate the residue of dominant mode according to Eq. 34. Since residues are often complex numbers, the magnitude of each pair of output signals and input signal/actuating point are shown as Table 6. The output signals (voltage, current and active power) are taken at point A_3. From Table 6, the best output signal and input signal actuating point are current and inner loop of RPC in RSC.

5.1.4.3 Results of geometric measures

Calculate geometric measures of dominant mode. From Table 7, the best output signal is current, while from Table 8, the best input signal actuating point is inner loop of RPC in RSC.

To summarize, the results of residue, participation factor do not consider the degree of observability and controllability independently, so they are not suitable for the situation where only observability needs to be measured. Besides, the results of residue and geometric measures show the same results as the metrics we proposed. However, as we consider the relative controllability of all the oscillation modes in MCCM, there is a greater difference between results of actuating point in RPC and APC (residue 22%, controllability geometric measure 25%, MCCM 42%). And from Table 5, we can find that the choice of RPC can avoid the damping ratio of 4.3 Hz being positive. Therefore, the results of MCCM are more reliable. Besides, the method of metrics can consider the coupled modes with same oscillation frequency together in system with repeated eigenvalues, which shows less limitation in application scene.

5.2 Application effect analysis with time domain simulation

In order to further confirm the effectiveness of the method above. With same test system shown in Figure 2, the time domain simulation model is established on PSCAD/EMTDC platform. After the system runs stably for 10s, the series compensation capacitor is put in, which causes subsynchronous oscillation with frequency of 8.3 Hz. All the quantities are shown in pu.

5.2.1 Validation of observability metric

Similarly, A_1, A_2 and A_3 are used as output signal monitoring points to compare the performance of voltage, current and active power signals on the dominant mode components. The oscillation waveform is shown in Figure 4.

It can be seen from Figures 4A–C that at 10.8s, the oscillation amplitude of power in A_3 is about 0.3, which is greater than A_2 (0.15) and A_1 (0.05); the oscillation amplitude of current in A_3 point is about 0.425, which is greater than A_2 (0.18) and A_1 (0.17), while the change of voltage is not obvious.

In order to intuitively compare the performance of three electrical quantities in A_3, the frequency spectrum of current, voltage and power waveform of monitoring point A_3 is analyzed. In order to improve the resolution of spectrum analysis, take the signals of P_3, I_{3d}, and U_{3d} at 10–12s for analysis. The result is shown in Figure 4D. Due to the property of Park transformation, the oscillation frequency is (50-f) Hz, i.e., 41.7 Hz. The oscillation amplitude of the current is 0.1344, and for active power, 0.1001, for voltage, only 0.01. In conclusion, the current in A_3 can better display the dominant mode components of the subsynchronous oscillation, which is consistent with the analysis results of the MCOM.

5.2.2 Validation of controllability metric

Then, the validity of the MCCM is verified. In 12s, the control signals obtained from I_3 through SSDC are input into the inner loop of APC and the inner loop of RPC in RSC respectively (B_1 and B_2). The time-domain simulation results show that the synchronous oscillation can be suppressed under the two control methods. The simulation waveform of suppression with the actuating point in RPC and APC is as Figure 5.

During the simulation time (12s–12.7s), It can be seen that: 1) at 12s, both kinds of SSDC have same oscillation amplitudes. At 12.7s, both of them can suppress the oscillation. 2) From Figure 5, for all the electrical quantities, actuating point in RPC loop has better control effect. Taking the result of P_3 as an example, oscillation amplitude of P_3 is decreased from about 0.5537 to 0.03 with control in RPC, which is less than half of the amplitude with control point in APC (from 0.5537 to 0.07). That is to say, when the actuating point is in RPC loop, the time for each electrical quantity to reach normal is shorter, and the suppression effect is more obvious, which is consistent with the analysis result of MCCM.

To summarize, applying the metrics, it is suggested that in the test power system, the current at the outlet of the wind farm is taken as the output signal, and the SSDC is installed in the inner loop of the RPC channel in RSC. From small-signal model and time-domain model we justify the result, which proves the effectiveness of MCOM and MCCM in the application on the oscillation suppression.

6 Conclusion

In this paper, the definitions of controllability metric and observability metric of oscillation modes are proposed. Based on these concepts, a theoretical system suitable for power systems with distinct or repeated eigenvalues is established. The main conclusions are as follows:

1) Modal observability metric represents the reflection degree of monitoring point measurement on an oscillation mode. Controllability metric characterizes the performance of

actuating point control input on an oscillation mode. Compared with the traditional modal analysis methods (residue measure, participation factor measure and geometric measure), CM and OM can reflect the characteristics of oscillation mode, and can be applied to system with or without repeated eigenvalues.

2) The simulation results show that the concepts of MCOM and MCCM are effective and generally applicable to multi-type oscillations of traditional power grid and wind power integrated power grid. By analyzing the results of different methods, it can be found that MCOM and MCCM can measure the degree of observability and controllability independently. And the large value of MCCM means not only strong influence on the dominant mode but also less influence on other oscillation modes, thus it is more reliable.
3) For systems with same repeated eigenvalues, the same eigenvalues cannot be fully decoupled. The MCOM and MCCM are proposed based on the Jordan canonical form of the system state space equation coefficient matrix. They can get rid of the repeated calculation of the same eigenvalues in the process of signal monitoring point and control signal selections by clustering the same eigenvalues into one modal and calculating once. This metric calculation process is simple and has clearer physical meaning.

Data availability statement

The raw data supporting the conclusions of this article will be made available by the authors, without undue reservation.

Author contributions

CZ designed the structure of the study and wrote the manuscript. XW contributed to the conception and idea of the study. ZL and SL built the simulation models. CZ and ZL performed the analysis. XW contributed to manuscript revision, proofreading, and approved the submitted version.

Funding

The Project Supported by National Natural Science Foundation of China (NSFC 51677114, 52077137).

Conflict of interest

The authors declare that the research was conducted in the absence of any commercial or financial relationships that could be construed as a potential conflict of interest.

Publisher's note

All claims expressed in this article are solely those of the authors and do not necessarily represent those of their affiliated organizations, or those of the publisher, the editors and the reviewers. Any product that may be evaluated in this article, or claim that may be made by its manufacturer, is not guaranteed or endorsed by the publisher.

References

Angulo, M. T., Aparicio, A., and Moog, C. H. (2020). Structural accessibility and structural observability of nonlinear networked systems. *IEEE Trans. Netw. Sci. Eng.* 7, 1656–1666. doi:10.1109/TNSE.2019.2946535

Dobson, I., Zhang, J., Greene, S., Engdahl, H., and Sauer, P. W. (2001). Is strong modal resonance a precursor to power system oscillations? *IEEE Trans. Circuits Syst. I.* 48, 340–349. doi:10.1109/81.915389

Domínguez-García, J. C., Ugalde-Loo, E., Bianchi, F., and Gomis-Bellmunt, O. (2014). Input–output signal selection for damping of power system oscillations using wind power plants. *Int. J. Electr. Power & Energy Syst.* 58, 75–84. doi:10.1016/j.ijepes.2014.01.001

Du, W., Fu, Q., and Wang, H. (2018). Method of open-loop modal analysis for examining the subsynchronous interactions introduced by VSC control in an MTDC/AC system. *IEEE Trans. Power Deliv.* 33, 840–850. doi:10.1109/TPWRD.2017.2774811

Gallardo, C., Herrera, M., Ocaña, M., Guanochanga, E., Camacho, O., and Cuichán, M. (2017). "Optimal location of sliding mode control and power system stabilizers in order to damp electromechanical oscillations using the residue," in 2017 IEEE PES Innovative Smart Grid Technologies Conference - Latin America (ISGT Latin America), Quito, Ecuador, 20-22 September 2017, 1–6. doi:10.1109/ISGT-LA.2017.8126711

Hamdan, H. M. A., and Hamdan, A. M. A. (1987). On the coupling measures between modes and state variables and subsynchronous resonance. *Electr. Power Syst. Res.* 13, 165–171. doi:10.1016/0378-7796(87)90001-0

He, J., Wu, X., Xu, Y., and Guerrero, J. M. (2019). Small-signal stability analysis and optimal parameters design of microgrid clusters. *IEEE Access* 7, 36896–36909. doi:10.1109/ACCESS.2019.2900728

Heniche, A., and Kamwa, I. (2002). *Control loops selection to damp inter-area oscillations of electrical networks*, Chicago, IL, USA: IEEE Power Engineering Society Summer Meeting, 240. doi:10.1109/PESS.2002.1043224

Huang, B., Sun, H., Liu, Y., Wang, L., and Chen, Y. (2019). Study on subsynchronous oscillation in D-PMSGs-based wind farm integrated to power system. *IET Renew. Power Gener.* 13, 16–26. doi:10.1049/iet-rpg.2018.5051

Lei, J., Shi, H., Jiang, P., Tang, Y., and Feng, S. (2019). An accurate forced oscillation location and participation assessment method for DFIG wind turbine. *IEEE Access* 7, 130505–130514. doi:10.1109/ACCESS.2019.2939871

Li, Y., Fan, L., and Miao, Z. (2020). Wind in weak grids: Low-frequency oscillations, subsynchronous oscillations, and torsional interactions. *IEEE Trans. Power Syst.* 35, 109–118. doi:10.1109/TPWRS.2019.2924412

Liu, H., Xie, X., Li, Y., Liu, H., and Hu, Y. (2017). Mitigation of SSR by embedding subsynchronous notch filters into DFIG converter controllers. *IET Gener. Transm. &amp. Distrib.* 11, 2888–2896. doi:10.1049/iet-gtd.2017.0138

Oscullo, J. A., and Gallardo, C. F. (2020). Residue method evaluation for the location of PSS with sliding mode control and fuzzy for power electromechanical oscillation damping control. *IEEE Lat. Am. Trans.* 18, 24–31. doi:10.1109/TLA.2020.9049458

Ping, J., Shuang, F., and Xi, W. (2014). Robust design method for power oscillation damping controller of STATCOM based on residue and TLS-ESPRIT. *Int. Trans. Electr. Energy Syst.* 24, 1385–1400. doi:10.1002/etep.1779

Pratzel-Wolters, D. (1982). "Jordan canonical forms for linear systems," in 1982 21st IEEE Conference on Decision and Control, Orlando, FL, USA, 08-10 December 1982, 950–951. doi:10.1109/CDC.1982.268285

Song, Y., and Blaabjerg, F. (2017). Overview of DFIG-based wind power system resonances under weak networks. *IEEE Trans. Power Electron.* 32, 4370–4394. doi:10.1109/TPEL.2016.2601643

Wang, C., Wen, C., and Lin, Y. (2017). Adaptive actuator failure compensation for a class of nonlinear systems with unknown control direction. *IEEE Trans. Autom. Contr.* 62, 385–392. doi:10.1109/TAC.2016.2524202

Wang, L., Xie, X., Jiang, Q., and Pota, H. R. (2014). Mitigation of multimodal subsynchronous resonance via controlled injection of supersynchronous and subsynchronous currents. *IEEE Trans. Power Syst.* 29, 1335–1344. doi:10.1109/TPWRS.2013.2292597

Wu, D., Tang, F., Dragicevic, T., Vasquez, J. C., and Guerrero, J. M. (2015). A control architecture to coordinate renewable energy sources and energy storage systems in islanded microgrids. *IEEE Trans. Smart Grid* 6, 1156–1166. doi:10.1109/TSG.2014.2377018

Wu, X., Ning, W., Yin, T., Yang, X., and Tang, Z. (2018). Robust design method for the SSDC of a DFIG based on the practical small-signal stability region considering multiple uncertainties. *IEEE Access* 6, 16696–16703. doi:10.1109/ACCESS.2018.2802698

Xie, X., Zhang, X., Liu, H., Liu, H., Li, Y., and Zhang, C. (2017). Characteristic analysis of subsynchronous resonance in practical wind farms connected to series-compensated transmissions. *IEEE Trans. Energy Convers.* 32, 1117–1126. doi:10.1109/TEC.2017.2676024

Zhou, Q., Ding, Y., Mai, K., Bian, X., and Zhou, B. (2019). Mitigation of subsynchronous oscillation in a VSC-HVDC connected offshore wind farm integrated to grid. *Int. J. Electr. Power & Energy Syst.* 09, 29–37. doi:10.1016/j.ijepes.2019.01.031

frontiers | Frontiers in Energy Research

TYPE Original Research
PUBLISHED 18 January 2023
DOI 10.3389/fenrg.2022.1039544

OPEN ACCESS

EDITED BY
Yanchi Zhang,
Shanghai Dianji University, China

REVIEWED BY
Yushuai Li,
University of Oslo, Norway
Zhengmao Li,
Nanyang Technological University, Singapore
Shuai Yao,
Southeast University, Nanjing, China,
in collaboration with reviewer ZL

*CORRESPONDENCE
Yafei Li,
3561146805@qq.com

SPECIALTY SECTION
This article was submitted to Smart Grids, a section of the journal Frontiers in Energy Research

RECEIVED 08 September 2022
ACCEPTED 11 November 2022
PUBLISHED 18 January 2023

CITATION
Cai R, Li Y and Qian K (2023), Optimal energy flow in integrated heat and electricity system considering multiple dynamics.
Front. Energy Res. 10:1039544.
doi: 10.3389/fenrg.2022.1039544

Optimal energy flow in integrated heat and electricity system considering multiple dynamics

Rong Cai, Yafei Li* and Kejun Qian

State Grid Suzhou Power Supply Company, Suzhou, China

Wide promotion of combined heat and power (CHP) units necessitates the combined operation of the power and heating system. However, the dynamics and nonlinearity in integrated heat and electricity systems (IHES) remain an obstacle to efficient and accurate analysis. To handle this issue, this paper constructs an optimal energy flow (OEF) model for the coordinated operation of the IHES considering the multiple dynamics. The dynamic heating system model is formulated as a set of nonlinear partial differential and algebraic equations (PDAE). The dynamic CHP model is formulated as a set of nonlinear differential and algebraic equations (DAEs). Then, the finite difference method (FDM) is adopted to make the dynamics tractable in the OEF. On this basis, a comprehensive OEF model for IHES is proposed. Simulations in two cases verify the effectiveness of the proposed method and highlight the significance of the dynamics in IHES.

KEYWORDS

combined heat and power, optimal energy flow, dynamics, integrated energy system, finite difference method

1 Introduction

Due to the increasingly severe energy crisis, the technology that can achieve higher energy utilization efficiency has attracted significant attention worldwide. The CHP unit, which co-generates the heat and electric power by recovering the waste heat, has been broadly utilized to reduce energy consumption (Ramsebner et al., 2021), (Zang et al., 2021), (Cruz et al., 2018). As a result, the power and heating systems are coupled more intensively, deriving the development of the IHES. On the one hand, the integration of the heating system provides additional flexibility for the power system because the dynamics in the heat network and load pose the energy storage property for operation (Zhang et al., 2021a). On the other hand, the intensive coupling introduces massive constraints for the power system operation because the heat power supply has priority over the electric power supply in the CHP unit. Thus, it is significant to perform a comprehensive analysis for the combined operation of the power system and heating system, thereby fully exploiting the economic potential of IHES (Shabanpour and Seifi, 2016).

To study the combined analysis in IHES, the modeling of heating system and CHP unit plays a fundamental role (Wu et al., 2016). Reference (Liu et al., 2016) firstly studied the modeling of IHES, where the static heating system model was proposed to describe the heat loss during the transmission process. The proposed static model has been widely employed in the planning (Gu et al., 2014), optimization (Sartor et al., 2014), and security analysis (Sartor et al., 2014) of IHES due to its superiority in brevity and clarity. However, such a model neglects the transmission delay of the heat power flow and is unsuitable for analysis in a large-scale system. Thus, various studies devoted their effort to accurately modeling the heating systems. A widely-used method is the node method proposed in (Palsson, 1999). In the node method, the mass flow inside a pipe is discretized into a set of small elements, and the temperature distribution along the pipe is considered as a combination of historic pipe inlet temperature (Li et al., 2016), (Zhang et al., 2022a). The node method performs better than the static model because it further considers the transmission delay of water flow. However, it suffers from the following deficiencies: 1) It is challenging to extend the node method into a heating system with the variable mass flow because the transmission delay in the node method needs to be continuously updated. Such a treatment is rather time-consuming (Dancker and Wolter, 2021). 2) The node method only focused on the relationships between the pipe inlet and outlet temperatures (Yao et al., 2021). Thus, the temperature distribution along the pipe cannot be obtained.

To address these issues, an efficient method is to formulate the energy conservation law for the mass flow infinitesimal, thereby deriving the thermal dynamics governed by PDE (Zhang et al., 2021b). However, implementing the combined analysis with PDE is challenging. Therefore, various methods have been proposed to handle the PDE and explore the dynamic heating system model for further analysis. Reference (Yao et al., 2021) adopted the FDM to discretize the PDE set, and the obtained model was verified through the OEF in the IHES at the distribution level. Since the step sizes significantly influence the numerical performance of FDM, reference (Wang et al., 2017) optimized the time and space size to make a trade-off between the modeling accuracy and complexity. In (Zhang N et al., 2022), the multiple timescales in IHES were considered. An event-triggered distributed hybrid control scheme was then proposed to guarantee secure and economic operation. On this basis, reference (Li et al., 2020) investigated the islanded and network-connected modes in IHES and developed a uniform dynamic Newton-Raphson algorithm to solve the multiple-mode energy management problem in a distributed IHES. Despite the FDM, the function transformation method is another mainstream method to solve thermal dynamics. In this regard, reference (Chen et al., 2021) transformed the PDE into the ODE in the Fourier domain. On this basis, an OEF model for IHES was developed to verify the effectiveness of the proposed method for economic analysis. However, the accuracy of the Fourier-based method depends on the number of sine components and scales with the modeling complexity. It is difficult to determine the suitable modeling accuracy for applications in different scenarios. In (Dai et al., 2019), a heat current model was further proposed using Fourier transform, and the thermal dynamics were modeled as an equivalent RLC circuit. In the proposed method, the dynamics of the heat network and load were both considered. Another type of function transformation method is the Laplace-based method in (Yang et al., 2020), where the time-frequency transformation is employed to construct the dynamic heating system model and solve the economic dispatch problem. To summarize, although great effort has been devoted to investigating the modeling and optimization of IHES, the following gaps still exist.

1) The current method mainly focused on the modeling of the heating system and proposed different solutions to the thermal dynamics. However, nonlinearity was neglected in most literature.
2) Most studies considered the coupling unit as the capacity constraint in the optimization problem, in which the physical properties and dynamics in the equipment are over-simplified, thereby influencing the practicality of the proposed work.

To overcome the deficiencies, this paper models the dynamics inside the heating system and the CHP units, with which a finite difference method is employed for numerical discretization. Also, a comprehensive OEF model is developed to investigate the coordinated operation of the IHES and explores the economic influences of heating system integration. The main contributions of this paper are summarized below.

1) We propose a complete characterization of the IHES model, including the heating system model governed by nonlinear PDAEs, the power system model governed by nonlinear algebraic equations, and the CHP unit model governed by nonlinear DAEs.
2) Based on the characterization of IHES, we develop a novel OEF model considering the dynamics and nonlinearity, where the operational and physical constraints of different components in IHES are considered.

The remainder of this paper is as follows. The IHES model considering multiple dynamics is presented in Section 2. The OEF model for IHES is developed in Section 3. The numerical simulation and conclusion are given in Section 4 and Section 5, respectively.

2 IHES model considering multiple dynamics

An IHES is a complex system containing the power system part and heating system part. The two subsystems are coupled

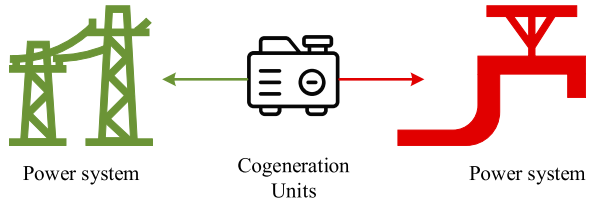

FIGURE 1
Sketch of IHES.

through energy cogeneration and conversion equipment, such as CHP units and electric boilers. In this section, we firstly give the basic model of the IHES and clarify the internal dynamics, which provide the basis for OEF modeling. The structure of the IHES is shown in Figure 1.

2.1 Heating system

The heating system is a two-layer system, including the supply and return networks. The heat power is generated at the heat sources and then transferred through the pipes in the supply network. After exchanging the heat power at consumers, the water reflows into the return work and is sent to the heat sources, thereby forcing a cycle. Since the heat power is mainly carried by the water and consumed as high-temperature water, the heating system model contains the hydraulic and thermal parts. The hydraulic part describes the mass flow rate and pressure distribution. The thermal part describes the temperature and heat power distribution (Liu et al., 2016). The explanations for the two-part model are given below.

2.1.1 Hydraulic part

Firstly, the mass flow distribution obeys mass conservation law at the nodes, which is expressed as (Liu et al., 2016):

$$\mathbf{A}\boldsymbol{m} = \boldsymbol{d} \tag{1}$$

where $\mathbf{A}$ is the node-branch incidence matrix in the heating system, $\boldsymbol{m}$ is the vector of mass flow rate along the pipes, $\boldsymbol{d}$ is the vector of mass flow rate injecting into the nodes.

Secondly, the pressure distribution obeys Kirchhoff's law in the loop, which is expressed as (Liu et al., 2016):

$$\mathbf{B}\Delta\boldsymbol{p} = \mathbf{0} \tag{2}$$

where $\mathbf{B}$ is the loop-branch incidence matrix in the heating system, $\Delta\boldsymbol{p}$ is the vector of pipe pressure drop. The pipe pressure drop is mainly determined by the mass flow rate, which is expressed as:

$$\Delta p = Km^2 \tag{3}$$

where K is the pipe friction resistance. The elements in $\mathbf{A}$ and $\mathbf{B}$ are given below.

$$\begin{cases} a_{ij} = \pm 1 & \dfrac{\text{node } i \text{ is the inlet}}{\text{outlet of pipe } j} \\ a_{ij} = 0 & \text{node } i \text{ is independent of pipe } j \end{cases} \tag{4}$$

$$\begin{cases} b_{ij} = 1 & \text{the direction of loop } i \text{ is the same as pipe } j \\ b_{ij} = -1 & \text{the direction of loop } i \text{ is opposite to pipe } j \\ b_{ij} = 0 & \text{loop } i \text{ is independent of pipe } j \end{cases} \tag{5}$$

2.1.2 Thermal part

Firstly, the nodes in the heating system are modeled as heat changers, which relate the mass flow rate with the temperature. The corresponding model is expressed as:

$$\phi = C_w d\left(T^{n,s} - T^{n,r}\right) \tag{6}$$

where C_w is the specific heat capacity of water, ϕ is the heat power, T is the temperature in the heating system, the superscript n denotes the variable at the nodes, the superscripts s and r denote the variables in the supply and return networks, respectively.

Secondly, the temperature distribution along the pipe is modeled as a function of time and space. For simplification, we neglect the thermal conduction between the adjacent flow infinitesimal since its value is sufficiently small (Palsson, 1999). On this basis, the temperature distribution along the pipe is expressed as (Yao et al., 2021):

$$\frac{\partial T^p}{\partial t} + v\frac{\partial T^p}{\partial x} + \frac{v}{C_w m\lambda}\left(T^p - T^a\right) = 0 \tag{7}$$

where the superscript p denotes the variables along the pipe, v is the flow velocity, λ is the thermal resistance of the pipe, T^a is the ambient temperature.

Thirdly, the heat water flow obeys the energy conservation law at nodes, i.e., the temperature mixture equation, which is expressed as:

$$T_i^n \sum_{b\in\aleph_{s,i}} m_b = \sum_{k\in\aleph_{e,i}} m_k T_k^{p,o} \tag{8}$$

where $T^{p,o}$ is the temperature at the pipe outlet, $Tn\ i$ is the temperature at node i, $\aleph_{s,i}$ is the set of pipes whose inlet is node i, $\aleph_{e,i}$ is the set of pipes whose outlet is node i.

Finally, the temperature at the pipe inlet equals the temperature at the corresponding inlet node, which is expressed as:

$$T_b^{p,i} = T_i^n \; b \in \aleph_{s,i} \tag{9}$$

It should be noted that Eqs 7–9 hold both in supply and return networks since they are symmetrical.

2.2 Power system

The power system mainly adopts the AC power flow model to describe the active/reactive power and voltage distribution. The power balance at buses is expressed as:

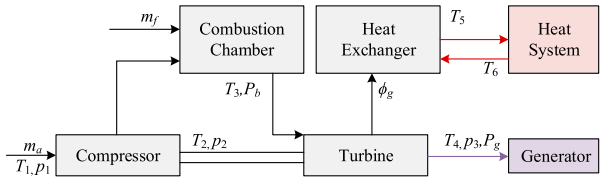

FIGURE 2
Sketch of CHP unit.

$$P_{G,i} - P_{L,i} = U_i \sum_j U_j \left(G_{ij} \cos \theta_{ij} + B_{ij} \sin \theta_{ij} \right) \tag{10}$$

$$Q_{G,i} - Q_{L,i} = U_i \sum_j U_j \left(G_{ij} \sin \theta_{ij} - B_{ij} \cos \theta_{ij} \right) \tag{11}$$

where P and Q are the net active and reactive power at buses, respectively; U and θ are the voltage magnitude and phase angle, respectively; G_{ij} and B_{ij} are the conductance and susceptance between bus i and bus j, respectively. The power flow balance at branches is expressed as:

$$P_{ij} = U_i U_j \left(G_{ij} \cos \theta_{ij} + B_{ij} \sin \theta_{ij} \right) - G_{ij} U_i^2 \tag{12}$$

$$Q_{ij} = U_i U_j \left(G_{ij} \sin \theta_{ij} - B_{ij} \cos \theta_{ij} \right) + B_{ij} U_i^2 \tag{13}$$

where P_{ij} and Q_{ij} are the active and reactive power flow between bus i and bus j, respectively.

2.3 Combined heat and power units

The CHP unit is a comprehensive system composed of different subsystems. A typical structure of the CHP unit is shown in Figure 2. In the CHP units, the gas turbine consumes the fuel flow to generate the electric power and high-temperature smoke flow. The high-temperature smoke flow is then sent into the heat exchanger to heat the water. Finally, the obtained hot water is provided for the consumers in the heating system (Zhou et al., 2021).

We assume that the heat loss is neglected inside the CHP unit because its value is sufficiently small. On this basis, the detailed model of the CHP unit is introduced below.

According to Figure 2, the compressor firstly consumes electric power to supercharge the air and obtain high-temperature and pressure for further processing, which is expressed as:

$$p_{2,t} = CPR_1 \times p_{1,t} \tag{14}$$

$$T_{2,t} = T_{1,t} \left[1 + \frac{\left(CPR_1^{\beta_1 - 1/\beta_1} - 1 \right)}{\eta_1} \right] \tag{15}$$

where p_1 and p_2 are the input and output pressure of the compressor, respectively; T_1 and T_2 are the input and output temperature of the compressor, respectively; CPR_1 is the compressor ratio, β_1 is the air isentropic index, which is 1.4 in this paper; η_1 is the efficiency of the compressor, which is 0.8 in this paper (Xu et al., 2015). The electric power consumption in the compressor is expressed as:

$$P_{c,t} = C_a m_{a,t} \left(T_{2,t} - T_{1,t} \right) \tag{16}$$

where C_a is the specific heat capacity of air, m_a is the mass flow rate of the input air. The energy balance in the combustion chamber is expressed as:

$$\beta_2 \frac{dT_{3,t}}{dt} = m_{a,t} C_a T_{2,t} + m_{f,t} \left(H_g + LHV \right) - C_s \left(m_{a,t} + m_{f,t} \right) T_{3,t} \tag{17}$$

where β_2 is the heat storage coefficient of the combustion chamber, T_3 is the temperature in the combustion chamber, m_f is the mass flow rate of input fuel, H_g is the fuel enthalpy, LHV is the low calorific value of the input fuel, C_s is the specific heat capacity of smoke.

The temperature and pressure at the inlet and outlet in the turbine are expressed as:

$$p_{3,t} = CPR_2 p_{2,t} \tag{18}$$

$$T_{4,t} = T_{3,t} \left[1 - \left(1 - CPR_2^{\frac{\beta_1 - 1}{\beta_1}} \right) \beta_3 \right] \tag{19}$$

where CPR_2 is the compressor ratio in the turbine, β_3 is the smoke isentropic index, p_3 is the output pressure of the turbine, T_4 is the output temperature of the turbine. The power carried by the turbine is expressed as (Ailer et al., 2001):

$$P_{b,t} = C_s \left(m_{a,t} + m_{f,t} \right) \left(T_{4,t} - T_{3,t} \right) \tag{20}$$

On this basis, the power supplied for the generator and the heat exchanger is expressed as:

$$P_{g,t} = \eta_2 \eta_3 \left(P_{b,t} - P_{c,t} \right) \tag{21}$$

$$\phi_{g,t} = \eta_2 \left(1 - \eta_3 \right) \left(P_{b,t} - P_{c,t} \right) \tag{22}$$

where η_2 is the mechanical efficiency of the turbine, η_3 is the ratio of power supplied for the generator, P_g and ϕ_g are the supplied electric power and heat power, respectively. The energy conservation in the heat exchanger is expressed as:

$$\beta_4 \frac{dT_{5,t}}{dt} = \phi_{g,t} - C_w m_{w,t} \left(T_{5,t} - T_{6,t} \right) \tag{23}$$

where β_4 is the heat storage coefficient of the heat exchanger, m_w is the water leaving the heat exchanger, T_5 and T_6 are the outlet and inlet temperatures of the heat exchanger. Eq. 23 indicates that the temperature change in the heat exchanger is caused by the injecting heat power and leaving heat water, T_5 and T_6 refer to the output and input temperature of the heat exchanger, respectively.

3 Optimal energy flow model in IHES

In this part, we present the optimal energy flow model in IHES. We firstly introduce the solution to the dynamics in IHES

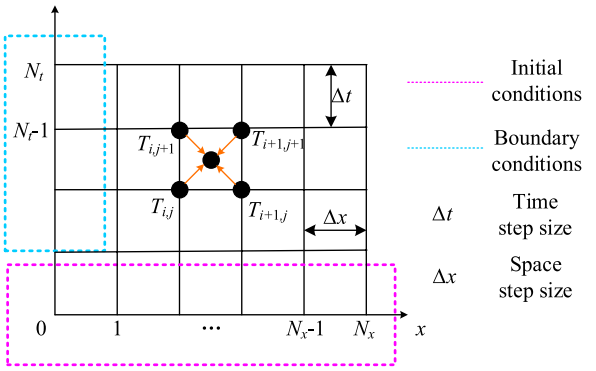

FIGURE 3
Illustration of FDM for thermal dynamics.

so that the corresponding ODEs and PDEs can be included in the OEF model. On this basis, we formulate the OEF model, where multiple dynamics are comprehensively considered.

3.1 Dynamics in integrated heat and electricity system

Under normal operations, the power system reaches steady-state rapidly because the electric power flow transfers at light speed. In contrast, the heat power transfers at the water flow velocity, and the corresponding processes are much longer. Thus, the dynamics in IEHS under regular operation mainly contain the thermal dynamics in the heating systems and coupling units. However, we cannot directly apply the PDE and ODE in Section 2 for optimization. Thus, the FDM is used here to discretize these equations into algebraic equations.

We adopt a second-order scheme to discretize (7) due to its superiority in convergence and stability (Yao et al., 2021). Firstly, we discretize the district ($0 \le x \le L$, $0 \le t \le \Gamma$) with two sets of lines to obtain the differential grid in Figure 3, where N_x and N_t denote the numbers of space and time steps, respectively; Δx and Δt denote the space and time step sizes, respectively.

Expanding Eq. 7 at $x = x_{i+1/2}$, $t = t_{j+1/2}$, we can replace the differential terms with the following quotients by neglecting the high-order remainders.

$$\frac{\partial T^p}{\partial x} = \frac{T^p_{i+1,j} + T^p_{i+1,j+1} - T^p_{i,j+1} - T^p_{i,j}}{2\Delta x} \tag{24}$$

$$\frac{\partial T^p}{\partial t} = \frac{T^p_{i,j+1} + T^p_{i+1,j+1} - T^p_{i,j} - T^p_{i+1,j}}{2\Delta t} \tag{25}$$

$$T^p = \frac{T^p_{i,j+1} + T^p_{i+1,j+1} + T^p_{i,j} + T^p_{i+1,j}}{4} \tag{26}$$

$$\Delta x = \frac{L}{N_x}, \Delta t = \frac{\Gamma}{N_t} \tag{27}$$

Substituting Eqs 24–26 into Eq. 7, the temperature distribution along the pipe can be expressed with the following algebraic equations.

$$T^p_{i+1,j+1} = J_1 T^p_{i,j} + J_2 T^p_{i,j+1} + J_3 T^p_{i+1,j} + J_4 T_a \tag{28}$$

$$\begin{cases} J_1 = \dfrac{2C_w m\lambda\Delta x + 2C_w m\lambda v\Delta t - v\Delta t\Delta x}{2C_w m\lambda\Delta x + 2C_w m\lambda v\Delta t + v\Delta t\Delta x} \\ J_2 = \dfrac{-2C_w m\lambda\Delta x + 2C_w m\lambda v\Delta t - v\Delta t\Delta x}{2C_w m\lambda\Delta x + 2C_w m\lambda v\Delta t + v\Delta t\Delta x} \\ J_3 = \dfrac{2C_w m\lambda\Delta x - 2C_w m\lambda v\Delta t - v\Delta t\Delta x}{2C_w m\lambda\Delta x + 2C_w m\lambda v\Delta t + v\Delta t\Delta x} \\ J_4 = \dfrac{4v\Delta t\Delta x}{2C_w m\lambda\Delta x + 2C_w m\lambda v\Delta t + v\Delta t\Delta x} \end{cases} \tag{29}$$

As for the PDE in Eqs 17, 23, we adopt the backward Euler scheme for discretization. The differential term is expressed as:

$$\frac{dT_{3,t}}{dt} = \frac{T_{3,t} - T_{3,t-1}}{\Delta t} \tag{30}$$

$$\frac{dT_{5,t}}{dt} = \frac{T_{5,t} - T_{5,t-1}}{\Delta t} \tag{31}$$

Substituting Eqs 30, 31 into Eqs 17, 23, we can get:

$$T_{3,t} = \frac{\beta_2 T_{3,t-1} + \Delta t\left(m_{a,t}C_a T_{2,t} + m_{f,t}\left(H_g + LHV\right)\right)}{\beta_2\left(1 + C_s\left(m_{a,t} + m_{f,t}\right)\right)} \tag{32}$$

$$T_{5,t} = \frac{\Delta t\phi_{g,t} + \Delta t C_w m_{w,t} T_{6,t} + \beta_4 T_{5,t-1}}{\beta_4 + C_w m_{w,t}\Delta t} \tag{33}$$

3.2 Constraints formulation

3.2.1 Constraints in power system

From the optimization view, computing the OEF in the power system with a complete AC power flow model is of a great computational burden. Thus, we adopt an improved DC power flow model to construct the constraints in the power system, where the reactive power and voltage amplitude are both considered (Yang et al., 2018). Firstly, the phase angles of different buses vary slightly in the power system at the transmission level. Thus, we can obtain the following expressions:

$$\sin\theta_{ij} \approx \theta_{ij}, \cos\theta_{ij} \approx 1 - \frac{\theta^2_{ij}}{2} \tag{34}$$

On this basis, we can get further approximations since voltage magnitude is commonly close to 1.0 p.u.

$$U_i U_j \theta_{ij} \approx \theta_{ij}, U_i U_j \theta^2_{ij} \approx \theta^2_{ij} \tag{35}$$

With the above equations, the power flow model can be reformulated as (Zhang et al., 2022a):

$$P_{G,i} - P_{L,i} = \sum_{i,j} P_{ij} + \sum_{i,j} G_{ij} U_i^2 \tag{36}$$

$$Q_{G,i} - Q_{L,i} = \sum_{i,j} Q_{ij} - \sum_{i,j} B_{ij} U_i^2 \tag{37}$$

$$P_{ij} = G_{ij} \frac{U_i^2 - U_j^2}{2} - B_{ij}\theta_{ij} + \frac{G_{ij}}{2}\left(\theta_{ij}^2 + U_{ij}^2\right) \tag{38}$$

$$Q_{ij} = B_{ij} \frac{U_j^2 - U_i^2}{2} - G_{ij}\theta_{ij} - \frac{B_{ij}}{2}\left(\theta_{ij}^2 + U_{ij}^2\right) \tag{39}$$

During the optimization, the electric states should not only satisfy the power flow equations but also satisfy the operational constraints as follows.

$$U_i^{\min} \le U_i \le U_i^{\max} \tag{40}$$

$$-\frac{\pi}{2} \le \theta_i \le \frac{\pi}{2} \tag{41}$$

$$\sqrt{P_{ij}^2 + Q_{ij}^2} \le S_{ij}^{\max} \tag{42}$$

$$P_{G,i}^{\min} \le P_{G,i} \le P_{G,i}^{\max} \tag{43}$$

$$Q_{G,i}^{\min} \le Q_{G,i} \le Q_{G,i}^{\max} \tag{44}$$

where Eq. 40 is the voltage magnitude constraints, Eq. 41 is the phase angle constraints, Eq. 42 is the thermal constraints along the branches, Eqs 43, 44 are the active and reactive power constraints at generators.

3.2.2 Constraints in heating system

Despite the constraints in Eqs 1–3, 8–9, the OEF problem in the heating system is supposed to include the following operational constraints:

$$p_i^{\min} \le p_i \le p_i^{\max} \tag{45}$$

$$m_i^{\min} \le m_i \le m_i^{\max}, d_i^{\min} \le d_i \le d_i^{\max} \tag{46}$$

$$\gamma^{\min} m_{i,t-1} \le m_{i,t} \le \gamma^{\max} m_{i,t-1}, \gamma^{\min} d_{i,t-1} \le d_{i,t} \le \gamma^{\max} d_{i,t-1} \tag{47}$$

$$T_{i,t}^{n,s,\min} \le T_{i,t}^{n,s} \le T_{i,t}^{n,s,\max} \tag{48}$$

$$T_{i,t}^{n,r,\min} \le T_{i,t}^{n,r} \le T_{i,t}^{n,r,\max} \tag{49}$$

where Eq. 45 is the security constraint for node pressure, Eq. 46 is the capacity constraint for mass flow rate, Eq. 47 is the changing ratio constraint for mass flow rate, Eqs 48, 49 are the supply and return temperature constraints at nodes, respectively.

3.2.3 Constraints in CHP units

The CHP units combine the power system and heating system. Thus, the constraints in CHP units should firstly include the connections between different systems, which are expressed as:

$$P_{g,t} = P_{G,i,t}\ i \in \aleph_{\mathrm{CHP}} \tag{50}$$

$$m_{w,t} = d_{i,t}\ i \in \aleph_{\mathrm{CHP}} \tag{51}$$

$$T_{5,t} = T_i^{n,s},\ T_{6,t} = T_i^{n,r}\ i \in \aleph_{\mathrm{CHP}} \tag{52}$$

In the above equations, $\aleph_{\mathrm{CHP}}$ is the set of buses/nodes equipped with the CHP units. Eq. 50 indicates that the supplied power of the turbine in the CHP unit equals the active power generation at electric sources; Eq. 51 indicates that the injecting mass flow rate at the sources nodes equals the water flow in the heat exchanger; Eq. 52 indicates that the supply and return temperature at the sources nodes equals to the output and input temperature of the heat exchanger.

Furthermore, the constraints for the secure operation of CHP units include:

$$T_1^{\min} \le T_{1,t} \le T_1^{\max} \tag{53}$$

$$p_1^{\min} \le p_{1,t} \le p_1^{\max} \tag{54}$$

$$m_f^{\min} \le m_{f,t} \le m_f^{\max} \tag{55}$$

$$p_3^{\min} \le p_{3,t} \le p_3^{\max} \tag{56}$$

$$\alpha^{\min} m_{f,t} \le m_{a,t} \le \alpha^{\max} m_{f,t} \tag{57}$$

$$T_3^{\min} \le T_{3,t} \le T_3^{\max} \tag{58}$$

$$T_4^{\min} \le T_{4,t} \le T_4^{\max} \tag{59}$$

In the above equations, Eqs 53, 54 refer to the constraints at the input temperature and pressure of the air flow in the compressor. Eq. 55 refers to the constraints at the input fuel flow in the combustion chamber. Eqs 56, 58 refer to the constraints at the input temperature and pressure of smoke flow in the turbine. Eq. 57 refers to the relationships between the input air and fuel flows, where $\mu^{\min}$ and $\mu^{\max}$ refer to the minimum and maximum mixture ratio between the air flow and fuel flow. Eq. 59 refers to the constraints at the output temperature in the turbine.

3.3 Summary of the optimization model

The OEF in IHES aims to minimize the operational cost over the period Γ. The objective function of the OEF problem is formulated as:

$$\min \sum_{t=1}^{N_t} \left(c_1 f_{i,t} + c_2 g_{j,t}\right) i \in \aleph_{\mathrm{CHP}}, j \in \aleph_G \tag{60}$$

where c_1 and c_2 are the unit prices of the fuel and coals for the CHP units and the traditional generators, $\mathbb{N}_G$ is the set of buses equipped with traditional generators, f is the function of consumed fuel regarding the electric power, g is the function of consumed coal regarding the electric power. f and g are expressed as (Yao et al., 2021):

$$f_i = \mu_{11} P_{G,i}^2 + \mu_{12} P_{G,i} + \mu_{13}\ i \in \aleph_{\mathrm{CHP}} \tag{61}$$

$$g_i = \mu_{21} P_{G,i}^2 + \mu_{22} P_{G,i} + \mu_{23}\ i \in \aleph_G \tag{62}$$

where μ_{11}-μ_{13} and μ_{21}-μ_{23} are the cost coefficients of the CHP units and generators, respectively. On this basis, the OEF model in IHES considering multiple dynamics is summarized as follows.

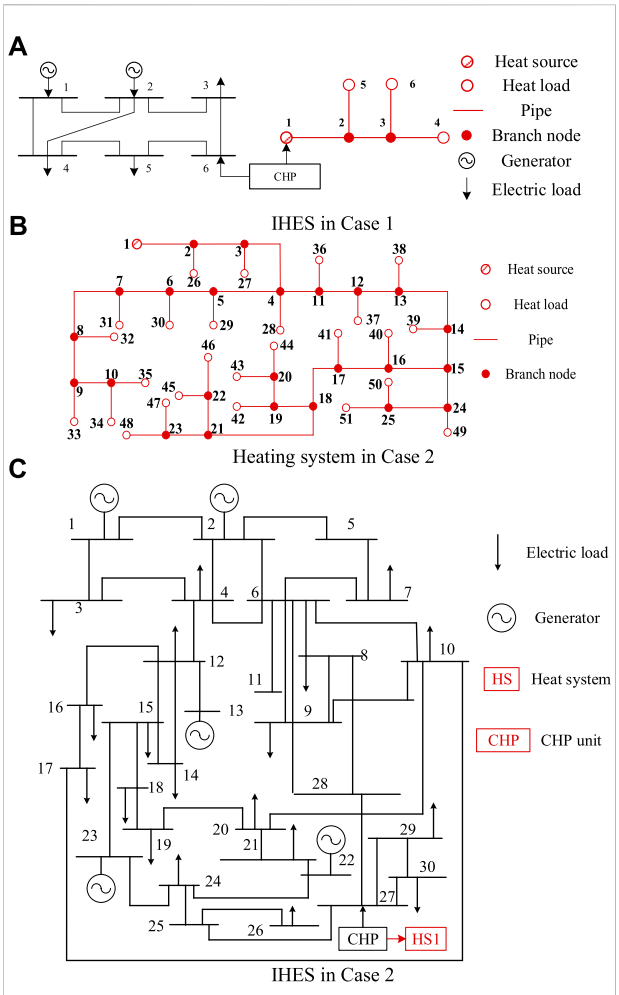

FIGURE 4
Structures of systems in case study.

$$\begin{aligned} &\min \sum_{t=1}^{N_t} \left(c_1 f_{i,t} + c_2 g_{j,t}\right) i \in \aleph_{\mathrm{CHP}}, j \in \aleph_G \\ &s.t.\ \text{Eqs. (36)} - \text{(44)} \\ &\quad \text{Eqs. (1)} - \text{(3)},\ \text{(8)} - \text{(9)},\ \text{(28)},\ \text{(45)} - \text{(49)} \\ &\quad \text{Eqs. (14)} - \text{(16)},\ \text{(18)} - \text{(22)},\ \text{(32)} - \text{(33)},\ \text{(50)} - \text{(59)} \\ &\quad \text{Eqs. (61)} - \text{(62)} \end{aligned} \tag{63}$$

The proposed model is a nonlinear programming problem with a quadratic objective function. In this paper, the problem is solved by the commercial software IPOPT.

4 Case studies

4.1 System description

To demonstrate the validity of the proposed IHES model and the effectiveness of the OEF method, numerical simulations are implemented in two different systems. Case 1 is a simple IHES,

TABLE 1 Parameters of CHP unit in Case 1.

Name	Value	Name	Value
β_1	1.4	H_g (kJ/kg)	48.91
η_1	0.85	LHV (kJ/kg)	5372
C_a (kJ/kg.K)	1004	η_2	0.9
C_s (kJ/kg.K)	1400	η_3	0.5
C_w (kJ/kg.K)	4182	β_2 (kJ/K)	4000
β_3	0.98	β_4	0.003

where a 6-bus power system and a 6-node heating system are coupled through a CHP unit. The structure of the IHES in Case 1 is shown in Figure 4A, and the detailed data can be found in (Lu et al., 2020). Case 2 is a complex IHES, where the IEEE 30-bus power system and two 51-node heating systems through 2 CHP units. The structures of the heating system and IHES in Case 2 are shown in Figures 4B,C, respectively. The detailed data of the power system and heating systems can be found in (Zhang et al., 2022b) and (Zhang et al., 2021a), respectively. All the simulations are performed on a PC with Intel i7 and 8GB RAM and coded by Matlab 2021b.

4.2 Case 1

In this section, we first perform the numerical simulation of the dynamic CHP unit model to analyze the operational property of the CHP unit in IHES. The parameters of the CHP unit are acquired from (Zhou et al., 2021) and (Ailer et al., 2001) and are summarized in Table 1. The time step is 60s and the simulation period is 1 h. The response of output temperature and electric power to the input fuel flow variation is shown in Figure 5.

As shown in Figure 5, the output temperature and generated electric power scales with the input mass flow rate of the fuel. However, a distinct time delay about 4min exists. Despite the capacity constraints in Eqs 21, 22, the coupling between the power and heating systems is also restricted by the pressure constraints in different components in the CHP unit, as shown in Eqs 54, 56. In this condition, the input and output states are not strictly linear, which indicates the significance of the dynamics and nonlinearity in the CHP unit model. According to Figure 5D, the initial temperature in the heat exchanger is higher and gradually decreases during the early period. As the simulation proceeds, the time-varying trend of the output temperature in the heat exchanger becomes consistent with the other states.

On this basis, we designed three scenarios to illustrate the effectiveness of the proposed method, as shown below.

S1: the proposed method with the variable hydraulic states and dynamic CHP unit model.

S2: the OEF method proposed in (Yao et al., 2021) with the fixed hydraulic states and dynamic CHP unit model. The

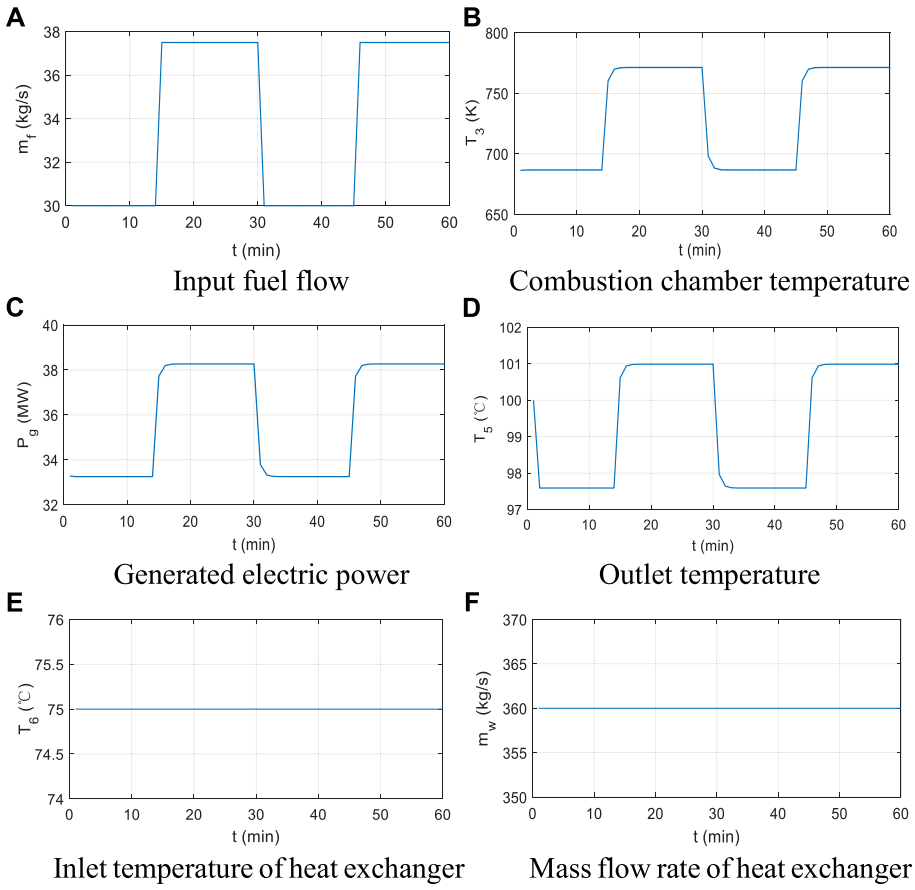

FIGURE 5
Simulation of dynamic CHP unit model.

initial conditions (hydraulic states at t = 0min) in S1 are selected as the fixed mass flow rate distribution in S2. The only difference between S1 and S2 is the adjustable mass flow rate distribution, i.e., Eqs 1–3 no longer act as constraints in S2.

S3: the proposed method without constraints in the heating system. The initial conditions in S3 are the same as that in S1. The only difference between S1 and S3 is the consideration of constraints from heating system side, i.e., Eqs 1–3, 8, 9, 32, 33, 51, 52 no longer act as constraints in S3.

The time and space steps are 15 min and 250 m, respectively. The simulation period is 4 h. The computational time and operational costs in different scenarios in Case 1 are summarized in Table 2. The optimized results are shown in Figure 6. Comparing the results in S1 and S2, we can find that the adjustable hydraulic states make the IHES more cost-effective. The savings are up to 3.3%. This is because the nonlinearity in heating system side provides more adjustable region for the operators. The operators are supposed to provide more power

TABLE 2 Results comparison in Case 1.

Scenario	1	2	3
Time/s	25.96	6.16	2.85
Cost/$	80363	82785	78293

to heat the water flow by reducing the mass flow rate and increasing the supply temperature. The comparison between S1 and S3 indicates that the integration of the heating system will increase the cost. It is understandable because the operators need to provide more heat power to satisfy the heat consumers' demands. Consequently, the supplied temperature and mass flow rate at the CHP unit are both increased. The differences in heating system states also influence the power system. Since the heat power provided by CHP units is the largest in S2, followed by S1, and that in S3 is the smallest. Correspondingly, the supplied electric power in S1 is the smallest due to the capacity constraints, as shown in Figure 6D.

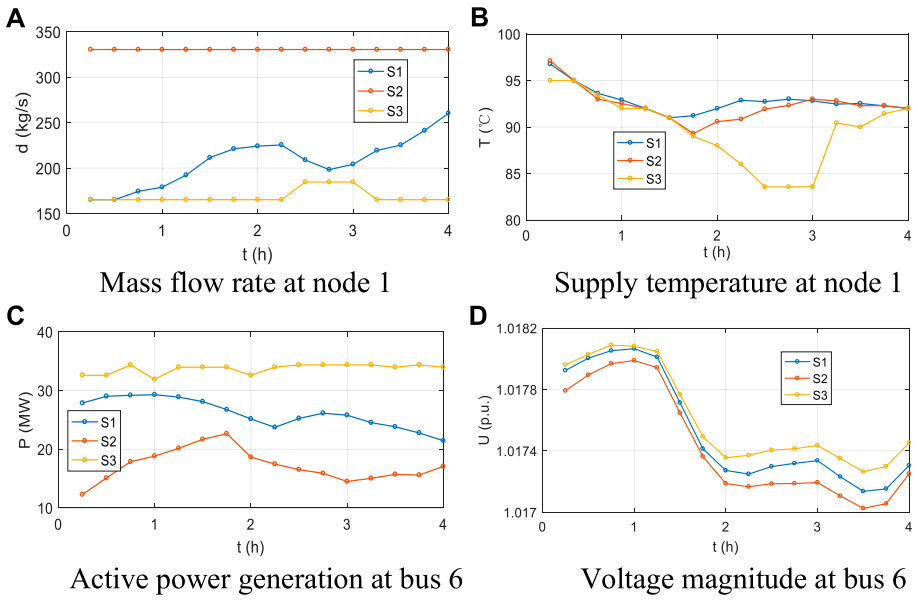

FIGURE 6
OEF results in three scenarios in Case 1.

Regarding the computational time, S3 is the most efficient because the constraints in the heating system are neglected. The computation in S1 is much more time-consuming in S2 due to the strong nonlinearity in the heating system. Nevertheless, it is still acceptable for the long time-interval dispatch.

TABLE 3 Results comparison in Case 2.

Scenario	1	2	3
Time/s	1768	909	951
Cost/$	13005	13896	12641

4.3 Case 2

In this section, we extended the analysis into a larger IHES for further investigation. Three scenarios are designed for verification, including:

S1: the proposed method with the variable hydraulic states and dynamic CHP unit model.

S2: the OEF method proposed in (Yao et al., 2021) with the fixed hydraulic states and dynamic CHP unit model. The initial conditions (hydraulic states at t = 0min) in S1 are selected as the fixed mass flow rate distribution in S2. The only difference between S1 and S2 is the adjustable mass flow rate distribution, i.e., Eqs 1–3 no longer act as constraints in S2.

S3: the proposed method with the variable hydraulic states, dynamic CHP unit model, and DC power flow model. The initial conditions in S3 are the same as that in S1. The difference between S1 and S3 is the utilization of the improved DC power flow model in S1.

The time and space steps are 15 min and 100 m, respectively. The simulation period is 3 h. The computational time and operational costs in different scenarios in Case 2 are summarized in Table 3. The optimized results are shown in Figure 7. According to Table 3, the operation of IHES with adjustable hydraulic states is more cost-effective than that with fixed hydraulic states. The savings in S1 are up to 6.9%, which is two times than that in Case 1. Since the mass flow rate in Case 2 is comparatively small, the thermal loss is more distinct. The proposed method optimizes the hydraulic states to minimize the thermal loss, leading to a lower cost. Although the computational time in S1 is much larger than S2 due to the strong nonlinearity, the economic advantages brought by adjustable hydraulic states are promising. Comparing the results in S1 and S3, we can find that the OEF results in the two scenarios are almost the same, with a slight difference of 2.7%. Since the power flow nonlinearity is considered in the improved DC power flow model, S1 further considers the power flow loss in the power system. Thus, its operational cost is higher.

As for the computational time, the simplification in the power system model also helps reduce the complexity. The computational time in S3 is almost half of that in S1.

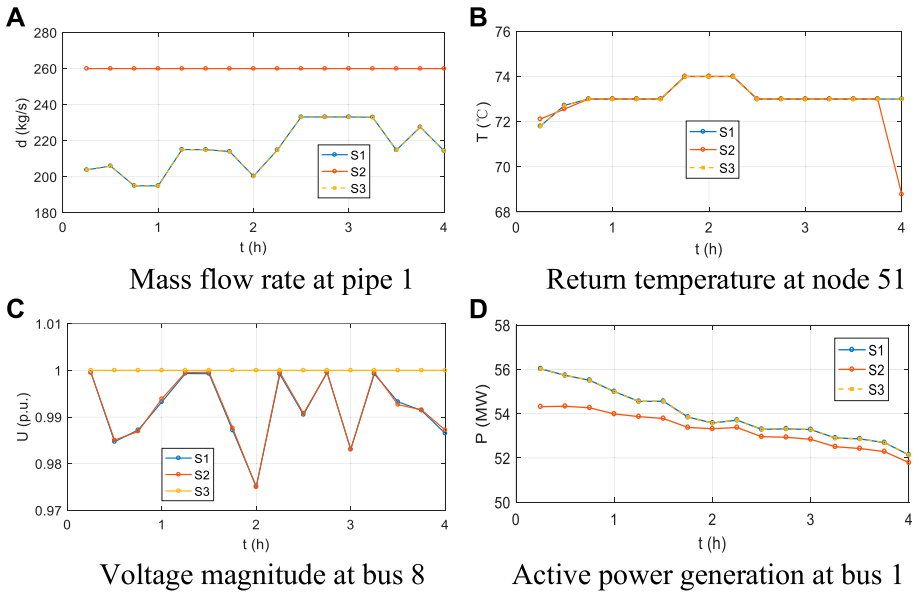

FIGURE 7
OEF results in three scenarios in Case 2.

However, the improved DC power flow model further considers the voltage magnitude variation. As shown in Figure 7C, the maximum mismatch at bus eight is distinct, which is up to 0.223p.u. The improvement indicates the superiority of the proposed in describing the electric states accurately, which is especially significant for the operational security of IHES.

5 Conclusion

In this paper, we investigated the OEF problem for the IHES considering multiple dynamics. First, we constructed the IHES model, including the AC power flow model, dynamic heating system model, and the dynamic CHP unit model. Then, we adopted the FDM to solve the different dynamics in IHES, respectively. The heating system model governed by nonlinear PDAEs was discretized using a second-order scheme. The CHP unit model governed by nonlinear DAEs was discretized using backward Euler scheme. Finally, we constructed the OEF model for the IHES, where the dynamic property and the operational security constraints are comprehensively analyzed. Case studies verify the effectiveness of the proposed method. The numerical results indicate the significance of the nonlinearity and dynamics for the operational optimization in IHES.

In our future work, the proposed method will be extended for the analysis in the market environment.

Data availability statement

The original contributions presented in the study are included in the article/supplementary material, further inquiries can be directed to the corresponding author.

Author contributions

Conceptualization, RC; methodology and software, YL; validation and writing, KQ.

Funding

This work was supported by Science and Technology Project of State Grid Jiangsu Electric Power Company (Granted No. J2022044).

Conflict of interest

RC, YL, and KQ were employed by the State Grid Suzhou Power Supply Company.

The authors declare that this study received funding from State Grid Jiangsu Electric Power Company. The funder had the following involvement in the study: Conceptualization, Software, Methodology, Validation and Writing.

Publisher's note

References

Ailer, P., Santa, I., Szederkenyi, G., and Hangos, K. (2001). Nonlinear model-building of a low-power gas turbine. *Peri. Poly. Ser. Trans. Eng.* 19 (12), 117–135.

Chen, Y., Guo, Q., Sun, H., and Pan, Z. (2021). Integrated heat and electricity dispatch for district heating networks with constant mass flow: A generalized phasor method. *IEEE Trans. Power Syst.* 36 (1), 426–437. doi:10.1109/tpwrs.2020.3008345

Cruz, M., Fitiwi, D., Santos, S., and Catalao, J. (2018). A comprehensive survey of flexibility options for supporting the low-carbon energy future. *Renew. Sustain. Energy Rev.* 97, 338–353. doi:10.1016/j.rser.2018.08.028

Dai, Y., Chen, L., Min, Y., Chen, Q., Hao, J., Fu, K., et al. (2019). Dispatch model for CHP with pipeline and building thermal energy storage considering heat transfer process. *IEEE Trans. Sustain. Energy* 10 (1), 192–203. doi:10.1109/tste.2018.2829536

Dancker, J., and Wolter, M. (2021). Improved quasi-steady-state power flow calculation for district heating systems: A coupled Newton-Raphson approach. *Appl. Energy* 295, 120–129.

Gu, W., Wu, Z., Bo, R., Liu, W., Zhou, G., Chen, W., et al. (2014). Modeling, planning and optimal energy management of combined cooling, heating and power microgrid: A review. *Int. J. Electr. Power & Energy Syst.* 54, 26–37. doi:10.1016/j.ijepes.2013.06.028

Li, Y., Gao, D. W., Gao, W., Zhang, H., and Zhou, J. (2020). Double-mode energy management for multi-energy system *via* distributed dynamic event-triggered Newton-Raphson algorithm. *IEEE Trans. Smart Grid* 11 (6), 5339–5356. doi:10.1109/tsg.2020.3005179

Li, Z., Wu, W., Shahidehpour, M., Wang, J., and Zhang, B. (2016). Combined heat and power dispatch considering pipeline energy storage of district heating network. *IEEE Trans. Sustain. Energy* 7 (1), 12–22. doi:10.1109/tste.2015.2467383

Liu, L., Wang, D., Hou, K., Jia, H., and Li, S. (2020). Region model and application of regional integrated energy system security analysis. *Appl. Energy* 260, 114268. doi:10.1016/j.apenergy.2019.114268

Liu, X., Wu, J., Jenkins, N., and Bagdanavicius, A. (2016). Combined analysis of electricity and heat networks. *Appl. Energy* 162, 1238–1250. doi:10.1016/j.apenergy.2015.01.102

Lu, S., Gu, W., Meng, K., Yao, S., Liu, B., and Dong, Z. Y. (2020). Thermal inertial aggregation model for integrated energy systems. *IEEE Trans. Power Syst.* 35 (3), 2374–2387. doi:10.1109/tpwrs.2019.2951719

Palsson, H. (1999). *Equivalent models of district heating systems*. Denmark: Technical University of Denmark.

Ramsebner, J., Haas, R., Auer, H., Ajanovic, A., Gawlikm, W., Maier, C., et al. (2021). From single to multi-energy and hybrid grids: Historic growth and future vision. *Rene. Sust. Energy Rev.* 151, 111520.

Sartor, K., Quoilin, S., and Dewallef, P. (2014). Simulation and optimization of a CHP biomass plant and district heating network. *Appl. Energy* 130 (S11), 474–483. doi:10.1016/j.apenergy.2014.01.097

Shabanpour, A., and Seifi, A. R. (2016). An integrated steady-state operation assessment of electrical, natural gas, and district heating networks. *IEEE Trans. Power Syst.* 31 (5), 3636–3647. doi:10.1109/tpwrs.2015.2486819

Wang, Y., You, S., Zhang, H., Zheng, X., Zheng, W., Miao, Q., et al. (2017). Thermal transient prediction of district heating pipeline: Optimal selection of the time and spatial steps for fast and accurate calculation. *Appl. Energy* 206, 900–910. doi:10.1016/j.apenergy.2017.08.061

Wu, J., Yan, J., Jia, H., Hatziargyriou, N., Djilali, N., and Sun, H. (2016). Integrated energy systems. *Appl. Energy* 167, 155–157. doi:10.1016/j.apenergy.2016.02.075

Xu, X., Jia, H., Chiang, H., Yu, D., and Wang, D. (2015). Dynamic modeling and interaction of hybrid natural gas and electricity supply system in microgrid. *IEEE Trans. Power Syst.* 30 (3), 1212–1221. doi:10.1109/tpwrs.2014.2343021

Yang, J., Zhang, N., Botterud, A., and Kang, C. (2020). On an equivalent representation of the dynamics in district heating networks for combined electricity-heat operation. *IEEE Trans. Power Syst.* 35 (1), 560–570. doi:10.1109/tpwrs.2019.2935748

Yang, Z., Zhong, H., Bose, A., Zheng, T., Xia, Q., and Kang, C. (2018). A Linearized OPF model with reactive power and voltage magnitude: A Pathway to Improve the MW-only DC OPF. *IEEE Trans. Power Syst.* 33 (2), 1734–1745. doi:10.1109/tpwrs.2017.2718551

Yao, S., Gu, W., Lu, S., Zhou, S., Wu, Z., Pan, G., et al. (2021). Dynamic optimal energy flow in the heat and electricity integrated energy system. *IEEE Trans. Sustain. Energy* 12 (1), 179–190. doi:10.1109/tste.2020.2988682

Zang, H., Xu, R., and Cheng, L. (2021). Residential load forecasting based on LSTM fusing self-attention mechanism with pooling. *Energy* 229, 120682.

Zhang, N., Sun, Q., Yang, L., and Li, Y. (2022). Event-triggered distributed hybrid control scheme for the integrated energy system. *IEEE Trans. Ind. Inf.* 18 (2), 835–846. doi:10.1109/tii.2021.3075718

Zhang, S., Gu, W., Lu, S., Yao, S., Zhou, S., and Chen, X. (2021). Dynamic security control in heat and electricity integrated energy system with an equivalent heating network model. *IEEE Trans. Smart Grid* 12 (6), 4788–4798. doi:10.1109/tsg.2021.3102057

Zhang, S., Gu, W., Yao, S., Lu, S., Zhou, S., and Wu, Z. (2021). Partitional decoupling method for fast calculation of energy flow in a large-scale heat and electricity integrated energy system. *IEEE Trans. Sustain. Energy* 12 (1), 501–513. doi:10.1109/tste.2020.3008189

Zhang, S., Gu, W., Zhang, X., Lu, H., Lu, S., Yu, R., et al. (2022a). Fully analytical model of heating networks for integrated energy systems. *Appl. Energy* 327, 120081. doi:10.1016/j.apenergy.2022.120081

Zhang, S., Gu, W., Zhang, X., Lu, H., Yu, R., Qiu, H., et al. (2022b). Dynamic modeling and simulation of integrated electricity and gas systems. *IEEE Trans. Smart Grid*, 1. doi:10.1109/TSG.2022.3203485

Zhou, Y., Wang, J., Dong, F., Qin, Y., Ma, Z., Ma, Y., et al. (2021). Novel flexibility evaluation of hybrid combined cooling, heating and power system with an improved operation strategy. *Appl. Energy* 300, 117358. doi:10.1016/j.apenergy.2021.117358

Nomenclature

Abbreviations

CHP Combined heat and power
IHES Integrated heat and electricity system
PDAE Partial differential and algebraic equation
DAE Differential and algebraic equation
OEF Optimal energy flow
FDM Finite difference method
PDE Partial differential equation
ODE Ordinary differential equation

Indices and sets

$\aleph_{s,i}$ Set of pipes starting at node i
$\aleph_{e,i}$ Set of pipes ending at node i
$\aleph_{CHP}$ Set of buses/nodes with the CHP unit
$\aleph_{G}$ Set of buses with the traditional generator
min Index of the minimum values
max Index of the maximum values

Parameters

A Node-branch incidence matrix
B Loop-branch incidence matrix
K Pipe friction resistance
$C_w/C_s/C_a$ Specific heat capacity of water/smoke/air
v Flow velocity
λ Pipe thermal resistance
γ Changing ratio of mass flow rate
T^a Ambient temperature
P_L Active power at electric load
Q_L Reactive power at electric load
G_{ij} Conductance between bus i and bus j
B_{ij} Susceptance between bus i and bus j
$CPR_{1\text{-}2}$ Compressor ratios in compressor and turbine
β_1/β_3 Air/smoke isentropic index
β_2 Heat storage coefficient of the combustion chamber
β_4 Heat storage coefficient of heat exchanger
H_g Fuel enthalpy
LHV Low calorific value
η_1 Efficiency of the compressor
η_2 Mechanical efficiency of the turbine
η_3 Energy efficiency of the turbine
N_x/N_t Number of space/time step
$\Delta x/\Delta t$ Size of space/time step
α Mixture ratio of air and fuel
$c_{1\text{-}2}$ Price of fuel and coal
f/g Cost function of CHP unit/generator
μ Cost coefficient of CHP unit/generator

Variables

m Vector of pipe mass flow rate
d Vector of node mass flow rate
Δp Vector of pipe pressure drop
$T^{n,s}/T^{n,r}$ Node supply/return temperature
ϕ Heat power
T^p Pipe temperature
P_G Active power at electric generator
Q_G Reactive power at electric generator
U Voltage magnitude
θ Voltage phase angle
P_{ij} Active power flow between bus i and bus j
Q_{ij} Reactive power flow between bus i and bus j
$p_{1\text{-}2}$ Input and output pressure of the compressor
p_3 Output pressure of the turbine
$T_{1\text{-}2}$ Input and output temperature of the compressor
$T_{3\text{-}4}$ Input and output temperature of the turbine
$T_{5\text{-}6}$ Input and output temperature of heat exchanger
m_a/m_f Mass flow rate of air/smoke
P_b Power carried by the turbine
P_c Power consumed by the compressor
P_g/ϕ_g Generated electric/heat power

frontiers | Frontiers in Energy Research

TYPE Original Research
PUBLISHED 23 January 2023
DOI 10.3389/fenrg.2022.978247

OPEN ACCESS

EDITED BY
Yanchi Zhang,
Shanghai Dianji University, China

REVIEWED BY
Zhe Chen,
Hohai University, China
Meng Ding,
Nanjing University of Aeronautics and Astronautics, China

*CORRESPONDENCE
Jun Liu,
liuj@sdju.edu.cn

SPECIALTY SECTION
This article was submitted to Smart Grids,
a section of the journal
Frontiers in Energy Research

RECEIVED 25 June 2022
ACCEPTED 06 December 2022
PUBLISHED 23 January 2023

CITATION
Liu J and Ji N (2023), A bright spot detection and analysis method for infrared photovoltaic panels based on image processing.
Front. Energy Res. 10:978247.
doi: 10.3389/fenrg.2022.978247

A bright spot detection and analysis method for infrared photovoltaic panels based on image processing

Jun Liu[1,2]* and Ning Ji[2]

[1]Institute of Logistics Science and Engineering, Shanghai Maritime University, Shanghai, China, [2]College of Mechanical Engineering, Shanghai Dianji University, Shanghai, China

The energy crisis and environmental problems have attracted global attention, thus the photovoltaic (PV) power generation technology comes to people's mind. The application of unmanned aerial vehicle (UAV) inspection technology can overcome the disadvantages of large scale and high risk of this project. The application of unmanned aerial vehicle (UAV) infrared detection technology in PV power generation can not only improve work efficiency, but also have high economic benefits. This paper based on U-Net network and HSV space, proposes a method of PV infrared image segmentation and location detection of hot spots, which is used to detect and analyze the shielding of PV panels. Firstly, the main PV modules are automatically split from the different infrared image background based on U-Net. In order to quickly locate the defection location, the mask image is multiplied by the original image and then converted to HSV. The discriminant of bright spot features is introduced, and the discriminant mechanism is summarized according to the experiment, and the formation reason is analyzed. The experiment result shows that the method is not affected by the infrared image under the different background, provides data for the maintenance of power station and improves the detection accuracy. The accuracy rate of analyzing the causes of defects is 92.5%.

KEYWORDS

UAV, PV infrared image, U-Net, HSV, bright spots detection

1 Introduction

With the rapid development of photovoltaic PV power generation industry, safe and reliable maintenance of power equipment is particularly important. Traditional detection methods are not suitable for large-scale PVPS because of low efficiency and high cost. However, the use of infrared imaging technology for fault detection is currently an effective method (Zhang et al., 2017). Cubukcu and Akanalci (2020) used infrared thermal imaging equipment to detect different PVPS and classify defects according to fault types. For the hotspots shown by the defect module in infrared image (Kamran et al., 2019), cluster segmentation was used to detect and provide quantitative data such as temperature and area (Salazar and Macabebe, 2016). Due to the resolution of infrared images and

FIGURE 1
Data acquisition equipment: **(A)** UAV equipment. **(B)** Infrared equipment. **(C)** UAV is capturing images.

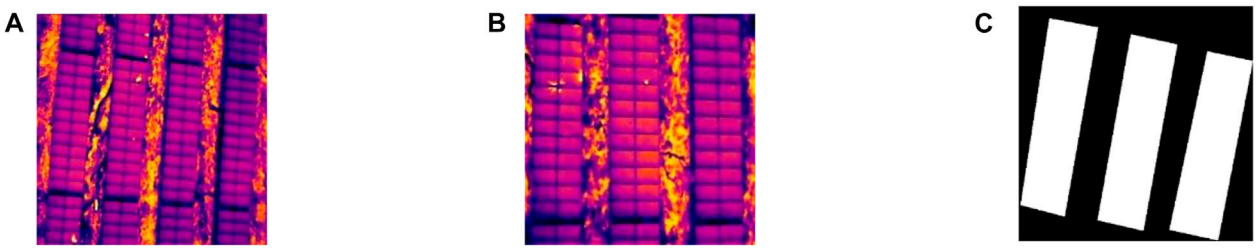

FIGURE 2
The acquired PV infrared images: **(A)** Image 1 **(B)** Image 2. **(C)** Masking sample.

blurry edges, image segmentation is also a concern. In order to improve the effect of infrared image segmentation, a method based on an improved genetic algorithm to optimize the OTSU segmentation function was proposed (Wang, 2018). Kumar, and Ansari (Kumar et al., 2018) used watershed transform and color space methods for infrared image segmentation and fault detection of electrical equipment. In fact, plants show too many bright spots in infrared image, which makes some methods ineffective and image processing methods based on deep learning has been widely applied.Nie et al. (2020) eliminated noise according to traditional image processing and crop the infrared Image, then proposed an automatic hot spot detection model based on CNN. Zhang et al. (2021) proposed an industrial smoke image segmentation method based on FCN-LSTM, during the basic feature extraction, the time information of image sequence was extracted by using the short and long time memory network, and the moving smoke and background were distinguished by the dynamic characteristics of smoke and dust. Tang et al. (2020) Combined Seg-Net network with low-altitude UAV image, established a ground feature information extraction model in Huixian dissolved rock wetland. Ronneberger et al. (2015) proposed a new network structure, U-Net, which is widely used in the segmentation of organs in medical images (Lei et al., 2019), prediction of different crop types in agriculture observations (Wei et al., 2019), forest ecological management (Wagner et al., 2019). Its effect is better than traditional pattern recognition methods.

In this paper, the U-Net network is used for infrared image segmentation, bright spots are detected in the HSV space and located in the original image. The classification standard of bright spots is proposed as the maintenance basis, which has accuracy and effectiveness. U-Net is a neural network composed of contraction path and symmetric expansion path, which can use fewer images for end-to-end training, with high segmentation accuracy and fast speed (Ronneberger et al., 2015). It is suitable for the case of small data sets in this paper. In order to remove more interference factors, this paper makes an improvement on the traditional U-Net, and increases the convolutional layer in the coding stage to improve the segmentation accuracy of infrared PV panels. Meanwhile, the Dropout layer is added behind the low-level network to improve the generalization ability of the data, reduce the over fitting probability. Then, in order to realize the quick location of the spot on the UAV infrared PV panel, according to the characteristics of the infrared PV panel and spot in HSV space, the infrared PV image and mask image can be multiplied to quickly detect the bright spot and locate it to the original image. At the same time, a classification standard for the bright spot of infrared PV panels is put forward, which is taken as the maintenance basis. Finally, the advanced and reliability of the method is verified by a detailed experiment. Although the U-net

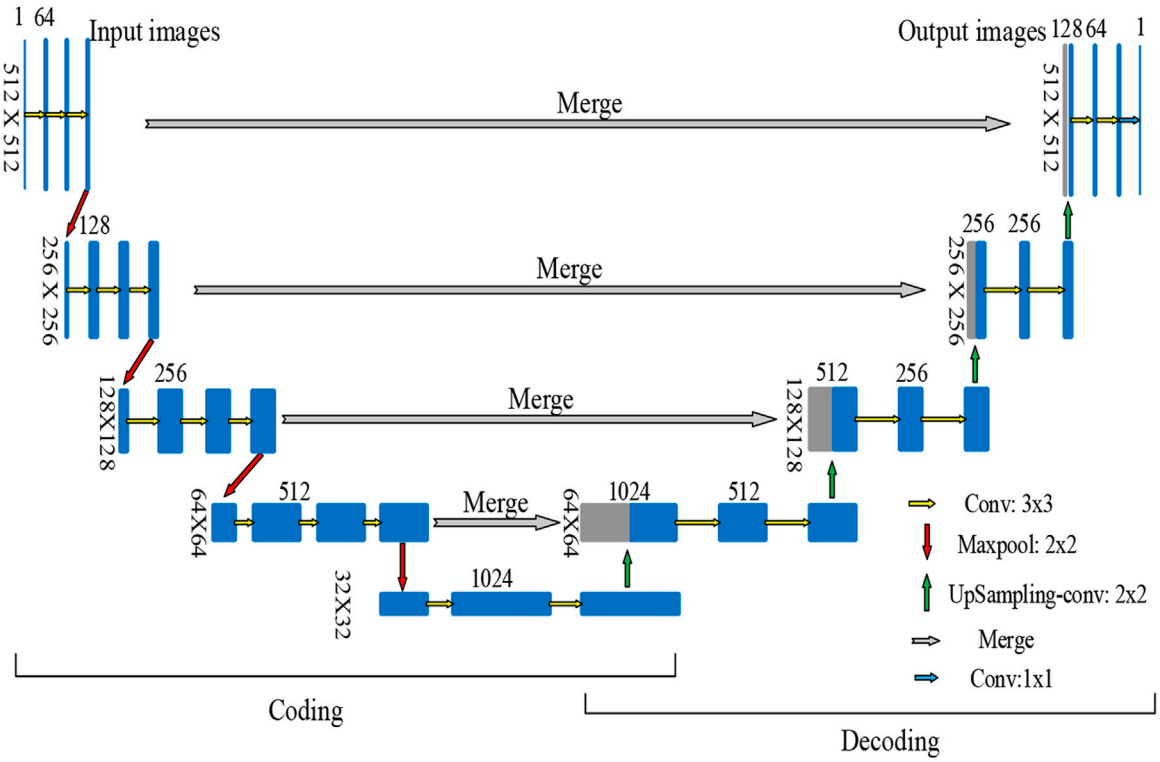

FIGURE 3
The structure of our U-Net network.

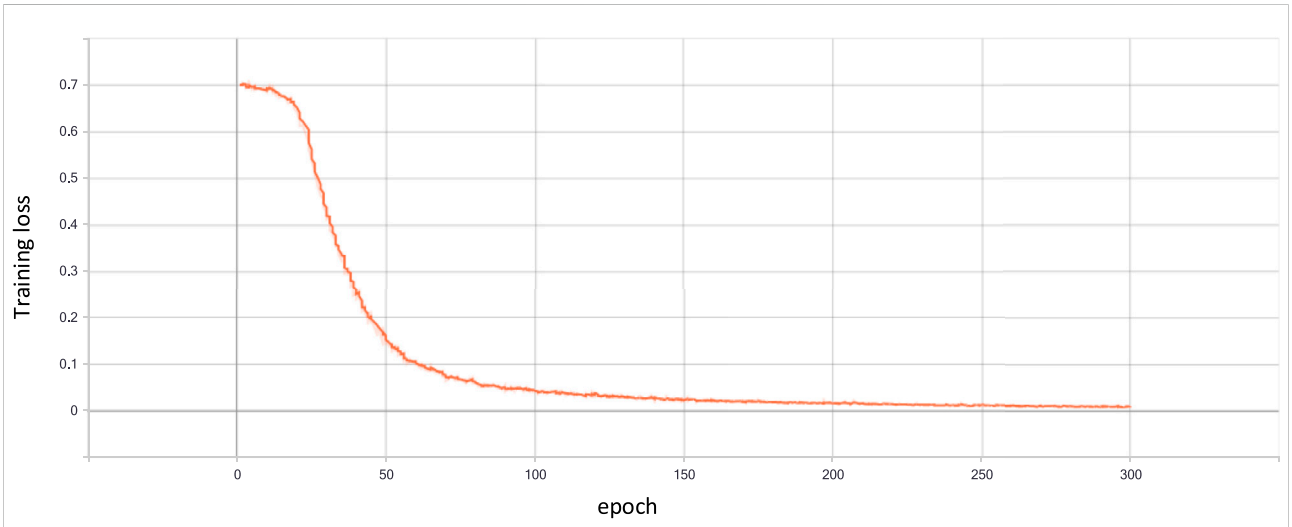

FIGURE 4
Training loss curves.

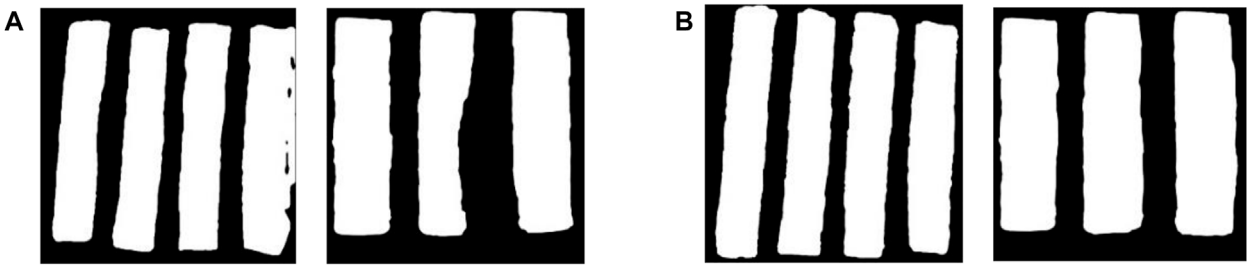

FIGURE 5
The segmentation results: **(A)** Original U-NET. **(B)** Our U-NET.

TABLE 1 The performance of different training model.

Model	FPS(f/s)	mAP	Detection Times (ms)
FCN	1.21	53.21	63.44
Seg-Net	15.53	40.52	29.86
U-Net	17.64	46.44	10.53
Our U-Net	19.62	49.53	12.53

network can train small data, in order to improve the training effect, image enhancement is carried out on the data set in advance. Through cutting and stitching images collected from PVPS, the data set eventually increases from 300 to 450.

1) This paper analyzes the applicability of the U-Net model in the field of infrared PV panel detection, and aim at providing a more robust and accurate solution to the specific problem of hot spots caused by green plants and dust accumulation.
2) Bright spots contained in the data set have been accurately tagged and located in advance, and our method is less affected by light. It also provides a benchmark for the rapid detection of bright spots on PV panels by using novel image processing methods.
3) In order to analyze the cause of defect formation, the bright spot measurement mechanisms N_d and N_g were introduced, and the analysis accuracy was proved to be 92.5% through experiments.

2 Data acquisition

Using unmanned aerial vehicle (UAV) to collect images can improve the efficiency and reduce monitoring costs (Grimaccia and Sonia LevaNiccolai, 2017). As shown in Figure 1A, the flight equipment used has strong wind resistance and stability. The image acquisition equipment of FLIR infrared thermal imager is chosen as shown in Figure 1B. Figure 1C shows the scenario where the UAV is at work.

A total of 450 images of the dataset set were used in the experiment, it contains 350 training sets and 100 test sets. We resized it to 512 × 512 (pixel) for the following image processing. Figures 2A, B shows the actual infrared image, and we use the LabelMe tool to mark the complete PV module. Figure 2C shows the label sample.

3 U-Net network model

U-Net network is a distributed structure on both sides of encoding and decoding, and it is a very robust model for edge extraction using a small amount of data (Ronneberger et al., 2015). The left encoding is used to extract image features, and the right decoding is used to restore image feature edge information. Figure 3 shows the U-Net network structure in this paper. The network adopts the 3 × 3 convolutional layer structure for 23 times (stride = 1, padding), the activation function of ReLU, and the maximum pooling layer structure of 2 × 2 (stride = 2). The characteristic graph output by each encoder unit is connected to the corresponding decoder reconstruction unit according to the jump connection mechanism. Add Dropout layer after the low-level network to improve the generalization ability of data and reduce the probability of overfitting. In order to improve the robustness of the model, reduce the semantic gap and ensure the operation speed, this paper adds one more 3 × 3 convolution layer for each subsampling process. Figure 3 shows our U-Net network structure in this paper.

In this paper, the experimental environment was Windows system (CPU Intel i7, NVIDIA GeForce RTX 2070, 16 GB memory), python 3.7.0. The deep learning network framework PyTorch was used for model training, with a learning rate of 0.0001, 300 iterations and batch size of 5 times. Figure 4 shows the loss value of PV infrared images training in TensorBoard. The training loss value is 0.01041. It shows that the U-Net model is feasible to segment the infrared PVP.

As shown in Figure 5, the PV modules segmented by U-Net in this paper are relatively complete. The phenomenon of over-segmentation or under-segmentation is relatively less.

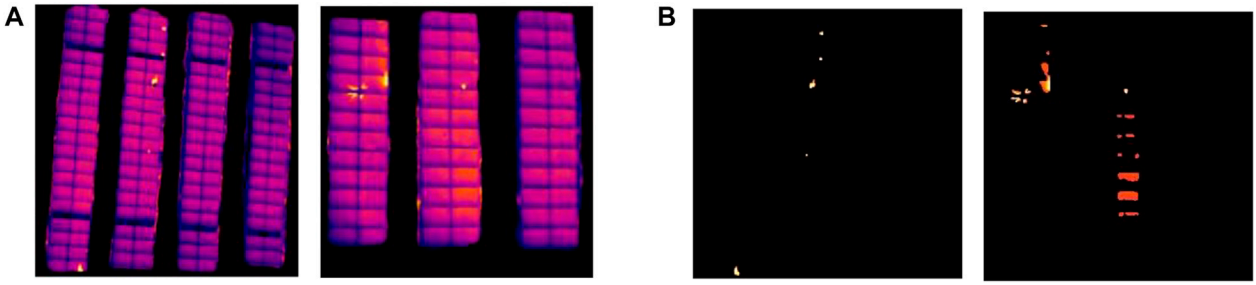

FIGURE 6
PV modules and bright spots results: **(A)** PV modules segmentation. **(B)** Bright spots segmentation.

TABLE 2 Centroid coordinate point.

Experimental images	The pixel point of tag (X, Y)	Calculated pixel coordinates (x_0, y_0)	Actual pixel coordinates
Image 1	(227.9, 143.9), (83.55, 499)	(313.4, 161.9), (114.8, 561.4)	(312, 161), (114, 561)
Image 2	(276.9, 313.9), (277.6, 350.6)	(380.7, 353.1), (381.7, 394.4)	(381, 353), (380, 393)

Table 1 proves the superiority of the U-Net with three layers compared with FPS, Seg-Net and U-Net through experiments. We can see our algorithm FPS get 19.62 f/s and detection times arrive 12.53 ms for one picture, its mAP compared to FCN just below 3.68. However, the overall evaluation is relatively better.

4 PV infrared image analysis process

4.1 Bright spots segmentation

RGB color mode (RGB) is more susceptible to lighting than HSV color model (Wang et al., 2021). So, Maiti and Chakraborty, (2012) converted RGB image into HSV space, processed and combined the images of each channel to obtain brain tumor segmentation image. Malik et al. (2018) proposed an improved tomato detection algorithm based on HSV color space and watershed segmentation, with high accuracy. So, in this paper, the infrared image was first converted into HSV space, the difference between the two channel images as shown in Eq. 1.

$$sub = double\,(V - H). \tag{1}$$

The sub image is processed by adaptive threshold segmentation and multiplied by the original infrared image to obtain the bright spots image, as shown in Eq. 2.

$$result = \frac{C(i,j)}{255} \cdot I(i,j), \tag{2}$$

where $C\,(i, j)$ is a three-channel image synthesized from result of threshold segmentation, $I\,(i, j)$ is an original infrared image.

The segmentation results are fused with the original infrared image and converted into HSV space, as shown in Figure 6.

The size of the image changed during U-Net network training, we use morphological opening operations to obtain the centroid coordinates of the connected regions and the marker points as shown in Table 2. In this paper, the original pixel size of the infrared image in the experiment is 704×576. Set the original bright spot centroid coordinate is (x_0, y_0), it can be calculated by

$$\frac{X}{x_0} = \frac{512}{704}, \frac{Y}{y_0} = \frac{512}{576}. \tag{3}$$

On the basis of the bright spots image, we use the human checking, the Nie's method (Nie et al., 2020) as benchmarks to demonstrate ours advantages. Nie's method eliminated noise according to traditional image processing and crop the infrared image. Figure 7 shows the detection accuracy of the three methods in different numbers of test images. As the number of test images grow, the accuracy of manual detection has huge decreased. The accuracy of Nie's method and our method still keep at 90%, and our method is more stable.

4.2 Infrared image surface features

The bright spots on the surface of the infrared image include hot spots and more dust covering the orange-red area. In order to

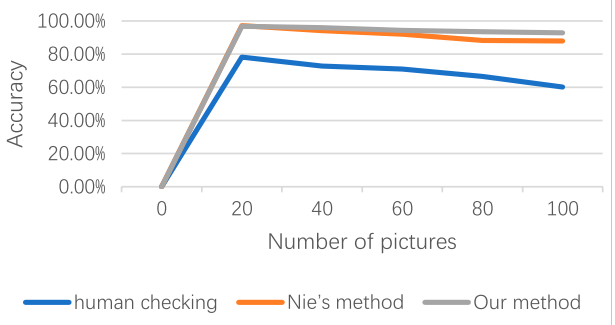

FIGURE 7
Comparison of detection accuracy.

analyse the image features, the image is first introduced into overview interface, the imtool command to display the image processing interface, select the target area to analyse the starting point, the block-by-block generated grey value and then the Pixel Region is used to move and select the target area (Peng and Liu, 2018; Liu et al., 2020).

In order to judge the feature of bright spots, it is convenient to calculate the average grey value and the number of pixels points the measurement standard as shown in Eq. 4.

$$A_g = \frac{\sum_{i,j\in[m,n]} \text{grey}(i,j)}{N(\text{grey}(i,j) \neq 0)}, \quad \begin{cases} 100 < \text{grey}(i,j) < 200, & N_d + 1, \\ \text{grey}(i,j) > 200, & N_g + 1, \end{cases} \tag{4}$$

where A_g is the average grey value of image, grey (i, j) is the grey value of the pixel with coordinate (i, j), N is number, N_d is the number of pixels with grey values between 100 and 200, N_g is greater than 200, we can get them from MATLAB.

In this paper, when A_g is less than 150 and N_d is greater than N_g, it can be considered that bright spots are mainly caused by dust, otherwise, the hotspots are mostly caused by green plants. Figure 8A are test areas including normal area,

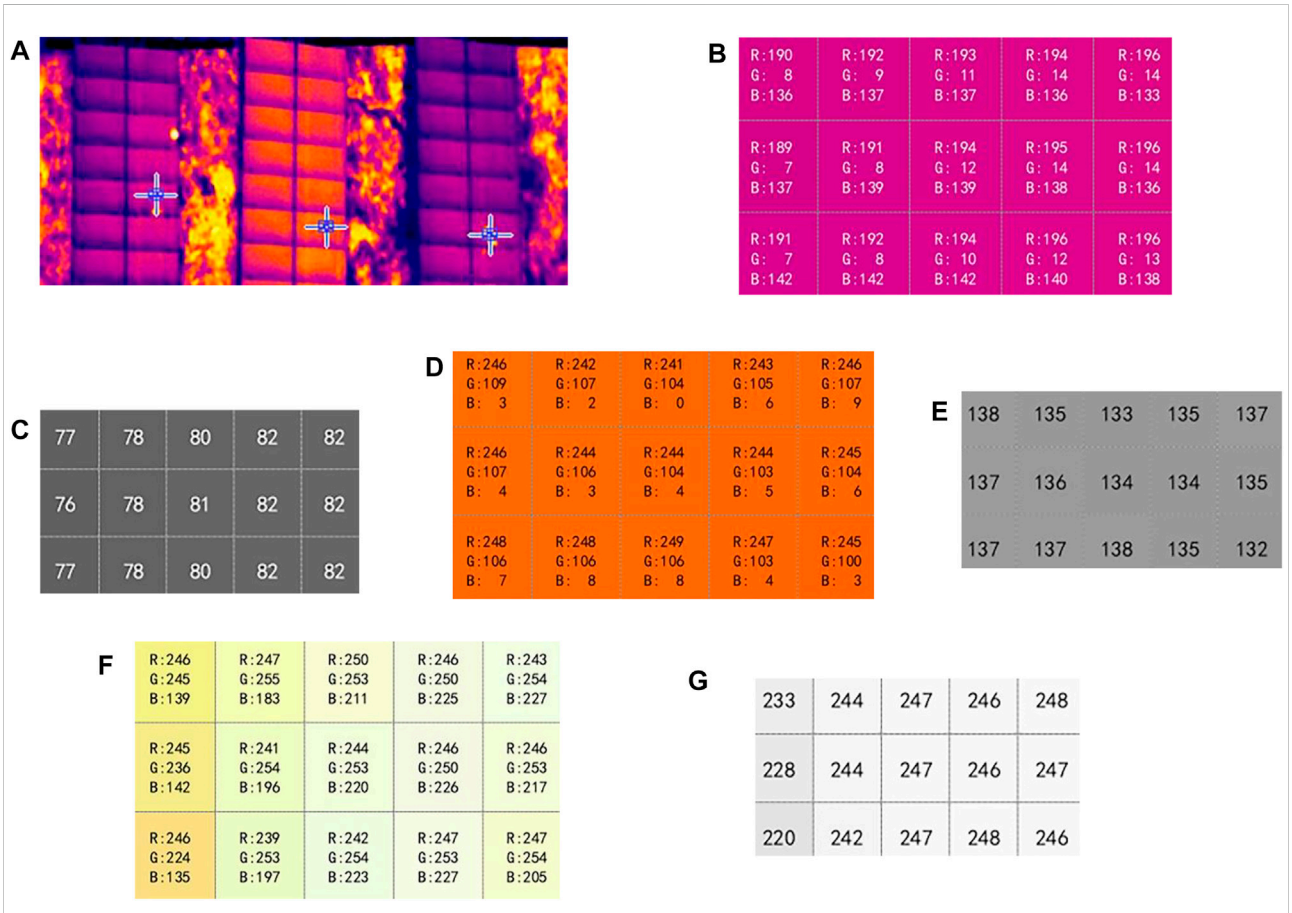

FIGURE 8
RGB and grey values of target areas: **(A)** Test areas from left to right: normal area, dust covered area, plants shelter area. **(B)** RGB values of normal area. **(C)** Grey values of normal area. **(D)** RGB values of dust covered area. **(E)** Grey values of dust covered area. **(F)** RGB values of the area shaded by plants. **(G)** Grey values of the area shaded by plants.

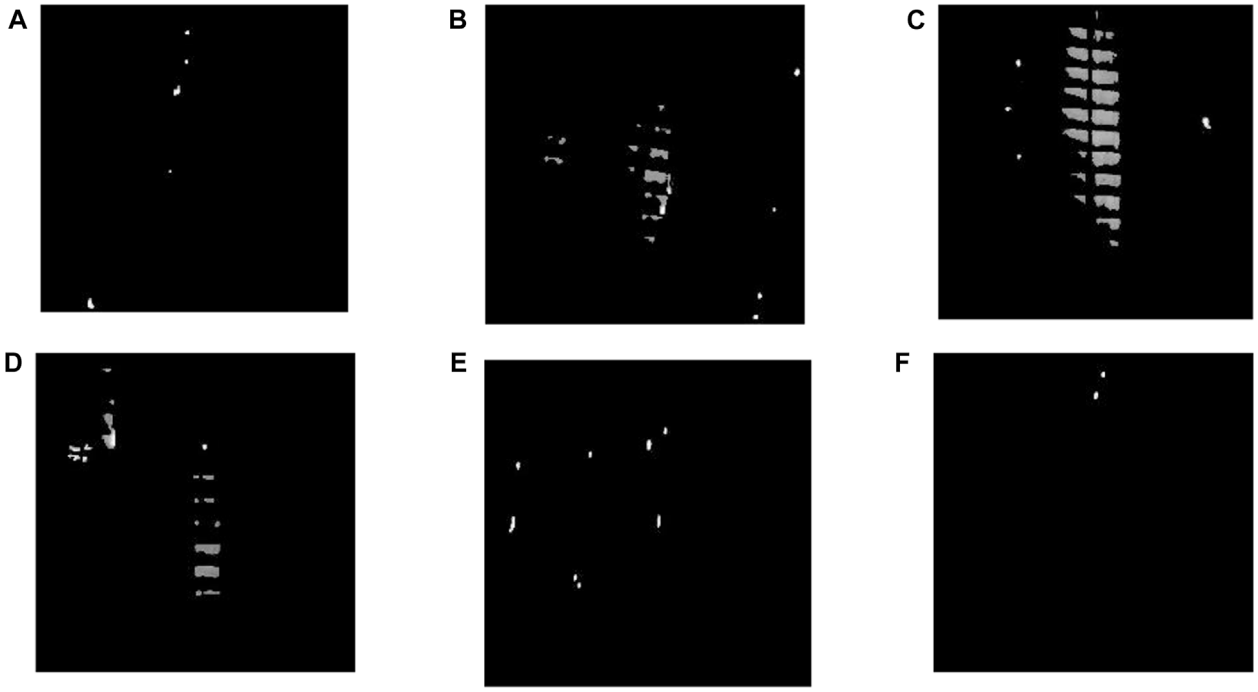

FIGURE 9
(A-F) shows the grayscale images of different image segmentation results.

TABLE 3 Different image detection results.

Images	A_g	$N_d > N_g$	Result
a	189.4441	Yes	plants
b	127.9128	Yes	Dust
c	124.4288	Yes	Dust
d	130.5545	Yes	Dust
e	187.1459	No	plants
f	195.2000	No	plants

dust covered area and plants shelter area. Figures 8B, C shows the normal area, the G value in the three channels of RGB is the smallest and the grey value is less than 100. Figures 8D, E shows dust covered area, the B values is the smallest and the grey value is between 100 and 200. Figures 8F, G shows plants shelter area, the RGB channel values and gray values are both greater than (b) and (d). Figure 9 shows the grayscale images of different image segmentation results. Table 3 shows the measured values and the main types of defects on the PV infrared image.

5 Conclusion

In this study, for the inspection and evaluation of large-scale PVPS, a method based on U-Net network and HSV space to segment and detect PV infrared images captured by UAV was proposed. The proposed method uses the U-Net network training model to segment PV modules from the different background, then locates the bright spot pixel coordinates in the HSV space, and classifies defects according to the image features. The experimental results show that the complex background can be effectively eliminated, and can provide qualitative and quantitative evaluation results. To prove its advantages, the other two methods are used for comparison. In future works, the combination of UAV, infrared thermal imaging and image processing technology can quickly patrol large-scale PVPS, find out the bright spots and analyze the defect in time which is conducive to the later maintenance of the power station.

Data availability statement

The original contributions presented in the study are included in the article/Supplementary Material, further inquiries can be directed to the corresponding author.

Author contributions

JL completed the main work, and NJ assisted in making some modifications of the paper, they approved it for publication.

Conflict of interest

The authors declare that the research was conducted in the absence of any commercial or financial relationships that could be construed as a potential conflict of interest.

The handling editor shares affiliation with author JL, HW.

Publisher's note

References

Cubukcu, M., and Akanalci, A. (2020). Real-time inspection and determination methods of faults on photovoltaic power systems by thermal imaging in Turkey. *Renew. Energy* 147 (1), 1231–1238. doi:10.1016/j.renene.2019.09.075

Grimaccia, Francesco, Leva, Sonia, and Niccolai, Alessandro (2017). PV plant digital mapping for modules' defects detection by unmanned aerial vehicles. *IET Renew. Power Gener.* 11 (10), 1221–1228. doi:10.1049/iet-rpg.2016.1041

Kamran, N., Wajahat, A., Abbas, K. H., Yang, Y., and Athar, S. (2019). Hotspot diagnosis for solar photovoltaic modules using a Naive Bayes classifier. *Sol. Energy* 190, 34–43. doi:10.1016/j.solener.2019.07.063

Kumar, Deepak, Amit, Kumar, and Ansari, M. A. (2018). "A flexible scheme to fault detection for electrical assets using infrared thermography," in *Advances in electronics, communication and computing* (Singapore: Springer). doi:10.1007/978-981-10-4765-7_57

Lei, Yang, Liu, Yingzi, Xue, Dong, Tian, Sibo, Wang, Tonghe, Jiang, Xiaojun, et al. (2019). Automatic multi-organ segmentation in thorax CT images using U-Net-GAN. *Computer-Aided Diagn.* 46 (5), 2157–2168. doi:10.1002/mp.13458

Liu, Jun, Liu, Yang, and Yichen, Ke (2020). Detection and analysis of a quay crane surface based on the images captured by a UAV. *Remote Sens. Lett.* 11 (1), 76–85. doi:10.1080/2150704x.2019.1686779

Maiti, Ishita, and Chakraborty, Monisha "A new method for brain tumor segmentation based on watershed and edge detection algorithms in HSV colour model," in Proceedings of the Paper presented at the 2012 National conference on computing and communication systems, Durgapur, India, November 2012, 192–196. doi:10.1109/NCCCS.2012.6413020

Malik, Muhammad Hammad, Zhang, Ting, Han, Li, Zhang, Man, Shabbir, Sana, and Ahmed, Saeed (2018). Mature tomato fruit detection algorithm based on improved HSV and watershed algorithm. *IFAC-PapersOnLine* 51 (17), 431–436. doi:10.1016/j.ifacol.2018.08.183

Nie, J. F., Luo, T., and Li, H. (2020). Automatic hotspots detection based on UAV infrared images for large-scale PV plant. *Electron. Lett.* 10 (18), 193–194. doi:10.1049/el.2020.1542

Peng, Lin, and Liu, Jun (2018). Detection and analysis of large-scale WT blade surface cracks based on UAV-taken images. *IET Image Process.* 12 (11), 2059–2064. doi:10.1049/iet-ipr.2018.5542

Ronneberger, Olaf, Fischer, Philipp, and Brox, Thomas (2015). "U-Net: Convolutional networks for biomedical image segmentation," in *Paper presented at the International Conference on Medical image computing and computer-assisted intervention* (Cham, Switzerland: Springer). doi:10.1007/978-3-319-24574-4_28

Salazar, April M., and Macabebe, Erees Queen B. (2016). Hotspots detection in photovoltaic modules using infrared thermography. *MATEC Web Conf.* 70, 10015. doi:10.1051/matecconf/20167010015

Tang, Tingyuan, Fu, Bolin, and Li, Ying (2020). Application of Seg-Net in extracting ground feature information of Huixian Karst Wetland from low-altitude UAV images. *Wetl. Sci.* 18 (04), 413–423. doi:10.13248/j.cnki.wetlandsci.2020.04.005

Wagner, Fabien H., Sanchez, Alber, Tarabalka, Yuliya, Lotte, Rodolfo G., Ferreira, Matheus P., Aidar, Marcos P. M., et al. (2019). Using the U-net convolutional network to map forest types and disturbance in the Atlantic rainforest with very high resolution images. *Remote Sens. Ecol. Conserv.* 5 (4), 360–375. doi:10.1002/rse2.111

Wang, Di, Dong, Sufen, and Cheng, Fang (2021). Improved intutitionistic fuzzy C-means clustering pork image detection in HSV space. *Acta Metrol. Sin.* 42 (08), 986–992.

Wang, Ya. "Improved OTSU and adaptive genetic algorithm for infrared image segmentation," in Proceedings of the Paper presented at the 2018 Chinese Control and Decision Conference (CCDC), Shenyang, China, June 2018. doi:10.1109/CCDC.2018.8408116

Wei, Sisi, Zhang, Hong, Wang, Chao, Wang, Yuanyuan, and Xu, Lu (2019). Multi-temporal SAR data large-scale crop mapping based on U-Net model. *Remote Sens.* 11 (1), 68. doi:10.3390/rs11010068

Zhang, Junpeng, Liu, Hui, and Li, Qingrong (2021). Industrial smoke image segmentation based on FCN-LSTM. *Comput. Eng. Sci.* 43 (05), 907–916.

Zhang, Peng, Zhang, Lifu, Wu, Taixia, Zhang, Hongming, and Sun, Xuejian (2017). Detection and location of fouling on photovoltaic panels using a drone-mounted infrared thermography system. *J. Appl. Remote Sens.* 11 (1), 016026–16111. doi:10.1117/1.jrs.11.016026

frontiers | Frontiers in Energy Research

TYPE Original Research
PUBLISHED 10 March 2023
DOI 10.3389/fenrg.2023.1037587

OPEN ACCESS

EDITED BY
S. M. Muyeen,
Qatar University, Qatar

REVIEWED BY
Mohammad Amir,
Jamia Millia Islamia, India
Haris M. Khalid,
Higher Colleges of Technology,
United Arab Emirates

*CORRESPONDENCE
Bo Xu,
xubo@shiep.edu.cn

SPECIALTY SECTION
This article was submitted to Smart Grids, a section of the journal Frontiers in Energy Research

RECEIVED 06 September 2022
ACCEPTED 17 February 2023
PUBLISHED 10 March 2023

CITATION
Li D, Wan R, Xu B, Yao Y, Dong N and Zhang X (2023), Optimal capacity configuration of the wind-storage combined frequency regulation system considering secondary frequency drop. *Front. Energy Res.* 11:1037587. doi: 10.3389/fenrg.2023.1037587

Optimal capacity configuration of the wind-storage combined frequency regulation system considering secondary frequency drop

Dongdong Li, Rui Wan, Bo Xu*, Yin Yao, Nan Dong and Xianming Zhang

College of Electrical Engineering, Shanghai University of Electric Power, Shanghai, China

With wind power integrated into the power system on a large scale, the system has become vulnerable to the frequency stability issue. The battery energy storage system (BESS) is considered the key solution to improving the system frequency regulation performance due to its fast response ability. Furthermore, the construction of wind-storage combined frequency regulation systems has been developed for many years, in which the optimal capacity configuration of the wind-storage system is getting more attention. However, the secondary frequency drop (SFD) caused by wind turbines (WTs) participating in primary frequency regulation (PFR) is neglected in most existing capacity configurations, which is worthy of further study. In this paper, the optimal capacity of the wind-storage combined frequency regulation system is studied from the perspective of SFD. The time-domain expressions of two-stage system frequency response considering SFD are derived based on the wind-storage combined frequency regulation model. Next, considering the technical and economic characteristics of wind-storage combined frequency regulation, an optimization model of the energy storage capacity configuration is established with the objective of minimizing the sum of the maximum frequency deviations in two stages and the energy storage cost. The optimization model is solved by the multi-objective salp swarm algorithm (MSSA) to obtain the setting value of wind-storage combined frequency regulation parameters and the optimal energy storage capacity. The effectiveness of the proposed method is verified in MATLAB. The simulation results show that the proposed model can effectively improve the frequency regulation effect of the system and ensure the optimal capacity configuration with better economy.

KEYWORDS

wind-storage system, primary frequency regulation, secondary frequency drop, capacity configuration, multi-objective salp swarm algorithm

1 Introduction

Wind power is the fastest developing and most competitive power generation technology in renewable energy generation with its outstanding advantages of low costs and mature technology (Amir et al., 2022). However, because wind turbines (WTs) are connected to the grid through power electronic converters, they have little or no inertial response, reducing

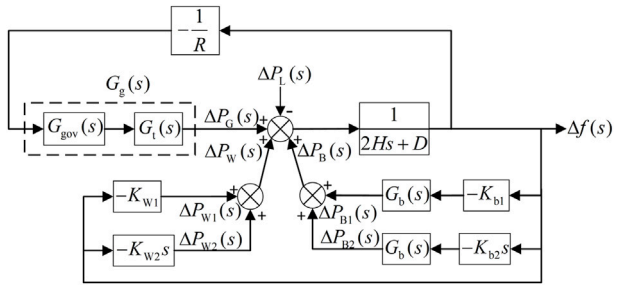

FIGURE 1
Dynamic model of the wind-storage system participating in PFR.

the overall inertia of the power system. Therefore, the increasing wind power penetration will threaten the frequency stability of the power system (Li et al., 2021; Zaheeruddin et al., 2021; Guo and Wu, 2022; Kheshti et al., 2022; Zhang et al., 2022). Rapid development of the energy storage system has provided a new solution for frequency regulation with its flexible charge–discharge ability and fast dynamic response (Zhang et al., 2020; Akram et al., 2021; Meng et al., 2021; Subroto et al., 2021; Guan, 2022). Moreover, the construction of the wind-storage combined frequency regulation system can effectively ensure the secure and stable operation of the system (Rahimi et al., 2021; Dantas et al., 2022; Xiong et al., 2022).

In recent years, the optimal configuration of energy storage capacity in the wind-storage combined system has received significant attention (Sandelic et al., 2018; Cao et al., 2019; Liu et al., 2020; Salman et al., 2020) because it will directly influence the security and economy of system operation (Wang et al., 2018; Wang et al., 2019; Shin and Hur, 2020). Excessive energy storage capacity will increase the investment and maintenance costs, whereas insufficient energy storage capacity cannot meet the demand of concentrated and large loads, making it hard to improve the power quality and the overall operation effect of the system in essence (Masaud et al., 2017; Chen et al., 2021; Wan et al., 2021).

The methods implemented for the energy storage capacity configuration in the wind-storage system mainly consider the two objectives of economy and reliability comprehensively to realize capacity optimization, in that both the economic and technical characteristics are of great significance in the wind-storage combined system. In fact, most studies on the optimal configuration of energy storage capacity in wind-storage systems mainly consider the costs or benefits of wind-storage combined frequency regulation as the objective constrained by frequency security (Peng et al., 2019; Bera et al., 2021). In Peng et al. (2019), based on the proposed fuzzy-based coordinated control and sizing strategy, an optimization model for minimizing the operation and frequency regulation costs of the wind-storage combined system is presented to determine the energy storage capacity. Meanwhile, in Bera et al. (2021), a novel planning strategy for optimally sizing an energy storage system is proposed to minimize the operational costs of the system and meet the frequency stability constraint. However, few research studies have considered secondary frequency drop (SFD) caused by wind turbines participating in frequency regulation. To eliminate SFD, the control method of the battery energy storage system (BESS) should be changed to add the extra active power output. Thus, the existing optimal configurations without considering SFD can easily contribute to the inaccuracy of the energy storage capacity, which will affect the overall system frequency regulation performance.

Since the SFD is an important factor indicating the effect of system frequency regulation, several wind-storage coordinated frequency regulation control strategies to reduce SFD were proposed, as in Wu et al. (2017), Rahimi et al. (2021), and Ma and Li (2022). In Wu et al. (2017), the BESS's fast and accurate active power control is fully used to resolve the SFD issue in wind rotor speed recovery. In Rahimi et al. (2021), the coordination of WTs and energy storage can improve the frequency stability of a low inertia microgrid, thus improving the second frequency nadir due to the inertia response of WTs. In Ma and Li (2022), a wind-storage combined virtual inertial control system based on quantization and regulation decoupling of active power increments is proposed to solve problems such as SFD by using the BESS to compensate for the power shortages of WTs. However, in these literature studies, the capacity configuration and the SFD issue have not been taken into account at the same time.

Motivated by the issues mentioned previously, we focus the scope of this paper on the optimal capacity configuration of the wind-storage combined frequency regulation system considering SFD. With the inspiration of the technical and economic characteristics of wind-storage combined frequency regulation, we aimed to effectively solve the problem of the energy storage capacity allocated without considering SFD (Peng et al., 2019; Salman et al., 2020; Bera et al., 2021), which has significant

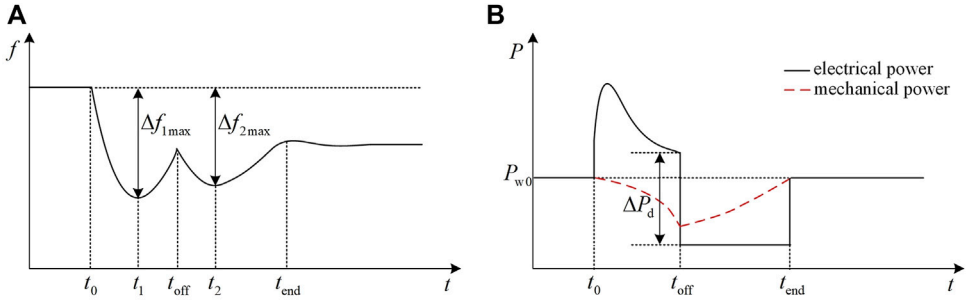

FIGURE 2
(A) Schematic diagram of the SFD. **(B)** Power output curves of WTs.

TABLE 1 Economic parameters of the energy storage system.

Parameter	Value	Parameter	Value
C_{pcs}	1,500 $/kW	C_{pscr}	1 $/kW
C_{ess}	1,500 $/(kW·h)	C_{escr}	1 $/(kW·h)
C_{pbop}	100 $/kW	n	2
C_{pom}	10 $/kW	i	10%
C_{eom}	0.01 $/(kW·h)	σ	4%

potential to improve both the effect of frequency regulation and the economy of the BESS participating in primary frequency regulation (PFR).

The contributions of this paper are as follows:

- Derive the time-domain expressions of the two-stage system frequency response with SFD under the establishment of the wind-storage combined frequency regulation model.
- Establish an optimal capacity configuration model constrained by the charge–discharge power and the state of charge (SOC) of the BESS with the minimum sum of the maximum frequency deviations in two stages and the minimum energy storage cost as the optimization objectives based on the life cycle cost (LCC) theory.
- The comparison of capacity configuration between considering and not considering SFD is presented to show the effectiveness of the proposed method.
- Different wind power penetration levels are considered and simulated to affirm the suitability of the proposed model for a power system with a high wind power penetration level.

The rest of this paper is organized as follows: Section 2 deduces time-domain expressions of the two-stage system frequency response considering SFD based on the model of the wind-storage combined system participating in PFR. Section 3 describes the objective functions and constraints of the optimal capacity configuration model of the wind-storage system. Section 4 presents the optimization results to analyze and prove the effectiveness of the proposed method. The last section concludes the paper.

2 Model of the wind-storage system participating in PFR

2.1 Establishment of the wind-storage combined frequency regulation model

The model of the wind-storage system participating in PFR of a power grid is shown in Figure 1. Wind turbines adopt integrated inertia control, and the BESS adopts virtual integrated inertia control to respond to system frequency change in a timely manner and provide active power support.

In Figure 1, $\Delta P_L(s)$ is the variation of load power; $\Delta P_G(s)$, $\Delta P_W(s)$, and $\Delta P_B(s)$ are the power output variation of traditional units, WTs, and BESS, respectively; $\Delta P_{W1}(s)$ and $\Delta P_{W2}(s)$ are the power output variation of WTs with droop control and inertia control, respectively; $\Delta P_{B1}(s)$ and $\Delta P_{B2}(s)$ are the power output variation of the BESS with virtual droop control and virtual inertia control, respectively; $\Delta f(s)$ is the frequency deviation of the power grid; R is the adjustment coefficient of traditional units; K_{w1} and K_{w2} are the droop control and inertia control coefficients of WTs, respectively; K_{b1} and K_{b2} are the virtual droop coefficient and the virtual inertia coefficient of the BESS, respectively; $G_g(s)$ and $G_b(s)$ are the transfer functions of traditional units and BESSs, respectively; H is the inertia time constant of the power grid; D is the damping factor of the system.

The model of thermal power units $G_g(s)$ consists of the governor model and the steam turbine model (Singh et al., 2021b; Singh and Zaheeruddin, 2021), as shown in Equation 1:

$$G_g(s) = G_{gov}(s)G_t(s), \tag{1}$$

where $G_{gov}(s)$ is the transfer function of the governor and $G_t(s)$ is the transfer function of a non-reheated steam turbine.

The specific expressions of $G_{gov}(s)$ and $G_t(s)$ are as follows:

$$G_{gov}(s) = \frac{1}{1 + sT_g}, \tag{2}$$

$$G_t(s) = \frac{1}{1 + sT_t}, \tag{3}$$

where T_g is the time constant of the governor and T_t is the time constant of the steam turbine.

The BESS model $G_b(s)$ is equivalent to a first-order inertia model (Singh et al., 2021a; Li C. P. et al., 2022), which can be expressed as follows:

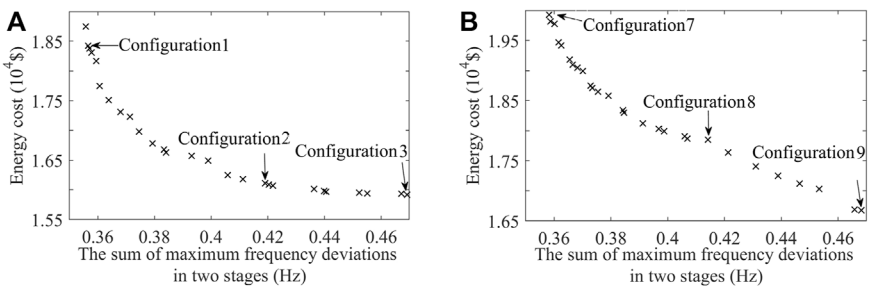

FIGURE 3
Pareto results considering SFD under **(A)** scenario 1 and **(B)** scenario 2.

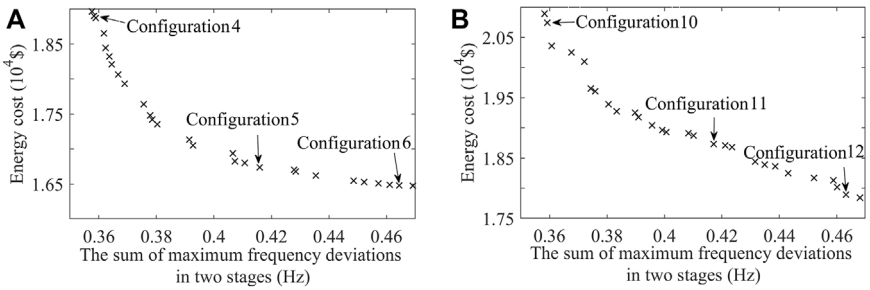

FIGURE 4
Pareto results without considering SFD under **(A)** scenario 1 and **(B)** scenario 2.

TABLE 2 Optimization results considering SFD.

Case	Optimization variables							Objectives	
	K_{w1}	K_{w2}	K_{b11}	K_{b12}	K_{b21}	K_{b22}	t_{off} (s)	Δf_{12max} (Hz)	C_{LCC} (×10^4\$)
Configuration 1	17	26	23	25	15	24	12	0.357	1.8428
Configuration 2	18	17	15	23	14	11	12	0.413	1.6122
Configuration 3	15	12	13	20	11	10	10	0.467	1.5919

TABLE 3 Optimization results without considering SFD.

Case	Optimization variables					Objectives	
	K_{w1}	K_{w2}	K_{b11}	K_{b12}	t_{off} (s)	Δf_{12max} (Hz)	C_{LCC} (×10^4\$)
Configuration 4	19	27	21	25	13	0.359	1.8971
Configuration 5	18	24	15	19	14	0.416	1.6739
Configuration 6	16	18	11	17	12	0.464	1.6478

$$G_b(s) = \frac{1}{1 + sT_b}, \tag{4}$$

where T_b is the response time constant of the BESS.

The dynamic grid frequency model of the wind-storage system is given in Figure 1

$$\Delta f(s) = (\Delta P_G(s) + \Delta P_W(s) + \Delta P_B(s) - \Delta P_L(s)) \cdot \frac{1}{2Hs + D}, \tag{5}$$

where

$$\begin{cases} \Delta P_G(s) = -\frac{1}{R} \cdot G_g(s) \cdot \Delta f(s) \\ \Delta P_W(s) = \Delta P_{W1}(s) + \Delta P_{W2}(s) = -K_{w1} \cdot \Delta f(s) - K_{w2} s \cdot \Delta f(s) \\ \Delta P_B(s) = \Delta P_{B1}(s) + \Delta P_{B2}(s) = -K_{b1} \cdot G_b(s) \cdot \Delta f(s) - K_{b2} s \cdot G_b(s) \cdot \Delta f(s) \end{cases} \tag{6}$$

2.2 Analysis of WTs participating in PFR

Wind turbines are expected to operate normally under maximum power point tracking (MPPT) conditions. The system frequency response and power output curves of WTs participating in PFR of the power grid are shown in Figures 2A, B respectively. In Figure 2, t_0 is the time when power disturbance occurs; t_{off} is the time of WTs exiting frequency regulation; t_{end} is the time when the operation mode of wind turbines changes to the MPPT mode; P_{w0} is the initial power output of wind turbines; ΔP_d is the variation of electrical power when WTs exit frequency regulation. Figure 2 shows that the process of WTs participating in PFR can be divided into two stages, i.e., stages I and II.

Stage I: A load increase of ΔP_L as the power disturbance at t_0 causes the system frequency to drop; then, WTs increase the electrical power output by releasing rotor kinetic energy to participate in PFR. As rotor speed decreases, the mechanical power input of WTs reduces.

Stage II: WTs exit frequency regulation to recover rotor speed at t_{off}. The sudden drop in electrical power causes the power imbalance in the system to change abruptly, leading to SFD. The electrical power P_w remains constant while being less than the mechanical power P_m during rotor speed recovery. When the rotor absorbs active power and returns to its initial speed, the WTs switch to the MPPT mode.

TABLE 4 Energy storage capacity configuration considering SFD.

Case	Energy storage capacity configuration	
	P_{rated} (MW)	E_{rated} (MW·h)
Configuration 1	7.69	8.5451
Configuration 2	7.18	8.2495
Configuration 3	7.31	8.1272

TABLE 5 Energy storage capacity configuration without considering SFD.

Case	Energy storage capacity configuration	
	P_{rated} (MW)	E_{rated} (MW·h)
Configuration 4	7.63	8.7508
Configuration 5	6.57	8.4011
Configuration 6	6.73	8.2763

2.3 Method of energy storage capacity configuration

BESS configuration for PFR can effectively compensate for the power deficit caused by wind turbines exiting frequency regulation. Since the capacity of the BESS directly affects the security and economy of system operation, it is imperative to allocate energy storage capacity reasonably to improve the effect of frequency regulation and reduce the economic cost.

Considering the power convert system (PCS) efficiency and charge–discharge efficiency of the BESS in the frequency regulation period of T_f, the rated power P_{rated} of the BESS can be expressed as in Eq. 7:

$$P_{rated} = \max\left\{\begin{array}{c}\max\limits_{t\in(t_0,t_0+T_f)}[\Delta P_B(t)]\eta_1\eta_2\eta_{ch},\\ \dfrac{-\min\limits_{t\in(t_0,t_0+T_f)}[\Delta P_B(t)]}{\eta_1\eta_2\eta_{dis}}\end{array}\right\}, \tag{7}$$

where t_0 is the initial time of frequency regulation; T_f is the time period of frequency regulation; η_1 and η_2 are the efficiencies of the DC–DC and DC–AC converters of the PCS, respectively; η_{ch} and η_{dis} are charging and discharging efficiencies of the BESS, respectively; $\Delta P_B(t)$ is the power instruction of the BESS at time t (it is assumed that when the BESS is in the charging mode, its power is positive, and it is negative in the discharging mode).

The SOC of the BESS and its constraint are given by Eqs 8, 9, respectively (Khalid et al., 2015a; Khalid et al., 2015b).

$$SOC(t) = SOC_0 + \frac{\int_0^{t\Delta t}\Delta P_B(t)dt}{E_{rated}}, \tag{8}$$

$$SOC_{min} \le SOC(t) \le SOC_{max}, \tag{9}$$

where SOC_0 and $SOC(t)$ are the SOC of the BESS at the initial time and t, respectively; SOC_{max} and SOC_{min} are the upper and lower limits of SOC, respectively; Δt is the time interval of power instruction; and E_{rated} is the rated capacity of the BESS.

Considering the PCS efficiency and charge–discharge efficiency of the BESS in the frequency regulation period of T_f, the rated capacity E_{rated} of the BESS can be expressed as follows:

$$E_{rated} = \max\left\{\begin{array}{c}\dfrac{\max\limits_{t\in T_f}\left[\int_0^{t\Delta t}\Delta P_B(t)dt\right]}{SOC_{max}-SOC_0},\\ \dfrac{-\min\limits_{t\in T_f}\left[\int_0^{t\Delta t}\Delta P_B(t)dt\right]}{SOC_0-SOC_{min}}\end{array}\right\}. \tag{10}$$

2.4 Wind-storage combined frequency regulation model considering SFD

2.4.1 PFR model of stage I

The frequency response model of wind-storage combined frequency regulation can be deduced according to Figure 1. When load disturbance occurs, the frequency response model of stage I is expressed as follows:

$$\Delta f_1(s) = \frac{-\Delta P_L(s)}{2Hs + D + G_{gen}(s) + G_{b1}(s) + G_w(s)}, \tag{11}$$

where $G_{gen}(s)$, $G_{b1}(s)$, and $G_w(s)$ are transfer functions of thermal power units, BESSs, and WTs, respectively.

The specific expressions of $G_{gen}(s)$, $G_{b1}(s)$, and $G_w(s)$ are

$$G_{gen}(s) = \frac{1}{R\left(1+sT_g\right)(1+sT_t)}, \tag{12}$$

$$G_{b1}(s) = (K_{b11} + K_{b12}s)\frac{1}{1+sT_b}, \tag{13}$$

$$G_w(s) = K_{w1} + K_{w2}s, \tag{14}$$

where K_{b11} and K_{b12} are, respectively, the virtual droop coefficient and the virtual inertia coefficient of the BESS at stage I.

Equation 11 can be simplified as

$$\Delta f_1(s) = -\frac{\Delta P_L}{s}\frac{m_0s^3 + m_1s^2 + m_2s + m_3}{n_0s^4 + n_1s^3 + n_2s^2 + n_3s + n_4}, \tag{15}$$

where m_i and n_j are the coefficients of the s-domain function, as shown in Supplementary Material.

Following the partial fraction expansion and the inverse Laplace transform given in Eq. 15, the time-domain expression of the system frequency response of stage I can be obtained as follows:

$$\Delta f_1(t) = -\frac{\Delta P_L m_0}{n_0}\left\{\begin{array}{l}A_0 + A_1e^{pt} + A_2e^{qt} +\\ A_3e^{-\zeta\omega t}\sin\left[\left(\omega\sqrt{1-\zeta^2}\right)t + \varphi\right]\end{array}\right\}, \tag{16}$$

where A_i, p, q, ζ, ω, and φ are the coefficients of the time-domain expression, as shown in Supplementary Material.

Based on Eq. 16, the maximum frequency deviation Δf_{1max} of stage I can be expressed as follows:

$$\Delta f_{1\,max} = -\frac{\Delta P_L m_0}{n_0}\left\{\begin{array}{l}A_0 + A_1e^{pt_1} + A_2e^{qt_1} +\\ A_3e^{-\zeta\omega t_1}\sin\left[\left(\omega\sqrt{1-\zeta^2}\right)t_1 + \varphi\right]\end{array}\right\}, \tag{17}$$

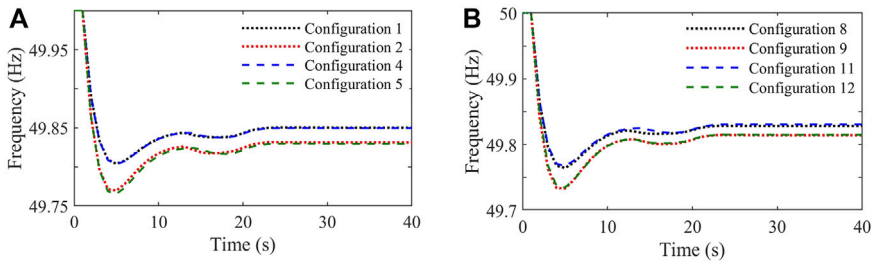

FIGURE 5
System frequency curves under **(A)** scenario 1 and **(B)** scenario 2.

where t_1 is the time at which the frequency nadir of stage I occurs. The derivation process is shown in Supplementary Material.

2.4.2 PFR model of stage II

At t_{off}, when stage I ends, WT exiting frequency regulation leads to SFD. The BESS and thermal power units participate in PFR together at stage II to compensate for the power deficit observed due to the rotor speed recovery of wind turbines.

When wind turbines exit frequency regulation, the frequency response model of stage II can be expressed as follows:

$$\Delta f_2(s) = \frac{-\Delta P_{off}(s)}{2Hs + D + G_{gen}(s) + G_{b2}(s)}, \tag{18}$$

where $G_{b2}(s)$ is the transfer function of the BESS and $\Delta P_{off}(s)$ is the power deficit at the time when WTs exit frequency regulation.

The specific expressions of $G_{b2}(s)$ and $\Delta P_{off}(s)$ are

$$G_{b2}(s) = (K_{b21} + K_{b22}s)\frac{1}{1 + sT_b}, \tag{19}$$

$$\Delta P_{off}(s) = \frac{1}{s}[(P_{L0} + \Delta P_L) - P_G(t_{off}) - P_B(t_{off}) - P_W(t_{off})], \tag{20}$$

$$P_W(t_{off}) = -\frac{3k_{opt}\omega_0 \Delta P_W}{2H_W} t_{off} + P_{W0}, \tag{21}$$

where K_{b21} and K_{b22} are, respectively, the virtual droop coefficient and virtual inertia coefficient of the BESS at stage II; P_{L0} is the initial load power; P_G (t_{off}), P_B(t_{off}), and P_W(t_{off}) are, respectively, the power output of thermal power units, BESSs, and WTs at the time when wind turbines exit frequency regulation; k_{opt} is the coefficient of the MPPT curve of wind turbines; ω_0 is the initial value of wind rotor speed; and H_W is the equivalent time constant of wind turbines.

Referring to the derivation process of stage I, the time-domain expression of system frequency response of stage II $\Delta f_2(t)$, the maximum frequency deviation Δf_{2max} as well as the time at which the maximum appears t_2 can be obtained.

3 Capacity optimization of the wind-storage system

3.1 Objective functions

Wind-storage combined frequency regulation can improve the effect of frequency regulation, but the economic cost should be taken into account. The wind-storage system participates in PFR from the perspective of SFD. Therefore, the sum of the maximum frequency deviations in two stages and the energy storage cost are considered objective functions so as to ensure frequency stability and improve the economy of BESSs participating in frequency regulation. The objective functions are expressed as follows:

$$\begin{cases} \min \Delta f_{12\,max} = |\Delta f_{1\,max}| + |\Delta f_{2\,max}| \\ \min C_{LCC} = C_{inv} + C_{bop} + C_{om} + C_{scr} - C_{res} \end{cases}, \tag{22}$$

where Δf_{12max} is the sum of the maximum frequency deviations in two stages; C_{LCC} is the energy storage cost; C_{inv} is the initial

TABLE 6 Optimization results considering SFD.

Case	Optimization variable							Objective	
	K_{w1}	K_{w2}	K_{b11}	K_{b12}	K_{b21}	K_{b22}	t_{off} (s)	Δ_{f12max} (Hz)	C_{LCC} (×10^4\$)
Configuration 7	24	27	18	25	23	28	12	0.355	1.9932
Configuration 8	13	22	19	21	15	13	12	0.418	1.7853
Configuration 9	14	20	15	16	11	12	13	0.468	1.6681

TABLE 7 Optimization results without considering SFD.

Case	Optimization variable					Objective	
	K_{w1}	K_{w2}	K_{b11}	K_{b12}	t_{off} (s)	Δf_{12max} (Hz)	C_{LCC} (×10^4\$)
Configuration 10	16	24	23	27	13	0.357	2.0737
Configuration 11	17	21	15	20	13	0.415	1.8734
Configuration 12	14	16	13	19	12	0.465	1.7886

investment and replacement cost; C_{bop} is the balance of plant cost; C_{om} is the operation and maintenance cost; C_{scr} is the scrap disposal cost; and C_{res} is the recovery residual value.

3.1.1 The sum of the maximum frequency deviations in two stages

The objective function is to minimize the sum of the maximum frequency deviations in two stages: the absolute value of the maximum frequency deviation of stage I Δf_{1max} and that of stage II Δf_{2max}. Since the maximum frequency deviations of stages I and II have been discussed in Sections 3.1 and 3.2, respectively, they will not be described here.

3.1.2 Energy storage cost

Based on the LCC theory considering the sum of all direct or indirect costs in the processes of investment, purchase, operation, maintenance, and recovery in the whole life cycle of the system (Swierczynski et al., 2015; Torkashvand et al., 2020), the economic model of the BESS is established for minimizing the energy storage cost, which includes the following five aspects.

3.1.2.1 Initial investment and replacement cost

The initial investment cost refers to the fixed capital of a one-time investment for the purchase of main equipment in the initial stage of energy storage project construction, which consists of the power cost and energy cost determined by the rated power P_{rated} and the rated capacity E_{rated} of the BESS, respectively. The replacement cost usually involves the replacement of energy storage elements, and the combination of these two costs can be described as follows:

$$C_{inv} = C_{pcs}P_{rated} + \sum_{k=0}^{n} C_{ess}E_{rated}(1+i)^{-[kT/(n+1)]}, \quad (23)$$

where C_{pcs} is the per unit cost of power of the PCS; C_{ess} is the per unit cost of energy; i is the interest rate; T is the lifetime; and n is the number of times energy storage must be replaced.

3.1.2.2 Balance of plant cost

The balance of plant cost refers to the purchase fund for auxiliary equipment of the energy storage system such as cables, network facilities, and control servers, that is:

$$C_{bop} = C_{pbop}P_{rated} \text{ or } C_{bop} = C_{ebop}E_{rated}, \quad (24)$$

where C_{pbop} and C_{ebop} are the per unit balance of plant cost corresponding to the power and capacity of BESSs, respectively.

3.1.2.3 Operation and maintenance cost

The operation and maintenance cost refers to the capital dynamically invested to ensure normal operation of energy storage during its lifetime, which usually includes the fixed part determined by the PCS and the variable part determined by the charging and discharging quantities of the energy storage system, namely,

$$C_{om} = C_{pom}P_{rated}\left[\frac{(1+i)^T - 1}{i(1+i)^T}\right] + \sum_{t=1}^{T} C_{eom}W(t)(1+i)^{-t}, \quad (25)$$

where C_{pom} is the per unit operation and maintenance cost of the power; C_{eom} is the per unit operation and maintenance cost of the electric quantity; $W(t)$ is the annual charging and discharging quantity of the energy storage system.

3.1.2.4 Scrap disposal cost

The scrap disposal cost refers to the cost generated by the harmless disposal and recycling after the scrapping of battery energy storage equipment in the lifetime, namely,

$$C_{scr} = C_{pscr}P_{rated}(1+i)^{-T} + \sum_{j=1}^{n+1} C_{escr}E_{rated}(1+i)^{-[jT/(n+1)]}, \quad (26)$$

where C_{pscr} is the per unit scrap disposal cost of power and C_{escr} is the per unit scrap disposal cost of capacity.

3.1.2.5 Recovery residual value

The recovery residual value refers to the recoverable residual value (negative cost) of the fixed assets of the energy storage system at the end of its lifetime, namely,

$$C_{res} = \sigma(C_{inv} + C_{bop})(1+i)^{-T}, \quad (27)$$

where σ is the rate of the recovery residual value, generally 3%–5%.

TABLE 8 Energy storage capacity configuration considering SFD.

Case	Energy storage capacity configuration	
	P_{rated} (MW)	E_{rated} (MW·h)
Configuration 7	6.94	9.0862
Configuration 8	8.15	8.4749
Configuration 9	6.79	8.3151

TABLE 9 Energy storage capacity configuration without considering SFD.

Case	Energy storage capacity configuration	
	P_{rated} (MW)	E_{rated} (MW·h)
Configuration 10	8.06	9.1257
Configuration 11	7.01	8.6814
Configuration 12	6.97	8.5241

3.2 Constraints

3.2.1 Charge–discharge power constraint of the BESS

The BESS charge–discharge power is limited to its rated power (Khalid and Peng, 2020; Khalid et al., 2022). This constraint is formulated as follows:

$$-P_{rated} \le P_e(t) \le P_{rated}, \tag{28}$$

where $P_e(t)$ is the charge–discharge power of the BESS at time t.

3.2.2 SOC constraint of the BESS

In order to avoid the influence of excessive charge and discharge on the lifetime of the BESS, the SOC constraint is shown in Eq. 9.

3.3 Optimization method

The salp swarm algorithm (SSA) is a novel heuristic intelligent algorithm inspired by the swarming behavior of salps (salp chain) (Mirjalili et al., 2017). It has been applied to solve problems such as multi-objective optimization, with the advantages of simple structure, few parameters, and easy realization. The SSA algorithm divides the population into two groups: leader and followers. The leader is the salp at the front of the chain, guiding the swarm, which is followed by the rest of the salps, namely, the followers.

In the SSA, the optimization target is taken as the food source called F; thus, the position of the leader can be expressed by Eq. 29.

$$x_j^1 = \begin{cases} F_j + c_1\left[(ub_j - lb_j)c_2 + lb_j\right] & c_3 \ge 0 \\ F_j - c_1\left[(ub_j - lb_j)c_2 + lb_j\right] & c_3 < 0 \end{cases}, \tag{29}$$

where $x^1{}_j$ is the position of the first salp (leader) in the jth dimension; F_j is the position of the food source in the jth dimension; ub_j and lb_j are the upper and lower bounds of the jth dimension, respectively; c_1 is the most important parameter balancing exploration and exploitation; c_2 and c_3 are random numbers ranging from 0 to 1.

The specific expression of c_1 is as follows:

$$c_1 = 2e^{-(4l/L)^2}, \tag{30}$$

where l is the current iteration and L is the maximum number of iterations.

The position of the followers can be expressed by Eq. 31.

$$x_j^i = \frac{1}{2}\left(x_j^i + x_j^{i-1}\right) \quad i \ge 2, \tag{31}$$

where x^i_j is the position of ith follower salp in the jth dimension.

In the optimization process of the multi-objective salp swarm algorithm (MSSA), the Pareto optimal set will be updated continuously and put in the repository having a limited size. Suppose the desired number of non-dominated solutions is M, the basic steps of the MSSA are as follows:

1) Design a repository to store non-dominated solutions obtained from the algorithm.
2) If a salp in the new population dominates one or several solutions in the repository, add the salp to the repository and remove the dominated solutions from it. If a salp is in a non-dominated relationship with all repository residents, add it to the repository. If a salp is dominated by at least one of the repository residents, discard it straight away.
3) Assign the non-dominated solution i a rank r_{anki} based on the density of its neighboring solutions. The higher the rank, the more neighboring solutions it has, implying that the solutions around it are denser. When the number of non-dominated solutions in the repository is more than M, discard the solutions with higher ranks to ensure the number of solutions in the repository remains M and make the distribution of the Pareto optimal set as wide and uniform as possible.
4) Since the individuals in the repository are all non-dominated solutions, there is no absolute optimal individual. The food source chased by the leader of the next generation can be determined by ranking the solutions and using a roulette wheel selection.

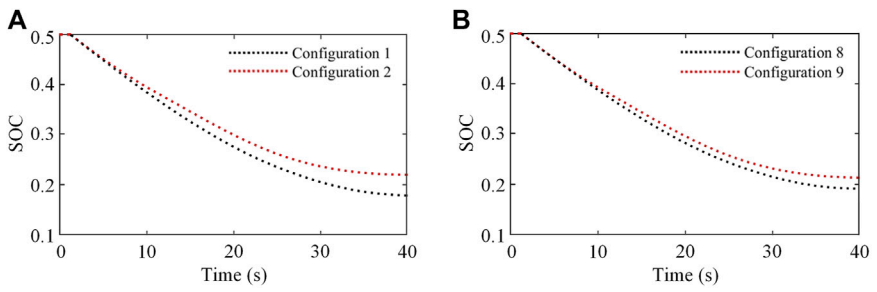

FIGURE 6
SOC curves under **(A)** scenario 1 and **(B)** scenario 2.

Input: $Kw1$, $Kw2$, $Kb11$, $Kb12$, $Kb21$, $Kb22$, and $toff$
Output: $\Delta f12max$ and C_{LCC}
1 **for** $t = 1 : t_{off}$ **do**
2 Obtain the value of $\Delta f1$ by Eq. 16
3 **end for**
4 **for** $t = t_{off} : 40$ **do**
5 Obtain the value of $\Delta f2$ by an equation similar to that of (16)
6 **end for**
7 $\Delta f_{12max} \leftarrow \Delta f_{1max} + \Delta f_{2max}$;
8 $CLCC \leftarrow Cinv + Cbop + Com + Cscr - Cres$;
9 Initialize the salp population x_i $(i = 1, 2, ., n)$ considering ub and lb;
10 **while** *end criterion is not met* **do**
11 Calculate the fitness of each search agent (salp);
12 Determine the non-dominated salps;
13 Update the repository considering the obtained non-dominated salps;
14 **if** *the repository becomes full*, **then**
15 Call the repository maintenance procedure to remove one repository resident;
16 Add the non-dominated salp to the repository;
17 **end if**
18 Choose a source of food from repository: F=SelectFood (repository);
19 Update c_1 by Eq. 30;
20 **for** *each salp* x_i **do**
21 **if** $(i = = 1)$ **then**
22 Update the position of the leading salp by Eq. 29;
23 **else**
24 Update the position of the follower salp by Eq. 31;
25 **end if**
26 **end for**
27 Amend the salps based on the upper and lower bounds of variables;
28 **end while**
29 return repository

Algorithm 1. Pseudo-code of the proposed method.

The proposed method can be transformed into a pseudo-code, as shown in Algorithm 1. The variables of input and output are defined at the top of the table. A for loop is applied for obtaining the values of Δf_1 and Δf_2, followed by the calculation of output variables Δf_{12max} and C_{LCC}, and the while loop for the MSSA optimizing the proposed model. These loops are shown in lines 1–3, 4–6, 7–8, and 9–29, respectively.

4 Case study

4.1 Simulation system

In order to verify the feasibility and effectiveness of the proposed model and method, the simulation system including thermal power units, WTs, load, and BESSs is taken as an example to study the optimal capacity configuration of the wind-storage system considering SFD. The rated capacity of thermal power units is 600 MW; the wind power system is made up of 100 WTs, each having a rated capacity of 2 MW; and the load capacity is 300 MW. The adjustment coefficient of thermal power units is 4%, the governor time constant is 0.2 s, and the steam turbine time constant is 0.3 s, the grid inertia time constant is 4 s, and the damping factor of the system is 2, the equivalent time constant of WTs is 10.38 s, the response time constant of the BESS is 0.1 s, the SOC ranges from 0.1 to 0.9 with an initial value of 0.5 (Tan et al., 2020; Li S. J. et al., 2022), and the PCS efficiency and charge–discharge efficiency of the BESS are both 90%. The lifetime of the BESS is 14 years. The population size and the maximum iteration of the MSSA are both 100.

4.2 Optimization parameters

The economic parameters of the BESS are shown in Table 1.

4.3 Optimization results

Assuming that the load increases from 300 MW to 320 MW at 1 s, the system frequency decreases. WTs, thermal power units, and BESSs participate in PFR, and SFD is considered only if the BESS reduces it. In order to study the optimal capacity configuration of the wind-storage combined frequency regulation system under different wind power penetration levels, two simulation scenarios with different wind power penetration levels are set: in scenario 1, the wind power penetration is 11%, with the power output of thermal power units and WTs being 267 and 33 MW, respectively. In scenario 2, the wind power penetration is 33%, with the power output of thermal power units and WTs being 201 and 99 MW, respectively.

According to the optimization model and the method proposed in this paper, the optimal capacity configuration of the wind-storage combined frequency regulation system under two different wind power penetration levels is simulated and analyzed. The Pareto results for the energy storage cost and the sum of the maximum frequency deviations in two stages are shown in Figures 3, 4. The comparison of the two figures shows that 1) the energy storage cost and the sum of the maximum frequency deviations in two stages are two contradictory goals, that is, the required energy storage capacity and cost will decrease as the sum of the maximum frequency deviations in two stages increases. 2) In the case of the same wind power penetration level, the Pareto results considering SFD are inclined to the lower left of the coordinate system when compared with those without considering SFD. The aforementioned phenomena indicate that the reasonable energy storage capacity configuration and considering SFD can improve the economy of energy storage participating in frequency regulation to a certain extent.

4.3.1 Simulation of scenario 1

In the Pareto results of scenario 1, three sets of configurations with the close sum of the maximum frequency deviations in two stages as shown in Figures 3A, 4A are chosen for analysis, among

which the sum of the maximum frequency deviations in two stages of configurations 1, 2, and 3 considering SFD is 0.357, 0.413, and 0.467 Hz and that of configurations 4, 5, and 6 without considering SFD is 0.359, 0.416, and 0.464 Hz, respectively. The corresponding optimization results are shown in Tables 2, 3, and the energy storage capacity configurations are shown in Tables 4, 5.

It can be seen from the optimization results that the active power output of the wind-storage system is low when its frequency regulation control parameters are small, leading to a large frequency deviation of the system. To reduce the system frequency deviation, the frequency regulation control parameters of the wind-storage system should be increased; thus, the energy storage cost increases with increase in energy storage capacity. The comparison of the energy storage costs of chosen configurations shows that the energy storage cost without considering SFD is about 3.43% higher on average than that considering SFD when the sums of the maximum frequency deviations in two stages are close in such circumstances.

Figure 5A shows the system frequency curves of configurations 1, 2, 4, and 5 in scenario 1. As can be seen from Figure 5A, the frequency nadir can be improved by increasing the frequency regulation control parameters of the wind-storage system, thus improving the frequency regulation effect of the system.

4.3.2 Simulation of scenario 2

Similar to scenario 1, in the Pareto results of scenario 2, three sets of configurations with the close sum of the maximum frequency deviations in two stages as shown in Figures 3B, 4B are chosen for analysis, among which the sum of the maximum frequency deviations in two stages of configurations 7, 8, and 9 considering SFD is 0.355, 0.418, and 0.468 Hz and that of configurations 10, 11, and 12 without considering SFD is 0.357, 0.415, and 0.465 Hz, respectively. The corresponding optimization results are shown in Tables 6, 7, and the energy storage capacity configurations are shown in Tables 8, 9. Figure 5B shows the system frequency curves of configurations 8, 9, 11, and 12 in Scenario 2. Figure 6 shows that the optimal capacity configuration of energy storage considering SFD is reasonable as its SOC value changes within the upper and lower limits.

The comparison of the energy storage costs of chosen configurations shows that the energy storage cost without considering SFD is about 5.40% higher on average than that considering SFD when the sums of the maximum frequency deviations in two stages are close in two such circumstances. Thus, according to the two scenarios, the energy storage cost without considering SFD is about 4.42% higher on average than that considering SFD. In addition, it can be seen from the optimization results under two different wind power penetration levels that the frequency drop is more severe in the higher wind power penetration level. In order to ensure the frequency regulation effect of the high wind power penetration level is basically the same as that of the low wind power penetration level, the energy storage cost will increase as the energy storage frequency regulation control parameters increase.

In conclusion, both SFD and wind power penetration levels will influence the optimal capacity configuration of the wind-storage combined frequency regulation system, in which the energy storage cost considering SFD is lower than that without considering SFD, and the sum of the maximum frequency deviations in two stages is smaller. Hence, it is beneficial to improve the economy of energy storage participating in frequency regulation and the system frequency regulation effect with SFD considered. When the sums of the maximum frequency deviations in two stages considering SFD are close to those without considering SFD, the comparison of energy storage costs in two such circumstances shows that the average growth rate of energy storage costs increases as the wind power penetration increases. It can be seen that the optimization effect considering SFD is more obvious with the high wind power penetration level.

5 Conclusion

In this paper, the time-domain expressions of two-stage system frequency response of wind-storage combined frequency regulation systems are derived by considering SFD. Under the constraints of charge–discharge power and the SOC of the BESS, an optimization model for minimizing the sum of the maximum frequency deviations in two stages and the energy storage cost is established. The MSSA is used to solve the optimization model and obtain the setting value of the frequency regulation control parameters of the wind-storage combined system and the optimal capacity configuration of energy storage. Based on the analysis of the optimization results, the following conclusions can be summarized:

1) The comparison of the optimization results of capacity configuration in different scenarios shows that the capacity configuration considering SFD can reduce the sum of the maximum frequency deviations in two stages and the energy storage cost than without considering SFD, thus improving the frequency regulation effect and the economy of the system.
2) The energy storage cost and the sum of the maximum frequency deviations in two stages are two contradictory objectives in the optimal capacity configuration of the wind-storage combined frequency regulation system. This is because the active power output of the wind-storage system is low when the frequency regulation control parameters are small, leading to the large frequency deviation of the system. The control parameters should be increased so as to reduce the frequency deviation, which results in an increase in the energy storage cost with more energy storage capacity required.
3) The optimization effect considering SFD is more obvious as the wind power penetration level increases, which is important and useful for the power system with high wind power integration.

The proposed model improves the PFR capability of the wind-storage system and the economy of energy storage participating in frequency regulation. As a result, the proposed method is expected to be a good choice for the optimal capacity configuration of wind-storage combined frequency regulation in the power system.

Data availability statement

The original contributions presented in the study are included in the article/Supplementary Material; further inquiries can be directed to the corresponding author.

Author contributions

All authors listed have made a substantial, direct, and intellectual contribution to the work and approved it for publication.

Funding

This research was supported by the National Natural Science Foundation of China (51977128) and the Shanghai Science and Technology Project (20142202600).

Conflict of interest

The authors declare that the research was conducted in the absence of any commercial or financial relationships that could be construed as a potential conflict of interest.

Publisher's note

All claims expressed in this article are solely those of the authors and do not necessarily represent those of their affiliated organizations, or those of the publisher, the editors, and the reviewers. Any product that may be evaluated in this article, or claim that may be made by its manufacturer, is not guaranteed or endorsed by the publisher.

Supplementary material

The Supplementary Material for this article can be found online at: https://www.frontiersin.org/articles/10.3389/fenrg.2023.1037587/full#supplementary-material

References

Akram, U., Mithulananthan, N., Raza, M. Q., Shah, R., and Milano, F. (2021). RoCoF restrictive planning framework and wind speed forecast informed operation strategy of energy storage system. *IEEE Trans. Power Syst.* 36 (1), 224–234. doi:10.1109/TPWRS.2020.3001997

Amir, M., Prajapati, A. K., and Refaat, S. S. S. (2022). Dynamic performance evaluation of grid-connected hybrid renewable energy-based power generation for stability and power quality enhancement in smart grid. *Front. Energy Res.* 10, 16. doi:10.3389/fenrg.2022.861282

Bera, A., Chalamala, B., Byrne, R. H., and Mitra, J. (2021). "Optimal planning of energy storage in wind integrated systems considering frequency stability," in 2021 IEEE Power and Energy Society General Meeting, Washington, DC, USA, 26-29 July 2021, 1–5. doi:10.1109/PESGM46819.2021.9638110

Cao, M. J., Xu, Q. S., Nazaripouya, H., Chu, C. C., Pota, H. R., and Gadh, R. (2019). Engineering energy storage sizing method considering the energy conversion loss on facilitating wind power integration. *IET Gener. Transm. Distrib.* 13 (9), 1693–1699. doi:10.1049/iet-gtd.2018.6358

Chen, H., Shi, J., Liu, R., Huang, L., Jia, Y., and Wu, H. (2021). "Optimal planning of primary frequency regulation capacity of wind-storage combined systems," in 2021 IEEE 5th Conference on Energy Internet and Energy System Integration (EI2), Taiyuan, China, 22-24 October 2021, 2178–2183. doi:10.1109/EI252483.2021.9713134

Dantas, N. K. L., Souza, A. C. M., Vasconcelos, A. S. M., Junior, W. D. S., Rissi, G., Dall'Orto, C., et al. (2022). Impact analysis of a battery energy storage system connected in parallel to a wind farm. *Energies* 15 (13), 4586. doi:10.3390/en15134586

Guan, M. (2022). Scheduled power control and autonomous energy control of grid-connected energy storage system (ESS) with virtual synchronous generator and primary frequency regulation capabilities. *IEEE Trans. Power Syst.* 37 (2), 942–954. doi:10.1109/TPWRS.2021.3105940

Guo, Z., and Wu, W. (2022). Data-driven model predictive control method for wind farms to provide frequency support. *IEEE Trans. Energy Convers.* 37 (2), 1304–1313. doi:10.1109/TEC.2021.3125369

Khalid, H. M., Ahmed, Q., and Peng, J. C. H. (2015a). Health monitoring of li-ion battery systems: A median expectation diagnosis approach (MEDA). *IEEE Trans. Transp. Electrif.* 1 (1), 94–105. doi:10.1109/tte.2015.2426431

Khalid, H. M., Ahmed, Q., Peng, J. C. H., and Rizzoni, G. (2015b). Current-split estimation in li-ion battery pack: An enhanced weighted recursive filter method. *IEEE Trans. Transp. Electrif.* 1 (4), 402–412. doi:10.1109/tte.2015.2492557

Khalid, H. M., Flitti, F., Muyeen, S. M., Elmoursi, M. S., Sweidan, T. O., and Yu, X. H. (2022). Parameter estimation of vehicle batteries in V2G systems: An exogenous function-based approach. *IEEE Trans. Ind. Electron.* 69 (9), 9535–9546. doi:10.1109/tie.2021.3112980

Khalid, H. M., and Peng, J. C. H. (2020). Bidirectional charging in V2G systems: An in-cell variation analysis of vehicle batteries. *IEEE Syst. J.* 14 (3), 3665–3675. doi:10.1109/jsyst.2019.2958967

Kheshti, M., Lin, S., Zhao, X., Ding, L., Yin, M., and Terzija, V. (2022). Gaussian distribution-based inertial control of wind turbine generators for fast frequency response in low inertia systems. *IEEE Trans. Sustain. Energ.* 13 (3), 1641–1653. doi:10.1109/TSTE.2022.3168778

Li, C. P., Li, J., Li, J. H., Zhang, X. C., and Hou, T. (2022). Optimization strategy of secondary frequency modulation based on dynamic loss model of the energy storage unit. *J. Energy Storage* 51, 104425. doi:10.1016/j.est.2022.104425

Li, H., Qiao, Y., Lu, Z., Zhang, B., and Teng, F. (2021). Frequency-constrained stochastic planning towards a high renewable target considering frequency response support from wind power. *IEEE Trans. Power Syst.* 36 (5), 4632–4644. doi:10.1109/TPWRS.2021.3066991

Li, S. J., Xu, Q. S., Xia, Y. X., and Hua, K. (2022). Comprehensive setting and optimization of Dead-Band for BESS participate in power grid primary frequency regulation. *Int. J. Electr. Power Energy Syst.* 141, 108195. doi:10.1016/j.ijepes.2022.108195

Liu, Y., Wu, X. G., Du, J. Y., Song, Z. Y., and Wu, G. L. (2020). Optimal sizing of a wind-energy storage system considering battery life. *Renew. Energy* 147, 2470–2483. doi:10.1016/j.renene.2019.09.123

Ma, D. Z., and Li, W. Y. (2022). Wind-storage combined virtual inertial control based on quantization and regulation decoupling of active power increments. *Energies* 15 (14), 5184. doi:10.3390/en15145184

Masaud, T. M., Oyebanjo, O., and Sen, P. K. (2017). Sizing of large-scale battery storage for off-grid wind power plant considering a flexible wind supply-demand balance. *IET Renew. Power Gener.* 11 (13), 1625–1632. doi:10.1049/iet-rpg.2016.0839

Meng, G., Chang, Q., Sun, Y., Rao, Y., Zhang, F., Wu, Y., et al. (2021). Energy storage auxiliary frequency modulation control strategy considering ACE and SOC of energy storage. *IEEE Access* 9, 26271–26277. doi:10.1109/ACCESS.2021.3058146

Mirjalili, S., Gandomi, A. H., Mirjalili, S. Z., Saremi, S., Faris, H., and Mirjalili, S. M. (2017). Salp swarm algorithm: A bio-inspired optimizer for engineering design problems. *Adv. Eng. Softw.* 114, 163–191. doi:10.1016/j.advengsoft.2017.07.002

Peng, B., Zhang, F., Liang, J., Ding, L., and Wu, Q. W. (2019). An optimal control and sizing strategy for a coordinated WTG-ES system to provide frequency support. *Int. J. Electr. Power Energ. Syst.* 113, 251–263. doi:10.1016/j.ijepes.2019.05.052

Rahimi, T., Ding, L., Kheshti, M., Faraji, R., Guerrero, J. M., and Tinajero, G. D. A. (2021). Inertia response coordination strategy of wind generators and hybrid energy storage and operation cost-based multi-objective optimizing of frequency control parameters. *IEEE Access* 9, 74684–74702. doi:10.1109/ACCESS.2021.3081676

Salman, U. T., Al-Ismail, F. S., and Khalid, M. (2020). Optimal sizing of battery energy storage for grid-connected and isolated wind-penetrated microgrid. *IEEE Access* 8, 91129–91138. doi:10.1109/ACCESS.2020.2992654

Sandelic, M., Stroe, D. I., and Iov, F. (2018). Battery storage-based frequency containment reserves in large wind penetrated scenarios: A practical approach to sizing. *Energies* 11 (11), 3065. doi:10.3390/en11113065

Shin, H., and Hur, J. (2020). Optimal energy storage sizing with battery augmentation for renewable-plus-storage power plants. *IEEE Access* 8, 187730–187743. doi:10.1109/ACCESS.2020.3031197

Singh, K., Amir, M., Ahmad, F., and Khan, M. A. (2021a). An integral tilt derivative control strategy for frequency control in multimicrogrid system. *IEEE Syst. J.* 15 (1), 1477–1488. doi:10.1109/jsyst.2020.2991634

Singh, K., Amir, M., Ahmad, F., and Refaat, S. S. (2021b). Enhancement of frequency control for stand-alone multi-microgrids. *IEEE Access* 9, 79128–79142. doi:10.1109/access.2021.3083960

Singh, K., and Zaheeruddin (2021). Enhancement of frequency regulation in tidal turbine power plant using virtual inertia from capacitive energy storage system. *J. Energy Storage* 35, 102332. doi:10.1016/j.est.2021.102332

Subroto, R. K., Lian, K. L., Chu, C. C., and Liao, C. J. (2021). A fast frequency control based on model predictive control taking into account of optimal allocation of power from the energy storage system. *IEEE Trans. Power Deliv.* 36 (4), 2467–2478. doi:10.1109/TPWRD.2021.3078217

Swierczynski, M., Stroe, D. I., Stan, A. I., and Teodorescu, R. (2015). Lifetime and economic analyses of lithium-ion batteries for balancing wind power forecast error. *Int. J. Energ. Res.* 39 (6), 760–770. doi:10.1002/er.3278

Tan, Z. X., Li, X. R., He, L., Li, Y., and Huang, J. Y. (2020). Primary frequency control with BESS considering adaptive SoC recovery. *Int. J. Electr. Power Energy Syst.* 117, 105588. doi:10.1016/j.ijepes.2019.105588

Torkashvand, M., Khodadadi, A., Sanjareh, M. B., and Nazary, M. H. (2020). A life cycle-cost analysis of li-ion and lead-acid besss and their actively hybridized ESSs with supercapacitors for islanded microgrid applications. *IEEE Access* 8, 153215–153225. doi:10.1109/access.2020.3017458

Wan, C., Qian, W. T., Zhao, C. F., Song, Y. H., and Yang, G. Y. (2021). Probabilistic forecasting based sizing and control of hybrid energy storage for wind power smoothing. *IEEE Trans. Sustain. Energ.* 12 (4), 1841–1852. doi:10.1109/tste.2021.3068043

Wang, C. F., Teng, Q. J., Liu, X. Y., Zhang, F., He, S. Y., Liang, Z. T., et al. (2019). Optimal sizing of energy storage considering the spatial-temporal correlation of wind power forecast errors. *IET Renew. Power Gener.* 13 (4), 530–538. doi:10.1049/iet-rpg.2018.5438

Wang, H., Wang, T. X., Xie, X. H., Ling, Z. X., Gao, G. L., and Dong, X. (2018). Optimal capacity configuration of a hybrid energy storage system for an isolated microgrid using quantum-behaved particle swarm optimization. *Energies* 11 (2), 454. doi:10.3390/en11020454

Wu, Z. P., Gao, D. W., Zhang, H. G., Yan, S. J., and Wang, X. (2017). Coordinated control strategy of battery energy storage system and PMSG-WTG to enhance system frequency regulation capability. *IEEE Trans. Sustain. Energ.* 8 (3), 1330–1343. doi:10.1109/tste.2017.2679716

Xiong, L., Yang, S., Huang, S., He, D., Li, P., Khan, M. W., et al. (2022). Optimal allocation of energy storage system in DFIG wind farms for frequency support considering wake effect. *IEEE Trans. Power Syst.* 37 (3), 2097–2112. doi:10.1109/TPWRS.2021.3111017

Zaheeruddin, Singh, K., and Amir, M. (2021). Intelligent fuzzy TIDF-II controller for load frequency control in hybrid energy system. *IETE Tech. Rev.* 17, 1355–1371. doi:10.1080/02564602.2021.1994476

Zhang, S. Q., Liu, H. Y., Wang, F., Yan, T., and Wang, K. F. (2020). Secondary frequency control strategy for BESS considering their degree of participation. *Energy Rep.* 6, 594–602. doi:10.1016/j.egyr.2020.11.183

Zhang, Z., Zhou, M., Wu, Z., Liu, S., Guo, Z., and Li, G. (2022). A frequency security constrained scheduling approach considering wind farm providing frequency support and reserve. *IEEE Trans. Sustain. Energ.* 13 (2), 1086–1100. doi:10.1109/TSTE.2022.3150965

Nomenclature

BESS Battery energy storage system

SFD Secondary frequency drop

WT Wind turbine

PFR Primary frequency regulation

LCC Life cycle cost

SOC State of charge

MPPT Maximum power point tracking

PCS Power convert system

SSA Salp swarm algorithm

MSSA Multi-objective salp swarm algorithm

ΔP_L Variation of load power

ΔP_G Power output variation of traditional units

ΔP_W Power output variation of WTs

ΔP_B Power output variation of the BESS

Δf Frequency deviation of the power grid

R Adjustment coefficient of traditional units

K_{w1} Droop control coefficient of WTs

K_{w2} Inertia control coefficient of WTs

K_{b1} Virtual droop coefficient of the BESS

K_{b2} Virtual inertia coefficient of the BESS

H Inertia time constant of the power grid

D Damping factor of the system

G_g Model of thermal power units

G_{gov} Transfer function of the governor

G_t Transfer function of the non-reheated steam turbine

T_g Time constant of the governor

T_t Time constant of the steam turbine

G_b BESS model

T_b Response time constant of the BESS

t_{off} The time of WTs exiting frequency regulation

t_0 Initial time of frequency regulation

T_f Time period of frequency regulation

η_1 Efficiency of the DC–DC converter of the PCS

η_2 Efficiency of the DC–AC converter of the PCS

η_{ch} Charging efficiency of the BESS

η_{dis} Discharging efficiency of the BESS

SOC_0 SOC of the BESS at the initial time

SOC_{max} Upper limit of the SOC

SOC_{min} Lower limit of the SOC

P_{rated} Rated power of the BESS

E_{rated} Rated capacity of the BESS

G_{gen} Transfer function of thermal power units

G_w Transfer function of WTs

Δf_{12max} Sum of the maximum frequency deviations in two stages

C_{LCC} Energy storage cost

C_{inv} Initial investment and replacement cost

C_{bop} Balance of plant cost

C_{om} Operation and maintenance cost

C_{scr} Scrap disposal cost

C_{res} Recovery residual value.

frontiers | Frontiers in Energy Research

TYPE Original Research
PUBLISHED 18 September 2023
DOI 10.3389/fenrg.2023.1220867

OPEN ACCESS

EDITED BY
Chenghong Gu,
University of Bath, United Kingdom

REVIEWED BY
Minh Quan Duong,
The University of Danang, Vietnam
Han Wang,
Shanghai Jiao Tong University, China

*CORRESPONDENCE
Ziheng Pu,
pzhdq@ctgu.edu.cn

RECEIVED 11 May 2023
ACCEPTED 28 August 2023
PUBLISHED 18 September 2023

CITATION
Wan Z, Fu L, Pu Z, Du Z, Chen Z, Zhu Y and Ma X (2023), Optimization of the lightning warning model for distribution network lines based on multiple meteorological factor thresholds.
Front. Energy Res. 11:1220867.
doi: 10.3389/fenrg.2023.1220867

Optimization of the lightning warning model for distribution network lines based on multiple meteorological factor thresholds

Ziyang Wan[1], Lixiang Fu[1], Ziheng Pu[2]*, Zhenchuan Du[1], Zhigang Chen[2], Yi Zhu[1] and Xiaoxin Ma[1]

[1]Nanchang Electric Power Supply Company, Jiangxi Nanchang, China, [2]College of Electrical Engineering and New Energy, China Three Gorges University, Hubei Yichang, China

Lightning is one of the frequent natural disasters, which seriously affects the secure and stable operation of the power system, especially the distribution network lines with weak reliability. In order to improve the power supply reliability of the distribution network, higher requirements are put forward for the accuracy of lightning warning. Therefore, this paper establishes a lightning warning model based on comprehensive multi-meteorological factor thresholds and analyzes the meteorological factor data such as atmospheric field strength, echo intensity, echo-top height, and vertical cumulative liquid water content under thunderstorm weather. The threshold value of each factor warning is obtained, and the corresponding threshold weight is calculated by the entropy weight method. According to the weight of each threshold, the comprehensive threshold index of lightning warning is obtained, and the lightning warning is based on this index. A total of 105 lightning data from May to June 2022 in Nanchang city were analyzed as samples. The thresholds of atmospheric field strength, echo intensity, echo-top height, and vertical cumulative liquid water content were 1.2 kV/m, 40 dBZ, 8 km, and 5.2 kg·m^{-2}, respectively. The corresponding weights of each factor were 0.4188, 0.2056, 0.2105, and 0.165, respectively. This model was used to warn a thunderstorm event in July 2022 in Nanchang area. The success rate of the model warning was 0.91, the false alarm rate (FAR) was 0.11, and the critical success index (CSI) was 0.80. Compared with the single-factor threshold lightning warning model, the warning FAR is decreased by 6%, and CSI is increased by 14% while ensuring the high warning success rate.

KEYWORDS

lightning warning, atmospheric field strength, echo intensity, echo-top height, vertical cumulative liquid water content, threshold, weight

1 Introduction

In recent years, the global climate change and extreme weather have become obvious, and the lightning activity is more frequent and intense. The frequent occurrence of lightning damage poses a great threat to the security of ground construction facilities, personnel life, and property; equipment communication; and the stable operation of transmission and distribution systems (Shi et al., 2021; Wu et al., 2021). With the development of economy, the scale of distribution network continues to expand, the frequency of lightning strikes on distribution network lines and equipment increases, the impact becomes larger, and the

requirements for lightning protection of distribution network are also increasing. Therefore, the demand for monitoring, early warning, forecasting and defense of lightning, and its disasters in distribution lines is becoming more and more urgent.

With lightning nowcasting and early warning based on weather radar, many scholars at home and abroad have carried out a lot of analysis work and achieved useful results. By analyzing 15 thunderstorm cases in Florida, Alabama, and New Mexico, Buechler et al. proposed to establish lightning warning indicators using two thresholds of echo intensity and echo-top height at −10°C (Romps et al., 2014). Through statistical analysis of 67,384 convective cells, Mosier et al. pointed out that 30-dBZ radar echoes can be detected by at least two continuous body scans at temperature levels of −15°C and −20°C. It can be used as a lightning warning indicator, and the critical success index of the indicator is 68% (Li et al., 2023). The lightning warning system of the Chinese Academy of Meteorological Sciences uses the double-echo intensity threshold and the echo intensity threshold at a certain temperature level, combined with the lightning location data, to predict the probability of a future lightning occurrence (Dokic et al., 2016). Based on the analysis of three strong thunderstorm processes in North China by Yixiaoyuan et al., it is found that there is a positive correlation between the frequency of CG lightning and the echo area of the convective cloud echo top higher than 11–12 km, and the echo area of the echo top higher than 11 km has an early warning significance for the intensity of CG lightning activity (Tong et al., 2021). However, the aforementioned studies only consider the use of single-radar meteorological data for lightning warning, and the radar data lack the information on thunderstorm clouds on electricity, so it will result in an insufficient success rate for lightning warning. In order to solve this problem, the researchers of the Shanghai Meteorological Disaster Prevention Engineering Technology Center analyzed the basic characteristics of the time series difference of the atmospheric electric field on sunny and thunderstorm days, and proposed a method of lightning warning by using the time series difference threshold of the atmospheric electric field instrument (Mostajabi et al., 2019). The researchers of Nanjing University of Information Science and Technology proposed to use the atmospheric electric field intensity value and its difference value as early warning parameters, and comprehensively consider the electric field, lightning location, and radar echo data to warn of lightning (Du et al., 2020). The researchers of the Xiamen Lightning Protection Center monitored the atmospheric electric field intensity and lightning distance using the atmospheric electric field instrument and the lightning location system, and comprehensively analyzed the lightning space and time to achieve a more accurate lightning short-term warning (Jun, 2017). Based on the radar meteorological data, these studies combine the electric field intensity and lightning location data to further improve the selection of lightning warning factors, and comprehensively carry out lightning warning, but they do not quantify the relationship between the threshold of each factor and the lightning warning results (Hieu et al., 2021).

In this paper, combined with the actual climatic characteristics of the Nanchang area in Jiangxi Province, a lightning warning model with a comprehensive meteorological factor threshold is established. First, the ground atmospheric electric field data and radar meteorological data are extracted and analyzed in combination with the lightning location data to obtain the optimized warning threshold of each meteorological warning factor. Then, the entropy weight method is used to quantify the warning threshold, and the atmospheric average ground electric field, radar meteorological data, and lightning location data are comprehensively used to warn the short-term approaching of the first ground flash of the thunderstorm cloud within a certain range of the distribution line electric field station, which provides a reference for the implementation of active lightning protection technology for distribution network lines.

2 Basic method of lightning warning

2.1 Lightning warning process

Radar, lightning locators, and electric field instruments can simultaneously observe the same thunderstorm activity. Figure 1 shows the observation of the electric field, radar, and lightning locator when thunderstorm clouds approach. The ROW in the figure represents the lightning threat area (as shown in CG), also known as the range of warning (ROW), which is within the effective range of electric field detection. In this area, when thunderstorm clouds develop, the changes in charge in the clouds can be observed using atmospheric electric field instruments, and the relevant information about thunderstorm clouds, such as strong echoes and thunderstorm cloud position information, can be detected by radar. These details can be used for lightning warnings. At the same time, all lightning positions, intensities, and other information that occur in thunderstorm clouds can be observed using lightning locators. Therefore, the temporal and spatial relationships between electric field, radar, and lightning location data make it possible to combine the three types of data for early warning. The lightning information generated by the thunderstorm cloud is detected by the lightning locator, and the electric field instrument detects the charge situation in the thunderstorm cloud, which can be used for lightning warning. However, due to different properties of these three types of data, this article considers quantifying them and calculating their weight values to fuse these data.

2.2 Lightning warning factor extraction

This paper extracted 105 thunderstorm cells and corresponding lightning warning factor data that occurred in the Nanchang area of Jiangxi Province from May to June 2022. The data are derived from radar, lightning location, and atmospheric electric field instrument data from the Jiangxi Meteorological Archives. The distribution of radar stations in Nanchang area is shown in Figure 2.

The lightning location system monitored the lightning situation in the Nanchang area from May to June, as shown in Figure 3. The red point represents the ground flash data monitored by the lightning location system in real time.

Four types of lightning warning index data on electric field amplitude, echo intensity, echo-top height, and vertical accumulated liquid water content of thunderstorm weather and thunderstorm ground flash data are compared and analyzed. According to the calculation method of the warning rate proposed in GB_T 38121 for

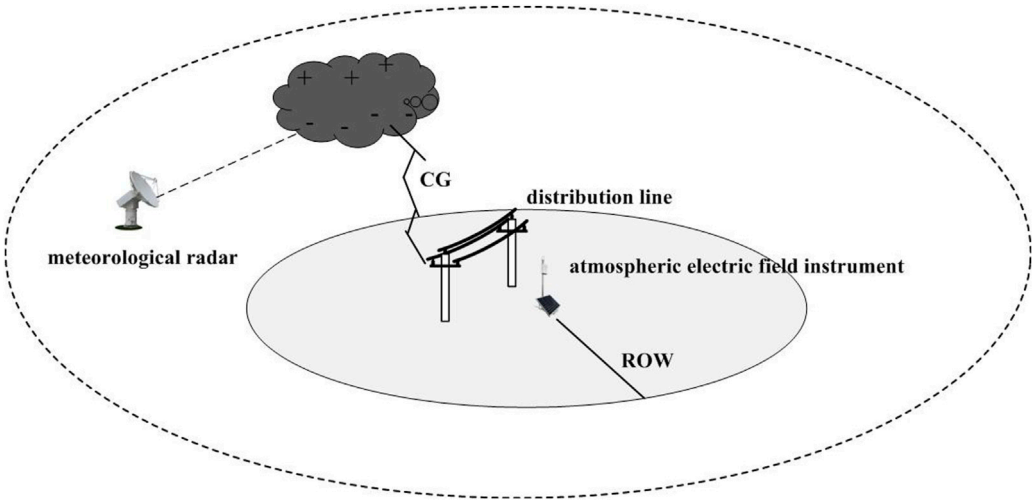

FIGURE 1
Electric field and radar measurement of the lightning process.

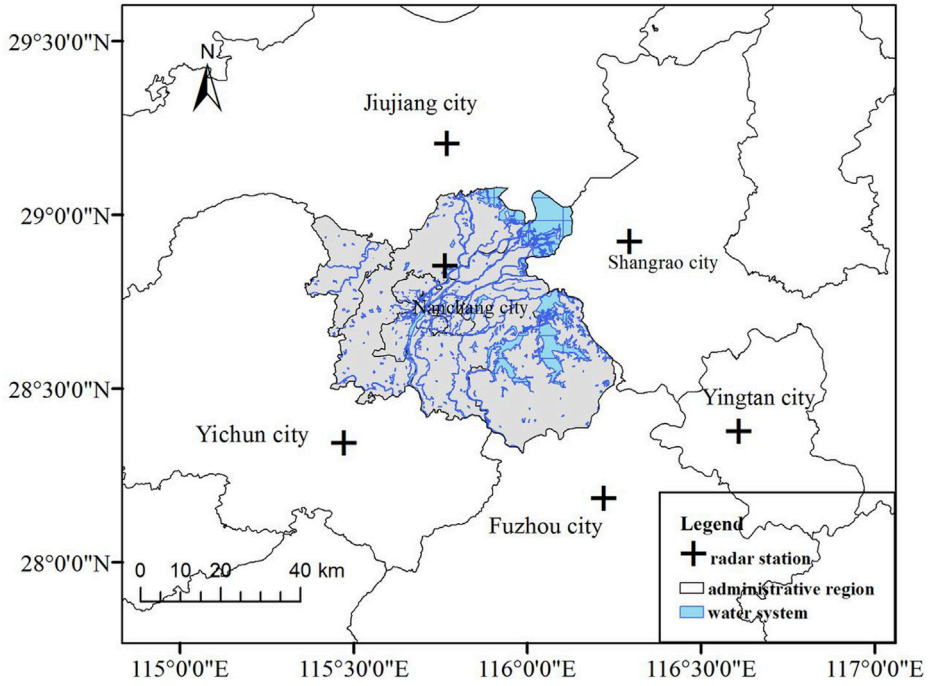

FIGURE 2
Radar site distribution map in the Nanchang area.

thunderstorm warning, the thresholds of a successful warning rate (POD), false alarm rate (FAR), and critical success index (CSI) (Leite et al., 2019; Xiao et al., 2019) of lightning warning factors under different warning thresholds are calculated and optimized.

The definitions of the POD, FAR), and CSI used in this paper are shown in Table 1.

The POD indicates the percentage of successful lightning warning in live observation, and its value is between 0 and 1. The larger the value, the closer it is to the successful early warning, which is defined as

$$\mathbf{POD} = \frac{\mathbf{A}}{\boldsymbol{A} + \boldsymbol{B}} \times \mathbf{100\%}. \quad (1)$$

The FAR represents the percentage of false alarms in a lightning warning, and its value is between 0 and 1. The smaller the value is, the closer it is to the successful warning, which is defined as

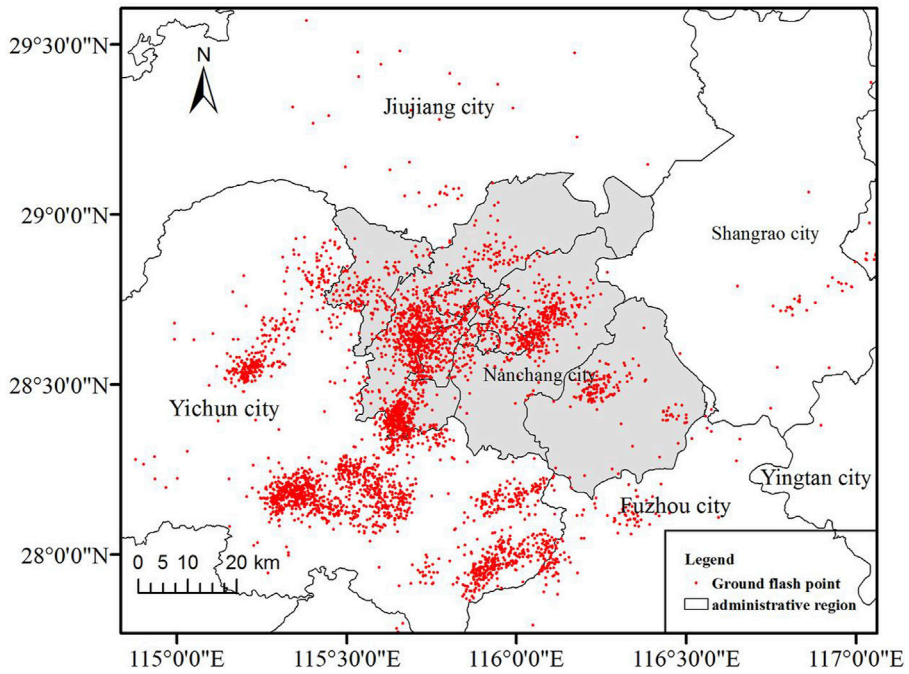

FIGURE 3
Real-time monitoring map of ground flash in the Nanchang area.

TABLE 1 Data definition table.

Early warning	Have thunderstorms		No thunderstorms	Total
Practical observation	Have thunderstorms	A	B	A+B
	No thunderstorms	C	D	C+D
Total		A+C	B+D	A+B+C+D

$$\mathbf{FAR} = \frac{\mathbf{C}}{\boldsymbol{A}+\boldsymbol{C}} \times \mathbf{100\%}. \quad (2)$$

The CSI is the percentage of correct warnings in the entire lightning warning event (including correct, false, and missed warnings). The value is between 0 and 1, and the larger the value, the closer it is to the successful warning, which is defined as

$$\mathbf{CSI} = \frac{\mathbf{A}}{\boldsymbol{A}+\boldsymbol{B}+\boldsymbol{C}} \times \mathbf{100\%}. \quad (3)$$

The concept of early warning advance time T is introduced, which is defined as the time interval between the time when the early warning index of radar echo appears and the time when the first ground flash occurs.

3 Threshold determination of the lightning warning factor

The Doppler effect was first discovered by the Austrian physicist J. Doppler in 1842 from a moving sound source (Ghaemi et al., 2022). The working principle of Doppler weather radar is based on the Doppler effect. The specific performance is when the precipitation particles are relatively moving relative to the radar transmitting beam, the difference between the high frequency of the received signal and the transmitted signal can be measured, and the required information can be obtained. Using this principle, the velocity of the scatterer relative to the radar can be measured, and the atmospheric wind field, the distribution of the vertical velocity of the airflow, and the turbulence can be inverted under certain conditions. Based on this principle, the monitoring data are analyzed and compared, and the threshold of the lightning warning factor suitable for the Nanchang area of Jiangxi Province is obtained.

3.1 The echo intensity threshold

It is found that the main activity center of lightning is related to the supercooled cloud layer, and the negative charge area of cloud-to-ground lightning is mainly located in the temperature level of −5 to −25°C (Bouchard et al., 2023). Considering that 40-dBZ echo intensity at the height of −10°C can be used as the best factor to predict the occurrence of the first lightning, Maribel analyzed several convective cells and found that the condition for lightning in the cell

TABLE 2 Early warning index number.

Early warning index number	Characteristic echo intensity/dBZ	Characteristic isothermal height layer/°C
1	20	−10
2	25	−10
3	30	−10
4	35	−10
5	40	−10
6	45	−10
7	20	−10
8	25	−15
9	30	−15
10	35	−15
11	40	−15
12	45	−15
13	20	−20
14	25	−20
15	30	−20
16	35	−20
17	40	−20
18	45	−20

is that the top height of the echo above 40 dBZ in the cell must be higher than 7 km. Wu et al. (2018) analyzed 20 cells in summer in Beijing and concluded that 40 dBZ is a more suitable radar echo characteristic parameter for a lightning warning. It is a practical method to use 0°C and other temperature height layers as the basic characteristic height, combined with the proportion of −10°C and other temperature height layers and strong echoes for lightning comprehensive warning. Based on the geographical location and climatic characteristics of some areas in Nanchang, this paper proposes 18 echo intensity indicators for lightning warning identification. Then, according to the time and occurrence of ground lightning in the lightning location data, the radar echo volume scan data corresponding to the ground lightning period in the selected cases are statistically analyzed. The effect of cloud-to-ground lightning warning and a best indicator are obtained, as shown in Table 2.

Through the statistics of the top heights of 20 dBz, 25 dBz, 30 dBz, 35 dBz, 40 dBz, and 45 dBz radar echo intensities in 105 cells in the process of cell development and evolution, combined with the sounding data on each cell on the day of occurrence, the temperature height layers of −10°C, −15°C, and −20°C are comprehensively analyzed. It is calculated that the top height of 30 dBZ echo intensity in all thunderstorm cells can break through the temperature height layer of −10°C, and the proportion of thunderstorm cells whose top heights of 35 dBZ, 40 dBZ, and 45 dBZ echo intensities breaks through this height gradually decreases. Only 26% of thunderstorm cells have 45-dBZ echo intensity peak height exceeding this height.

For the non-thunderstorm cell, the proportion of the echo intensity top height of 30 dBZ and aforementioned breaking through −reak is much smaller than that of the thunderstorm cell. There are only cases of 40 dBZ and 45 dBZ echo-top heights breaking through the height of the non-thunderstorm cell. For −15°C and other temperature height layers, the results are similar to those of −10°C and other temperature height layers, but the statistical echo intensity of this layer is 5 dBZ smaller than that of the previous height layer. On this layer, the difference between thunderstorm cells and non-thunderstorm cells is larger at the top of 35 dBZ echo intensity, and the proportion of the two breaking through this height accounts for 77% and 23% of the total number of their respective cells. For −20°C and other temperature height layers, the results are also consistent with the statistics of the first two layers. The proportion of the top height breaking through the layer gradually decreases, and the proportion of the non-thunderstorm monomer breaking through the layer is always smaller than that of the thunderstorm monomer breaking through the layer.

Table 3 shows the results of the list calculation, and the actual effect statistics of different indicators in the selected 105 single cases are tested and analyzed. It can be seen that for a certain temperature height layer, POD decreases with the increase in the echo intensity threshold that breaks through the echo-top height of the height layer. At the same time, with the increase in the temperature height layer (corresponding to the decrease in the stratification temperature), the use of the top height of the same echo intensity threshold to break through the temperature height layer to warn the thunderstorm POD also gradually decreases because the lower the threshold, the easier it is to meet the requirements; the

TABLE 3 Three kinds of echo intensity warning comparison.

Temperature layer (°C)		Echo intensity/dBZ					
		20	25	30	35	40	45
−10	POD	1.00	1.00	1.00	1.00	0.94	0.58
	FAR	0.38	0.37	0.35	0.26	0.13	0.16
	CSI	0.63	0.63	0.69	0.74	0.83	0.53
	T/min	39	35	38	37	21	17
−15	POD	1.00	1.00	1.00	1.00	0.85	0.59
	FAR	0.35	0.34	0.31	0.19	0.08	0.07
	CSI	0.65	0.68	0.70	0.81	0.79	0.57
	T/min	36	37	26	18	16	15
−20	POD	1.00	1.00	0.96	0.88	0.82	0.50
	FAR	0.30	0.26	0.22	0.19	0.10	0.10
	CSI	0.70	0.74	0.76	0.73	0.75	0.47
	T/min	31	28	20	21	8	7

TABLE 4 Distribution table of the echo-top height cell.

ET/km	0–1.9	2.0–3.9	4.0–5.9	6.0–7.9	8.0–9.9	10.0–11.9	12.0–13.9
Thunderstorm	0	0	0	8	43	47	7
Non-thunderstorm	0	0	15	18	4	0	0

FAR value has a similar transformation trend with the POD value, but the effect is opposite, that is, the stronger the threshold, the smaller the FAR, which means that the stronger the convection, the higher the possibility of thunderstorms, and the lower the FAR.

Therefore, in order to find a most suitable early warning index, we must weigh the different performances of each index (POD, FAR, and CSI). By analyzing the aforementioned table, it can be seen that the three indexes of the 35-dBZ echo intensity top breakthrough −10°C, the 40 dBZ echo intensity top breakthrough −10°C, and the 35-dBZ echo intensity top breakthrough −15°C have the best early warning. The POD of the three indexes is 1.0, 0.96, and 1.0, respectively, and the FAR of the three indexes is not more than 0.3. The concept of early warning advance time is introduced, which is defined as the time interval between the time of the radar echo early warning index and the time of the first ground flash. The early warning time of the three indexes is 37 min, 21 min, and 18 min, respectively. Finally, considering the early warning effect of the three indicators, the two indicators with the maximum CSI of 0.83 and the 40-dBZ echo intensity top height breakthrough −echo are selected as the lightning warning indicators.

3.2 Echo-top height threshold

From the statistical results of the number of thunderstorm and non-thunderstorm cells with different echo-top heights in 105 thunderstorm cells from May to June 2022, it can be seen that the echo-top heights of all thunderstorm cells are greater than 6.0 km, specifically distributed in the range of 8.0–11.9 km, accounting for 88.0% of the total number of thunderstorms. The echo-top height of non-thunderstorm cells is mainly distributed in the range of 4.0–7.9 km, accounting for 89.18% of the total non-thunderstorm cells. The range of 6.0–7.9 km is another peak area of the proportion of non-thunderstorm cells, and there are 18 thunderstorms in this area. There are four non-thunderstorm cells in the range of 8.0–9.9 km. There is no monomer distribution below 4.0 km and above 10.0 km. It is not difficult to see that the ET values of thunderstorm cells and non-thunderstorm cells have obvious interval distribution. With 8.0 km as the threshold, the proportion of thunderstorm cells with the ET value above 8.0 km is 94.2% higher than that of total thunderstorm cells, while the proportion of non-thunderstorm cells with the ET value below 8.0 km is 89.2%. This shows that the intensity of the vertical development of the echo is closely related to the occurrence of lightning. The higher the development of the cloud top, the stronger the updraft of the thunderstorm cloud, and the greater the possibility of lightning.

In order to evaluate the early warning effect of different echo-top height warning thresholds, the POD, FAR, and CSI values under different warning threshold conditions are calculated according to the distribution table of echo-top height cells in Table 4. The calculation results are shown in Figure 4.

From the analysis of Figure 4, it can be seen that for Nanchang, Jiangxi, when the echo-top height threshold is set to 2 km and 4 km, the correct warning rate can reach 1, but the FAR is at a high threshold of

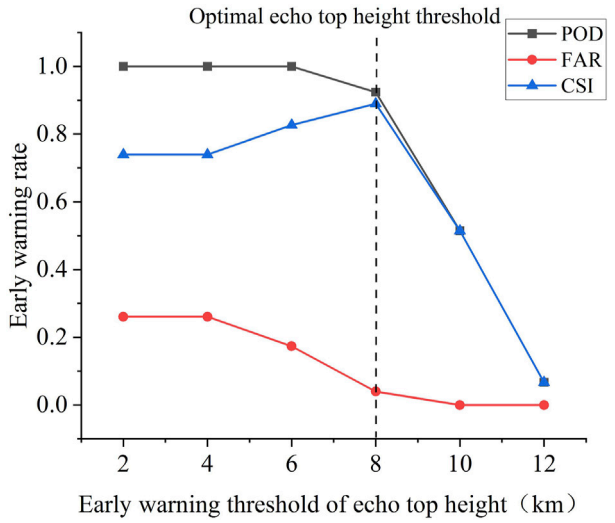

FIGURE 4
Early warning rate changes with the early warning threshold of echo-top height.

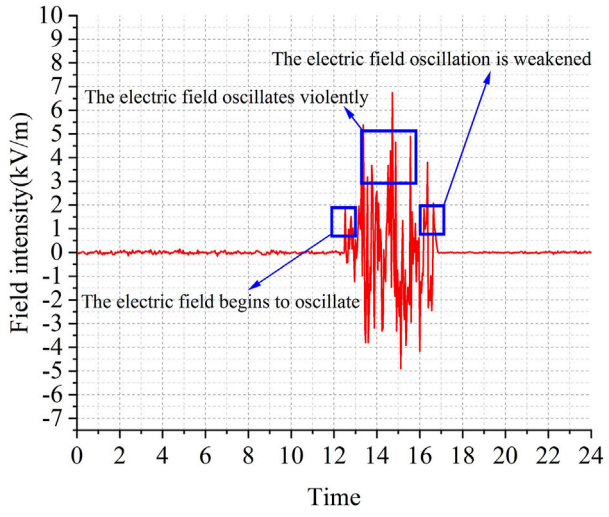

FIGURE 5
Atmospheric electric field intensity value of Nanchang on a certain day in May.

0.28, and the CSI value is also at a low threshold of 0.73. When the threshold of the echo-top height is increased, the POD value begins to decrease, and the FAR value gradually increases. When the ET value is 8.0 km, the POD of this index is as high as 0.90, and FAR is 0.20, which is still a large FAR. The CSI is 0.79, and the early warning advance time is 11 min, which almost reaches two individual scanning times. Therefore, the ET value of 8.0 km is a better index for discrimination.

3.3 Vertical cumulative liquid water content threshold

Yu et al. (2021) pointed out that the VIL value should not be very small or very large in the lightning warning when studying the radar threshold on the northeastern side of the plateau. If the VIL value is too small, the water vapor flux is insufficient so that the water vapor condenses into precipitation before the freezing height. It can be seen from the statistical analysis results (Table 5) that there is a good correspondence between lightning activity and VIL value. For thunderstorm cells, 66.7% of thunderstorm cells have a VIL value of 10.0–14.9 kg•m^{-2}, 92.6% of thunderstorm cells have a VIL value of 5.2–14.9 kg•m^{-2}, and 70.3% of non-thunderstorm cells have a VIL value below 5.2 kg•m^{-2}. Therefore, when the VIL value is 5.2 and less than 15.0 kg•m^{-2}, the possibility of lightning is greater.

According to the distribution of VIL values of 105 convective cells, it is found that there is no obvious regularity in the changes in VIL values in the lightning activity area. The VIL values of both thunderstorm cells and non-thunderstorm cells are almost less than 15 kg•m^{-2}, and the remaining thunderstorm cells are distributed in the range of 15–30 kg•m^{-2}, and the non-thunderstorm cells are almost not greater than 15 kg•m^{-2}.

The aforementioned analysis shows that VIL has little significance for the indication of the lightning warning value, and its index is not a necessary condition. It can be used as a sufficient condition to judge whether thunderstorms occur, that is, when other conditions are met, as long as the value is greater than 5.2 kg•m^{-2}, it can be judged as thunderstorms occur, but its value should not be very large. It is found that it is advisable that the value should be less than 15 kg•m^{-2}. Therefore, 5.2 kg•m^{-2} was selected as the early warning threshold for vertically accumulated liquid water content.

3.4 Atmospheric field strength threshold

Atmospheric field strength is the amplitude of the atmospheric electric field. The atmospheric electric field is the electric field existing in the atmosphere. Because the ground is negatively charged and the atmosphere contains net positive charges, there is always an electric field in the atmosphere. The direction of the atmospheric electric field points to the ground, and its intensity, the atmospheric field strength, changes with time, place, weather, and altitude. Figure 5 shows the characteristic curve of the atmospheric electric field change in Nanchang (28.69°N and 115.906°E) under thunderstorm weather on a certain day. It can be seen from the figure that the atmospheric value fluctuates greatly at 12:30–17:00 on

TABLE 5 Vertical cumulative liquid water content monomer distribution.

VIL/(kg·m^{-2})	0–4.9	5.0–9.9	10.0–14.9	15.0–19.9	20.0–24.9	25.0–29.9	30.0–34.9
Thunderstorm	1	25	72	3	1	2	1
Non-thunderstorm	26	3	5	2	1	0	0

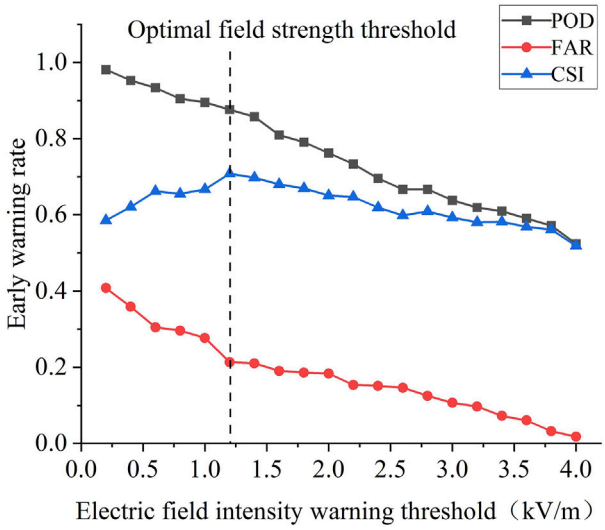

FIGURE 6
Early warning rate changes with the early warning threshold of electric field intensity.

the same day, and the amplitude is generally greater than 1.0 kV/m. Then, the lightning location system detected the occurrence of lightning.

In order to evaluate the warning effect of different warning thresholds and obtain the appropriate warning threshold, this paper sets a series of warning thresholds between 0.2 kV and 4.0 kV, and counts the A (normal warning), B (missed warning), and C (false warning) events corresponding to different electric field thresholds under 105 thunderstorm cells.

In order to more intuitively reflect the accuracy of the early warning, according to the number of events in the cases of correct, false, and missing warnings under different electric field intensity thresholds, the POD, FAR, and CSI under different electric field warning thresholds are calculated and analyzed. The results are shown in Figure 6.

Figure 6 shows that with the increase in the early warning threshold of electric field intensity, the values of POD, FAR, and CSI decrease to varying degrees on the whole. When the early warning threshold is set in the range of 0.2~1.2 kV/m, the POD value decreases from 0.96 to 0.88. The analysis shows that the increase in the threshold needs to lose the early warning accuracy. The FAR value decreased from 0.41 to 0.22, but it was still a relatively large FAR. The CSI value increased from 0.58 to 0.70, and the overall result was smaller. When the warning threshold is greater than 1.2 kV/m, the decrease in the POD value increases. When the threshold is set to 1.2 kV/m, the FAR value reaches the minimum value under the adjacent threshold, and the CSI reaches the maximum value under the adjacent threshold. According to the definition of POD, FAR, and CSI, in order to select the most suitable early warning threshold of atmospheric electric field strength, it is necessary to comprehensively analyze and select the atmospheric field strength amplitude corresponding to the point with the largest POD value, the smallest FAR value, and the largest CSI value. Therefore, 1.2 kV/m is selected as the threshold of the atmospheric electric field strength in the Nanchang area. Under this threshold, the POD of thunderstorms reaches 0.88, the FAR is 0.21, and the maximum value of CSI is 0.70.

4 Multi-factor fusion lightning warning model

It can be seen from the previous section that the separate warning effect of different data shows that whether it is electric field data or radar data, the FAR obtained by taking a small threshold is quite high. Increasing the threshold will reduce the FAR, but the detection probability must be sacrificed. Different data can reflect different characteristics of thunderstorm clouds from different angles, so these data have different contributions to lightning warning, that is, they have different weight values. The optimal weight combination can be found from the quantitative values of different data to comprehensively utilize these data for early warning.

4.1 Construction of the lightning warning comprehensive threshold model

According to the theory of information entropy, the smaller the information entropy of the index, the greater the degree of change in the index value, the greater the amount of information provided, and the more obvious the role played in the evaluation system. Therefore, the information entropy under the lightning warning index can be used to objectively determine the weight (Zhang et al., 2023).

First, the four lightning warning indicators of electric field intensity, echo intensity, echo-top height, and vertically accumulated liquid water content are equivalent to positive indicators. The entropy weight method treats the positive indicators as follows:

$$y_{ab} = \frac{x_{ab} - min(x_{ab})}{max(x_{ab}) - min(x_{ab})}, \tag{4}$$

where x_{ab} is the bth sample value of index a, which is an element in the original matrix $\boldsymbol{G_0}$.

Furthermore, the normalized matrix $\boldsymbol{G}$ is

$$g_{ab} = y_{ab} \Big/ \sum_{a=1}^{m} y_{ab}, \tag{5}$$

$$\boldsymbol{G}_{m\times n} = \begin{bmatrix} g_{11} & g_{12} & \cdots & g_{1n} \\ g_{21} & g_{22} & \cdots & g_{2n} \\ \vdots & \vdots & \ddots & \vdots \\ g_{m1} & g_{m2} & \cdots & g_{mn} \end{bmatrix}. \tag{6}$$

Then, the entropy weight of each lightning warning factor is calculated. First, the entropy of each lightning warning factor is calculated. The calculation formula is as follows:

$$\mathbf{E}_j = \frac{\sum_{a=1}^{m} g_{ab} - ln(g_{ab})}{lnm}. \tag{7}$$

Here, $\mathbf{E}_j$ is the entropy of index j.

Finally, the entropy weight w_j of each index is calculated by entropy, and the calculation formula is as follows:

$$\mathbf{w}_j = \frac{1 - E_j}{\sum_{b=1}^{n} (1 - E_j)}. \tag{8}$$

The entropy weight of the electric field intensity (QV_{EF}), echo intensity (QV_{dBZ}), echo-top height (QV_{ET}), and vertical

TABLE 6 Comprehensive threshold index of lightning warning results.

Prediction		Thunderstorm	Non-thunderstorm
Practical observation	Thunderstorm	97	8
	Non-thunderstorm	4	503

TABLE 7 Early warning results of different forecasting methods.

Forecasting	POD	FAR	CSI
Single electric field intensity threshold	0.92	0.21	0.73
Single echo intensity threshold	0.84	0.17	0.72
Single echo-top height threshold	0.86	0.26	0.65
Single vertical cumulative liquid water content threshold	0.77	0.15	0.69
Multi-factor comprehensive threshold	0.91	0.11	0.80

accumulated liquid water content ($\boldsymbol{QV}_{VIL}$) is $\mathbf{w}_j$ = [0.4188, 0.2056, 0.2105, 0.165]. The influence weight of the electric field intensity is obviously greater than that of other factors, followed by echo-top height, echo intensity, and vertical cumulative liquid water content. The entropy weight is used to construct the comprehensive threshold index of lightning early warning, which is composed of the normalized electric field intensity component ($\boldsymbol{QV}'_{EF}$), the normalized echo intensity component ($\boldsymbol{QV}'_{dBZ}$), the normalized echo-top height component ($\boldsymbol{QV}'_{ET}$), and the normalized vertical accumulated liquid water content component ($\boldsymbol{QV}'_{VIL}$). The four components are added together as follows:

$$\mathbf{Q}'_y = \mathbf{0.4188}\boldsymbol{QV}'_{EF} + \mathbf{0.2056}\boldsymbol{QV}'_{dBZ} + \mathbf{0.2105}\boldsymbol{QV}'_{ET} + \mathbf{0.165}\boldsymbol{QV}'_{VIL}. \quad (9)$$

The aforementioned single-lightning factor threshold has been calculated. According to the comprehensive threshold calculation method, 105 thunderstorm cells are listed and analyzed. The threshold of the atmospheric field strength is 1.2 kV/m, the echo intensity is 40 dBZ, the echo-top height is 8km, and the vertical cumulative liquid water content is 5.2 kg·m^{-2}. The single threshold normalized offspring is calculated into the formula, and the early warning comprehensive index threshold $\mathbf{Q}'_y$ is 0.623. According to Table 6, POD was 92.38%, FAR was 3.0%, and CSI was 89%.

4.2 Example verification

On 23 July 2022, a severe thunderstorm occurred in Nanchang, Jiangxi Province, accompanied by short-term precipitation and strong winds. In this process, 35 lightning return strokes, 8 positive ground flashes, 17 negative ground flashes, and more negative ground flashes were monitored within 15 km of a 10-kV distribution line of Anyi Company in the Nanchang area. The whole process lasted about 2 h, and the influence time was 16:00–18:00. According to the records of the local power grid, the thunderstorm process caused the distribution line in Nanchang to trip many times. Real-time weather radar data were retrieved; according to the data record, 16:42, in the northwest and south of this line, there is sporadic convective cloud cluster development. At 16:45, the echo intensity reached more than 40 dBZ, the echo-top height reached 6 km, and the vertical accumulated liquid water content was 4.5 kg·m^{-2}. At 16:55, the atmospheric electric field instrument detected the fluctuation of the electric field, and the atmospheric electric field intensity reached 1.2 kV/m. The result of calculating the lightning warning comprehensive index $\mathbf{Q}'_1$ was 0.585. There were new echoes generated and developed over the center of the 17: 10 line. The echo intensity reached 45 dBZ, the echo-top height increased to 8.5 m, and the vertical accumulated liquid water content reached 8.6 kg·m^{-2}, 17:21. The lightning warning comprehensive index $\mathbf{Q}'_2$ is 0.721, which exceeds the aforementioned threshold $\mathbf{Q}'_y$ of 0.623, and the warning model sends an early warning signal. At 18: 30, the thunderstorm cloud gradually weakened and moved away from the distribution line. The model lifted the lightning warning at 18:35, and it was tested by the monitoring data on Nanchang lightning positioning systems. The warning advance for this process was 31 min.

On 22 July 2023, a new round of strong thunderstorms occurred in Nanchang, Jiangxi Province, due to the impact of a typhoon, accompanied by precipitation and strong winds. During this process, a 10-kV distribution line within a 15 km range of Nanchang company detected a total of 158 lightning strikes, 11 positive ground flashes, and 27 negative ground flashes, with more negative ground flashes. The entire process lasted for about 4.5 h, with an impact time of 12:00 to 14: 30. According to the local power grid power supply ledger records, this thunderstorm caused multiple trips on this distribution line in Nanchang city. Real-time weather radar data were retrieved, and according to data records, at 12:42, there are sporadic convective cloud clusters developing in the northwest and south of this route. At 12:45, the echo intensity was detected to be above 41.5 dBz, and the echo peak height reached 6.3 km. At this time, the vertically accumulated liquid water content was 4.6 kg/m^2. At 13:05, the atmospheric electric field instrument detected fluctuations in the electric field, and the atmospheric electric field intensity reached 1.3 kV/m. The calculation of the lightning warning comprehensive index $\mathbf{Q}'_1$ at this time was 0.596. At 17:10, there was a new echo generation and development enhancement above the center of the line, with the echo intensity reaching 45 dBz and the echo peak height increasing to 8.3 m, The vertical cumulative liquid water content reaches 9.0 kg/m^2 at 13:21, and the lightning warning

comprehensive index $\mathbf{Q}_2^{'}$ is 0.707, exceeding the aforementioned threshold $\mathbf{Q}_y^{'}$ of 0.596. The warning model sends a warning signal. At 14:20, the thunderstorm cloud cluster gradually weakened and moved away from the power distribution line. The model lifted the lightning warning at 14:30 and tested it with the monitoring data on the Nanchang lightning positioning system. The warning advance for this process was 27 min.

The comparison and analysis of these two lightning events using single-factor threshold warning and the multi-factor comprehensive warning method in this article are shown in Table 7:

According to Table 7, the multi-factor comprehensive threshold method comprehensively considers the weight of four kinds of meteorological factors. Compared with the single-lightning factor threshold warning method, although the early warning accuracy is lower than the single electric field intensity threshold warning, POD can still reach 91%, and the multi-factor comprehensive threshold warning method FAR is 11%, which is 6% lower than the minimum value of FAR in single-factor warning, and CSI is 80%, which is obviously better than each single-factor threshold method.

5 Conclusion

Lightning is one of the frequent natural disasters, which seriously affects the secure and stable operation of the power system, especially the distribution network lines with weak reliability. In order to improve the power supply reliability of the distribution network, higher requirements are put forward for the accuracy of lightning warning. To this end, this paper combines the atmospheric field strength, echo intensity, echo-top height, vertical cumulative liquid water content, and other meteorological factor data under thunderstorm weather to make a list of analysis that obtains the threshold value of each factor warning, uses the entropy weight method to calculate the corresponding threshold weight, and establishes a lightning warning model with a comprehensive meteorological factor threshold. The conclusions are as follows:

(1) When the thunderstorm weather is approaching, the electric field amplitude, echo intensity, echo-top height, and vertical accumulated liquid water content will change to varying degrees, and the more severe the thunderstorm weather, the greater the change.
(2) The thresholds of four types of lightning warning factors are determined in the list, and a single factor is obtained for lightning warning. The threshold of electric field amplitude is 1.2 kV/m, the threshold of echo intensity is 40 dBZ, the threshold of echo-top height is 8 km, and the threshold of vertical accumulated liquid water content is 5.2 $kg \cdot m^{-2}$.
(3) The comprehensive threshold index of lightning warning is composed of four components: electric field intensity component, echo intensity component, echo-top height component, and vertical accumulated liquid water content component. After data analysis, the weight of the electric field intensity component is 0.4188, the weight of the echo intensity component is 0.2056, the echo-top height component is 0.2105, and the vertical accumulated liquid water content component is 0.165.
(4) The comprehensive threshold method was used to warn strong thunderstorm weather in Nanchang in July 2022. The success rate of early warning was 0.91, the FAR of early warning was 0.11, and the CSI was 0.80. When ensuring the success rate of early warning to reach more than 90%, the minimum FAR was reduced by 6% compared with the single-factor early warning method, and the maximum CSI was increased by 7%. The early warning method has been further improved.

Data availability statement

The original contributions presented in the study are included in the article/Supplementary Material; further inquiries can be directed to the corresponding author.

Author contributions

ZW put forward research ideas. ZW guided the research methods. ZP wrote the original draft and is the corresponding author. LF reviewed the paper. ZD and ZC conducted field tests. YZ edited figures and tables. XM performed the data analysis. All authors contributed to the article and approved the submitted version.

Funding

This study is funded by a key research technology project funded by State Grid Jiangxi Electric Power Company. The project name is Research and Application of Key Technologies for Lightning Protection in Distribution Networks, and the project number is 5218A022000G.

Conflict of interest

Authors ZW, LF, ZD, YZ, and XM were employed by Nanchang Electric Power Supply Company.

The authors declare that this study has received funding from the State Grid Corporation of China, Nanchang City, Jiangxi Province. Authors ZW, LF, ZD, YZ, and XM were employed by Nanchang Electric Power Supply Company. The sponsor participated in the following research: the design of the research plan, the collection and analysis of lightning data, and also participated in the writing and revision of this article.

Publisher's note

References

Bouchard, A., Buguet, M., Chan-Hon-Tong, A., Dezert, J., and Lalande, P. (2023). Comparison of different forecasting tools for short-range lightning strike risk assessment. *Nat. Hazards* 115 (2), 1011–1047. doi:10.1007/s11069-022-05546-x

Dokic, T., Dehghanian, P., Chen, P. C., Kezunovic, M., Medina-Cetina, Z., Stojanovic, J., et al. (2016). "January). Risk assessment of a transmission line insulation breakdown due to lightning and severe weather," in *2016 49th Hawaii international conference on system Sciences (HICSS)* (USA: IEEE), 2488–2497. doi:10.1109/HICSS.2016.311

Du, Y., Liu, Y., Wang, X., Fang, J., Sheng, G., and Jiang, X. (2020). Predicting weather-related failure risk in distribution systems using Bayesian neural network. *IEEE Trans. Smart Grid* 12 (1), 350–360. doi:10.1109/TSG.2020.3019263

Ghaemi, A., Safari, A., Afsharirad, H., and Shayeghi, H. (2022). Situational awareness and deficiency warning system in a smart distribution network based on stacking ensemble learning. *Appl. Soft Comput.* 128, 109427. doi:10.1016/j.asoc.2022.109427

Hieu, T. T., Vinh, T. T., Duong, M. Q., et al. (2021). Analysis of protective solutions for underground cable system-application for Danang distribution grid *10th international conference on ENERGY and ENVIRONMENT (CIEM)*. USA, IEEE, 1–5.

Jun, X. (2017). "May). Study of distribution transmission line lightning stroke risk forecasting based on nonlinear time series analysis," in *International conference on Smart grid and electrical automation (ICSGEA)* (USA: IEEE), 282–285. doi:10.1109/ICSGEA.2017.46

Leite, J. B., Mantovani, J. R. S., Dokic, T., Yan, Q., Chen, P. C., and Kezunovic, M. (2019). Resiliency assessment in distribution networks using GIS-based predictive risk analytics. *IEEE Trans. Power Syst.* 34 (6), 4249–4257. doi:10.1109/TPWRS.2019.2913090

Li, Y., Liu, Y., Sun, R., Guo, F., Xu, X., and Xu, H. (2023). Convective storm VIL and lightning nowcasting using satellite and weather radar measurements based on multi-task learning models. *Adv. Atmos. Sci.* 40, 887–899. doi:10.1007/s00376-022-2082-6

Mostajabi, A., Finney, D. L., Rubinstein, M., and Rachidi, F. (2019). Nowcasting lightning occurrence from commonly available meteorological parameters using machine learning techniques. *Npj Clim. Atmos. Sci.* 2 (1), 41. doi:10.1038/s41612-019-0098-0

Romps, D. M., Seeley, J. T., Vollaro, D., and Molinari, J. (2014). Projected increase in lightning strikes in the United States due to global warming. *Science* 346 (6211), 851–854. doi:10.1126/science.1259100

Shi, T., Hu, D., Ren, X., Huang, Z., Zhang, Y., and Yang, J. (2021). Investigation on the lightning location and warning system using artificial intelligence. *J. Sensors* 2021, 1–11. doi:10.1155/2021/6108223

Tong, C., Wang, J., Xu, J., Cai, Y., Xu, Y., Hua, X., and Wang, T. (2021). "A power flow transfer optimization strategy for important transmission channels based on lightning early warning," in *2021 35th international conference on lightning protection (ICLP) and XVI international symposium on lightning protection (SIPDA)* (USA: IEEE), 1, 1–7.

Wu, F., Cui, X., and Zhang, D. L. (2018). A lightning-based nowcast-warning approach for short-duration rainfall events: development and testing over Beijing during the warm seasons of 2006–2007. *Atmos. Res.* 205, 2–17. doi:10.1016/j.atmosres.2018.02.003

Wu, M., Yang, C., and Liu, X. (2021). Forecast of thunderstorm cloud trend based on monitoring data of thunder mobile positioning system. *Mob. Inf. Syst.* 2021, 1–11. doi:10.1155/2021/8062549

Xiao, M., Sun, Y., and Li, K. (2019). "Research on fault-environment association rules of distribution network based on improved Apriori algorithm," in *IOP conference series: Materials science and engineering* (New York: IOP Publishing), 569. doi:10.1088/1757-899X/569/3/032079032079

Yu, H. Y., Suh, M. S., and Ryu, S. O. (2021). Improvement of thunderstorm detection method using GK2A/AMI, RADAR, lightning, and numerical model data. *Korean J. Remote Sens.* 37 (1), 41–55. doi:10.7780/kjrs.2021.37.1.4

Zhang, H., Liu, H., Ma, G., Zhang, Y., Yao, J., and Gu, C. (2023). A wildfire occurrence risk model based on a back-propagation neural network-optimized genetic algorithm. *Front. Energy Res.* 10. doi:10.3389/fenrg.2022.1031762

Frontiers in
Energy Research

Advances and innovation in sustainable, reliable and affordable energy

Explores sustainable and environmental developments in energy. It focuses on technological advances supporting Sustainable Development Goal 7: access to affordable, reliable, sustainable and modern energy for all.

Discover the latest Research Topics

See more →

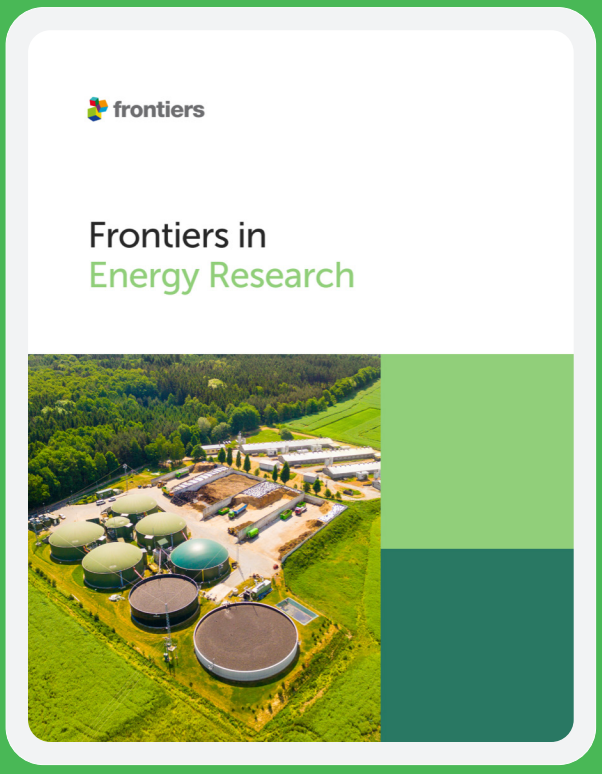

Frontiers

Avenue du Tribunal-Fédéral 34
1005 Lausanne, Switzerland
frontiersin.org

Contact us

+41 (0)21 510 17 00
frontiersin.org/about/contact